DISCRETE ELEMENT MODELLING INVESTIGATING THE EFFECT OF PARTICLE SHAPE ON BACKFILL RESPONSE BEHIND INTEGRAL BRIDGE ABUTMENTS

SACHIN RAVJEE

DISCRETE ELEMENT MODELLING INVESTIGATING THE EFFECT OF PARTICLE SHAPE ON BACKFILL RESPONSE BEHIND INTEGRAL BRIDGE ABUTMENTS

SACHIN RAVJEE

A dissertation submitted in partial fulfilment of the requirements for the degree of

MASTER OF ENGINEERING (STRUCTURAL ENGINEERING)

In the

FACULTY OF ENGINEERING

UNIVERSITY OF PRETORIA

February 2018

DISSERTATION SUMMARY

DISCRETE ELEMENT MODELLING INVESTIGATING THE EFFECT OF PARTICLE SHAPE ON BACKFILL RESPONSE BEHIND INTEGRAL BRIDGE ABUTMENTS

SACHIN RAVJEE

Supervisor:	Professor SW Jacobsz
Co-supervisor:	Doctor DN Wilke
Department:	Civil Engineering
University:	University of Pretoria
Degree:	Master of Engineering (Structural Engineering)

Integral bridges are designed without expansion joints or bearings to eliminate the maintenance and repair costs associated with them. Thus, the expansion and contraction due to daily and seasonal temperature variations of the deck of the bridge are restricted by the abutments, causing the abutments to move cyclically towards and away from the granular material used as backfill. This movement results in a stress accumulation in the backfill retained by the abutments.

A numerical sensitivity analysis was performed in this study, investigating the effect of granular particle shape on the response of backfill material retained by integral bridge abutments. The backfill was subjected to cyclic thermal loading. The particle shapes modelled included spheres, dodecahedrons, tetrahedrons, truncated tetrahedrons, triangular prisms and cubes.

The Discrete Element Method (DEM) was used to perform the numerical sensitivity analysis. The calibration of DEM and the methods used to reduce the computational times of the simulations are included. The Young’s Modulus of the DEM particles was reduced from a theoretical value of 70 GPa to 70 MPa to reduce the computational costs by a factor of 32.9. Justification for the reduction of the Young’s Modulus value is presented.

Two DEM software suites were used to perform the simulations, namely STAR-CCM+, a commercial code, and Blaze-DEM, a research code under development. Blaze-DEM was created at the University of Pretoria, which makes use of Graphics Processing Unit (GPU) computing as opposed to

traditional Central Processing Unit (CPU) computing. Blaze-DEM delivered computational times over 150 times faster than the equivalent simulation in STAR-CCM+.

Various parameters observed in the backfill were investigated for the selected particle shapes. These parameters were the bulk densities, lateral earth pressure coefficients, particle settlements, horizontal stress distributions, mean interparticle contact forces and force chains. The parameters' initial and final values, as well as the difference in these values, were analysed to perform the sensitivity analysis. The effect of the particles' sphericities and angles of repose on these parameters were studied.

It was found that the magnitudes of the horizontal stresses acting on the abutment were related to the angle of repose of a particle. The particles with higher angles of repose resulted in higher magnitudes of stresses. The amount of build-up of horizontal stresses was more closely related to the sphericity of the particle shape than its angle of repose. The particles with lower sphericities (higher angularities) experienced larger accumulations of stresses on the abutment. This was suggested to be a result of particle interlocking and reorientation.

The study also shows that Blaze-DEM can offer increased performance for DEM simulations in Geotechnical Engineering compared to commercial codes which are constrained by the computational costs. This enables parameter studies using DEM to become more feasible.

Future work includes modelling the response of non-convex polyhedral particles. The non-convex polyhedral particles are expected to enable greater degrees of reorientation and interlocking between the particles, which could result in a larger build-up of stress when compared to the spherical and convex polyhedral shapes.

DECLARATION

I, the undersigned hereby declare that:

I understand what plagiarism is and I am aware of the University’s policy in this regard;

The work contained in this thesis is my own original work;

I did not refer to work of current or previous students, lecture notes, handbooks or any other study material without proper referencing;

Where other people’s work has been used this has been properly acknowledged and referenced;

I have not allowed anyone to copy any part of my thesis;

I have not previously in its entirety or in part submitted this thesis at any university for a degree.

Signature of student:

Name of student: Sachin Ravjee

Student number: 12022820

Date: 05/02/2018

ACKNOWLEDGEMENTS

I would like to extend my sincerest gratitude to my supervisor, *Professor SW Jacobsz*, for introducing me to a topic which I have thoroughly enjoyed working on and for always having the time and willingness to assist me with my research. Thank you for your vital advice and encouragement during my time spent on this study and for allowing me the opportunity to work with you. It has been an incredible learning experience filled with enjoyment.

I would also like to express my gratitude to my co-supervisor, *Doctor DN Wilke*, for introducing me to Blaze-DEM and the tremendous capabilities it has. Thank you for your assistance and advice regarding Blaze-DEM, there were many setbacks, however, we still managed to get it done! It has been an immense pleasure to be a part of such a ground-breaking development.

Thank you to *Mr. C de Wet*, from Aerotherm, for training me in the fundamentals of STAR-CCM+ and DEM modelling and for assisting me in setting up my problem in STAR-CCM+.

I would like to thank my best friend on campus, *Louis*, who has been a tremendous help to me, both with my studies and on a personal level. Thank you for all the motivation during the last two years, particularly during the times spent at Nando’s.

I want to thank my long-time friends; *Dallion, Jeff* and *Tumie*, who constantly motivated me to complete my studies to the best of my abilities. I want to also thank them for always listening to my ramblings about “imaginary sand falling” and for always amusing me when I needed a break.

I would like to thank *Aurecon* for providing me with the financial support which allowed me to undertake my postgraduate studies.

Lastly, however certainly not least, I would like to thank *my family* for their editorial assistance of this paper. Most importantly, I would like to thank them for their tremendous love and encouragement throughout the course of my studies.

“To the edge of the universe and back.

Endure and survive”

(Neil Druckmann, The Last of Us)

TABLE OF CONTENTS

PAGE

1 INTRODUCTION 1-1

1.1 BACKGROUND 1-1
1.2 OBJECTIVE OF THE STUDY 1-2
1.3 SCOPE OF THE STUDY 1-2
1.4 METHODOLOGY 1-3
1.5 ORGANISATION OF THE REPORT 1-3

2 LITERATURE STUDY 2-1

2.1 INTRODUCTION 2-1
2.2 CONVENTIONAL BRIDGES 2-2
2.3 INTEGRAL BRIDGES 2-3
2.3.1 Types of integral bridge abutments 2-3
2.3.2 Advantages of integral bridges 2-4
2.3.3 Disadvantages of integral bridges 2-4
2.3.4 Integral bridge abutment movements 2-5
2.3.5 Integral bridge example in South Africa 2-6
2.4 EFFECTS OF INTEGRAL BRIDGE ABUTMENT MOVEMENTS 2-8
2.4.1 Backfill settlement behind the bridge abutment 2-8
2.4.2 Increase in horizontal earth pressures 2-9
2.4.3 Influence of backfill particle shape 2-13
2.4.4 Sphericity of a particle shape 2-15
2.5 DISCRETE ELEMENT METHOD 2-16
2.5.1 Description of the method 2-16
2.5.2 The calculation cycle 2-17
2.5.3 Contact models used in DEM 2-19
2.5.4 Frictional coefficients used in DEM 2-22
2.5.5 Calibration of DEM 2-23
2.5.6 Reducing computational costs of DEM 2-27
2.6 DEM SOFTWARE AND APPLICATIONS 2-29
2.6.1 CPU based DEM software packages 2-29
2.6.2 Blaze-DEM 2-30
2.6.3 Particle shapes in DEM 2-35
2.6.4 DEM versus FEM 2-39

2.6.5 Applications of DEM 2-40
2.7 SUMMARY 2-44

3 DEM MODELLING OF GRANULAR BACKFILL RETAINED BY INTEGRAL BRIDGE ABUTMENTS 3-1

3.1 INTRODUCTION 3-1
3.2 THEORETICAL INTEGRAL BRIDGE MODELLING 3-2
3.3 PARTICLE SHAPES USED IN DEM ANALYSES 3-4
3.4 INTEGRAL BRIDGE ABUTMENT MODELLING 3-9
3.4.1 Small abutment model 3-10
3.4.2 Medium abutment model 3-11
3.4.3 Large abutment model 3-12
3.5 SOFTWARE COMPARISON 3-14
3.6 PARAMETERS USED FOR DEM SIMULATIONS 3-17
3.7 CALIBRATION OF DEM PARAMETERS 3-17
3.7.1 Drop tests for particle-particle friction coefficient 3-18
3.7.2 Reduction of Young’s Modulus value 3-22
3.8 SOFTWARE AND NUMERICAL MODEL VERIFICATION TESTS 3-24
3.8.1 Software verification test 3-24
3.8.2 Particle size independence study 3-26
3.8.3 Rotation rate independence study 3-27
3.8.4 Model size independence study 3-27
3.9 PARTICLE SHAPE NUMERICAL SENSITIVITY ANALYSIS 3-28
3.10 SUMMARY 3-30

4 PRESENTATION AND ANALYSIS OF RESULTS 4-1

4.1 INTRODUCTION 4-1
4.2 CALIBRATION OF PARTICLE-PARTICLE FRICTION COEFFICIENT 4-2
4.2.1 STAR-CCM+ drop tests 4-2
4.2.2 Blaze-DEM drop tests 4-3
4.3 REDUCTION OF YOUNG’S MODULUS VALUE 4-6
4.3.1 Computational times of reduced Young’s Modulus values 4-7
4.3.2 Density and average normal particle overlap with depth 4-8
4.3.3 Coefficient of active state lateral earth pressure 4-10
4.3.4 Average normal overlap between the particles 4-11
4.4 SOFTWARE COMPARISON 4-13
4.4.1 Computational times of software packages 4-15

4.4.2 Software comparison – Spheres 4-17
4.4.3 Software comparison – Cubes 4-19
4.5 NUMERICAL MODEL VERIFICATION TESTS 4-21
4.5.1 Particle size independence study 4-22
4.5.2 Rotation rate independence study 4-24
4.5.3 Model size independence study 4-25
4.6 PARTICLE SHAPE NUMERICAL SENSITIVITY ANALYSIS 4-26
4.6.1 Bulk backfill density 4-29
4.6.2 Lateral earth pressure coefficient 4-34
4.6.3 Backfill settlement 4-38
4.6.4 Horizontal stress distribution 4-42
4.6.5 Mean interparticle contact forces 4-47
4.6.6 Force chain magnitudes 4-51
4.7 SUMMARY 4-53

5 CONCLUSIONS AND RECOMMENDATIONS 5-1

5.1 CONCLUSIONS FROM CALIBRATION TESTS 5-1
5.2 CONCLUSIONS FROM VERIFICATION TESTS 5-2
5.3 CONCLUSIONS FROM NUMERICAL SENSITIVITY ANALYSIS 5-3
5.4 RECOMMENDATIONS 5-4

6 REFERENCES 6-1

APPENDIX A: ADDITIONAL BULK DENSITY GRAPHS A-1
APPENDIX B: ADDITIONAL EARTH PRESSURE GRAPHS B-1
APPENDIX C: ADDITIONAL SETTLEMENT GRAPHS C-1

LIST OF TABLES

PAGE

Table 2.1: Material properties of quartz sand used by Derakhshani *et al. (*2015) 2-26

Table 2.2: Performance level comparison between Blaze-DEM and other codes – Cundall number (Govender *et al.*, 2016) 2-32

Table 2.3: Performance level comparison between Blaze-DEM and other codes – Computational time (Govender *et al.*, 2016) 2-32

Table 3.1: Sphericities of particle shapes used in DEM analyses 3-9

Table 3.2: Summary of processing units used for STAR-CCM+ and Blaze-DEM 3-15

Table 3.3: DEM parameters obtained from literature 3-17

Table 3.4: Varied parameters used for drop tests 3-21

Table 3.5: Varied parameters used for Young's Modulus reduction verification tests 3-24

Table 3.6: Initial and final bulk densities for software verification test with spheres 3-25

Table 3.7: Initial and final bulk densities for software verification test with cubes 3-26

Table 3.8: Varied parameters used for particle size independence study 3-26

Table 3.9: Varied parameters used for rotation rate independence study 3-27

Table 3.10: Final parameters used for numerical sensitivity analysis 3-28

Table 3.11: Varied parameters used for numerical sensitivity analysis 3-29

Table 4.1: Results of angles of repose from drop tests in STAR-CCM+ 4-3

Table 4.2: Results of angles of repose from drop tests in Blaze-DEM 4-4

Table 4.3: Summary of computational times for different Young's Modulus values 4-8

Table 4.4: Summary of computational times from software verification tests 4-16

Table 4.5: Summary of parameters for sphere comparison test 4-18

Table 4.6: Summary of parameters for cube comparison test 4-21

Table 4.7: Summary of particle size verification test 4-23

Table 4.8: Correlation coefficients obtained from bulk densities 4-34

Table 4.9: Correlation coefficients obtained from normalised lateral earth pressures 4-38

Table 4.10: Correlation coefficients obtained from backfill settlement values 4-41

LIST OF FIGURES

PAGE

Figure 2.1: Conventional bridge (Clayton *et al.* 2006) 2-2

Figure 2.2: Integral bridge (Clayton *et al.* 2006) 2-3

Figure 2.3: Four types of integral bridge abutments (Highway Agency, 2003) 2-4

Figure 2.4: Rigid body movements and bending deflections (Springman *et al.*, 1996) 2-6

Figure 2.5: Van Zylspruit Bridge under construction (Skorpen *et al.*, 2016) 2-7

Figure 2.6: Backfill settlement observed in centrifuge model after 100 cycles for: dense backfill (top) and loose backfill (bottom) (Ng *et al.*, 1998) 2-8

Figure 2.7: Backfill settlement observed in scaled model after 65 cycles (England *et al.*, 2000) 2-9

Figure 2.8: Daily build-up in granular backfill pressure observed by Khodair (2006) 2-10

Figure 2.9: Comparison between maximum measured pressure distributions with classical pressure theories (Khodair, 2006) 2-11

Figure 2.10: Curves of earth pressure coefficient against local radial strain for loose sand under a cyclic radial strain range of 0.05% (Xu *et al.*, 2007) 2-12

Figure 2.11: Scanning Electron Micrographs of: (a) Leighton Buzzard B sand and (b) glass ballotini particles (Xu *et al.*, 2007) 2-13

Figure 2.12: Influence of particle shape on stiffness of granular assembly: (a) before cycling and (b) after cycling (Xu *et al.*, 2007) 2-14

Figure 2.13: Lateral stress increases in loose sand and dense glass ballotini (Lehane, 2011) 2-15

Figure 2.14: Two discs compressed between rigid walls (Cundall and Strack, 1979) 2-18

Figure 2.15: Normal and tangential components (Boac *et al.*, 2014) 2-20

Figure 2.16: 2-clumps, 4-clumps and 8-clumps for each of the 10 particles (Coetzee, 2016) 2-23

Figure 2.17: Volume error for 10 particles versus number of sphere clumps (Coetzee, 2016) 2-24

Figure 2.18: Angle of repose versus particle-particle friction coefficient (Coetzee, 2016) 2-25

Figure 2.19: Angle of repose defined by DEM results (Nakashima *et al.*, 2011) 2-25

Figure 2.20: Effect of rolling and sliding coefficients of friction on angle of repose for quartz sand (Derakhshani *et al.*, 2015) 2-26

Figure 2.21: Chip layouts for: Quad-core Intel CPU (left) and NVIDIA Kepler GPU (right) from Govender *et al.* (2014) 2-30

Figure 2.22: Comparison of task processing between i7 Quad-core CPU and NVIDIA GK110 GPU (Govender *et al.*, 2014) 2-31

Figure 2.23: Validation between: (a) CPU and (b) GPU charge profiles with 5 344 particles (Govender *et al.*, 2015) 2-33

Figure 2.24: Validation between: (a) experimental data (Venugopal and Rajamani, 2001) and (b) GPU charge profiles with 243 particles (Govender *et al.*, 2015) 2-33

Figure 2.25: Validation between: (a) experimental data (Hlungwani *et al.*, 2003), (b) GPU and (c) CPU charge profiles with 168 particles (Govender *et al.*, 2015) 2-34

Figure 2.26: Comparison of experimental and Blaze-DEM results for hopper flow of 836 spherical particles (Govender *et al.*, 2014) 2-34

Figure 2.27: Hopper flow test results with 13 824 corn-shaped polyhedra particles (Govender *et al.*, 2014) 2-35

Figure 2.28: Restricted flow as a result of polyhedra arching (Govender *et al.*, 2014) 2-36

Figure 2.29: Particle shapes tested by Höhner *et al.* (2014) from left to right: sphere, icosahedron, dodecahedron and hexahedron 2-37

Figure 2.30: Particle shapes investigated by Höhner *et al.* (2012) 2-37

Figure 2.31: 2D DEM (a) circular and (b) pentagonal particles used by Azéma *et al.* (2009) 2-38

Figure 2.32: Normal forces in: (a) discs and (b) pentagons with line thickness proportional to the normal force (Azéma *et al.*, 2009) 2-38

Figure 2.33: Difference between FEM and DEM for granular material behaviour (Yap, 2011) 2-39

Figure 2.34: Box test samples of: (a) single-sphere clump and (b) eight-sphere clumps (Lim and McDowell, 2005) 2-40

Figure 2.35: Deformed FE mesh (left) and deformed DE granular body (right) for a rotating wall (Widulinski *et al.*, 2010) 2-41

Figure 2.36: Sample cyclically loaded by Hu *et al.* (2010) 2-42

Figure 2.37: Axial strain curves of cyclic loading obtained by Hu *et al.* (2010) 2-43

Figure 2.38: Porosity variation of cyclic loading obtained by Hu *et al.* (2010) 2-43

Figure 3.1: Theoretical integral bridge geometry 3-2

Figure 3.2: Representation of the displacement of the deck 3-3

Figure 3.3: Representation of the rotation of the abutment 3-4

Figure 3.4: DEM particle – Sphere 3-5

Figure 3.5: Maximum (left) and minimum (right) void ratios of spheres (Lu and Likos, 2004) 3-5

Figure 3.6: DEM particle – Cube 3-6

Figure 3.7: DEM particle – Triangular prism 3-7

Figure 3.8: DEM particle – Dodecahedron 3-7

Figure 3.9: DEM particle – Tetrahedron 3-8

Figure 3.10: DEM particle – Truncated tetrahedron 3-8

Figure 3.11: Small abutment model side view 3-10

Figure 3.12: Small abutment model 3-11

Figure 3.13: Medium abutment model 3-12

Figure 3.14: Large abutment model 3-13

Figure 3.15: Comparison of geometries between medium and large abutment models 3-14
Figure 3.16: Computer used for Blaze-DEM simulations 3-16
Figure 3.17: Three GPUs used for Blaze-DEM simulations 3-16
Figure 3.18: Two-sphere clumps used in drop tests 3-18
Figure 3.19: Three-sphere clumps used in drop tests 3-19
Figure 3.20: Intermediate step of drop test in STAR-CCM+ 3-20
Figure 3.21: Perspective view of intermediate step of drop test in Blaze-DEM 3-22
Figure 4.1: Angle of repose of two-sphere clumps from STAR-CCM+ 4-2
Figure 4.2: Angle of repose of spheres from Blaze-DEM 4-4
Figure 4.3: Angle of repose of dodecahedrons from Blaze-DEM 4-5
Figure 4.4: Angle of repose of tetrahedrons from Blaze-DEM 4-5
Figure 4.5: Angle of repose of cubes from Blaze-DEM 4-5
Figure 4.6: Effect of sphericity on average angle of repose 4-6
Figure 4.7: Computational time versus Young’s Modulus 4-7
Figure 4.8: Densities with depth comparison for various Young’s Modulus values 4-9
Figure 4.9: Particle overlap with depth comparison for various Young’s Modulus values 4-9
Figure 4.10: Active earth pressure coefficient comparison for various Young’s Modulus values 4-11
Figure 4.11: Average normal overlap comparison for various Young’s Modulus values 4-12
Figure 4.12: DEM model with spheres after 25 cycles in STAR-CCM+ 4-14
Figure 4.13: DEM model with spheres after 25 cycles in Blaze-DEM 4-15
Figure 4.14: Graph of computational times from software verification tests 4-16
Figure 4.15: Spheres’ earth pressure comparison between STAR-CCM+ and Blaze-DEM 4-17
Figure 4.16: Spheres’ bulk density comparison between STAR-CCM+ and Blaze-DEM 4-18
Figure 4.17: Cubes’ earth pressure comparison between STAR-CCM+ and Blaze-DEM 4-20
Figure 4.18: Cubes’ bulk density comparison between STAR-CCM+ and Blaze-DEM 4-20
Figure 4.19: Lateral earth pressure coefficient comparison for various particle sizes 4-22
Figure 4.20: Bulk density comparison of various particle sizes 4-23
Figure 4.21: Lateral earth pressure coefficient comparison for different cycling rates 4-24
Figure 4.22: Lateral earth pressure coefficient comparison for different model sizes 4-25
Figure 4.23: Bulk density comparison for different model sizes 4-26
Figure 4.24: 140 000 spheres after injection in Blaze-DEM 4-27
Figure 4.25: 110 000 dodecahedrons after injection in Blaze-DEM 4-28
Figure 4.26: 100 000 triangular prisms after injection in Blaze-DEM 4-28
Figure 4.27: Effect of sphericity on initial porosities 4-29
Figure 4.28: Bulk density comparison for various particle shapes 4-30
Figure 4.29: Effect of average AoR on increase in bulk density 4-30
Figure 4.30: Zones used for spatial density distribution investigation 4-31

Figure 4.31: Spatial density distributions for spheres 4-32
Figure 4.32: Spatial density distributions for cubes 4-32
Figure 4.33: Spatial density distributions for tetrahedrons 4-33
Figure 4.34: Effect of sphericity on spatial density distribution difference 4-33
Figure 4.35: Lateral earth pressure coefficient comparison for six particle shapes 4-35
Figure 4.36: Normalised earth pressure coefficient comparison for six particle shapes 4-36
Figure 4.37: Effect of average AoR on normalised initial earth pressure coefficient 4-37
Figure 4.38: Effect of sphericity on increase in normalised lateral earth pressure coefficient 4-37
Figure 4.39: Backfill settlement comparison for six particle shapes 4-39
Figure 4.40: Normalised backfill settlement comparison for six particle shapes 4-39
Figure 4.41: Effect of average AoR on normalised final backfill settlement values 4-40
Figure 4.42: Effect of sphericity on increase in normalised backfill settlement values 4-41
Figure 4.43: Horizontal stress distributions acting on the model abutment after 1 cycle 4-43
Figure 4.44: Horizontal stress distributions acting on the model abutment after 10 cycles 4-44
Figure 4.45: Horizontal stress distributions acting on the model abutment after 25 cycles 4-45
Figure 4.46: Difference in horizontal stress distributions between first and last cycles 4-46
Figure 4.47: Contact force distribution in spheres after first cycle 4-47
Figure 4.48: Contact force distribution in spheres after last cycle 4-48
Figure 4.49: Contact force distribution in cubes after first cycle 4-49
Figure 4.50: Contact force distribution in cubes after last cycle 4-49
Figure 4.51: Cubes from medium abutment model after first cycle in Blaze-DEM 4-50
Figure 4.52: Cubes from medium abutment model after last cycle in Blaze-DEM 4-50
Figure 4.53: Force chain magnitudes observed in selected particle shapes 4-52
Figure A.1: Effect of average AoR on initial bulk density A-2
Figure A.2: Effect of sphericity on final porosity A-2
Figure A.3: Effect of average AoR on final bulk density A-3
Figure A.4: Effect of sphericity on difference in porosity A-3
Figure A.5: Effect of average AoR on difference in spatial density distributions A-4
Figure B.1: Effect of sphericity on initial lateral earth pressure coefficients B-2
Figure B.2: Effect of sphericity on final lateral earth pressure coefficients B-2
Figure B.3: Effect of average AoR on final lateral earth pressure coefficients B-3
Figure B.4: Effect of average AoR on change in lateral earth pressure coefficients B-3
Figure C.1: Effect of sphericity on initial backfill settlements C-2
Figure C.2: Effect of sphericity on final backfill settlements C-2
Figure C.3: Effect of average AoR on final backfill settlements C-3
Figure C.4: Effect of average AoR on change in backfill settlements C-3

LIST OF EQUATIONS

PAGE

Equation 2.1: Displacement of bridge deck 2-5
Equation 2.2: Effective Bridge Temperature 2-6
Equation 2.3: Derivation of sphericity 2-16
Equation 2.4: Derivation of sphericity 2-16
Equation 2.5: Sphericity of a particle shape 2-16
Equation 2.6: Force on DEM disc 2-18
Equation 2.7: Acceleration of DEM disc 2-18
Equation 2.8: Displacement of DEM disc 2-19
Equation 2.9: Normal contact force 2-20
Equation 2.10: Tangential contact force 2-20
Equation 2.11: Normal spring stiffness 2-21
Equation 2.12: Tangential spring stiffness 2-21
Equation 2.13: Normal damping 2-21
Equation 2.14: Tangential damping 2-21
Equation 2.15: Equivalent Young’s Modulus 2-21
Equation 2.16: Equivalent radius 2-22
Equation 2.17: Equivalent Shear Modulus 2-22
Equation 2.18: Equivalent mass 2-22
Equation 2.19: Rayleigh time-step 2-27
Equation 2.20: Rayleigh velocity 2-27
Equation 2.21: Shear Modulus 2-27
Equation 2.22: DEM simulation time-step 2-28
Equation 2.23: Modified DEM simulation time-step 2-28
Equation 3.1: Active lateral earth pressure coefficient 3-23
Equation 3.2: Passive lateral earth pressure coefficient 3-29

NOMENCLATURE

a	Acceleration of DEM disc $[m/s^2]$
A_i	Cross-sectional area of the i^{th} segment $[m^2]$
A_p	Surface area of a particle shape $[m^2]$
C	Cundall Number
e	Coefficient of restitution
E	Young's Modulus $[Pa]$
E^*	Equivalent Young's Modulus $[Pa]$
EBT	Effective Bridge Temperature $[°C]$
E_i	Elastic modulus of the i^{th} segment $[Pa]$
e_n	Normal restitution coefficient
e_t	Tangential restitution coefficient
F	Force on DEM disc $[N]$
F_n	Normal contact force $[N]$
F_t	Tangential contact force $[N]$
G	Shear Modulus $[Pa]$
G^*	Equivalent Shear Modulus $[Pa]$
k	DEM disc stiffness $[N/m]$
K_a	Active lateral earth pressure coefficient
K_n	Normal spring stiffness value $[N/m]$
K_p	Passive lateral earth pressure coefficient
K_t	Tangential spring stiffness value $[N/m]$
L	Expansion length between the fixed supports $[m]$
m	Mass of DEM disc $[kg]$
m^*	Equivalent mass $[kg]$
r	Particle radius $[m]$
R^*	Equivalent radius $[m]$

s	Displacement of DEM disc $[m]$
T_i	Temperature of the i^{th} segment $[°C]$
t_R	Rayleigh time-step $[s]$
v	Velocity of DEM disc $[m/s]$
V_p	Volume of a particle shape $[m^3]$
v_R	Rayleigh velocity $[m/s]$
α	Coefficient of thermal expansion $[°C^{-1}]$
α_i	Coefficient of thermal expansion of the i^{th} segment $[°C^{-1}]$
δ	Magnitudes of overlap between DEM discs $[m]$
δ_n	Normal overlap $[m]$
δ_t	Tangential overlap $[m]$
$\dot{\delta}_n$	Normal velocity $[m/s]$
$\dot{\delta}_t$	Tangential velocity $[m/s]$
Δ	Displacement $[m]$
Δt	DEM simulation time-step $[s]$
ΔT	Change in temperature $[°C]$
η_n	Normal damping value
η_t	Tangential damping value
μ_p	Particle-particle friction coefficient
μ_r	Coefficient of rolling friction
μ_w	Particle-wall friction coefficient
ρ	Density $[kg/m^3]$
$\rho_{X,Y}$	Coefficient of correlation between parameters X and Y
ν	Poisson's ratio
Φ'	Angle of repose [°]
ψ	Sphericity of a particle shape
ω	Rotation rate

1 INTRODUCTION

1.1 BACKGROUND

Over the past 30 years, engineers have become progressively more aware of the disadvantages of the use of expansion joints and bearings in conventional bridges. These joints and bearings are known to have relatively short lifespans and are expensive to purchase, install, repair as well as maintain (Clayton *et al.*, 2006). The replacement of the expansion joints and bearings results in traffic disruptions. Failing to maintain or replace these joints and bearings when necessary may result in increased longitudinal deck loading. This may cause overstressing and damage occurring in the weaker bridge components (Biddle *et al.*, 1997).

Integral bridges are designed without expansion joints or bearings where the abutments are connected to the superstructure. This design eliminates the problems associated with these joints and bearings present in conventional bridges. Integral bridge designs have been widely adopted in the USA as well as the UK. The use of integral bridges simplifies the construction process, reduces maintenance costs, removes the cost of movement joints and bearings as well as provides greater earthquake resistance (Biddle *et al.*, 1997).

A problem that arises with integral bridges is related to the temperature variations experienced by the deck. With no joints or bearings present, the expansion and contraction of the deck cause the abutments of a bridge to move cyclically towards and away from the granular backfill it retains (Clayton *et al.*, 2006). Therefore, as a result of the movements of the abutment, the granular backfill retained by the abutments is exposed to temperature induced cyclic loading.

Previous research has shown that the particle shape of the granular backfill retained by integral bridge abutments plays a significant role in the development of the lateral earth pressures acting on it. It was found that particle shapes which could allow possible interlocking resulted in a larger build-up of horizontal stresses in the granular backfill. The particle shape, specifically its sphericity, has a considerable effect on the accumulation of the earth pressures acting on the abutment (Xu *et al.*, 2007).

The Discrete Element Method (DEM), proposed by Cundall and Strack (1979), is a popular computational method which can be used to analyse, design and optimise bulk systems with varying shapes of granular materials. Therefore, this method is well suited to be used to investigate the effects of granular particle shape on the response of backfill material retained by integral bridge abutments.

1.2 OBJECTIVE OF THE STUDY

The objective of the study was to use the Discrete Element Method to perform a numerical sensitivity analysis, investigating the effect of granular particle shape on the response of backfill material retained by integral bridge abutments. This was performed by considering the effect of the particles' sphericities and angles of repose on the following parameters during cyclic thermal displacements of a model abutment:

- The changes in bulk density of the granular backfill in the model.
- The lateral earth pressure coefficients mobilised in the backfill retained by the abutment.
- The particle settlements of the backfill.
- The changes in horizontal stress distributions of the backfill acting on the abutment.
- The mean interparticle contact forces in the granular backfill.
- The force chain distributions in the backfill.

1.3 SCOPE OF THE STUDY

The numerical sensitivity analysis in this study was performed using DEM simulations. The particles used in the simulations were calibrated to a desired angle of repose by performing drop tests with only gravitational loads. Two software packages were used for the simulations, namely, STAR-CCM+ and Blaze-DEM. Six different shaped particles were used with varying sphericities. These shapes ranged from perfect spheres (highest sphericity) to tetrahedrons (highest angularity).

The following restrictions and approximations were present in this study:

- The drop tests used to calibrate the particle-particle friction coefficient were only performed in STAR-CCM+ with spheres.
- The DEM simulations performed only modelled a portion of the abutment and adjacent granular backfill in contact with it.
- The deck of the model integral bridge was assumed to freely expand and contract with temperature variations.
- No physical experiments were performed to validate the results of the sensitivity analysis.
- A single set of material properties for the backfill material was considered for the sensitivity analysis.

1.4 METHODOLOGY

The following methodology was followed during the course of this study:

- A literature study was compiled on integral bridge abutments and the effect of cyclic thermal loads on the backfill material. Research was conducted on DEM modelling of granular materials as well as the calibration of the DEM particles. Further research was performed on reducing the computational times of DEM simulations.
- Drop tests were performed in STAR-CCM+ to calibrate the particle-particle friction coefficient of the particles used in the DEM simulations.
- The Young's Modulus value of the DEM particles was reduced to speed up the computational times. Simulations were performed in STAR-CCM+ to determine the extent to which the value could be reduced, while still delivering realistic results. The lateral earth pressures, densities with depth and overlaps between the particles were investigated to verify the performance of the reduced Young's Modulus values.
- Two sets of simulations were performed in STAR-CCM+ and Blaze-DEM to verify the results from Blaze-DEM, since Blaze-DEM is a research code under development.
- The numerical sensitivity analysis was performed in Blaze-DEM using spheres and the following polyhedral shaped particles: dodecahedrons, tetrahedrons, truncated tetrahedrons, triangular prisms and cubes. Support for polyhedral shaped particles was only introduced in STAR-CCM+ in July 2017.
- The results from the numerical sensitivity analysis were investigated. The bulk densities, lateral earth pressure coefficients, particle settlements, horizontal stress distributions, mean interparticle contact forces and force chains of the granular backfill were studied and compared.
- The relevant conclusions were made based on the results of the sensitivity analysis and recommendations for further work was presented.

1.5 ORGANISATION OF THE REPORT

The report covers the following chapters and their respective contents:

- Chapter 1 serves as an introduction to the study. The objectives, scope and methodology of the study are presented.
- Chapter 2 covers a literature study which first focuses on integral bridge abutments and the effect of temperature-induced cyclic movements of the abutment on the granular backfill it

retains. Secondly, DEM modelling of granular materials is discussed. Lastly, the calibration and reduction of the computational times in DEM modelling are highlighted.

- Chapter 3 describes the methods used to model integral bridge abutments with DEM. The chapter includes a description of the calibration and verification tests performed. The method followed to perform the numerical sensitivity analysis of granular backfill particle shape retained by integral bridge abutments is described.
- Chapter 4 comprises of the results of the calibration and verification tests. The chapter includes the results and a discussion of the numerical sensitivity analysis performed in Blaze-DEM.
- Chapter 5 consists of the conclusions drawn based on the results of the verification and calibration tests as well as the results of the numerical sensitivity analysis. The recommendations for further research are included in this chapter.

2 LITERATURE STUDY

2.1 INTRODUCTION

An integral bridge is designed as a single structural unit. The abutments of an integral bridge are constructed without expansion joints or bearings where the superstructure is connected. The advantages of integral bridges include a faster and simpler construction process as well as the reduction of maintenance and repair costs. The need for integral bridges resulted from the excessive repair costs of the joints and bearings used in conventional bridges (Bloodworth *et al.*, 2012).

The problem that arises with integral bridges is the daily and seasonal temperature variations which cause expansion and contraction of the deck. These thermal variations in the deck cause a cyclical loading of the abutment. Previous research has shown that this loading may cause a build-up of horizontal stresses in the granular backfill retained by the abutment (Xu *et al.*, 2007).

Research by Xu *et al.* (2007) and Clayton *et al.* (2006) found that the shape of a particle, specifically its sphericity, used as granular backfill plays a significant role in the amount of stress accumulation as a result of the cyclical loading. The Discrete Element Method (DEM) proposed by Cundall and Strack (1979) is a popular computational method used to analyse, design and optimise bulk systems with varying shapes of granular materials.

This chapter presents available literature regarding integral bridge abutments. The types of integral bridge abutments, as well as the advantages and disadvantages of integral bridges, are discussed. The chapter focuses on the rotational movements of the abutment caused by daily and seasonal temperature variations. The effects of these movements on the behaviour of the granular backfill retained by the abutment are presented.

A description of DEM modelling is shown along with the contact models which it requires. Previous research which has been done using DEM, which focussed on the behaviour of granular materials for different particle shapes, is also included. The calibration of the frictional parameters used in DEM as well as the benefits and limitations of this method are presented. Common practices to reduce the computational costs of DEM simulations are given with examples from previous research.

A number of available DEM packages are discussed which include STAR-CCM+, a commercial package, as well as Blaze-DEM, a high-performance Graphics Processing Unit (GPU) based framework which allows for the simulation of spherical, convex polyhedral and non-convex polyhedral particles.

2.2 CONVENTIONAL BRIDGES

Daily and seasonal temperature variations cause the deck of a bridge to expand and contract. However, the abutments which support the deck remain spatially fixed as they are not exceedingly sensitive to changes in air temperature. Conventional bridges make use of expansion joints and bearings to accommodate the relative movement between the deck and the abutments. This prevents temperature-induced stresses from developing between the abutments and the superstructure (Clayton *et al.*, 2006). Figure 2.1 shows an illustration of a conventional bridge with expansion joints and bearings.

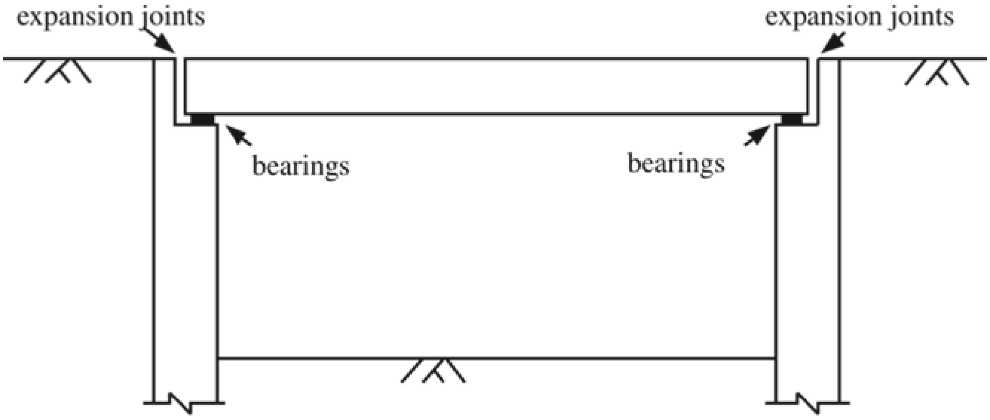

Figure 2.1: Conventional bridge (Clayton *et al.* 2006)

Expansion joints and bearings are known to have relatively short lifespans. These joints and bearings are expensive to purchase, install, repair and maintain (Clayton *et al.*, 2006). The inevitable need for replacement of these joints and bearings cause traffic disruptions. Failing to maintain or replace the expansion joints and bearings when necessary may result in increased longitudinal deck loading. This may cause overstressing and damage to occur in the weaker bridge components (Biddle *et al.*, 1997).

Over the past 30 years, engineers have become progressively more aware of the disadvantages of the use of expansion joints and bearings in bridges (Clayton *et al.*, 2006).

2.3 INTEGRAL BRIDGES

Integral bridges have been designed to eliminate the problems associated with expansion joints and bearings. Since there are no bearings or joints present in an integral bridge, the bridge can be viewed as a single structural unit. The use of integral bridges simplifies the construction process, reduces maintenance costs, removes the cost of movement joints and bearings as well as provides greater earthquake resistance (Biddle *et al.*, 1997).

The above-mentioned advantages point toward the reason that integral bridges have been widely adopted in the USA as well as the UK. However, there are still concerns regarding the levels of lateral stresses that may be imposed on the integral bridge abutments (Biddle *et al.*, 1997). An illustration of an integral bridge, which can be viewed as a single structural unit, is illustrated in Figure 2.2.

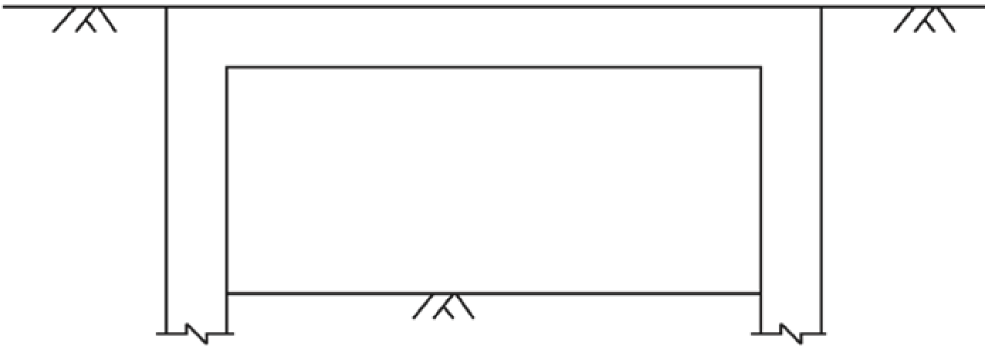

Figure 2.2: Integral bridge (Clayton *et al.* 2006)

2.3.1 Types of integral bridge abutments

The Design Manual for Roads and Bridges from the UK (Highway Agency, 2003) has identified four types of integral bridge abutments, namely frame, embedded, bank pad and end screen abutments. Figure 2.3 depicts these four types of abutments.

The frame and embedded abutments are considered to be full height abutments since the backfill is retained over the full height of the bridge. The frame abutment behaves as a retaining wall against the embankment earth pressure and supports the vertical load from the bridge. The depth of the embedded abutment extends below the retained backfill (Highway Agency, 2003).

The bank pad and end screen abutments are known as shallow abutments as only a shallow layer of granular backfill is retained behind the abutment. The bank pad abutment behaves as an end support for the thermal expansion and contraction movements of the bridge in the horizontal direction. The end screen abutments act as a retaining wall and transfer the vertical loads to separate supports (Highway Agency, 2003).

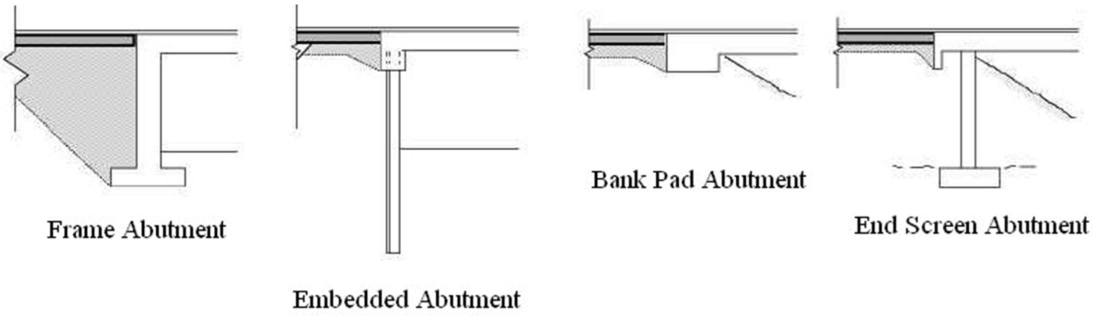

Figure 2.3: Four types of integral bridge abutments (Highway Agency, 2003)

2.3.2 Advantages of integral bridges

Some of the major advantages of integral bridges include the reduction of the maintenance required, as well as the simpler and quicker construction of the bridge (Biddle *et al.*, 1997). However, previous research has been done to identify other possible advantages of integral bridges as opposed to traditional bridges.

Mourad and Tabsh (1999) performed a numerical study to compare the transverse and longitudinal stresses in the deck slab for integral and conventional bridges. The results from the study indicated that the loads in the deck slab are more uniformly distributed in the integral bridges when compared to the equivalent jointed bridges.

The maximum stresses measured by Mourad and Tabsh (1999) in the transverse direction of the deck slab of the integral bridge were 25% to 50% lower than in the corresponding conventional bridge. This was suggested to be a result of the integral joints providing a partially fixed connection, which reduced the maximum bending moment experienced by the superstructure of the bridge.

2.3.3 Disadvantages of integral bridges

The major problem with integral bridges arises from the temperature variations experienced by the deck. Since there is an integral connection between the abutments and the superstructure, the abutments are forced to move relative to the granular backfill it retains. The abutments move away from the backfill when the deck contracts as a result of a temperature decrease and move towards the backfill when the bridge expands as a result of a temperature increase (Xu *et al.*, 2007).

Due to the movements of the abutments, the granular backfill retained by the abutment is exposed to temperature induced cyclic loading. Uncertainties about the ultimate magnitude of the lateral earth pressure behind the abutments have arisen. Limited experimental research has been performed on the development of these earth pressures (Xu *et al.*, 2007).

Centrifuge tests have been carried out by Springman *et al.* (1996), Ng *et al.* (1998) and Tapper and Lehane (2004), as well as small-scale tests under normal gravity by England *et al.* (2000), Goh (2001) and Cosgrove and Lehane (2003).

2.3.4 Integral bridge abutment movements

Solar radiation and changes in the outside temperature cause the deck of the bridge to expand and contract. These movements, Δ, can be estimated as shown by Roeder (2003) with Equation 2.1 as follows.

$$\Delta = \alpha L \Delta T \tag{2.1}$$

With:

Δ	Displacement $[m]$
α	Coefficient of thermal expansion $[°C^{-1}]$
L	Expansion length between the fixed supports $[m]$
ΔT	Change in temperature $[°C]$

A free expansion is assumed for the deck of the bridge when calculating the movements with Equation 2.1. However, Bloodworth *et al.* (2012) stated that the movements of the deck are not free to expand and contract since the deck is constrained by the abutments and the granular backfill it retains. The backfill retained by integral abutments experiences a complex type of loading, where the total vertical stress remains approximately constant, while the horizontal stress varies. Bloodworth *et al.* (2012) also suggested that the imposed cyclic strain magnitudes are small and that the backfill stiffness has a negligible effect in restraining the deck.

Emerson (1976) stated that the Effective Bridge Temperature (EBT) should be used when calculating the movements of the deck. The EBT is defined as an average temperature within the superstructure which governs the longitudinal movement of the deck. Roeder (2003) stated that the EBT can be calculated with Equation 2.2 as follows:

$$EBT = \frac{\sum A_i E_i \alpha_i T_i}{\sum A_i E_i \alpha_i} \tag{2.2}$$

With:

EBT	Effective Bridge Temperature $[°C]$
A_i	Cross-sectional area of the ith segment $[m^2]$
E_i	Elastic Modulus of the ith segment $[Pa]$
α_i	Coefficient of thermal expansion of the ith segment $[°C^{-1}]$
T_i	Temperature of the ith segment $[°C]$

Springman *et al.* (1996) identified two possible forms of abutment movements, namely rigid body motions (rotational or translational) and bending deflections, as depicted in Figure 2.4. Rigid body motions, specifically rotational movements, of the abutments are more common than bending deflections as reported in the literature on field observations of integral bridges (Yap, 2011).

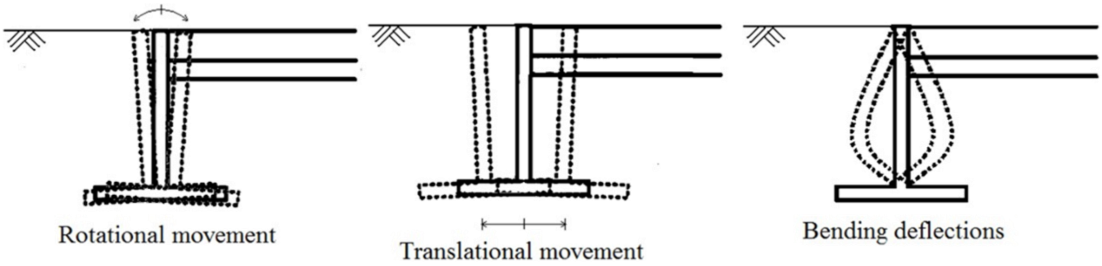

Figure 2.4: Rigid body movements and bending deflections (Springman *et al.*, 1996)

2.3.5 Integral bridge example in South Africa

The Van Zylspruit Bridge is a reinforced concrete, 90 m long, 5 span, fully integral bridge on the N1 between Bloemfontein and Colesberg in South Africa. The Civil Engineering Department at the University of Pretoria is monitoring the bridge to investigate integral bridges in a South African climate (hot and dry), where they have not been widely used

(Skorpen *et al.*, 2016). Figure 2.5 shows a picture of the Van Zylspruit Bridge during construction in May 2016.

Figure 2.5: Van Zylspruit Bridge under construction (Skorpen *et al.*, 2016)

The Van Zylspruit Bridge was instrumented with strain gauges across the bridge to measure strain and temperature changes. The abutments of the bridge were instrumented with accelerometers and pressure cells to monitor the abutment movements as well as the earth pressures acting on them. Thermocouples were placed along the deck of the bridge to measure the temperature gradient (Skorpen *et al.*, 2016).

Skorpen *et al.* (2016) calculated the Effective Bridge Temperature, as proposed by Emerson (1976), from the thermocouple data obtained. It was found that the average change in daily temperature of the EBT measured over a 4-month period was 6 °C. The maximum daily temperature change was found to be 8.2 °C for the same period. Skorpen *et al.* (2016) also found that the maximum change in the EBT over a 5-month period could be as high as 36 °C for the Van Zylspruit Bridge.

The daily and seasonal EBT changes play a key role in predicting the movements of the abutments of the bridge. There are extensive uncertainties regarding the estimation of the lateral stresses which develop in the abutments of integral bridges as a result of these thermal movements. The effect of these abutment movements on the build-up of lateral earth pressures needs to be further studied (Bloodworth *et al.*, 2012).

2.4 EFFECTS OF INTEGRAL BRIDGE ABUTMENT MOVEMENTS

The effects of the cyclic movements of the integral bridge abutments due to seasonal and daily temperature changes are separated into two categories. These categories include backfill settlement behind the bridge abutment and an increase in horizontal earth pressure (Yap, 2011).

2.4.1 Backfill settlement behind the bridge abutment

Ng *et al.* (1998) used centrifuge models of an integral bridge abutment with loose and dense backfill which was cyclically loaded. After 100 cycles of 60 mm perturbations, the loose backfill developed a uniform gradient of backfill settlement, while significant backfill settlement also occurred for the dense backfill. Figure 2.6 shows observable backfill settlement with a sketch of the centrifuge model after 100 cycles. This settlement was suggested to be the result of strain ratcheting, horizontal sliding, backfill densification and the rocking motion of the abutment.

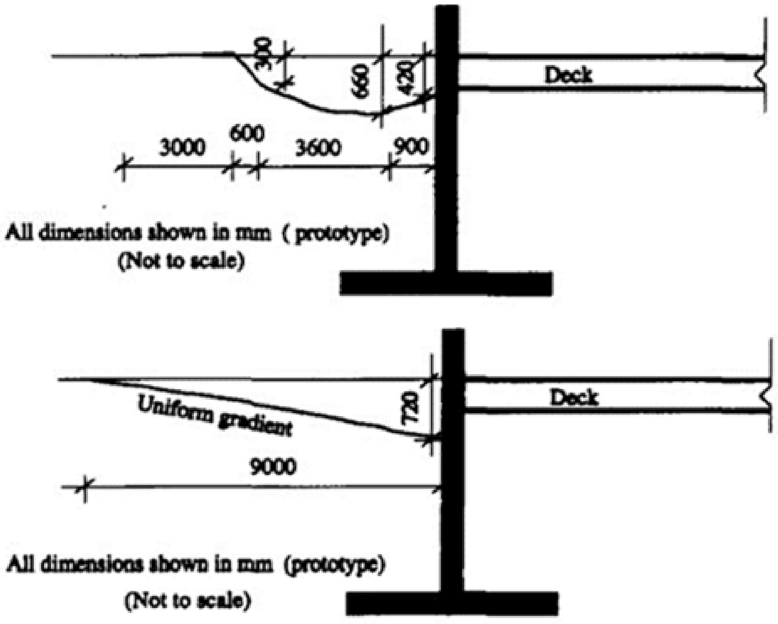

Figure 2.6: Backfill settlement observed in centrifuge model after 100 cycles for: dense backfill (top) and loose backfill (bottom) (Ng *et al.*, 1998)

England *et al.* (2000) performed similar tests to Ng *et al.* (1998) using a scaled model retaining wall. Figure 2.7 illustrates the backfill settlement from the model after 65 seasonal cycles of 65 mm perturbations. The extent of settlement adjacent to the abutment was suggested to be caused by the magnitude of the EBT fluctuations and the bridge dimensions, which was effectively the magnitude of the integral bridge abutment movement.

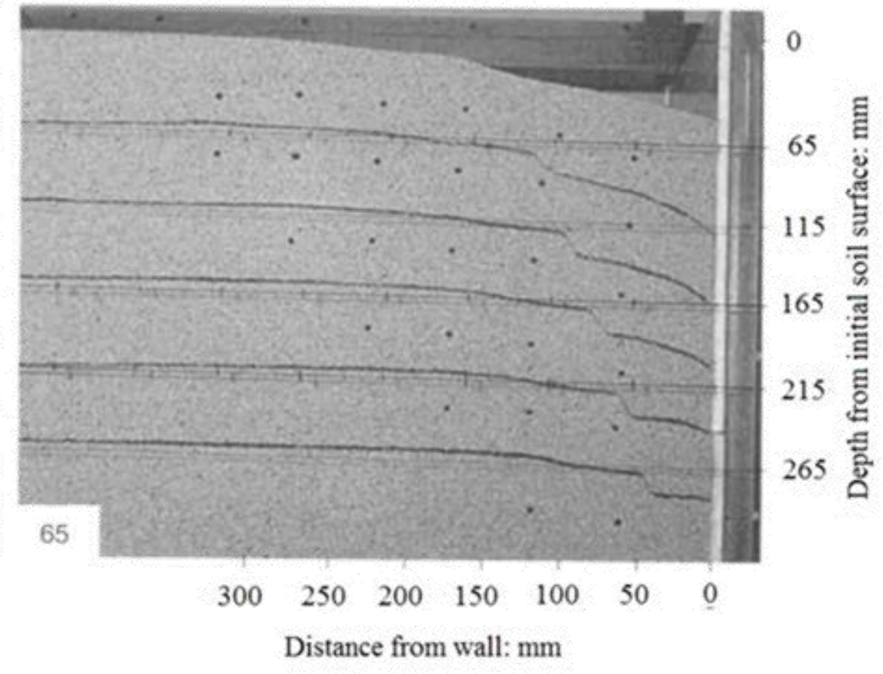

Figure 2.7: Backfill settlement observed in scaled model after 65 cycles (England *et al.*, 2000)

Cosgrove and Lehane (2003) performed a scaled model, laboratory test of an abutment with loose backfill. The abutment was cyclically rotated and this resulted in significant volumetric contraction of the sand mass near the abutment. Active conditions of the backfill were reached from the first cycle of applied displacements at the top of the abutment. The sand contraction which occurred was within the associated active wedge as well as where significant surface settlement occurred.

The tests performed by Ng *et al.* (1998), England *et al.* (2000) as well as Cosgrove and Lehane (2003) showed that the settlement observed in the granular backfill retained by integral bridge abutments is primarily due to the daily and seasonal cyclic thermal loading effects.

2.4.2 Increase in horizontal earth pressures

An integral bridge which crosses the Millers River between the towns of Orange and Wendell in the US was instrumented and monitored for a period of three years from 2002 to 2004. The bridge has a total length of 82.3 m, supported on integral abutments at each end, and consists of three continuous spans. The peak earth pressure at a total depth of 2.5 m from the top of the abutment was observed to increase yearly from 245 kPa in 2002 to 280 kPa in 2003 and 315 kPa in 2004. Increases in earth pressure were also observed from the pressure cells located at various other depths behind the abutment (Breña *et al.*, 2007).

Khodair (2006) also observed the behaviour of granular backfill retained behind an integral abutment subjected to cyclic loading. The bridge monitored is a 90.9 m long, two-span, continuous steel-girder structure with integral abutments at both ends in Scotch Road, Trenton, New Jersey (USA). The bridge was instrumented with thermocouples, strain gauges and pressure gauges during construction and was continually monitored for two years thereafter. It was observed by Khodair (2006), that a steady build-up of backfill pressure was measured behind the abutment. This pressure build-up was a result of sand particle flow and densification due to cyclic loading. Figure 2.8 illustrates the pressure build-up on the abutment at different time intervals during a single day.

Khodair (2006) compared the maximum measured pressure distribution in the abutment with the calculated pressure distributions according to Rankine theory as presented in Figure 2.9. The figure shows that Rankine theory failed to predict the actual shape of the granular backfill pressures for integral abutments subjected to cyclic loading.

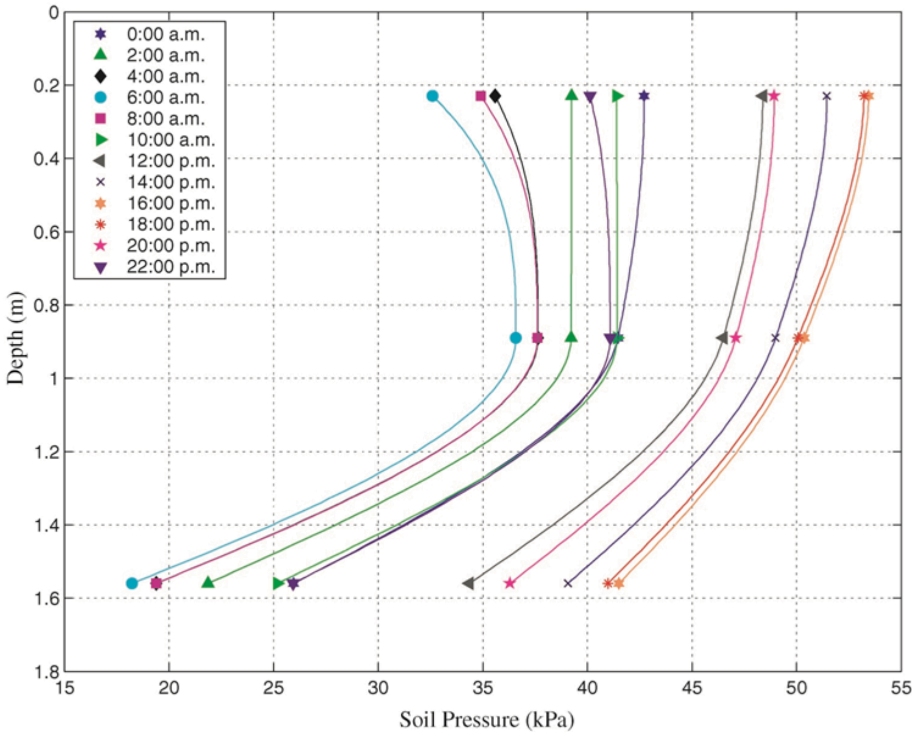

Figure 2.8: Daily build-up in granular backfill pressure observed by Khodair (2006)

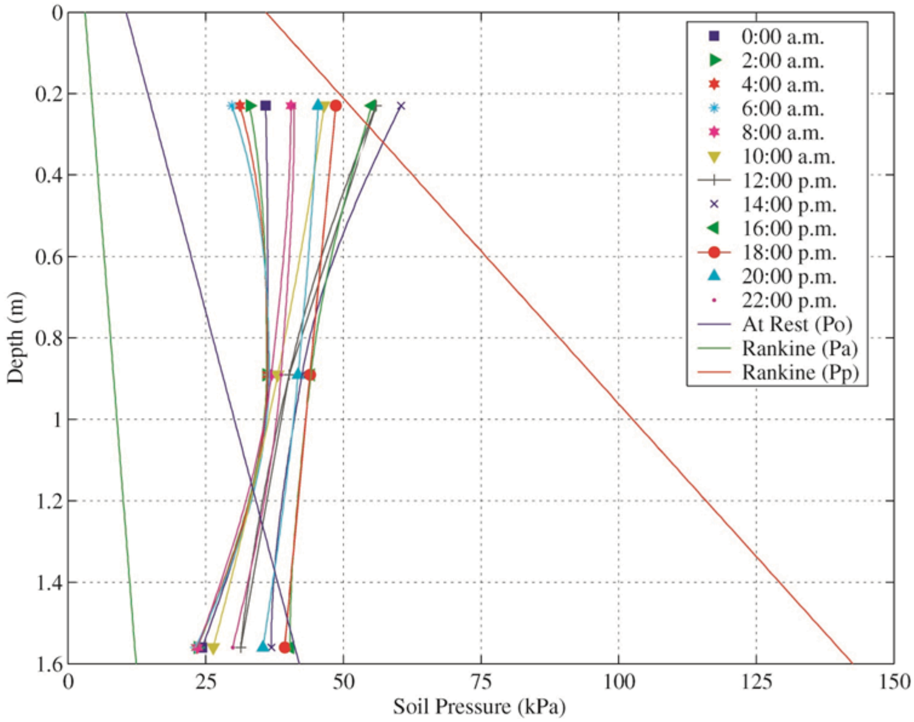

Figure 2.9: Comparison between maximum measured pressure distributions with classical pressure theories (Khodair, 2006)

Xu *et al.* (2007) performed deviator stress, cyclic loading laboratory tests on Leighton Buzzard Fraction B sand. The radial strain-controlled cycles were performed under undrained conditions. For the cyclic loading tests, the rate of relaxation of the deviator stress was allowed to reduce to less than 1% of the initial deviator stress increase rate before the next radial strain excursion was performed. The stress-strain behaviour of the sand was found to be highly non-linear and non-symmetrical under cyclic loading. Figure 2.10 shows the curves of the earth pressure coefficient (K) against local radial strain for loose sand under a cyclic radial strain range of 0.05%.

For the experiment performed by Xu *et al.* (2007), radial extension was equivalent to the integral abutment moving away from the backfill and radial compression was equivalent to the abutment moving towards the backfill. The value of K decreased sharply with each radial extension cycle and the specimen approached the active conditions quickly. During each radial compression, K increased to its maximum value. There was an accumulation in the maximum lateral pressure with cycling, without any sign of stabilising after 100 cycles.

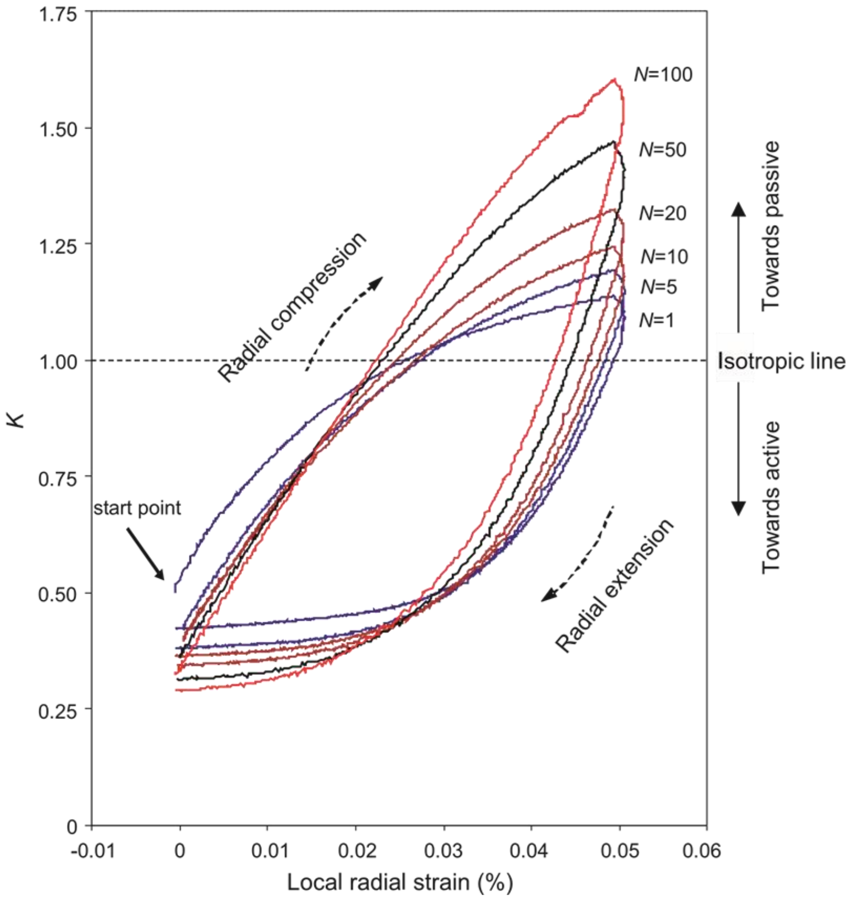

Figure 2.10: Curves of earth pressure coefficient against local radial strain for loose sand under a cyclic radial strain range of 0.05% (Xu *et al.*, 2007)

Barker and Carder (2001) monitored the field performance of a two-span integral bridge with a total length of 50 m in North Yorkshire in the UK. Measurements were obtained during construction and over the first three years of service. The lateral earth pressures measured after backfilling were consistent with the values predicted from the coefficient of earth pressure at rest (K_0). The coefficient was calculated based on an estimated value of effective angle of friction (ϕ'). The data indicated that the lateral earth pressures were slightly higher than the K_0 values each following summer.

The work done by Breña *et al.* (2007), Khodair (2006), Xu *et al.* (2007) as well as Barker and Carder (2001) showed that the cyclic thermal movements of integral bridges abutments result in lateral earth pressure build-up in the granular backfill.

2.4.3 Influence of backfill particle shape

Xu *et al.* (2007) performed cyclic loading laboratory tests on two types of materials, namely Leighton Buzzard Fraction B sand and spherical glass ballotini. The sand was coarse and was tested to study the behaviour of granular materials used as backfill retained by integral bridge abutments. The glass ballotini had a diameter of 1 mm and was tested to study the influence of the particle shape of backfill used behind integral abutments. Figures 2.11 (a) and (b) depict the results of a Scanning Electron Microscope (SEM) used to inspect the particle shape of the Leighton Buzzard B sand and glass ballotini respectively. Figure 2.11 (a) illustrates that the Leighton Buzzard Fraction B sand was quite rounded, however, was not completely spherical, while Figure 2.11 (b) shows that the glass ballotinis were perfect spheres.

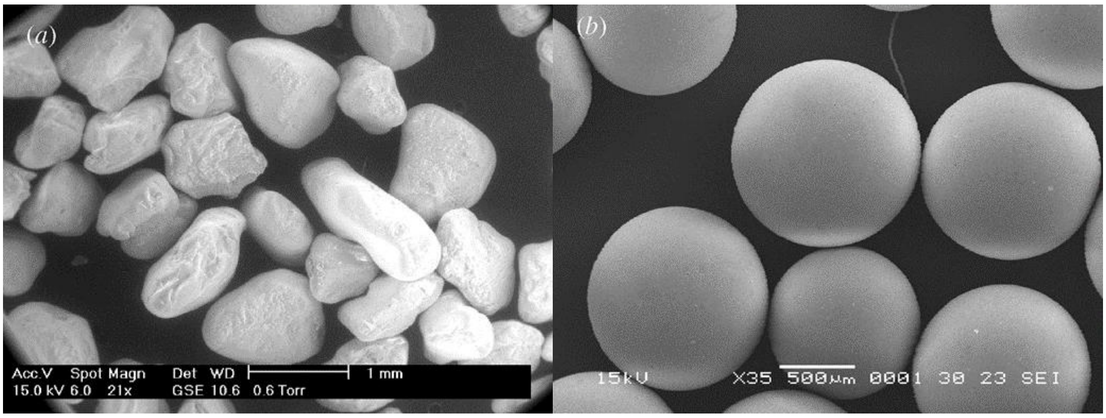

Figure 2.11: Scanning Electron Micrographs of: (a) Leighton Buzzard B sand and (b) glass ballotini particles (Xu *et al.*, 2007)

The tests by Xu *et al.* (2007) were performed on three types of densities, namely loose, dense and very dense specimens. The test results indicated that the mechanism leading to a progressive horizontal stress increase during thermal cyclic loading was not related to the densification of the backfill.

The strain-controlled stress path triaxial tests performed by Xu *et al.* (2007) indicated that the gradual increase of maximum horizontal stress during cycling was related to the rotation of the particles. A build-up of horizontal stress with horizontal strain cycling was observed for the Leighton Buzzard B sand over a wide range of densities. These results indicated that it is associated with the irregular, albeit rounded, particle shape and is not a result of the densification during cycling. No significant signs of stress increases were apparent for the perfectly spherical glass ballotini, even for wide ranges of cyclic strain levels.

The importance of the effect of the particle shape on the behaviour of granular materials is highlighted by the difference in behaviour between the glass ballotini and the sand specimens. Xu *et al.* (2007) suggested that the build-up of lateral stress in the sand specimens are a result of increased grain interlocking that develops between the particles as the number of load cycles increases. This interlocking is achieved progressively as the particles rotate when close to the active state. Figure 2.12 illustrates this proposed mechanism of interlocking. The void ratio in Figure 2.12 (a) is smaller, however, the assembly in Figure 2.12 (b) achieves a higher stiffness as a result of a larger degree of interlocking. The degree of interlocking during cycling was not increased for the spherical glass ballotini.

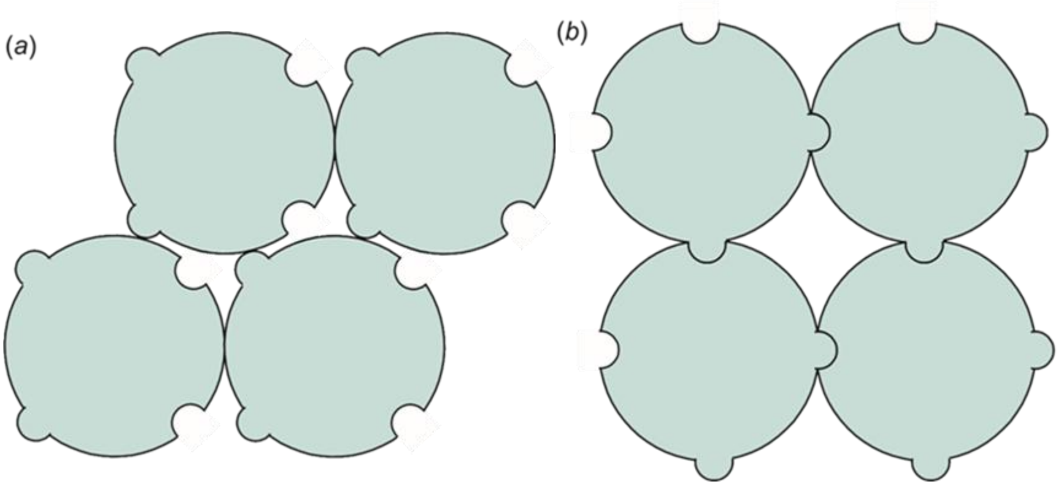

Figure 2.12: Influence of particle shape on stiffness of granular assembly: (a) before cycling and (b) after cycling (Xu *et al.*, 2007)

Lehane (2011) performed centrifuge experiments on loose University of Western Australia (UWA) sand and dense glass ballotini spheres. The specimens were cyclically loaded several times. Figure 2.13 presents the increases in lateral stress as the materials were cyclically loaded. These results contradict the findings obtained from Xu *et al.* (2007) as the lateral stresses in the ballotini spheres increased at the same rate as in the loose sand. The values of lateral stress in both the silica sand and the ballotini increased by a factor of 3 after 100 cycles.

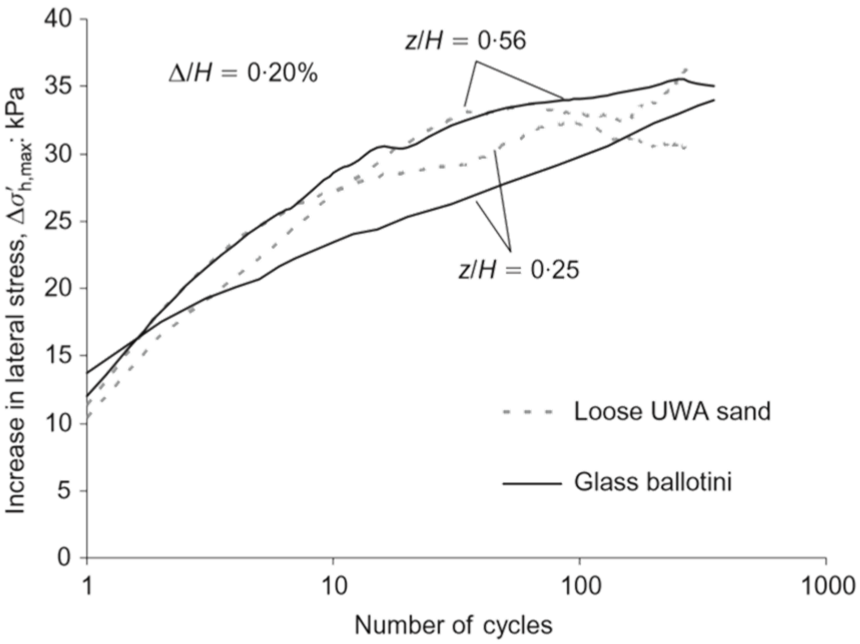

Figure 2.13: Lateral stress increases in loose sand and dense glass ballotini (Lehane, 2011)

The tests performed by Xu *et al.* (2007) showed that the shape, specifically its sphericity, of the granular backfill particles plays an important role in the lateral earth pressure build-up behind integral bridge abutments.

2.4.4 Sphericity of a particle shape

To be able to study the effect of different particle shapes used as backfill retained by integral bridge abutments, the shapes require classification. Wadell (1935) proposed a formula to measure the sphericity of a particle shape. The sphericity is the measure of how closely the shape of a particle approaches that of a mathematically perfect sphere.

The sphericity is defined as the surface area of a sphere with the same volume as the particle shape considered, divided by the actual surface area of that particle. The sphericity of a shape is a dimensionless parameter which ranges from values of 0 to 1. A perfect sphere has a sphericity of 1.

The derivation of sphericity is obtained by first relating the surface area of a sphere $(A_s = 4\pi r^2)$ to its volume $\left(V_p = \frac{4\pi}{3} r^3\right)$. This is illustrated in Equations 2.3 and 2.4 as follows:

$$A_s^3 = (4\pi r^2)^3 = 4^3\pi^3 r^6 = 4\pi \cdot 3^2 \left(\frac{4^2\pi^2}{3^2} r^6\right) = 36\pi \left(\frac{4\pi}{3} r^3\right)^2 = 36\pi V_p^2 \tag{2.3}$$

$$\therefore A_s = \left(36\pi V_p^2\right)^{\frac{1}{3}} = 36^{\frac{1}{3}}\pi^{\frac{1}{3}}V_p^{\frac{2}{3}} = 6^{\frac{2}{3}}\pi^{\frac{1}{3}}V_p^{\frac{2}{3}} = \pi^{\frac{1}{3}}\left(6V_p\right)^{\frac{2}{3}} \tag{2.4}$$

The sphericity of a shape can then be calculated using Equation 2.5 as follows:

$$\psi = \frac{A_s}{A_p} = \frac{\pi^{\frac{1}{3}}\left(6V_p\right)^{\frac{2}{3}}}{A_p} \tag{2.5}$$

Where:

ψ	Sphericity of a particle shape
V_p	Volume of a particle shape $[m^3]$
A_p	Surface area of a particle shape $[m^2]$

The sphericity of a particle can be used to classify the shapes of different particles used as granular backfill retained by integral bridge abutments subject to cyclic thermal loads.

2.5 DISCRETE ELEMENT METHOD

The Discrete Element Method was first proposed as a calculation cycle that is repeated to solve for forces, accelerations and finally displacements of discs in two dimensions (Cundall and Strack, 1979). This method has been modified to work with spheres in three dimensions (Cundall, 1988). The method makes use of discs defined in terms of geometry and stiffness. The forces on these discs are found using a force-displacement law. These resulting forces are then substituted into Newton’s second law to obtain the accelerations. The accelerations are then used with equations of motion to solve for the displacements of the discs. DEM analyses compose of cycling through a force-displacement law and the laws of motion to solve boundary value problems in a particulate medium (Cundall and Strack, 1979).

2.5.1 Description of the method

The Discrete Element Method finds the equilibrium contact forces and displacements of a disc through a series of calculations which trace the movements of individual particles. These movements are a result of imposed disturbances originating at the boundaries. The speed of the spread of disturbances is a function of the physical properties of the discrete medium. To describe this dynamic behaviour numerically, time steps are taken over stages in which the velocities and accelerations are assumed to be constant (Cundall and Strack, 1979).

The time step is chosen to be small enough that disturbances can only propagate from any disc to its immediate neighbours. The resultant forces can then be determined at any time by its interaction with the discs which it is in contact with. This feature allows DEM to follow a non-linear interaction between a large number of discs without extreme memory requirements or the need for an iterative process (Cundall and Strack, 1979).

2.5.2 The calculation cycle

The calculations used in DEM modelling are derived from two laws used in general physics, i.e. Newton’s second law applied to the discs and a force-displacement law applied to the contacts. The motion of a disc as a result of the forces acting on it is given by Newton’s second law. The contact forces resulting from displacements are found from the force-displacement law (Cundall and Strack, 1979).

The deformations of the individual particles of DEM used by Cundall and Strack (1979) are small when compared to the deformations of a granular assembly as a whole. The deformations of a granular assembly are largely due to the particles moving as rigid bodies. This means that the particle deformations do not necessarily need to be modelled exactly to obtain an accurate approximation of the mechanical behaviour. Particles may slightly overlap one another at contact points to act as an equivalent to the deformations of the individual particles. Cundall and Strack (1979) state that these overlaps are small with respect to the size of the particles.

Figure 2.14 (a) demonstrates how forces and displacements are determined in the DEM calculation cycle. The figure shows two weightless discs, namely disc x and disc y, being squashed between a pair of rigid walls. The walls are moved together at a constant velocity, denoted by v, at time, $t = t_0$, when the discs and walls are just touching each other and when there are no contact forces between them yet. The walls move inward at distances, $v\Delta t$, after a time step Δt. Adhering to the assumption that the disturbances can only propagate from one disc to its immediate neighbours, both discs are therefore assumed to maintain their initial positions from times $t = t_0$ to $t = t_1 = t_0 + \Delta t$.

Figure 2.14 (b) depicts the overlaps that exist at points A and C on the rigid walls at the time $t_1 = t_0 + \Delta t$. These overlaps have a magnitude of $\delta = v\Delta t$. There is no overlap between the discs at time t_1. Figure 2.14 (c) shows the contacts and their magnitudes at the time

$t_2 = t_0 + 2\Delta t$. An overlap exists between the discs at time t_2. Cundall and Strack (1979) gives a more detailed derivation of the calculations behind DEM which uses the above-mentioned variables.

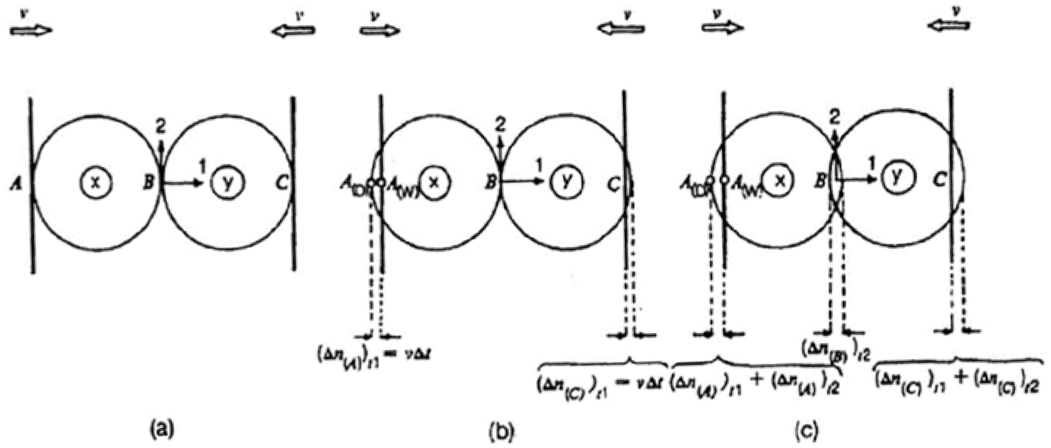

Figure 2.14: Two discs compressed between rigid walls (Cundall and Strack, 1979)

The forces on the discs can be found from the force-displacement law (Equation 2.6) using a known disc stiffness and the solved magnitudes of overlaps. The resulting forces are then used to solve for the accelerations of the discs using Newton's second law as presented in Equation 2.7. The relative displacements are found at the contact points using the solved forces and accelerations along with the equation of motion expressed in Equation 2.8. This cycle may be repeated for a number of time steps (Cundall and Strack, 1979).

$$F = k\delta \tag{2.6}$$

With:

F	Force on DEM disc $[N]$
k	DEM disc stiffness $[N/m]$
δ	Magnitudes of overlap between DEM discs $[m]$

$$F = ma \tag{2.7}$$

With:

m	Mass of DEM disc $[kg]$
a	Acceleration of DEM disc $[m/s^2]$

$$s = v\Delta t + \frac{1}{2}a\Delta t^2 \tag{2.8}$$

With:

s	Displacement of DEM disc $[m]$
v	Velocity of DEM disc $[m/s]$

In the general assembly case, the force-displacement law is first applied to each contact of any individual disc. The vectorial sum of these contact forces is then determined to return the resultant force acting on that disc. Once this has been performed for each of the discs, Newton’s second law is applied to solve for the new accelerations. Finally, the equation of motion is used to solve for the displacements (Cundall and Strack, 1979).

2.5.3 Contact models used in DEM

Various contact models exist which are used in DEM simulations. These contact models are used to determine how particles behave when they come into contact with each other or solid boundaries. The most commonly used of these models include the linear spring-dashpot model and the non-linear Hertz-Mindlin model (Coetzee, 2017).

In the linear and non-linear models, the contact force is split into two components, namely a spring component and a damping component. These two components are each split into two further sections, specifically the normal and tangential components. The normal and tangential components are dependent on the constant stiffness of the material and the incremental overlap in the normal and tangential directions respectively (Coetzee, 2017). An illustration of these components for the linear and non-linear models is depicted in Figure 2.15.

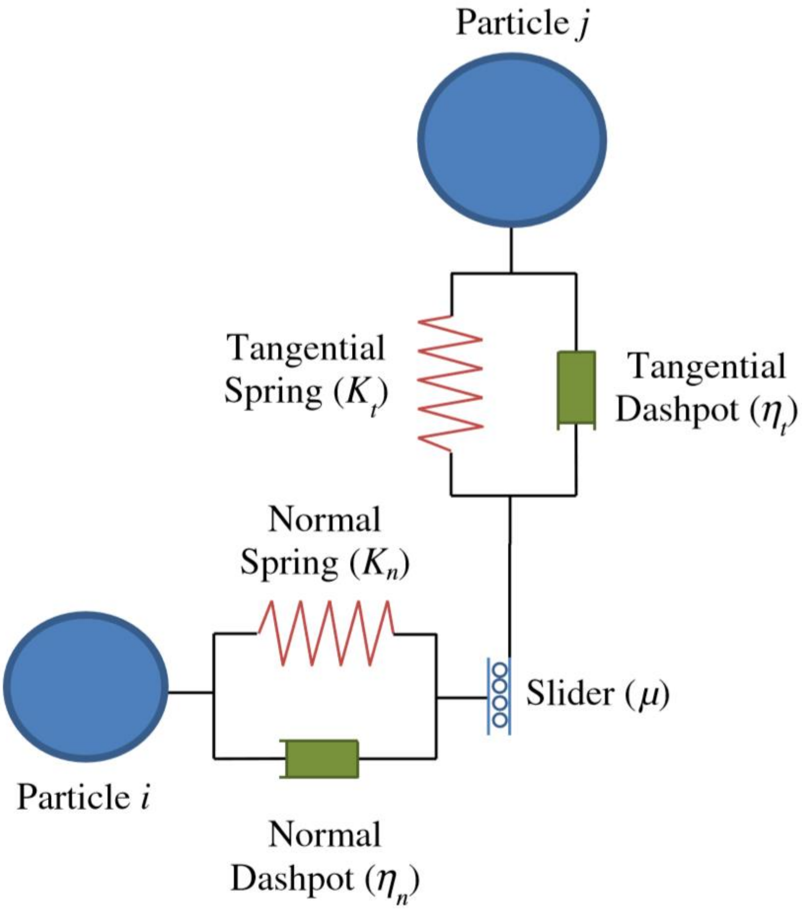

Figure 2.15: Normal and tangential components (Boac *et al.*, 2014)

The linear spring-dashpot model is the simplest contact model available in which the spring stiffness and damping values in the two components are assumed to be constant. The Hertz-Mindlin model is a non-linear contact model where the stiffness in the normal and tangential directions of a particle varies with the amount of overlap. The damping values also vary with the coefficient of restitution in the normal and tangential directions in the Hertz-Mindlin model (Boac *et al.*, 2014).

The contact forces, described by Boac *et al.* (2014), in the normal and tangential directions can be calculated using Equations 2.9 and 2.10 respectively for the linear and non-linear models as follows:

$$F_n = -K_n \delta_n^{\frac{3}{2}} - \eta_n \dot{\delta}_n \delta_n^{\frac{1}{4}} \tag{2.9}$$

$$F_t = -K_t \delta_t - \eta_t \dot{\delta}_t \delta_n^{\frac{1}{4}} \tag{2.10}$$

Where:

F_n	Normal contact force $[N]$
F_t	Tangential contact force $[N]$
K_n	Normal spring stiffness value $[N/m]$
K_t	Tangential spring stiffness value $[N/m]$
δ_n	Normal overlap $[m]$
δ_t	Tangential overlap $[m]$
$\dot{\delta}_n$	Normal velocity $[m/s]$
$\dot{\delta}_t$	Tangential velocity $[m/s]$
η_n	Normal damping value
η_t	Tangential damping value

Boac *et al.* (2014) stated that the linear spring-dashpot model uses constant values for the normal and tangential stiffness and damping values. However, for the non-linear Hertz-Mindlin model, these values are calculated using Equations 2.11 to 2.14 as follows:

$$K_n = \frac{4}{3} E^* \sqrt{R^*} \tag{2.11}$$

$$K_t = 8G^* \sqrt{R^* \delta_n} \tag{2.12}$$

$$\eta_n = \frac{\ln e}{\sqrt{\ln^2 e + \pi^2}} \sqrt{m^* K_n} \tag{2.13}$$

$$\eta_t = \frac{\ln e}{\sqrt{\ln^2 e + \pi^2}} \sqrt{m^* K_t} \tag{2.14}$$

The parameters E^*, R^*, G^* and m^* (Equations 2.15 to 2.16) are equivalent properties calculated from particles i and j depicted in Figure 2.15.

$$E^* = \left(\frac{1 - \upsilon_i^2}{E_i} + \frac{1 - \upsilon_j^2}{E_j} \right)^{-1} \tag{2.15}$$

$$R^* = \left(\frac{1}{R_i} + \frac{1}{R_j}\right)^{-1} \tag{2.16}$$

$$G^* = \left(\frac{2 - \upsilon_i}{G_i} + \frac{2 - \upsilon_j}{G_j}\right)^{-1} \tag{2.17}$$

$$m^* = \left(\frac{1}{m_i} + \frac{1}{m_j}\right)^{-1} \tag{2.18}$$

Where:

E^*	Equivalent Young’s Modulus $[Pa]$
R^*	Equivalent radius $[m]$
G^*	Equivalent Shear Modulus $[Pa]$
e	Coefficient of restitution
m^*	Equivalent mass $[kg]$
υ	Poisson’s ratio

There has been little research done to compare the results of the linear spring-dashpot and the Hertz-Mindlin models for identical applications and conditions. However, from the research that has been conducted, it has been suggested that these models yield comparable results when used on a large scale (Coetzee, 2017).

2.5.4 Frictional coefficients used in DEM

Three frictional coefficients are required when performing DEM simulations. These coefficients are the coefficient of rolling friction (μ_r), the particle-wall friction coefficient (μ_w) and the particle-particle friction (μ_p) coefficient, also known as the coefficient of sliding friction (Coetzee, 2017).

Coetzee (2016) suggested that the particle-wall friction coefficient can be calculated with $\mu_w = \tan\theta$, where θ is the angle at which a particle just begins to slide down the wall which it is contact with. However, the two remaining frictional coefficients require calibration by means of drop tests with only gravitational loads.

2.5.5 Calibration of DEM

The predictions of DEM simulations are largely dependent on the input parameters of the particles. Coetzee (2016) proposed a process to accurately calibrate these parameters for granular materials. Two important parameters are required to be correctly determined to predict accurate results when using DEM. The first of these parameters is the particle-particle friction coefficient, which relates to the angle of repose of the granular material. The second relates to the shape of the particle i.e. the number of particles clumped together to be used to generate the material grain (Coetzee, 2016).

Tests were done on different particle shapes using various numbers of clumps by Coetzee (2016) to determine the number of clumps needed to accurately model the desired particle behaviour. Figure 2.16 presents the 10 particles which were modelled using 2, 4 and 8 spheres. Figure 2.17 shows the volume error obtained for each of the particles and the respective number of spheres used to generate the equivalent particle (Coetzee, 2016).

It is known that the computational time increases as the number of spheres used to model a particle's shape are increased. The results indicated that the 4-clump and 8-clump models were only slightly more accurate than the 2-clump models. It was therefore concluded by Coetzee (2016), that most non-spherical particles can be adequately modelled using 2 spheres if the parameter values are properly calibrated.

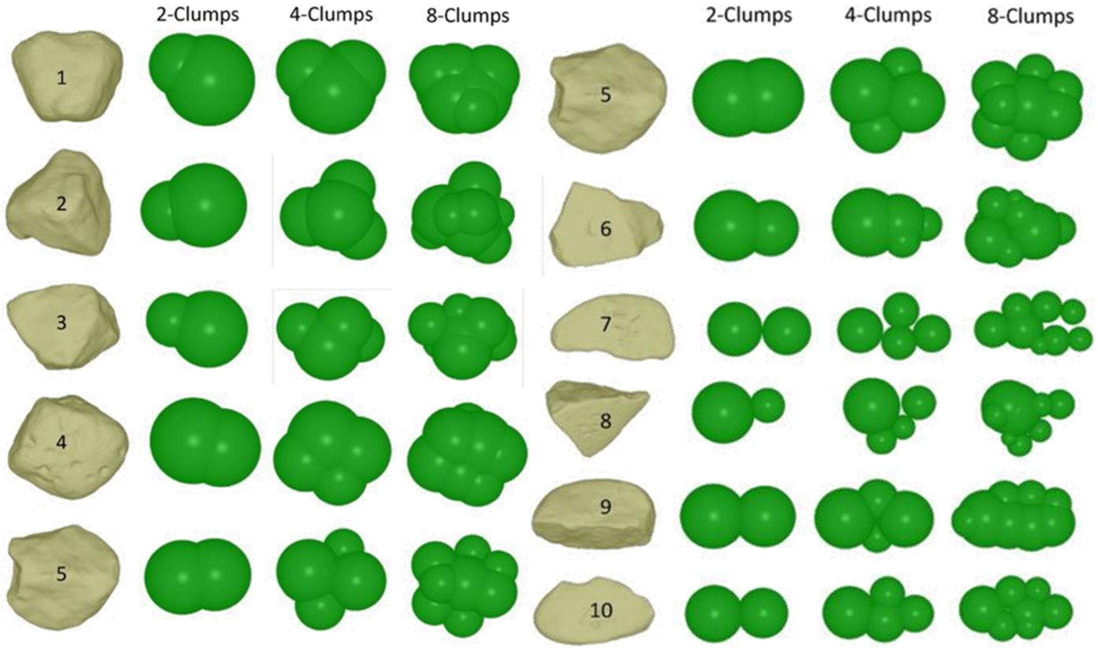

Figure 2.16: 2-clumps, 4-clumps and 8-clumps for each of the 10 particles (Coetzee, 2016)

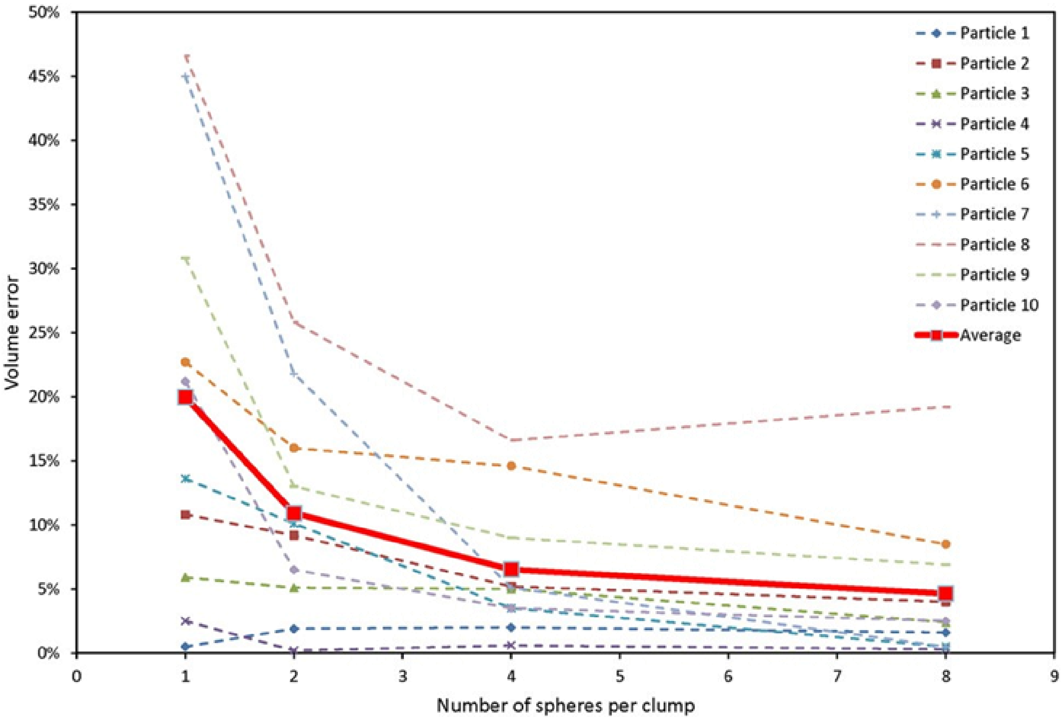

Figure 2.17: Volume error for 10 particles versus number of sphere clumps (Coetzee, 2016)

Using the 10 particle shapes modelled by combining various numbers of spheres, Coetzee (2016) also varied the particle-particle friction coefficient of the material to obtain the angles of repose for the material. Figure 2.18 shows the plot of the angle of repose versus the particle-particle friction coefficient for the various clumps used. It was notable that for single spheres, the angles were much lower than for the clumps. This was due to the perfect spheres rolling away during the drop tests. This suggested that to accurately obtain the angle of repose of a material, drop tests with at least two clumped particles should be used (Coetzee, 2016).

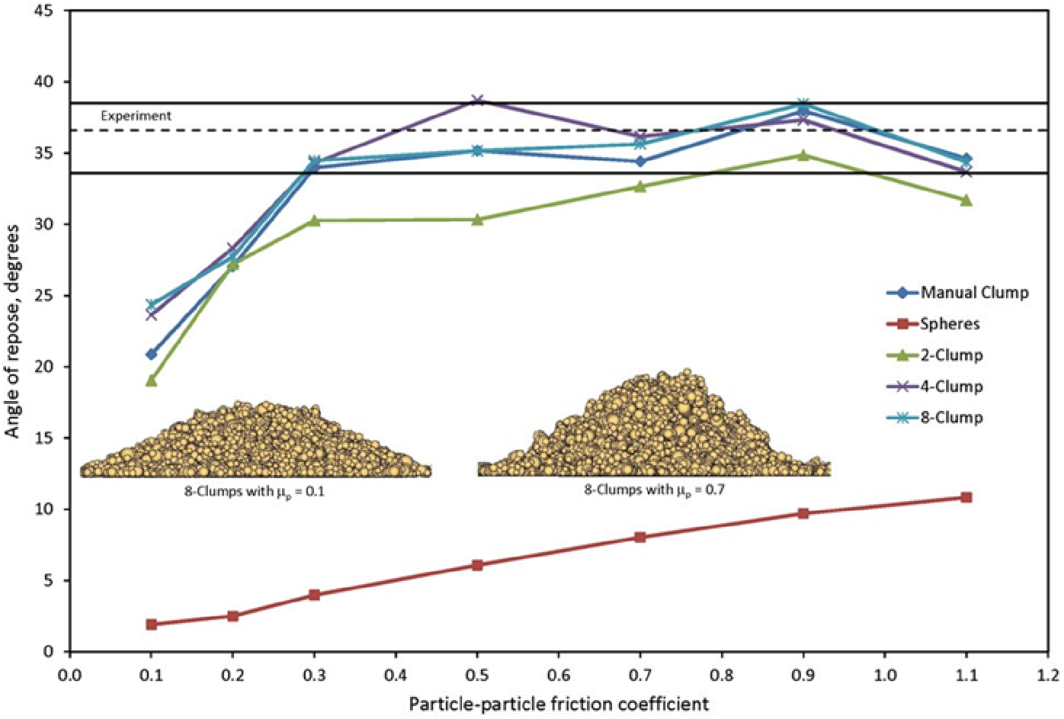

Figure 2.18: Angle of repose versus particle-particle friction coefficient (Coetzee, 2016)

Nakashima *et al.* (2011) and Coetzee (2016) state that the angle of repose of a granular material is directly related to the particle-particle friction coefficient of the material. Using DEM simulations, Nakashima *et al.* (2011) performed drop tests under only gravitational loads to obtain a particle's angle of repose. The angle of repose as defined by the results from the DEM simulations is illustrated in Figure 2.19.

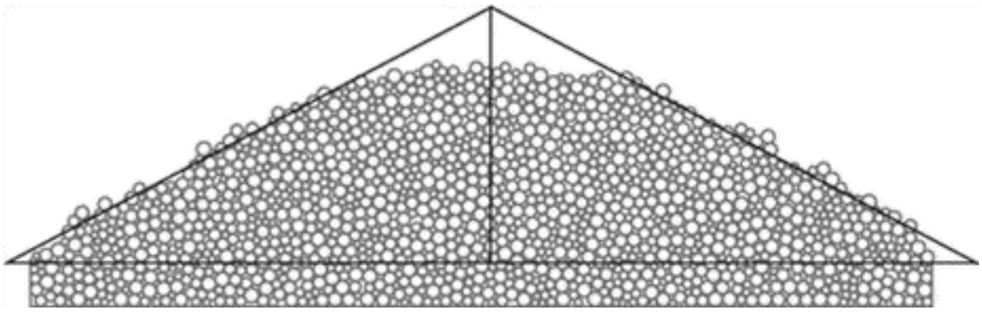

Figure 2.19: Angle of repose defined by DEM results (Nakashima *et al.*, 2011)

Derakhshani *et al.* (2015) performed numerical and experimental tests on quartz sand to calibrate the material to a desired angle of repose. The coefficients of sliding friction (particle-particle friction coefficient) and rolling friction were varied in the calibration tests.

Table 2.1 presents the material properties used in the calibration tests by Derakhshani *et al.* (2015).

Table 2.1: Material properties of quartz sand used by Derakhshani *et al.* (2015)

Parameter (symbol)	**Base value**
Particle radius (r)	Distributed from 300 to 600 µm
Particle density (ρ)	2653 kg/m^3
Young's modulus (E)	50 MPa
Poisson ratio (ν)	0.30
Coefficient of restitution (e)	0.90

Figure 2.20 depicts the effect of the coefficients of sliding friction and rolling friction on the resulting angle of repose of the material. The figure illustrates that the coefficient of rolling friction had a small effect for lower angles of repose and sliding friction coefficient values. The results from the tests performed by Derakhshani *et al.* (2015) therefore show that the particle-particle friction coefficient should be the focal parameter to be changed when calibrating a material to a desired angle of repose less than 35°.

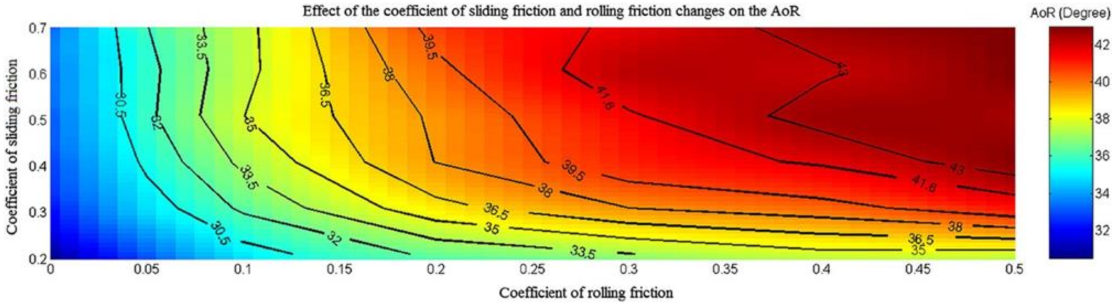

Figure 2.20: Effect of rolling and sliding coefficients of friction on angle of repose for quartz sand (Derakhshani *et al.*, 2015)

2.5.6 Reducing computational costs of DEM

DEM is becoming a popular computational method used by engineers and researchers to design, analyse and optimise systems where granular materials are involved. However, this method may result in extremely high computational costs. Possible methods to reduce these computational costs include scaling the particle sizes or reducing the contact stiffness of the materials (Coetzee, 2017).

The size of the time-step required, to ensure convergence used for DEM simulations, is related to the stiffness, density and size of the particle (Coetzee, 2017). This time-step can be calculated from the Rayleigh velocity as presented in Equation 2.19 below:

$$t_R = \frac{\pi r}{v_R} \tag{2.19}$$

With:

$$v_R = \sqrt{\frac{G}{\rho}} + \frac{0.87 + 1.12v}{1 + v} \tag{2.20}$$

$$G = \frac{E}{2(1 + v)} \tag{2.21}$$

Where:

t_R	Rayleigh time-step $[s]$
r	Particle radius $[m]$
v_R	Rayleigh velocity $[m/s]$
G	Shear Modulus $[Pa]$
ρ	Density $[kg/m^3]$
v	Poisson's ratio
E	Young's Modulus $[Pa]$

It is common practice in DEM simulations, to use a time-step 5 times smaller than the calculated Rayleigh time-step (Siemens PLM, 2017). Equation 2.22 shows that the size of the time-step used in the simulations decreases with larger Young's Modulus values. The equation also shows that the greater the particle density or radius, the larger the time-step required. It is ideal that the time-step for DEM simulations is as large as possible, since a greater number of iterations are required as the size of the time-step decreases (Coetzee, 2017).

$$\Delta t = 0.2 t_R \tag{2.22}$$

$$\therefore \Delta t = \frac{0.2\pi r}{\left(\sqrt{\frac{E}{2\rho(1+\nu)}} + \frac{0.87+1.12\nu}{1+\nu}\right)} \tag{2.23}$$

Where:

Δt DEM simulation time-step $[s]$

Xu *et al.* (2002) investigated the effect of contact stiffness on silo discharge for granular materials. No physical experiments were performed, however, only DEM simulations of circular particles in 2D were executed. The tests were performed on two sets of materials, namely a soft material and a hard material. The hard material had a contact stiffness 1 000 times greater than the soft material, i.e. 70 MPa for the soft material and 70 GPa for the hard material. The discharge deviated by an average of 2.7% while the hard material resulted in a computational time 31.6 times slower than the soft material. Xu *et al.* (2002) concluded that the contact stiffness could be greatly reduced without any significant effects for gravity-driven flow.

The computational time required to model direct shear of glass beads was reduced by Härtl and Ooi (2008) by decreasing the shear stiffness of the glass beads by a factor of 100. It was also concluded that there was no significant effect on the shear force when decreasing the shear stiffness by a factor of 1 000. Yan *et al.* (2015) successfully reduced the stiffness by a factor of 10 000 without affecting the discharge of mono-sized spherical particles.

Lommen (2014) proposed that the amount of reduction applied to the particle stiffness can be verified with the magnitude of the normal overlap of the particles. Lommen (2014) suggested that the normal overlap between particles should not be greater than 0.3% of the particle radius, which is comparable to the 0.1% to 0.5% overlap proposed by Cleary (2010). Coetzee (2017) proposed that the stiffness should be chosen such that the maximum overlap between particles is not greater than 1% of the particle radius.

Feng and Loughran (2009) developed scaling laws for granular systems and showed that the basic linear contact law is scale invariant only for 2D problems but not for 3D problems. It was also proposed that the mechanical and dynamic conditions can be maintained if scaling laws are applied. However, the geometric conditions (packing configuration) would not be held.

Geometric similarity could only be maintained if the number of particles remained the same. It was shown by Obermayr *et al.* (2014) that the non-linear Hertz-Mindlin contact law was scale invariant in 3D when only spherical particles were used.

Performing simulations by using DEM may result in excessively high computational times. The most common practice used to speed up the computational times is to reduce the Young’s Modulus value (Coetzee, 2017).

2.6 DEM SOFTWARE AND APPLICATIONS

The most common commercial DEM packages available are EDEM (DEM Solutions, 2017) and STAR-CCM+ (Siemens PLM, 2017). EDEM is the market-leading DEM software package while STAR-CCM+ is primarily a Computational Fluid Dynamics (CFD) package with DEM capabilities, developed by CD-adapco. LIGGGHTS is the most popular open-source DEM package available (Kloss *et al.*, 2012).

Finally, Blaze-DEM is a Graphics Processing Unit based DEM framework, which offers an elevated level of performance as opposed to packages which make use of traditional Central Processing Unit (CPU) processing. Blaze-DEM was developed by Govender (2015) at the University of Pretoria.

2.6.1 CPU based DEM software packages

STAR-CCM+ is a software package capable of solving multidisciplinary problems in both fluid and solid continuum mechanics. The software is primarily a Computational Fluid Dynamics package. However, the Discrete Element Method can be utilised within the solid mechanics continuum. The software uses classical mechanics DEM based on soft-particle formulations. This formulation allows particles to develop an overlap, where the overlap is then used to calculate a contact force. This contact force is proportional to the overlap, particle material and geometric properties. The software offers a single integrated user interface (Siemens PLM, 2017).

EDEM is primarily a DEM simulation software package and is the market-leading software for bulk material simulation (DEM Solutions, 2017). EDEM is capable of simulating particle-particle, particle-fluid, particle-structure or particle-electromagnetic interactions. As with STAR-CCM+, EDEM offers a single integrated graphical user interface. EDEM is limited to particle shapes being created from only sphere-clumps (DEM Solutions, 2017).

LIGGGHTS (LAMMPS Improved for General Granular and Granular Heat Transfer Simulations) is an open source, DEM particle simulation software. LAMMPS is a classical molecular dynamics simulator which can be used for the simulation of particulate materials. Unlike STAR-CCM+ and EDEM, LIGGGHTS does not offer a single integrated graphical user interface (Kloss *et al.*, 2012).

2.6.2 Blaze-DEM

Blaze-DEM is a Graphics Processing Unit based framework that makes use of collision detection algorithms and various heuristics optimised for parallel GPU architecture. The architecture of a GPU allows for a large number of simple independent processes to be performed in parallel (Govender, 2015).

Blaze-DEM supports simulations with both spherical and polyhedral shaped particles. The framework offers a high-level of performance as opposed to commercial DEM packages available. Most commercial DEM packages use multi-core Central Processing Units to simulate particles. The use of the CPUs restricts the number of particles which can be simulated due to the limited number of high-performance computing cores available in most computers (Govender *et al.*, 2016).

The hardware designs of the CPU and GPU processors are compared in Figure 2.21. One of the major differences between the two processors is the number of cores and threads present. A core refers to physical hardware which can be concurrently split into virtual threads, each capable of performing separate operations. This process is known as multithreading. The Streaming Multi-Processor (SM) in a GPU is the closest equivalent to a core in a CPU (Govender *et al.*, 2014).

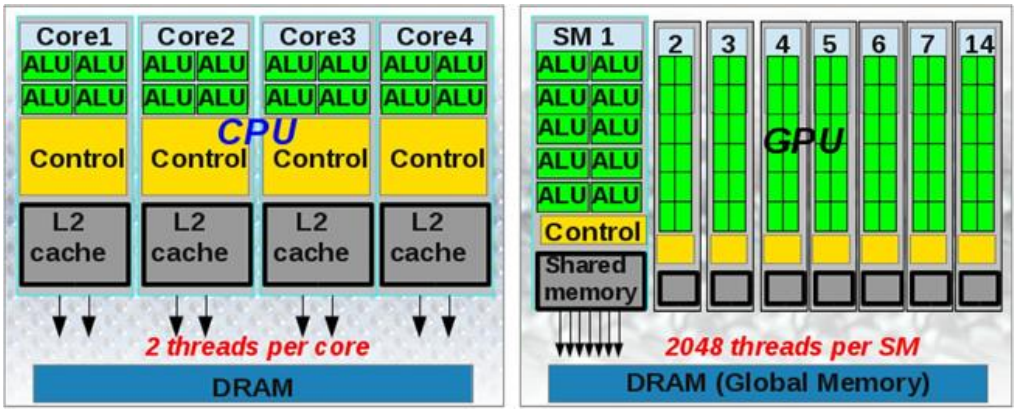

Figure 2.21: Chip layouts for: Quad-core Intel CPU (left) and NVIDIA Kepler GPU (right) from Govender *et al.* (2014)

The cores in CPUs are designed to be used for complex logical operations such as running an operating system, while still being able to perform arithmetical operations. GPUs are designed to render graphics, which involves the simultaneous operation of potentially millions of pixels. This requires many parallel algebraic operations and therefore benefits applications which require a large number of parallel arithmetic operations (Govender *et al.*, 2014).

The typical computational tasks at which the CPU and GPU units excel are compared in Figure 2.22. The cores in the CPU are capable of each launching two threads which can work independently from one another and perform complex logical operations. The SMs in the GPU considered can launch 2 048 threads capable of only performing the same task. This means that GPUs outclass the more flexible CPUs when processing similar data packets. Blaze-DEM exploits this computational power of the GPU to achieve much higher performance levels than DEM codes which use traditional CPU based architectures (Govender *et al.*, 2014).

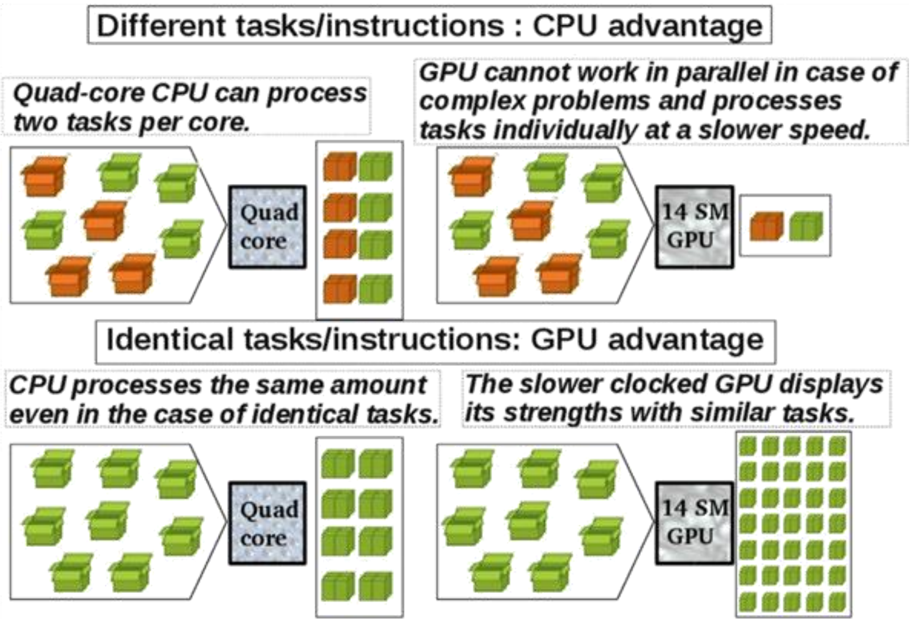

Figure 2.22: Comparison of task processing between i7 Quad-core CPU and NVIDIA GK110 GPU (Govender *et al.*, 2014)

Govender *et al.* (2016) demonstrated a comparison of the performance levels between Blaze-DEM and other codes by comparing the Cundall Numbers (C) of gravity stacking simulations. The Cundall Number is calculated as the number of particles (N) multiplied by the number of frames per step which can be performed per second (FPS). A higher Cundall Number represents a better performance. Tables 2.2 and 2.3 present the results of this comparison. The tables show that Blaze-DEM offers a much higher level of performance as opposed to other codes even when a large number of particles are used. BLOCKS and iDEM are codes presented by Jae Lee (2014) which support polyhedra shapes, however offer much slower computational times when compared to Blaze-DEM.

Table 2.2: Performance level comparison between Blaze-DEM and other codes – Cundall number (Govender *et al.*, 2016)

Author	Particle shape	Physics fidelity	Number of particles	Cundall Number
Harada *et al.* (2008)	Clumped	Low	1.64×10^4	0.66×10^6
Longmore *et al.* (2013)	Clumped	High	2.56×10^5	1.49×10^6
Neubauer and Radek (2014)	Sphere	High	20×10^6	20×10^6
Blaze-DEM	Sphere	High	60×10^6	100×10^6

Table 2.3: Performance level comparison between Blaze-DEM and other codes – Computational time (Govender *et al.*, 2016)

Author	Particle shape	Physics fidelity	Number of particles	Computational time
BLOCKS (2013)	Polyhedra	Highest	5×10^3	186 days
iDEM (2013)	Polyhedra	Low	5×10^5	2.8 days
Blaze-DEM	Polyhedra	High	32×10^6	32 min

The results from Blaze-DEM have been extensively validated against experimental results and traditional CPU DEM codes. Govender *et al.* (2015) performed mill charge simulations in Blaze-DEM using various numbers of spherical particles. The results were compared to simulations from the CPU based code Millsoft and experimental data obtained from Venugopal and Rajamani (2001) as well as Hlungwani *et al.* (2003). The validations of Blaze-DEM for the mill charge simulations are shown in Figures 2.23, 2.24 and 2.25.

The comparison between the simulation results from Blaze-DEM and Millsoft is depicted in Figure 2.23. The figure illustrates the mill charge profiles with 5 344 spherical particles. The profiles were similar for the CPU and GPU based packages. The validation with the experimental data from Venugopal and Rajamani (2001) is depicted in Figure 2.24. The figure shows 243 spherical particles for the mill charge profiles. The profiles were almost identical for the results from the experimental work and the GPU based simulation.

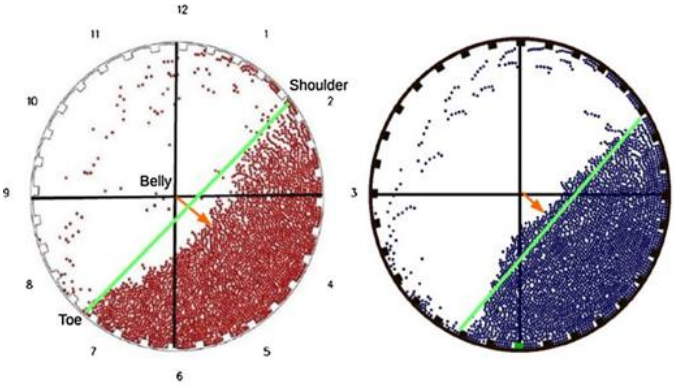

(a) (b)

Figure 2.23: Validation between: (a) CPU and (b) GPU charge profiles with 5 344 particles (Govender *et al.*, 2015)

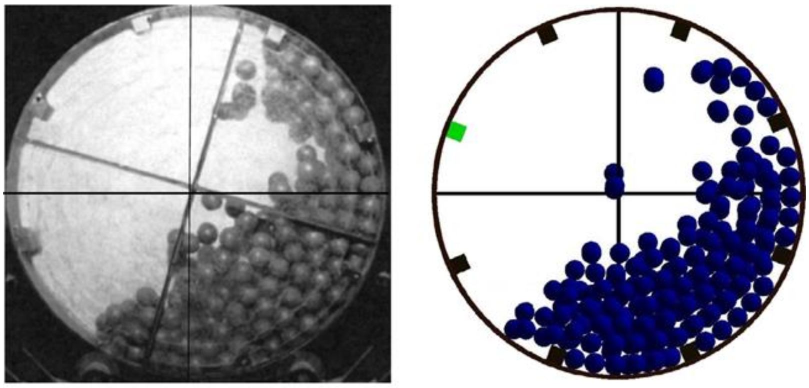

(a) (b)

Figure 2.24: Validation between: (a) experimental data (Venugopal and Rajamani, 2001) and (b) GPU charge profiles with 243 particles (Govender *et al.*, 2015)

The comparison of 168 spherical particles with experimental data from Hlungwani *et al.* (2003) and simulations with GPU and CPU based packages is depicted in Figure 2.25. The figure shows that the GPU package yielded comparable results to those obtained from experimental work as well as those obtained from the CPU based code Millsoft. The results from the validations showed that Blaze-DEM could offer realistic results as well as much faster computational times.

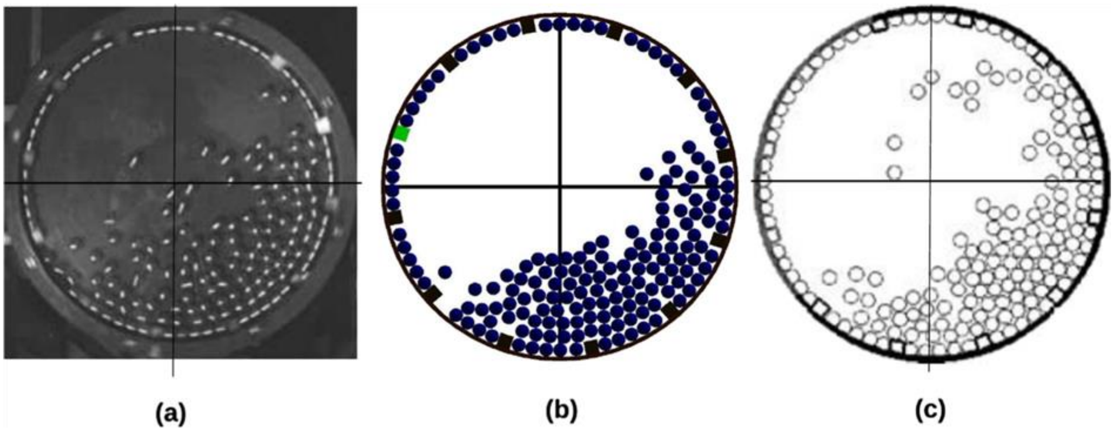

Figure 2.25: Validation between: (a) experimental data (Hlungwani *et al.*, 2003), (b) GPU and (c) CPU charge profiles with 168 particles (Govender *et al.*, 2015)

Govender *et al.* (2014) performed further validations on the results of Blaze-DEM with comparisons to results from experimental and numerical hopper flow tests. Tests were performed with spherical and convex polyhedra particles. The flow patterns from the experimental data and simulation with spheres are presented in Figure 2.26. The figure shows that the bulk behaviour of the hopper flow was similar for both tests. Govender *et al.* (2014) concluded that the GPU is well suited to DEM analyses where a simple physics model is used.

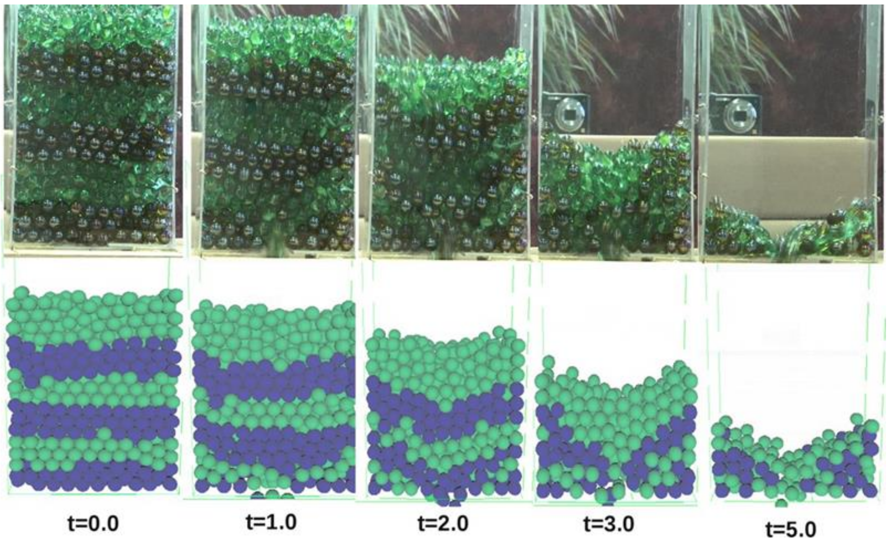

Figure 2.26: Comparison of experimental and Blaze-DEM results for hopper flow of 836 spherical particles (Govender *et al.*, 2014)

2.6.3 Particle shapes in DEM

The hopper flow tests performed by Govender *et al.* (2014) also included convex polyhedra simulations. A convex polyhedron is a polyhedron with the property that for any two points inside that shape, the line segment joining them is contained within the polyhedron. The results of the hopper flow test with 13 824 corn-shaped polyhedra particles are depicted in Figure 2.27. The figure illustrates that the polyhedra shapes form a denser packing in the corners which is suggested to be a result of interlocking. The rate of flow of the polyhedra was also slower than the same simulation when spheres were used.

Govender *et al.* (2014) suggested that the particle shape plays an important role in particle dynamics as illustrated in Figure 2.28. The figure shows significantly restricted flow from the hopper tests due to polyhedra arching which would not have been possible with spheres.

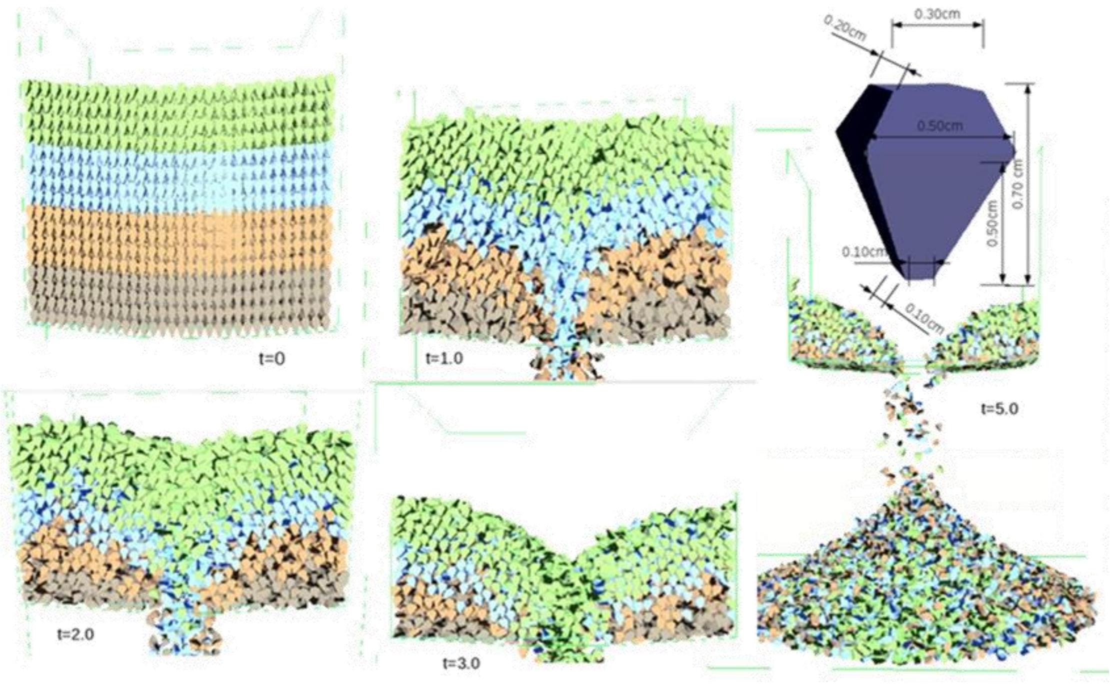

Figure 2.27: Hopper flow test results with 13 824 corn-shaped polyhedra particles (Govender *et al.*, 2014)

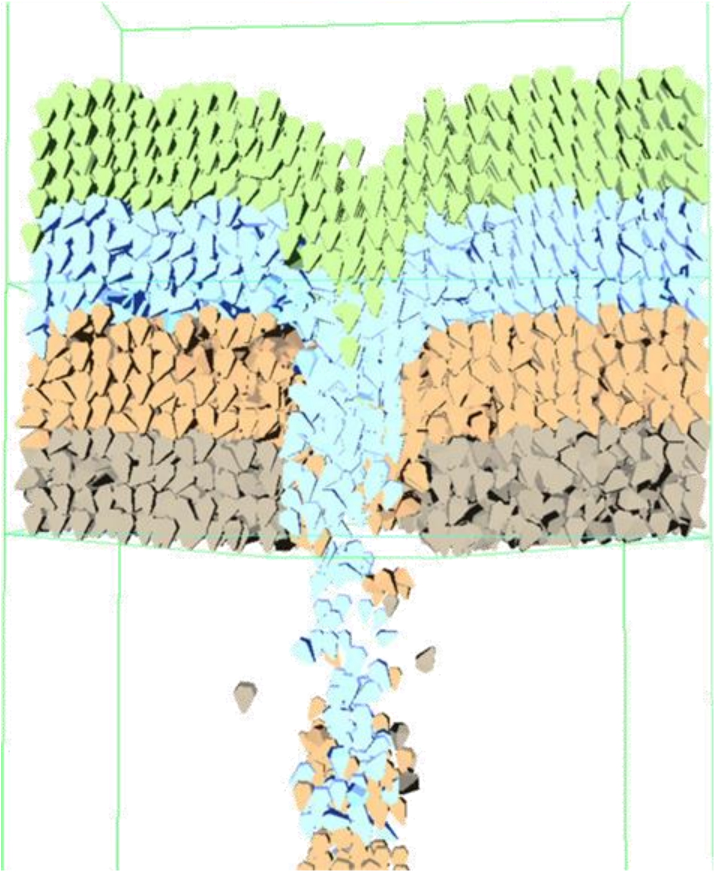

Figure 2.28: Restricted flow as a result of polyhedra arching (Govender *et al.*, 2014)

Höhner *et al.* (2014) performed rotating drum experiments and DEM simulations to study the influence of particle shape and shape approximation on particle mechanics. Four particle shapes were used, as illustrated in Figure 2.29. The dynamic angles of repose of the particle shapes were observed for the study. The shapes were tested experimentally as well as in simulations as polyhedra and smoothed polyhedra. The DEM simulations with the polyhedra and smoothed polyhedra showed good agreement with the experimental results.

The results from the study by Höhner *et al.* (2014) showed that the polyhedra particles tended to form slightly higher dynamic angles of repose when compared to the smoothed polyhedral counterparts. This suggested that the sharply-edged particle shapes increased the interlocking of particles as well as increased the formation of pile-ups.

Figure 2.29: Particle shapes tested by Höhner *et al.* (2014) from left to right: sphere, icosahedron, dodecahedron and hexahedron

DEM simulations of hopper discharge tests were performed by Höhner *et al.* (2012). The simulations were performed with non-cohesive polyhedra as well as particle shapes generated with the multi-sphere method. Figure 2.30 illustrates the particles shapes investigated. The particles referred to as CLS 1–3 (Clustered Shapes) consisted of 30, 20 and 10 sub-spheres respectively. The particles denoted by PS 1–3 (Polyhedral Shapes) comprised of 112, 24 and 12 triangular surface elements respectively.

The results from the hopper discharge simulations showed that significant differences between polyhedral and clustered particles were present. The mass flow rate was not reduced with the clustered particles with the same degree as observed with the polyhedral particles. Höhner *et al.* (2012) stated that this was attributed to the multi-sphere particles having relatively smooth surfaces while the polyhedral surfaces had multiple sharp edges and vertices. This suggested that the type of particle shape approximation plays an important role in DEM simulations.

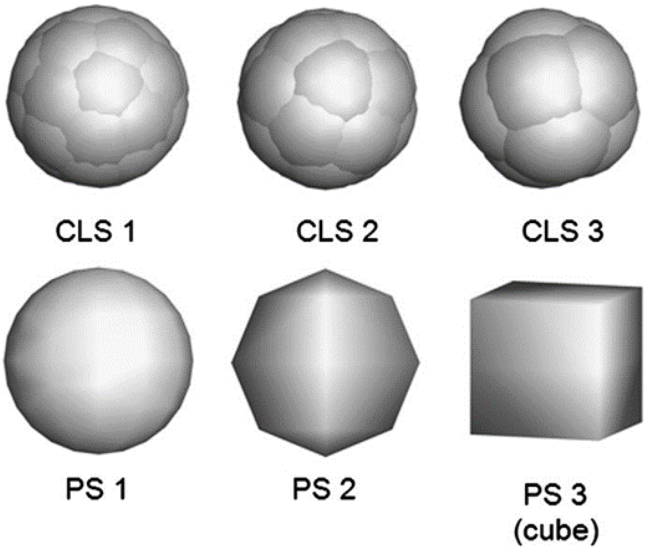

Figure 2.30: Particle shapes investigated by Höhner *et al.* (2012)

Azéma *et al.* (2009) performed 2D DEM simulations to study the effect of particle shape on shear strength in granular media. Pentagons and circular discs were used for the simulations as presented in Figure 2.31. The contact and force networks in dense confined packings of the particles were analysed.

Azéma *et al.* (2009) suggested that the force anisotropy in a granular material depends on the particle shapes. Figure 2.32 depicts the normal force chains obtained from the discs and pentagons. The figure shows that the pentagonal shapes gave rise to large force anisotropy and strong force chains which are suggested to be accredited to edge-to-edge contacts which allowed for this strong force localisation along the contacts in the packing.

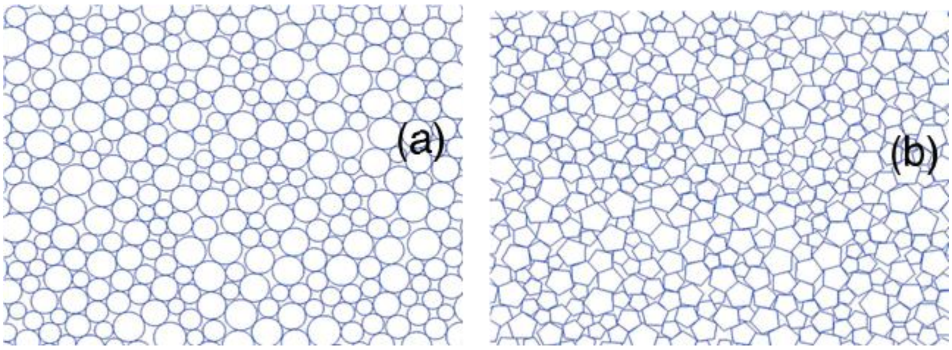

Figure 2.31: 2D DEM (a) circular and (b) pentagonal particles used by Azéma *et al.* (2009)

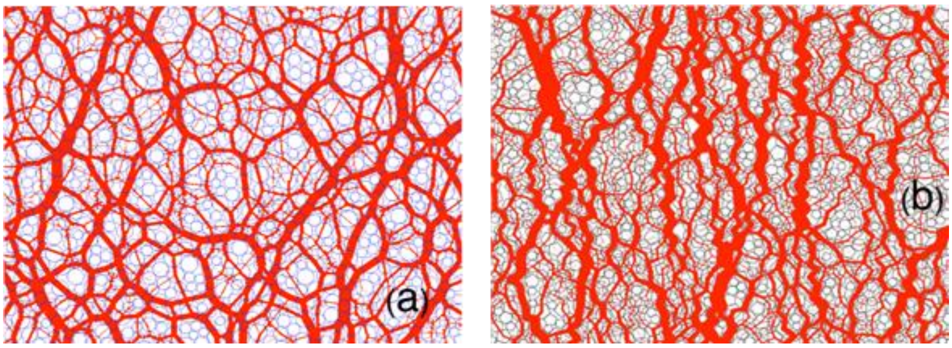

Figure 2.32: Normal forces in: (a) discs and (b) pentagons with line thickness proportional to the normal force (Azéma *et al.*, 2009)

Azéma *et al.* (2009), Höhner *et al.* (2014) and Govender *et al.* (2014) all state that the particle shape used in DEM simulations plays a significant role when modelling granular materials. Cleary and Sawley (2002) and Azéma *et al.* (2009) stated that the locking of 3D DEM particles needs to be further studied.

2.6.4 DEM versus FEM

The Finite Element Method (FEM) is an example of a continuum model which has been used to model granular material behaviour. The continuum model is a simplification of the behaviour of the granular material, inspired by experimental observations. To increase the complexity of the model will require an increase in the number of material properties that must be defined from laboratory or in-situ tests (Wood, 2004).

A disadvantage of continuum models is that constitutive relationships (stress-strain laws) are required. This relationship may not exist or could be excessively complicated, with many parameters, which may be difficult to obtain. In DEM modelling, the assembly of the discrete particles can capture the complicated behaviour of actual granular materials (Yap, 2011). Figure 2.33 depicts the difference between FEM and DEM for this behaviour. The figure shows that granular materials consist of irregularly shaped particles. A FEM analysis would require continuum elements with complex relationships to model the granular material, whereas a DEM analysis could better represent the granular material with circular particles or polygons.

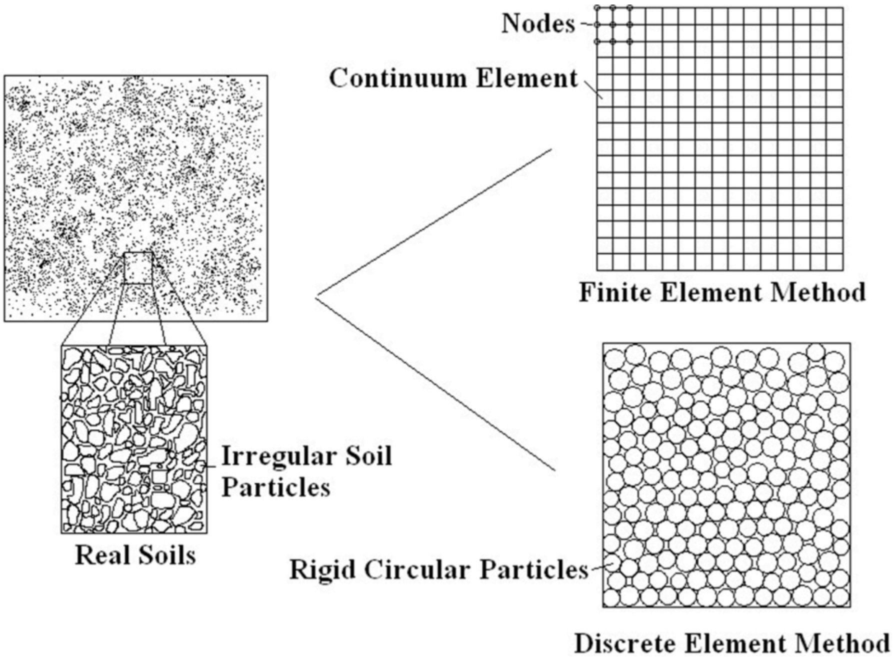

Figure 2.33: Difference between FEM and DEM for granular material behaviour (Yap, 2011)

2.6.5 Applications of DEM

Over the years, DEM simulations have advanced to a point where the interactions of a complex mechanical system can be modelled in three dimensions. This method, therefore, has many applications in engineering problems (Cundall, 1988). A few examples of DEM used in civil engineering problems are discussed.

Lu and Frost (2010) used 3D DEM simulations to model the triaxial compression of sands. The results were compared to physical laboratory tests. The global stress and strain responses, as well as the void ratios and coordination numbers, were investigated for the comparison. The sand was modelled as single-spheres and unbreakable two-sphere clumps. It was found that the two-sphere clumps better matched the results from the physical laboratory tests since an interlocking mechanism between the particles could develop.

DEM was used to model the behaviour of railway ballast under various test conditions by Lim and McDowell (2005). The ballast was modelled using single-spheres as well as eight-sphere clumps and it was found that the eight-sphere clumps resulted in much more realistic behaviour due to the clumps allowing for particle interlocking.

Lim and McDowell (2005) performed simulations of oedometer tests on the ballast and compared the results with laboratory tests. It was also found that the numerical results produced lower yield stresses which were suggested to be due to the spherical shape of the aggregates. Figure 2.35 illustrates the box tests performed using the single-sphere and eight-sphere particle clumps.

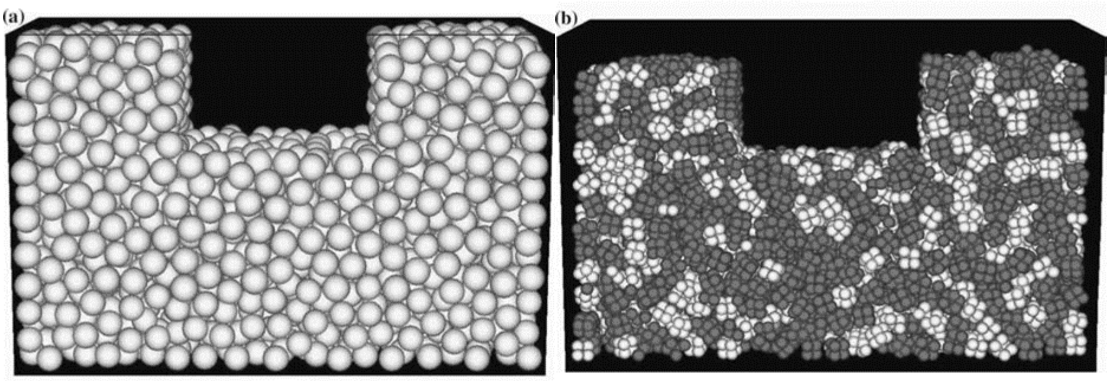

Figure 2.34: Box test samples of: (a) single-sphere clump and (b) eight-sphere clumps (Lim and McDowell, 2005)

Brookes (2010) used a combination of FEM and DEM to model masonry arch bridges. The masonry arch was modelled using discrete elements, whereas the steel reinforcement was modelled using finite elements. The behaviour of mortar required the modelling of interfaces between the discrete and finite elements. A no-tension Mohr-Coulomb friction relationship was used to model these interfaces. The results were compared to full-scale tests and it is suggested by Brookes (2010) that this combination of methods can be used in both special assessment as well as advancing the design of arch bridges.

Widulinski *et al.* (2010) compared the calculations of zero shear zones in granular materials by using FEM and DEM simulations. The simulations were performed for a passive case of a rotating and translating retaining wall. The deformed FE mesh and DE granular body are shown in Figure 2.35. It was suggested that the continuum model (FEM) was more suitable to the problem than the discrete model since both analyses produced comparable results, however, the DEM simulations were much more limited by the computational time.

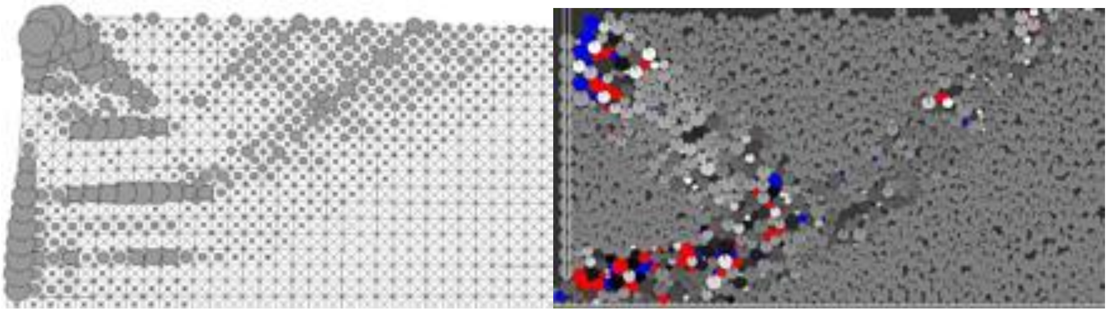

Figure 2.35: Deformed FE mesh (left) and deformed DE granular body (right) for a rotating wall (Widulinski *et al.*, 2010)

Hu *et al.* (2010) analysed the cyclic loading of sand by using 2D DEM simulations. The sand was loaded with three different amplitudes, with the top wall moving up and down cyclically as shown by the loading plate in Figure 2.36. The void ratios, as well as the deviatoric and axial strain accumulations during cyclic loading for the different amplitudes, were investigated.

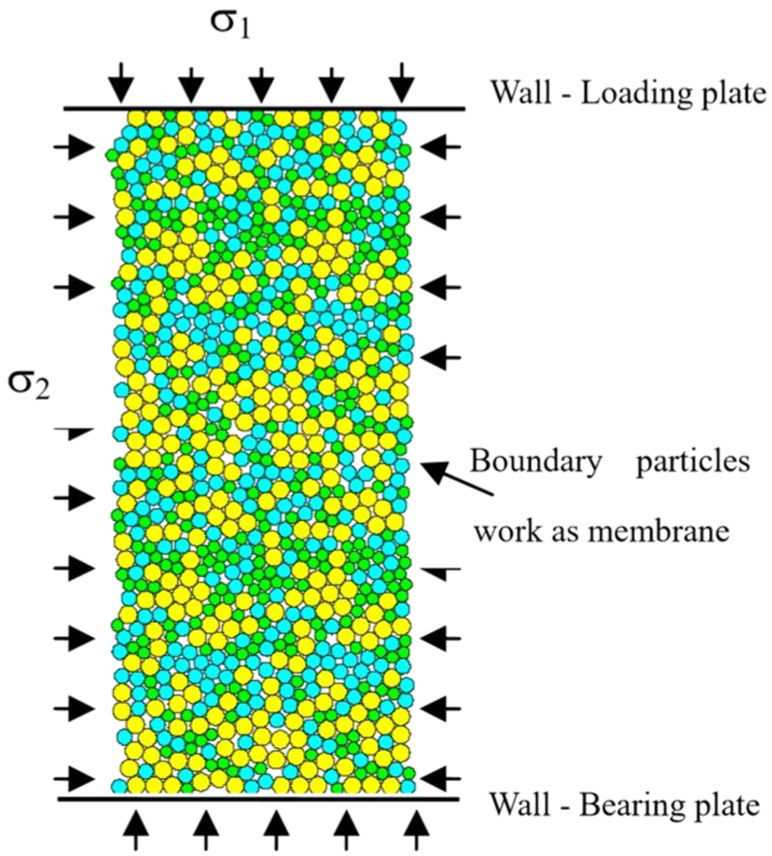

Figure 2.36: Sample cyclically loaded by Hu *et al.* (2010)

Hu *et al.* (2010) found that for smaller cyclic amplitudes, the deviatoric and axial strain accumulation increased smoothly, however for larger cyclic amplitudes, these strain accumulations increased drastically after a large number of cycles. The axial strain results are presented in Figure 2.37. The erratic accumulation seen in the strains for the larger amplitudes was also observed with a void ratio fluctuation for these amplitudes as presented in Figure 2.38.

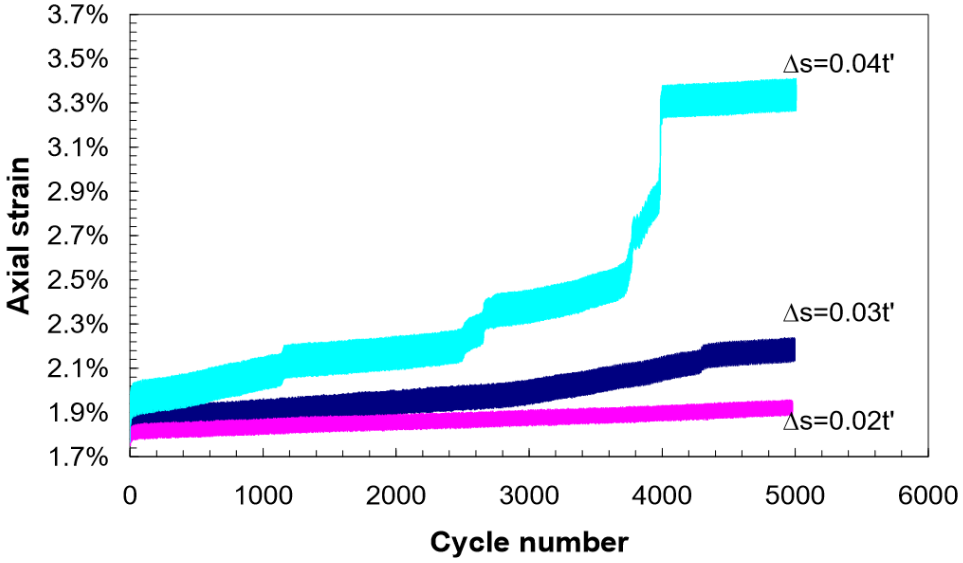

Figure 2.37: Axial strain curves of cyclic loading obtained by Hu *et al.* (2010)

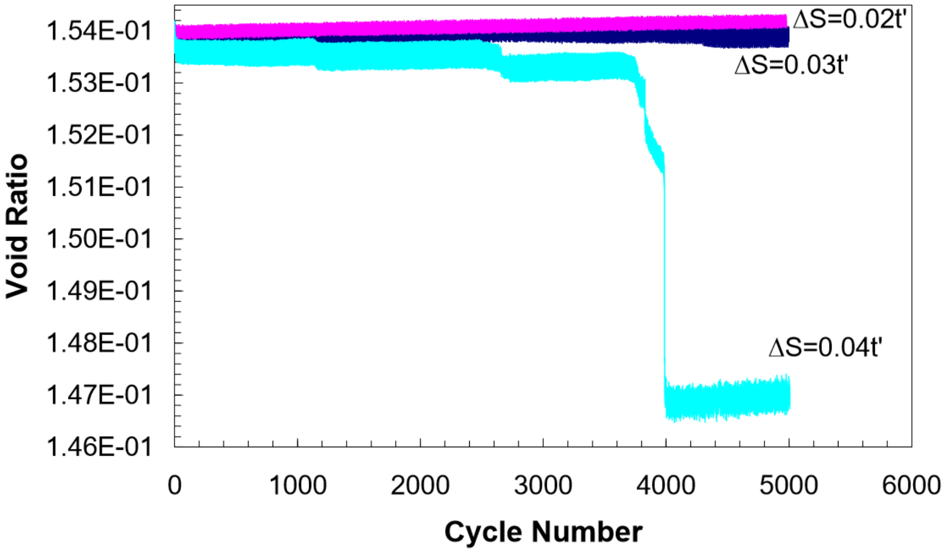

Figure 2.38: Porosity variation of cyclic loading obtained by Hu *et al.* (2010)

2.7 SUMMARY

Integral bridges are designed to eliminate the need for expansion joints and bearings. This means that the bridge can be viewed as a single structural unit and therefore provides greater earthquake resistance as well as reduces the construction time and costs when compared to conventional bridges. The lack of expansion joints and bearings also reduces the amount of repairs and maintenance required on the bridge.

The problem that arises with the lack of expansion joints is the cyclic movements of the abutment due to temperature changes in the deck. The daily and seasonal temperature variations cause expansion and contraction of the deck which results in a cyclical loading of the abutment. Previous research has shown that this cyclical loading causes a build-up of horizontal stresses in the granular backfill retained by the abutment.

Xu *et al.* (2007) and Clayton *et al.* (2006) have illustrated that the particle shape of the granular backfill plays an imperative role in the amount of stress accumulation as a result of the cyclical loading. It was shown in previous research that the increase in horizontal stresses was negligible when spherical granular particles were used. However, when non-spherical particle shapes were used, the stress accumulation was significantly higher. This build-up of horizontal stress is suggested to be a result of particle reorientation as well as particle interlocking and is not a result of densification.

The Discrete Element Method is a calculation cycle that can be used to model the behaviour of granular materials. DEM requires accurate calibration of the materials used in order to obtain realistic results. The calibration of the particle-particle friction coefficient to a desired angle of repose is important when modelling granular materials.

There are numerous DEM packages available, one of which is Blaze-DEM, a high-performance GPU based framework. Blaze-DEM offers the possibility of simulations being performed with polyhedral shaped particles as opposed to multi-sphere generated particles. Previous research by Azéma *et al.* (2009), Höhner *et al.* (2014) and Govender *et al.* (2014) has found that modelling granular materials as polyhedra provides a more realistic representation of the behaviour of the material. The availability of this software allows the effect of particle shape on stress build-up behind integral bridge abutments subject to cyclical loading to be studied.

This research uses the Discrete Element Method within STAR-CCM+ and Blaze-DEM to perform a numerical sensitivity analysis, investigating the effect of granular particle shape on the response of backfill retained by a model bridge abutment. It is expected that the granular backfill with higher sphericities will result in a smaller build-up of stresses when exposed to cyclical loads compared to a larger stress build-up in the case of polyhedral shapes (lower sphericities), due to possible particle interlocking or reorientation.

3 DEM MODELLING OF GRANULAR BACKFILL RETAINED BY INTEGRAL BRIDGE ABUTMENTS

3.1 INTRODUCTION

This chapter presents the methodology followed to perform a numerical sensitivity analysis, investigating the effect of granular particle shape on the response of backfill retained by integral bridge abutments. This was performed by using the Discrete Element Method (DEM). The theoretical integral bridge models used for the analyses are shown. The various particle shapes used for the numerical sensitivity analysis are described. These shapes included perfect spheres as well as convex polyhedra with numerous sphericities.

A comparison is presented of the software packages and processing units used for the numerical sensitivity analysis. The packages used were STAR-CCM+, a commercial code, and Blaze-DEM, a research code under development, produced at the University of Pretoria. Blaze-DEM offers an elevated level of performance since it makes use of Graphics Processing Unit (GPU) computing as opposed to traditional Central Processing Unit (CPU) computing. The methodology that was followed to verify the results from Blaze-DEM is presented.

The method used for calibrating the parameters of the particles for the DEM simulations is presented. The drop tests used to calibrate the particle-particle friction coefficient of the granular material are explained. This was followed by a description of the reduction of the Young's Modulus value for the purpose of reducing the computational times. The method used to verify the reduced Young's Modulus values is also shown. Verification tests on the particle size, rotation rate and number of particles chosen for the simulations are described.

Lastly, the chapter describes the procedure used to perform the numerical sensitivity analysis. The parameters investigated for the sensitivity analysis are presented.

3.2 THEORETICAL INTEGRAL BRIDGE MODELLING

The dimensions of the deck and abutments of a theoretical integral bridge were chosen to perform the numerical sensitivity analysis of particle shape of granular backfill retained by integral bridge abutments. It was decided that a 25 m deck with 2 m high abutments would be used for the DEM simulations. The expansion and contraction of the deck due to thermal variations was replicated by rotating the abutment about its base. The angle of rotation was determined by calculating the movements expected by the deck of the bridge due to temperature changes. Figure 3.1 shows the geometry of the theoretical integral bridge. The figure also illustrates the loading (passive movement) and unloading (active movement) directions for the abutment.

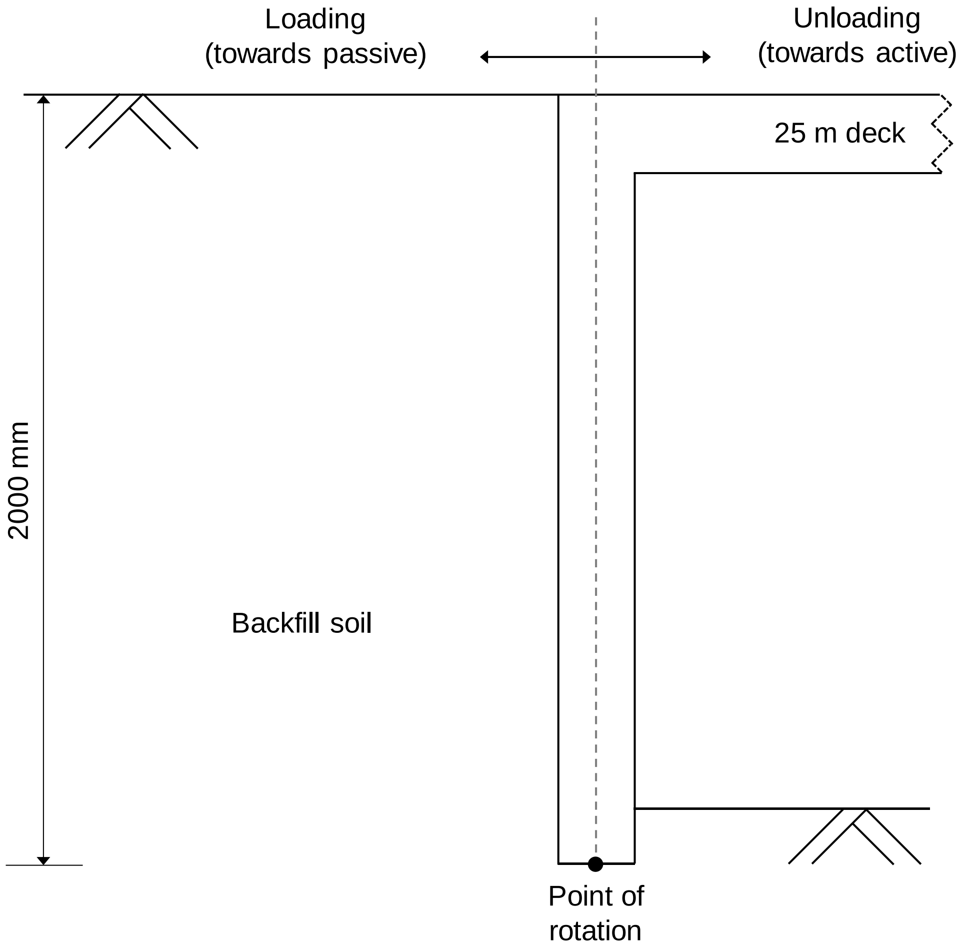

Figure 3.1: Theoretical integral bridge geometry

The movements of the deck due to temperature variations were used to determine the angle of rotation of the abutment. This rotation angle was used to cyclically rotate the abutment in the passive and active directions for the DEM analyses. The temperature data from the

Van Zylspruit integral bridge in South Africa was used to calculate the expected expansion of the deck. Skorpen *et al.* (2016) found that the maximum change in Effective Bridge Temperature (EBT) for the Van Zylspruit Bridge was 36 °C over a 5-month period.

A linear thermal coefficient of expansion of 12 x 10^{-6} °C^{-1} for concrete (Xu *et al.*, 2007), a maximum EBT of 36 °C and a length of 25 m was used to calculate the expansion of the deck of the bridge. It was calculated, as proposed by Roeder (2003), that the theoretical integral bridge would experience a maximum displacement of 10.8 mm on either side of the deck, assuming free expansion.

It was assumed that the deck would expand and contract the same amount i.e. half of the maximum displacement. The height of 2 m for the abutments of the theoretical bridge was used and a horizontal displacement of 5.4 mm was calculated at one side of the deck. Therefore, a total rotation angle of 0.0027 radians (0.154°) was calculated for the abutment.

The angle of rotation and horizontal displacement were assumed to be from the maximum loading position to the maximum unloading position of the abutment. Therefore, the horizontal displacement and rotation angle needed to be halved to be considered from the origin of the abutment. These representations for the magnitude of the displacements and rotations are illustrated in Figures 3.2 and 3.3 respectively.

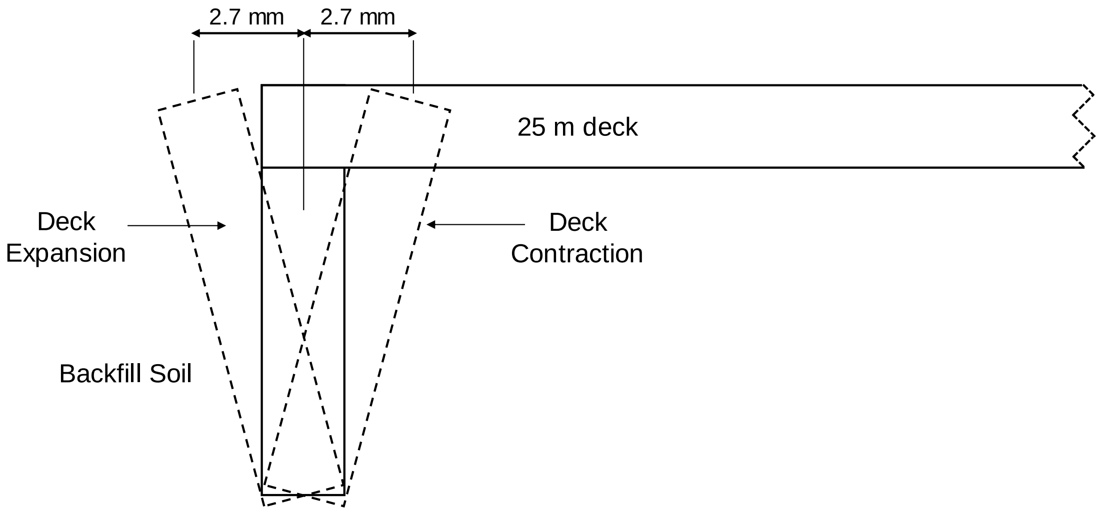

Figure 3.2: Representation of the displacement of the deck

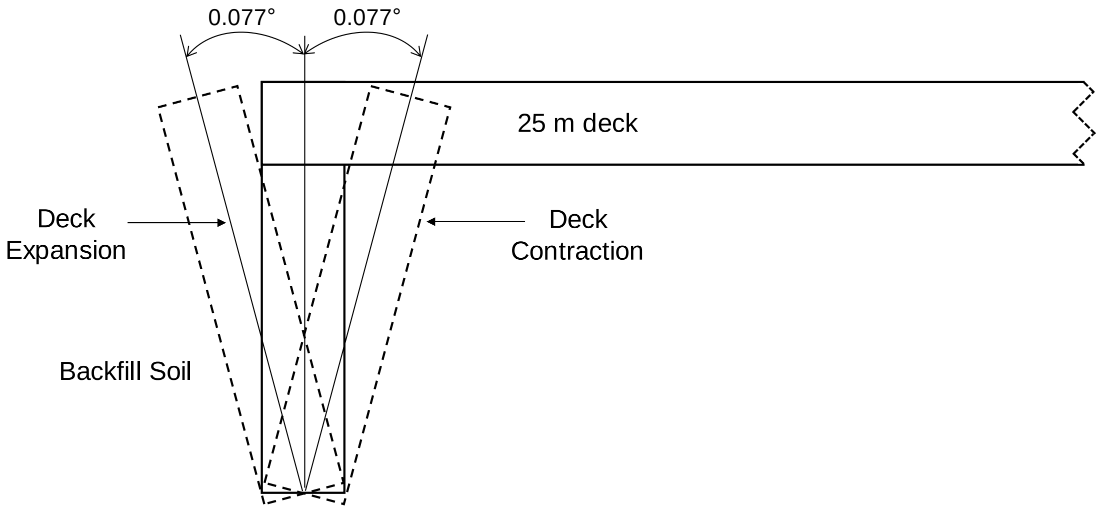

Figure 3.3: Representation of the rotation of the abutment

3.3 PARTICLE SHAPES USED IN DEM ANALYSES

Various particle shapes were modelled to perform the numerical sensitivity analysis investigating the effect of granular particle shape on the response of backfill retained by integral bridge abutments. Govender *et al.* (2014) reported that the particle shape plays a significant role in DEM simulations and a wide range of shapes was therefore used. The shapes were spheres and the following polyhedral shaped particles: dodecahedrons, tetrahedrons, truncated tetrahedrons, triangular prisms and cubes. For each of the shapes modelled the largest dimension was approximately 5 mm. This was done to keep the overall size of the various shapes similar. The perfect sphere with a 5 mm diameter is illustrated in Figure 3.4.

The maximum and minimum possible void ratios for packed spheres are shown in Figure 3.5. The maximum void ratio is obtained when spheres are packed in a simple cubic packing. This occurs when each of the centres of the spheres is at 90° angles to the centre of the spheres with which it is in contact with. This results in a void ratio of 0.91. The minimum void ratio is obtained when there are 60° angles between the spheres’ centres, i.e. a tetrahedral packing. The minimum void ratio of packed spheres is 0.34 (Lu and Likos, 2004).

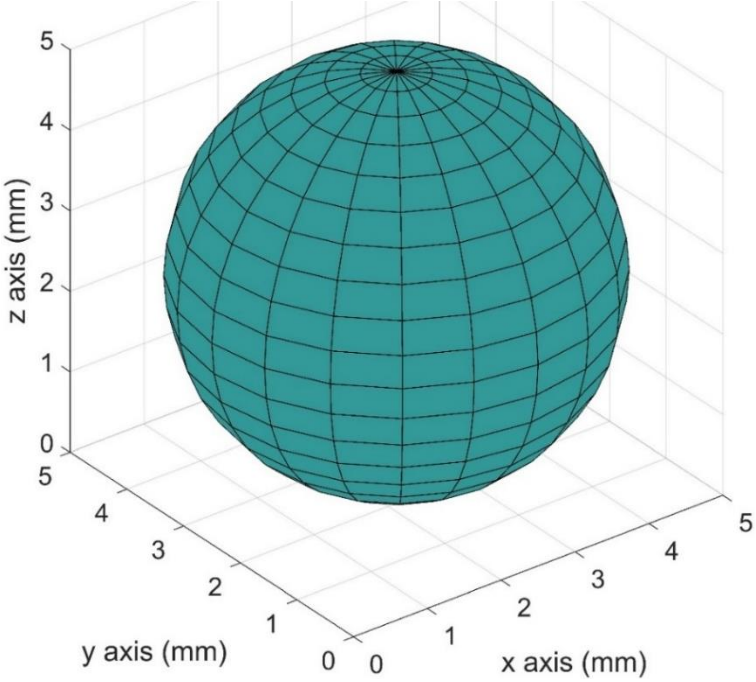

Figure 3.4: DEM particle – Sphere

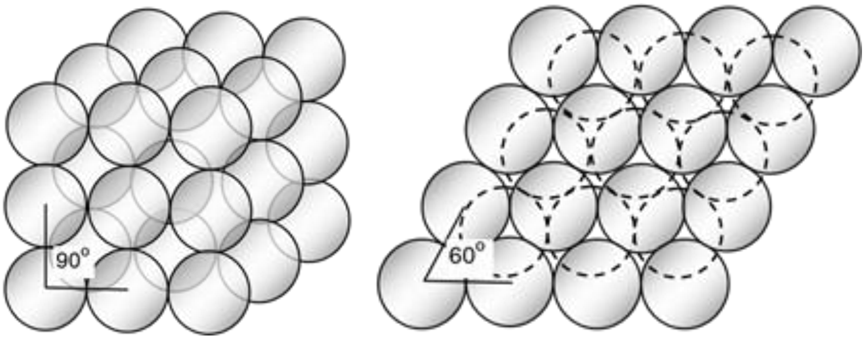

Figure 3.5: Maximum (left) and minimum (right) void ratios of spheres (Lu and Likos, 2004)

Höhner *et al.* (2012) stated that the type of particle shape approximation plays an important role in DEM simulations. Convex polyhedra were therefore used for the sensitivity analysis. A convex polyhedron is a polyhedron with the property that for any two points inside that shape, the line segment joining them is contained within the polyhedron. The convex polyhedra were not rounded or modelled as sphere-clumped particles. This was done since the polyhedra could provide angularity to the shape, while the equivalent sphere-clumped shapes would have rounded edges. It was suggested that the angularity of the shapes provided a better representation of a granular material and would, therefore, yield more realistic results in the sensitivity analysis (Govender *et al.*, 2014).

A vertex of a polyhedral shape is defined as a corner of the shape, while an edge refers to a line segment that joins two vertices. A face of a polyhedral shape refers to an individual surface made up of edges and vertices as the boundaries. The cubes used in the sensitivity analysis had edge lengths of 5 mm as depicted in Figure 3.6.

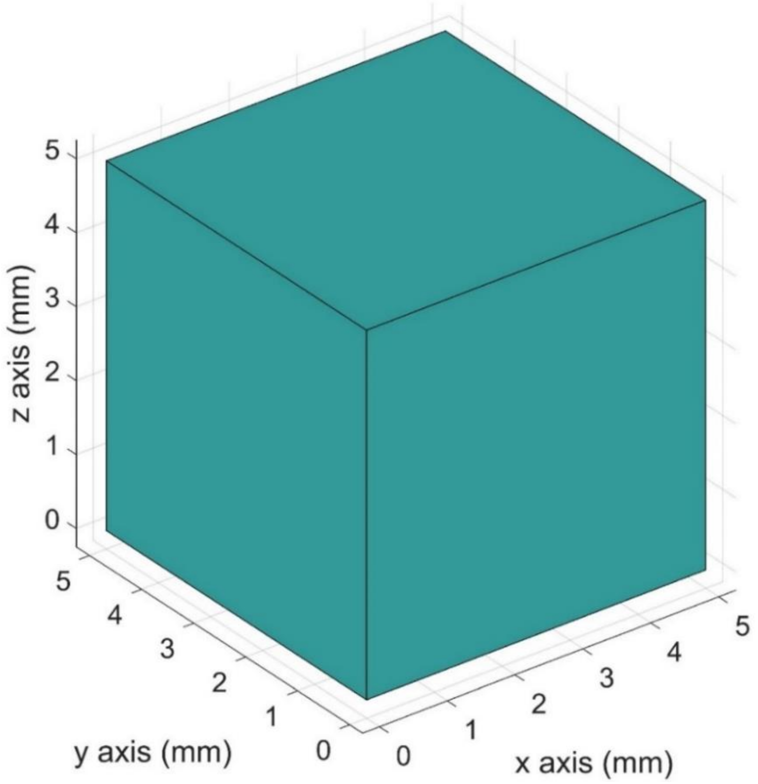

.

Figure 3.6: DEM particle – Cube

The triangular prisms (Figure 3.7) consisted of two equilateral triangular faces and three square faces. These faces had edge lengths of 5.77 mm and a height of 5 mm. The dodecahedrons used in the sensitivity analysis were regular convex dodecahedrons. Dodecahedrons are polyhedra with 12 flat faces, 20 vertices and 30 edges. A regular dodecahedron has 12 flat pentagonal faces. The dodecahedrons used in the simulations had an edge length of 2.1 mm and a maximum diagonal length of 5.89 mm as illustrated in Figure 3.8.

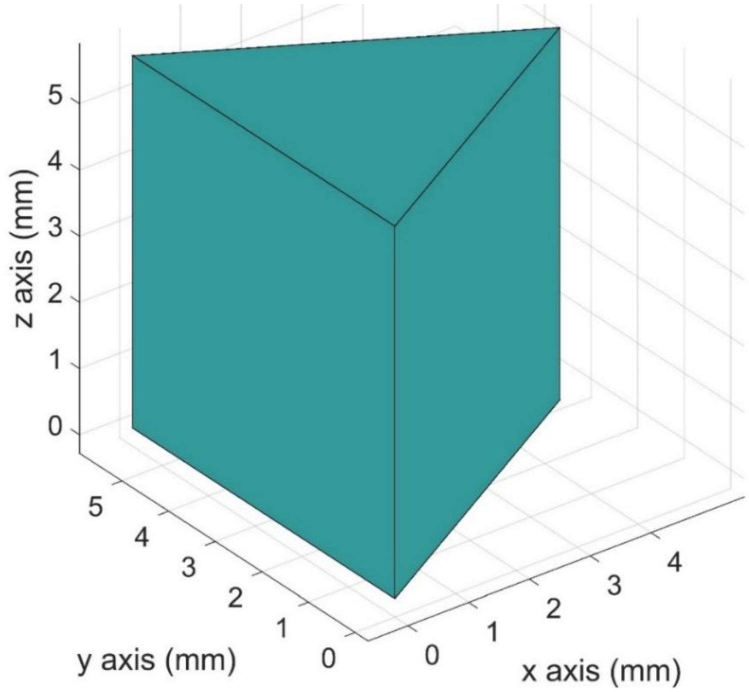

Figure 3.7: DEM particle – Triangular prism

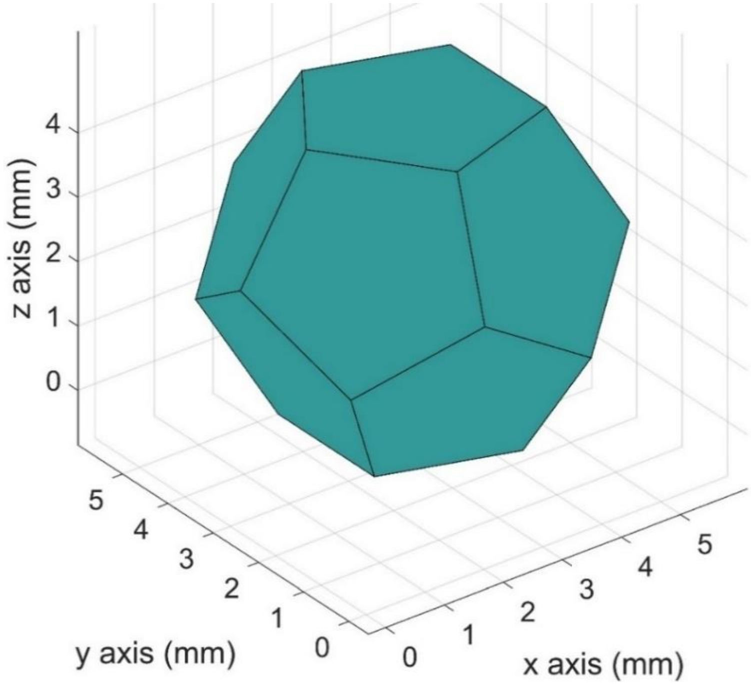

Figure 3.8: DEM particle – Dodecahedron

The convex polyhedra particles simulated also included tetrahedrons and truncated tetrahedrons. The tetrahedrons consisted of three equilateral triangular faces with lengths of 5 mm as shown in Figure 3.9. A truncated tetrahedron has 4 regular hexagonal faces and

4 equilateral triangular faces. Truncated tetrahedrons have 12 vertices and 18 edges. The truncated tetrahedrons, as illustrated in Figure 3.10, were constructed by truncating all 4 vertices of the regular tetrahedrons.

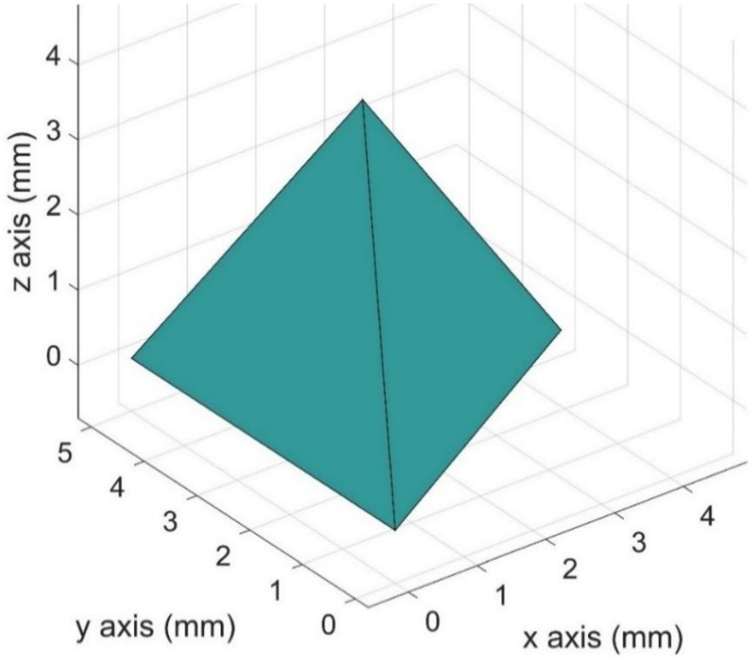

Figure 3.9: DEM particle – Tetrahedron

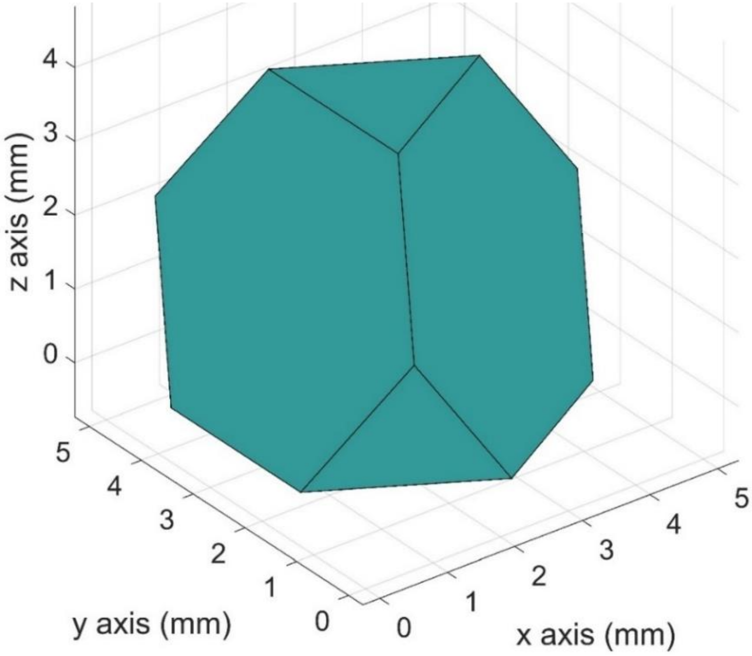

Figure 3.10: DEM particle – Truncated tetrahedron

The sphericities were calculated for the six particle shapes selected for the numerical sensitivity analysis. This was performed by using the surface areas and volumes of the various shapes with the method proposed by Wadell (1935).

The sphericities were calculated to quantify the angularity of the various particle shapes used in the sensitivity analysis. A lower sphericity value for a particle signified a higher angularity. Table 3.1 presents the sphericities for the six particle shapes. The table shows that the sphere had the highest sphericity (lowest angularity) with a value of 1.0, while the tetrahedron had the lowest sphericity (highest angularity) with a value of 0.671.

Table 3.1: Sphericities of particle shapes used in DEM analyses

Particle shape	Sphericity
Spheres	1.00
Dodecahedrons	0.911
Cubes	0.806
Truncated tetrahedrons	0.775
Triangular prisms	0.716
Tetrahedrons	0.671

3.4 INTEGRAL BRIDGE ABUTMENT MODELLING

Three integral bridge abutment models were chosen to perform the necessary calibration and verification tests as well as to perform the numerical sensitivity analysis. A small abutment model, which replicated a scaled-down version of the theoretical integral bridge, was initially used. This model was used for the Young’s Modulus reduction, rotation rate, particle size and software verification tests.

Medium and large abutment models were also prepared to replicate a full-scale model of a portion of the granular backfill from the theoretical integral bridge. The medium abutment model was used for the software verification as well as for the sensitivity analysis of the six particle shapes considered. The large abutment model was used to verify the size of the medium abutment model. In each of the models, the number of particles used were chosen such that the particles would fill the entire model space. These numbers were rounded to the nearest 1 000.

3.4.1 Small abutment model

A small abutment model was the first DEM model used. The model consisted of a rigid abutment which rotated about its base. The granular backfill particles were placed within a 150 mm x 150 mm x 350 mm container as illustrated in Figure 3.11. The model was considered to be a scaled-down version of the theoretical integral bridge with the point of rotation at the bottom of the abutment.

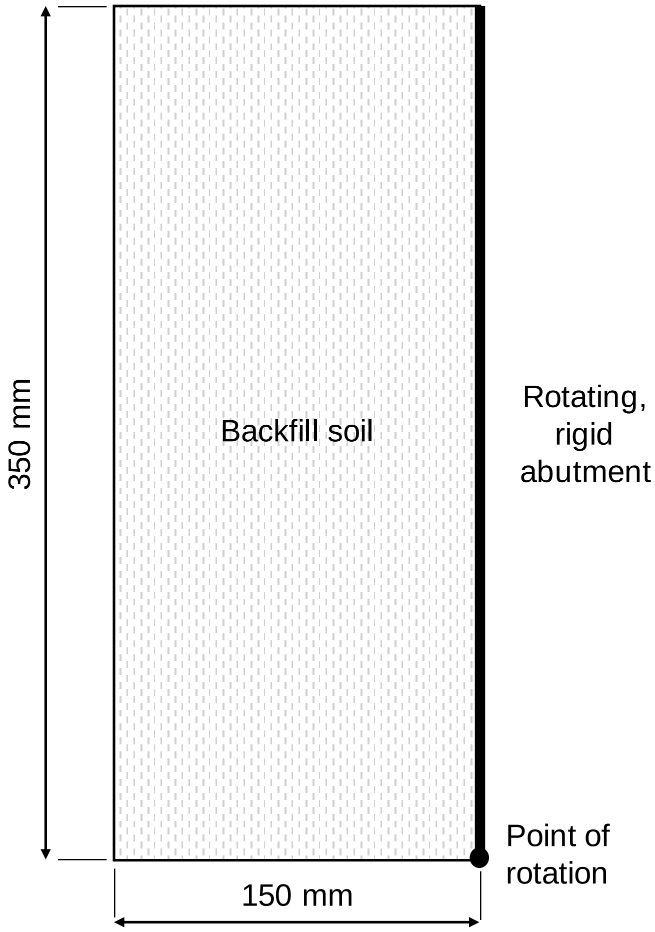

Figure 3.11: Small abutment model side view

Three of the sides as well as the bottom of the container within which the backfill particles were placed were rough, rigid and fixed boundaries. The abutment was rough and rigid, however, was also allowed to rotate about a hinge at its base. Figure 3.12 shows this in a 3D view of the model.

The small abutment model was used to perform the verification of the reduction of the Young's Modulus for the purpose of reducing the computational times. The model was also used in the software, particle size and rotation rate verification tests. The small abutment model could hold approximately 60 000 spherical particles with diameters of 5 mm.

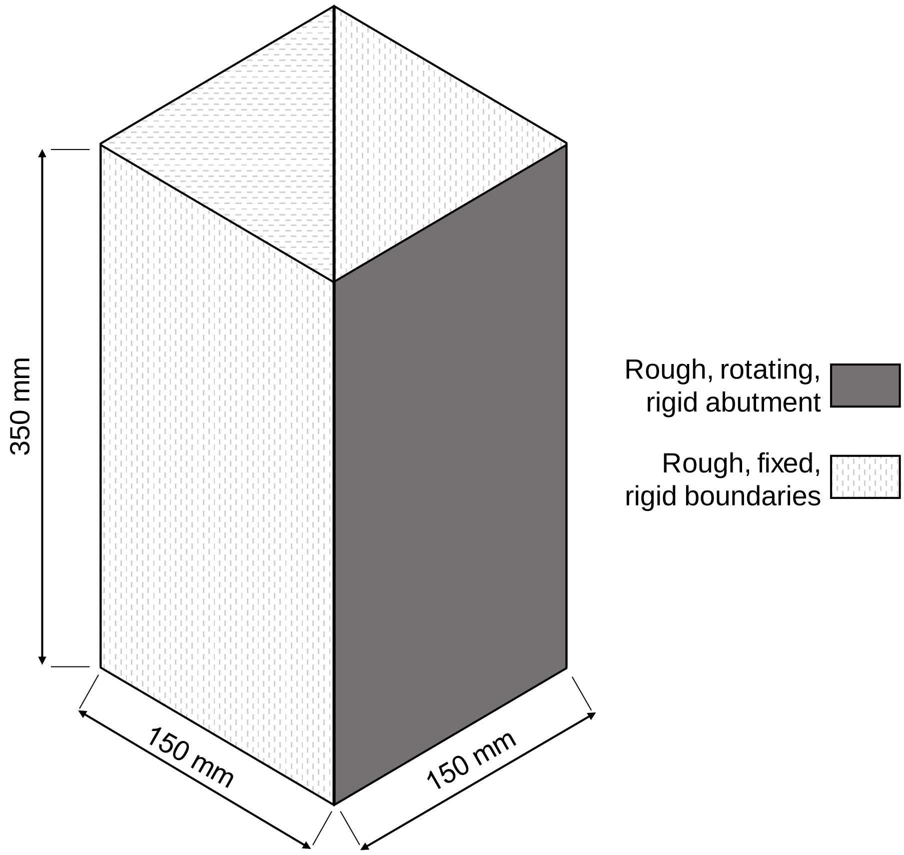

Figure 3.12: Small abutment model

Using the rotation angle of 0.154° at the base of the 350 mm abutment resulted in horizontal movements at the top of the model which were only 0.945 mm. The particle sizes of 5 mm used were much larger than the movements imposed on the abutment for the small abutment model. Larger movements were therefore required for a more realistic representation of a granular material's behaviour.

3.4.2 Medium abutment model

To increase the magnitudes of the horizontal movements, the point of rotation of the modelled abutment was moved from the base of the 350 mm abutment to 2 m below the top of the abutment, i.e. 1.65 m below the base. The container which the particles were placed within had dimensions of 300 mm x 150 mm x 350 mm.

Using the same rotation angle with the new rotation point resulted in larger horizontal movements. However, for the medium abutment model, all of the granular backfill was not modelled, since over 50 000 000 spheres would have been required and therefore would have drastically increased the computational times. Rather, a portion of the top of the backfill adjacent to the abutment was modelled. A 3D view of the medium abutment model is depicted in Figure 3.13. The figure shows the rotating abutment and the fixed boundaries.

The medium abutment model was used for the software verification as well as for the sensitivity analysis investigating the effect of granular particle shape on the response of backfill retained by integral bridge abutments. This model could hold approximately 140 000 spherical particles with diameters of 5 mm.

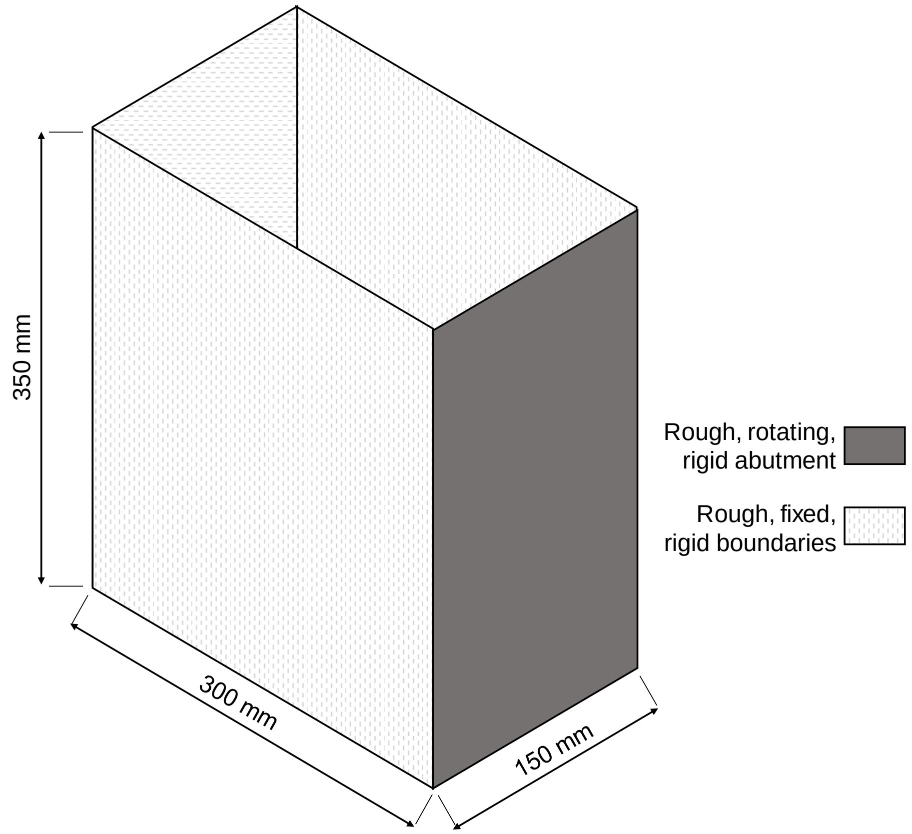

Figure 3.13: Medium abutment model

3.4.3 Large abutment model

A large abutment model was used to verify that the number of particles used in the medium abutment model would be sufficient to accurately model granular backfill material behaviour for the sensitivity analysis. The large abutment model is illustrated in Figure 3.14. The figure shows that the dimensions of the large abutment model were double the size of the medium abutment model i.e. a container with a size of 600 mm x 300 mm x 700 mm was used. The point of rotation of the large abutment model was also 2 m below the top of the abutment, i.e. 1.3 m below the base. The large abutment model could hold approximately 1 500 000 spherical particles with diameters of 5 mm.

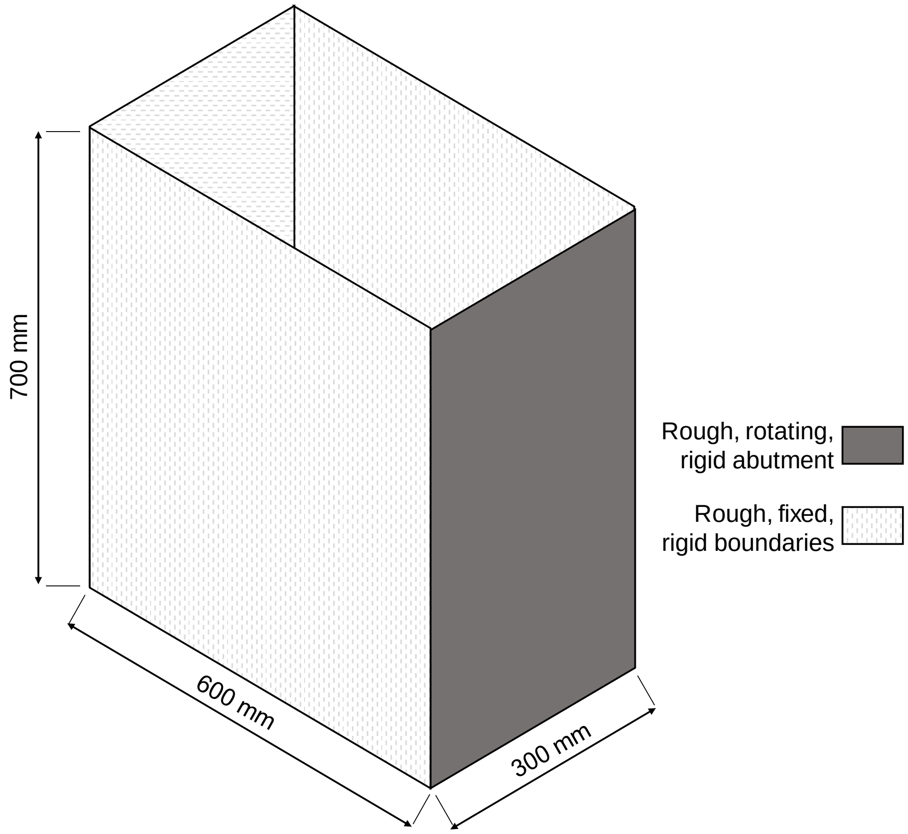

Figure 3.14: Large abutment model

A comparison of the geometries of the medium and large abutment models to the theoretical integral bridge is presented in Figure 3.15. The figure shows the point of rotation as well as the loading and unloading directions of the abutment which was rotated cyclically for the verification tests and sensitivity analysis simulations.

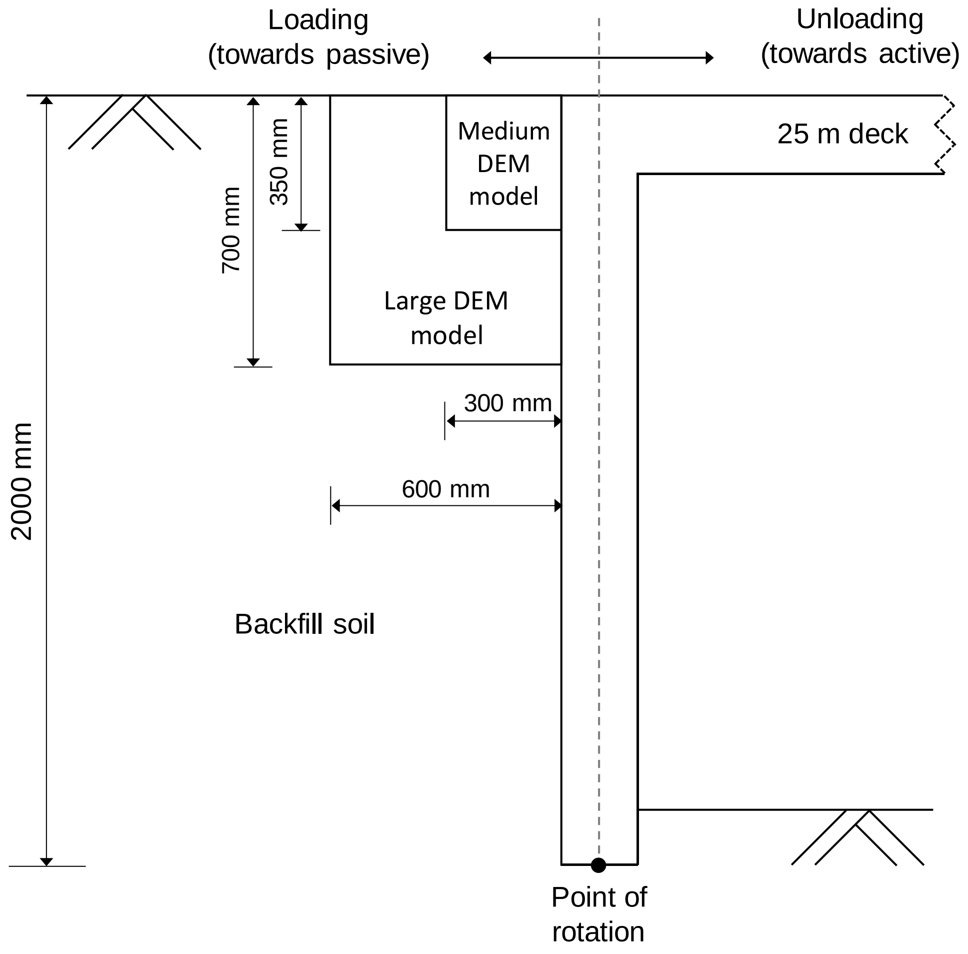

Figure 3.15: Comparison of geometries between medium and large abutment models

3.5 SOFTWARE COMPARISON

Two DEM software packages were used for the verifications and calibrations of the modelling. These software packages were STAR-CCM+, a commercial suite developed by CD-adapco, and Blaze-DEM, a research code under development introduced by Govender (2015) at the University of Pretoria.

One of the main differences between these packages is the use of different processing units to perform the simulations. STAR-CCM+ makes use of the Central Processing Unit, which is the traditional method used to perform DEM simulations. Blaze-DEM, however, makes use of the Graphics Processing Unit which therefore results in an elevated level of performance.

Another difference between the software packages is in the particle shapes which could be modelled. Blaze-DEM offered the possibility of modelling spheres, convex and non-convex polyhedra shapes since its introduction in 2015 (Govender, 2015). However, STAR-CCM+ only introduced the modelling of convex polyhedra shapes in July 2017, without the possibility of modelling non-convex polyhedra shapes (Siemens PLM, 2017). STAR-CCM+ allows multi-sphere clumped particles to be modelled, whereas only single particles can be modelled in Blaze-DEM.

The software packages were installed on separate computers at the University of Pretoria. Table 3.2 summarises the specifications for the CPU of the computer used for the STAR-CCM+ simulations and the GPU of the computer used for the Blaze-DEM simulations. The table shows that while the GPU had a slower clock frequency as opposed to the CPU, it contained many more cores and threads which are ideally used for parallel processing. The computer with which the Blaze-DEM simulations were performed held three GPUs, meaning that three parallel simulations could be performed as opposed to the single simulation with the computer used for STAR-CCM+ simulations.

Table 3.2: Summary of processing units used for STAR-CCM+ and Blaze-DEM

Component	STAR-CCM+ processing unit specifications	Blaze-DEM processing unit specifications
Processing unit	CPU	GPU
Processing unit make	Intel	GIGABYTE
Processing unit model	Core i7-4930K	GeForce GTX 1080 G1
Number of processing units	1	3
Number of cores per unit	6 (12 Threads)	2 560 (327 680 Threads)
Base clock frequency	3.40 GHz	1.72 GHz
Boost clock frequency	3.90 GHz	1.86 GHz
Power usage	130 W	180 W
Recommended price in USA	$594.00	$699.00
Recommended price in SA	R7 199.00	R10 999.00

Figure 3.16 depicts the computer used for the Blaze-DEM simulations. Figure 3.17 shows the three GIGABYTE GeForce GTX 1080 G1 GPUs used for Blaze-DEM simulations.

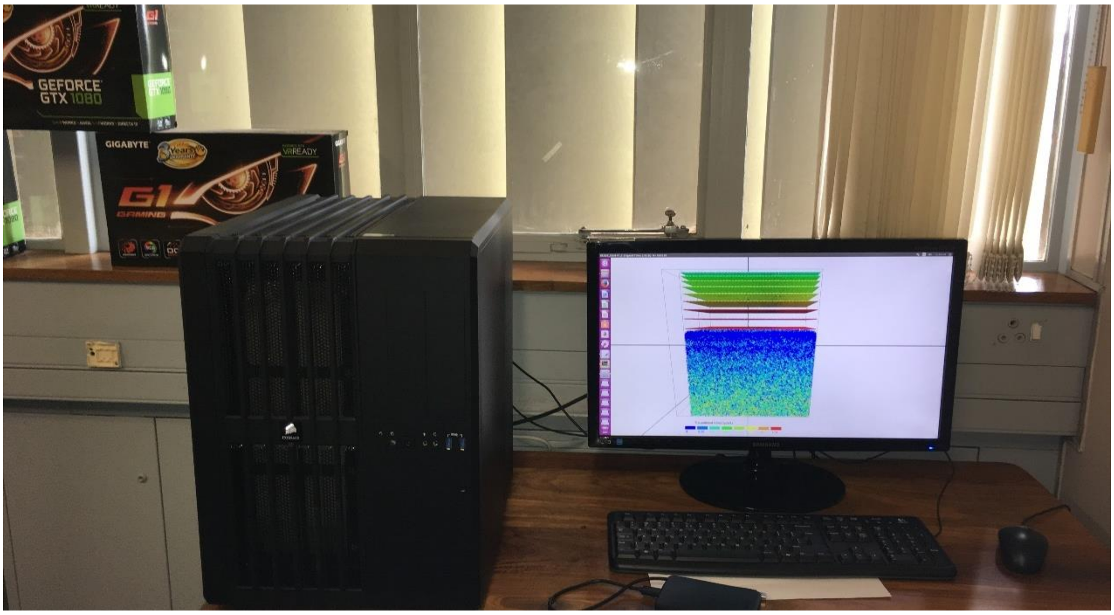

Figure 3.16: Computer used for Blaze-DEM simulations

Figure 3.17: Three GPUs used for Blaze-DEM simulations

3.6 PARAMETERS USED FOR DEM SIMULATIONS

As reported by Coetzee (2017), the input parameters used in DEM simulations play an important role in the accuracy of the results obtained. Certain parameters used in this study required calibration and verification. These parameters were the particle-particle friction coefficient, the Young's Modulus, the particle size, the rotation rate and the number of particles. However, the remaining parameters used for the numerical sensitivity analysis were obtained from literature.

Table 3.3 presents the values of the parameters obtained from literature which remained unchanged for the various calibration and verification tests as well as for the sensitivity analysis. The density value in the table refers to the density of an individual granular particle. The coefficient of rolling friction was not calibrated since the desired angle of repose of the granular particles was less than 35° (Derakhshani *et al.*, 2015). The parameters shown in Table 3.3 were for an individual silica quartz sand particle. The density and particle-wall friction coefficient were obtained from Xu *et al.* (2002), while the restitution coefficients and the coefficient of rolling resistance were obtained from Coetzee (2017).

Table 3.3: DEM parameters obtained from literature

Parameter (Symbol)	Value	Source
Density (ρ)	2650 kg/m^3	Xu *et al.* (2002)
Normal Restitution Coefficient (e_n)	0.50	Coetzee (2017)
Tangential Restitution Coefficient (e_t)	0.60	Coetzee (2017)
Particle-wall friction coefficient (μ_w)	0.70	Xu *et al.* (2002)
Coefficient of rolling friction (μ_r)	0.001	Coetzee (2017)

3.7 CALIBRATION OF DEM PARAMETERS

The predictions of DEM simulations are largely dependent on the input parameters of the particles (Coetzee, 2017). A drop test with only gravitational loads, as proposed by Nakashima *et al.* (2011) and Coetzee (2016), was performed to calibrate the DEM particles to a desired angle of repose. The particle-particle friction coefficient (coefficient of sliding friction) was changed until the angle of repose was obtained. The angle of repose was measured from the heap of granular particles acquired from the drop test.

Coetzee (2016) proposed reducing the Young’s Modulus of the particles to speed up the computational times of the DEM simulations. The value of the Young’s Modulus was reduced from a theoretical value of 70 GPa for an individual silica quartz sand particle (Xu *et al.,* 2002). Verification tests were performed on reduced Young’s Modulus values to determine to what extent the value could be reduced, yet still deliver realistic results.

3.7.1 Drop tests for particle-particle friction coefficient

The particle-particle friction coefficient (coefficient of sliding friction) required calibration before the sensitivity analysis could be performed. The coefficient of the DEM particles was calibrated by performing drop tests with only gravitational loads. As suggested by Coetzee (2016), the particles were modelled as two-sphere and three-sphere clumps, rather than single spheres, for the calibration tests.

The two-sphere and three-sphere clumps used for the drop tests are depicted in Figures 3.18 and 3.19 respectively. The figures show that each single sphere had a radius of 2.5 mm and the clumps were joined at the surfaces of the spheres. Therefore, no overlaps were created between the spheres for the clumped models. The spheres were clumped together since single spherical particles would not form a heap of granular material as required for the drop test.

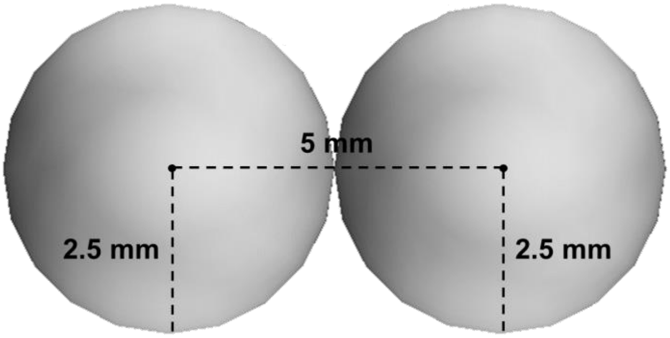

Figure 3.18: Two-sphere clumps used in drop tests

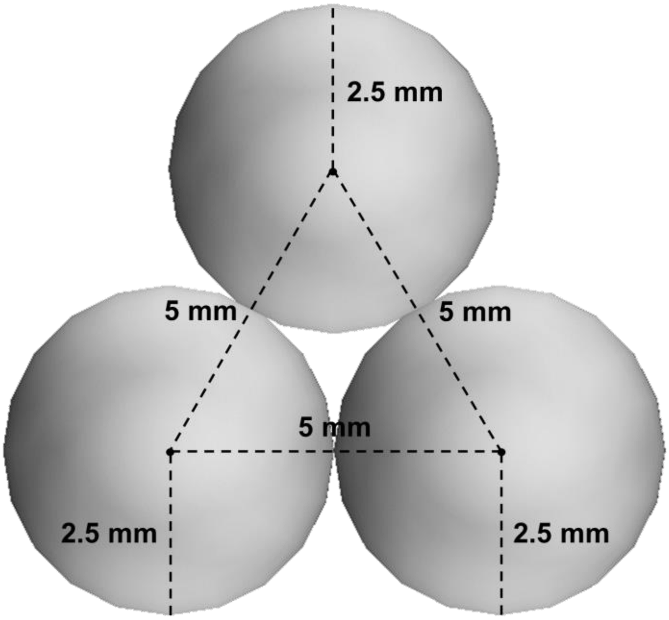

Figure 3.19: Three-sphere clumps used in drop tests

A total of 9 000 spherical particles (1 560 g) were dropped with random orientations from a height of 150 mm for the calibration tests. This meant that 4 500 two-sphere clumps and 3 000 three-sphere clumps were used for the respective drop tests. The 9 000 particles were dropped in 9 seconds within a 30 mm x 30 mm injection grid. This meant that an injection rate of 1 000 particles per second (173.33 g/s) was used for the drop tests.

Once the 9 000 particles were injected, the particles were allowed to settle under gravitational loads until a state of zero velocity was reached. The angle of repose of the heap of the granular materials was then measured for the various particle-particle friction coefficients and number of sphere clumps. Figure 3.20 illustrates an intermediate step of a drop test with the two-sphere clump particles. The figure also shows the 30 mm x 30 mm injection grid used.

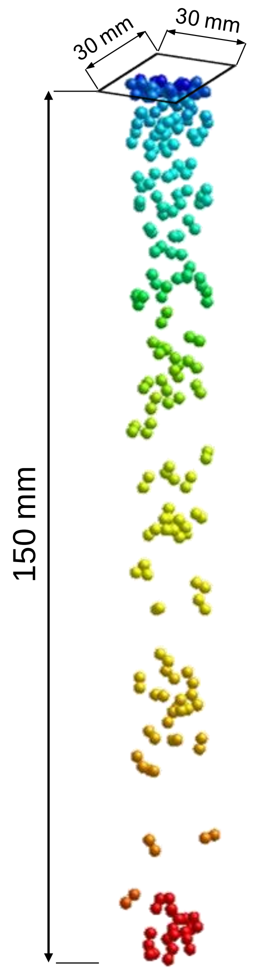

Figure 3.20: Intermediate step of drop test in STAR-CCM+

A total of six drop tests were simulated with various particle-particle friction coefficients and number of clumps used. The particle-particle friction coefficients and number of clumps used were changed until an angle of repose between 30° to 35° was obtained. This range was suggested to replicate that of a typical sand (Derakhshani *et al.*, 2015).

As reported by the results from Derakhshani *et al.* (2015) the coefficient of rolling friction was not calibrated since the desired angle of repose was less than 35°. Table 3.4 summarises the parameters which were changed for the six drop tests. The six drop tests were performed in only STAR-CCM+, since Blaze-DEM did not support multi-sphere clumping.

Table 3.4: Varied parameters used for drop tests

Drop test number	**Number of sphere clumps**	**Particle-particle friction coefficient (μ_p)**
1	3	0.30
2	2	0.30
3	3	0.45
4	2	0.45
5	3	0.60
6	2	0.60

Further drop tests were performed using the six particle shapes selected for the sensitivity analysis. These drop tests were performed in Blaze-DEM since the computational times of simulating the various convex polyhedra shapes in STAR-CCM+ would have been impracticable.

The 30 mm x 30 mm injection grid was also used for the second set of drop tests and the particles were injected from a height of 150 mm with a rate of 1 000 particles per second. The difference between the drop tests in STAR-CCM+ and Blaze-DEM was that a confinement was required, since the particles used in Blaze-DEM were not clumped together. A rigid 150 mm x 150 mm confinement boundary was placed on the base to prevent the particles from rolling away. Figure 3.21 illustrates an intermediate step of the drop test with single spheres in Blaze-DEM which illustrates the confinement boundary. The dimensions in the figure are distorted since it is shown in perspective view.

The drop tests performed in Blaze-DEM were not intended to calibrate the particles, however, were performed to investigate the influence of sphericity on the angle of repose. The particle-particle friction coefficient obtained from the calibration drop tests performed in STAR-CCM+ was used for the drop tests in Blaze-DEM.

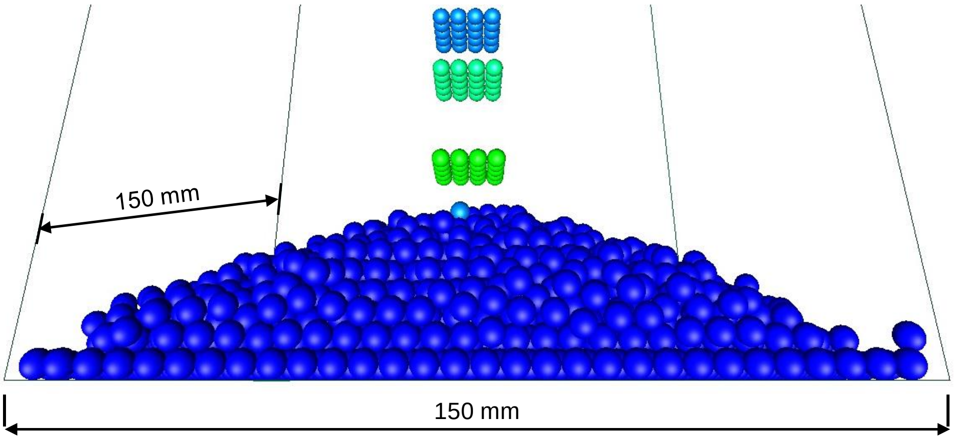

Figure 3.21: Perspective view of intermediate step of drop test in Blaze-DEM

3.7.2 Reduction of Young's Modulus value

Coetzee (2017) reported that the size of the time-step required to ensure convergence used for DEM simulations is related to the stiffness, density and size of the particle. To have the largest possible time-step, the Young's Modulus was required to be as low as possible while the particle density and radius were required to be as high as possible. The particle density and radius could only be increased realistically by small factors and therefore did not have a significant impact on the time-step calculation. However, the Young's Modulus value had the largest influence of all the parameters on the size of the time-step and therefore drastically influenced the time-step required. Coetzee (2016) therefore proposed reducing the Young's Modulus of the particles to speed up the computational times of the DEM simulations.

The theoretical Young's Modulus value for an individual silica quartz sand particle is approximately 70 GPa (Xu *et al.*, 2002). This Young's Modulus value resulted in extremely high computational times in STAR-CCM+. Reduced values for the Young's Modulus were tested, as proposed by Coetzee (2017), to determine a suitable value which would yield realistic results as well as faster simulation times. The Young's Modulus of 70 GPa was reduced with factors of 100, 1 000 and 10 000, i.e. to values of 700 MPa, 70 MPa and 7 MPa respectively.

Coetzee (2017) suggested that the verification of the reduction of the particle's Young's Modulus is application dependent. The small abutment model was used for the verifications. The model space was filled with 60 000 spherical particles with diameters of 5 mm. The DEM particles had to be calibrated for cyclic loading and unloading movements to perform the sensitivity analysis. The abutment model was therefore cycled once in the passive direction (loading) and once in the active direction (unloading). The lateral earth pressure coefficients and bulk densities were investigated for the numerical sensitivity analysis. The following parameters were therefore analysed to perform the verification tests for the reduction of the Young’s Modulus value:

- The density and average normal particle overlap with depth of the abutment model.
- The coefficient of active state lateral earth pressure.
- The average normal overlap between the particles.

The amount of deformation of a particle is related to the overlap that is generated between the particles. The overlap is related to the Young’s Modulus of the particles (Cundall and Strack, 1979). This means that a Young’s Modulus which is too low would result in excessively large overlaps between the particles. Consequently, this would result in an unrealistically high bulk density of the system.

An additional outcome of a Young’s Modulus which is too low would be that the densities and particle overlap at the bottom of a packed system would be much higher than at the top. Therefore, a comparison of the densities and normal overlaps between the particles with depth for the various Young’s Modulus values was performed.

Another method used to verify the reduction in Young’s Modulus was to compare the calculated lateral earth pressure coefficients against the theoretical coefficients. The lateral earth pressure coefficient could be calculated by dividing the total horizontal force on the wall by the force calculated by integrating the vertical stress determined from the bulk density distribution with depth over the area of the wall. The theoretical coefficients could be estimated from the angle of repose of a particle acquired from the drop tests. Previous work by Xu *et al.* (2007) as well as Cosgrove and Lehane (2003) indicated that active conditions are reached in the backfill during the first thermal displacement cycle of an integral bridge abutment. Only one cycle was imposed on the granular backfill and the imposed movement of the rotating wall was small. For these reasons, the coefficients compared were only for the active state.

The active lateral earth pressure coefficient (K_a) could be calculated using the angle of repose obtained from the drop tests and Equation 3.1 as follows:

$$K_a = \frac{1 - \sin \Phi'}{1 + \sin \Phi'} \qquad \textbf{(3.1)}$$

Where:

K_a Active lateral earth pressure coefficient

Φ' Angle of repose [°]

The final method used to verify the reduction in Young’s Modulus was to assess the average normal overlap between the particles. The literature has suggested that this overlap should not exceed a certain percentage of the radius of the particle. Limits for the overlap of 1% (Coetzee, 2017), 0.5% (Cleary, 2010) and 0.3% (Lommen, 2014) of the particle radius were used for this assessment.

Table 3.5 summarises the three reduced Young’s Modulus values and their respective reduction factors. The tests of the reduction of the Young’s Modulus verification were performed in STAR-CCM+. A rotation rate of 0.0027 rad/s and the particle-particle coefficient of 0.45 obtained from the drop tests was used for the tests.

Table 3.5: Varied parameters used for Young’s Modulus reduction verification tests

Test number	**Young’s Modulus ($\boldsymbol{E}$)**	**Reduction factor**
1	7 MPa	10 000
2	70 MPa	1 000
3	700 MPa	100

3.8 SOFTWARE AND NUMERICAL MODEL VERIFICATION TESTS

The software packages and abutment models required verification before the numerical sensitivity analysis was performed. The results obtained from Blaze-DEM required verification since it is a research code. A comparison between the results from STAR-CCM+ and Blaze-DEM was therefore performed. Three sets of simulations were performed to verify that the particle sizes, rotation rates and number of particles were practical before the sensitivity analysis was conducted.

3.8.1 Software verification test

Blaze-DEM is a research code under development, meaning that the results obtained from it needed to be verified for it to be deemed suitable for use (Govender *et al.*, 2016). Two comparison tests were performed to determine whether the results from Blaze-DEM were suitable for the sensitivity analysis. The first comparison test involved spheres with the small abutment model and the second comparison test consisted of cubes with the medium abutment model.

The small abutment model, used in the verification of the reduction of the Young's Modulus, was used in STAR-CCM+ and Blaze-DEM to perform the first comparison test. In both software suites, the model space was filled with 60 000 spherical particles with diameters of 5 mm. For the second comparison test, a total of 90 000 cubes with edge lengths of 5 mm were used in both STAR-CCM+ and Blaze-DEM.

The Young's Modulus (70 MPa) obtained from the reduction verification tests and the particle-particle friction coefficient (0.45) obtained from the drop tests were used for the comparison tests. A rotation rate of 0.0027 rad/s was used for the imposed cyclic loading of the abutment.

In both tests, the model abutment was rotated towards and away from the particles 25 times. The lateral earth pressure coefficients and densities versus number of cycles of the abutment were observed to compare the software suites. Similar values and behaviours for these earth pressure coefficients and densities versus number of cycles from both the suites would suggest that Blaze-DEM would later provide accurate results for the numerical sensitivity analysis.

The parameters and conditions used in both software suites were identical apart from the methods used to inject the particles. In both tests in STAR-CCM+, the particles were placed in a grid (with random orientations for the cubes) and allowed to settle under gravitational loads, until a state of zero velocity was reached. This method was utilised as it greatly reduced the computational times in STAR-CCM+, since all the particles could be generated in the first iteration. Since the computational times in Blaze-DEM were not a drawback, the particles were dropped into the respective models from a height of 350 mm.

The different injection methods resulted in a minor variation between the initial bulk densities in the two software packages. The initial bulk densities were slightly lower in STAR-CCM+ as opposed to Blaze-DEM. However, after the 25 cycles, the differences between the densities were negligible i.e. less than 1% difference for both tests. It was therefore suggested that the different injection methods would not greatly affect the results from the software verification. The initial and final bulk densities for the comparison tests are presented in Tables 3.6 and 3.7.

Table 3.6: Initial and final bulk densities for software verification test with spheres

Parameter	STAR-CCM+	Blaze-DEM	Difference between software
Density after 1 cycle	1765 kg/m^3	1800 kg/m^3	1.94%
Density after 25 cycles	1798 kg/m^3	1807 kg/m^3	0.50%

Table 3.7: Initial and final bulk densities for software verification test with cubes

Parameter	STAR-CCM+	Blaze-DEM	Difference between software
Density after 1 cycle	1845 kg/m^3	1891 kg/m^3	2.43%
Density after 25 cycles	1979 kg/m^3	1992 kg/m^3	0.65%

3.8.2 Particle size independence study

The computational time of a DEM simulation is directly proportional to the radius of the spherical particle used. Therefore, the granular particle sizes had to be increased significantly to obtain practical simulation times. A study was performed to determine the extent to which the particle sizes could be increased by and still yield a realistic granular particle behaviour.

Blaze-DEM was used to simulate particles with smaller and larger diameters than the 5 mm diameter spheres used previously. A total of four simulations with various particle diameters were performed. The small abutment model was used for these simulations in Blaze-DEM. The abutment was cyclically rotated 25 times in the active and passive directions of the backfill material in each simulation.

The Young's Modulus of 70 MPa and particle-particle friction coefficient of 0.45 obtained from the previous calibration tests were used for the particle size verification. A rotation rate of 0.0027 rad/s was used for the imposed cyclic loading of the model abutment. Table 3.8 presents a summary of the simulations performed to investigate the effect of particle size in the DEM simulations. The lateral earth pressure coefficients and bulk densities for these particles were compared for the independence study.

Table 3.8: Varied parameters used for particle size independence study

Test number	Particle diameter	Number of particles
1	2.5 mm	500 000
2	4 mm	150 000
3	5 mm	60 000
4	10 mm	8 000

3.8.3 Rotation rate independence study

Three simulations were performed with different rotation rates to investigate the choice of the rate used, such that it was slow enough to model seasonal temperature variations, avoiding unrealistic dynamic or inertial effects. Tests with rates of 0.0009 rad/s, 0.0027 rad/s and 0.0081 rad/s were performed. The lateral earth pressure coefficients for these rates were compared for the verification. The rotation rate verification tests were performed using the small abutment model in Blaze-DEM.

The particle-particle friction coefficient of 0.45 and the Young's Modulus of 70 MPa obtained from the previous calibration tests was used for the particle size verification. A total of 60 000 spherical particles with 5 mm diameters were filled into the space of the small abutment model. Table 3.9 shows the three rotation rates and their equivalent frequencies used for the independence study. The model abutment was cyclically rotated with the various rotation rates in the passive (loading) and active (unloading) directions of the backfill material 25 times.

Table 3.9: Varied parameters used for rotation rate independence study

Test number	**Rotation rate** $(\boldsymbol{\omega})$	**Frequency** $(\boldsymbol{f})$
1	0.0009 rad/s	0.1667 Hz
2	0.0027 rad/s	0.5000 Hz
3	0.0081 rad/s	1.500 Hz

3.8.4 Model size independence study

The medium and large abutment models were used to investigate the number of particles required to accurately model granular backfill for the numerical sensitivity analysis. A total of 140 000 spherical particles were used for the medium abutment model, while the large abutment model required 1 500 000 spherical particles. The spherical particles had diameters of 5 mm. These tests were performed in Blaze-DEM with a Young's Modulus of 70 MPa, a rotation rate of 0.0027 rad/s and a particle-particle friction coefficient of 0.45.

The abutment from the medium abutment model was cyclically rotated in the active and passive directions 25 times, whereas the abutment was cyclically rotated 100 times with the large abutment model. This was performed to investigate whether enough cycles were used to perform the sensitivity analysis. The lateral earth pressure coefficients and bulk densities were investigated for the independence study of the size of the model.

3.9 PARTICLE SHAPE NUMERICAL SENSITIVITY ANALYSIS

Once the calibration and verifications tests were complete, the numerical sensitivity analysis could be performed, investigating the effect of granular particle shape on the response of backfill retained by integral bridge abutments. The final set of parameters used with the medium abutment model in Blaze-DEM is presented in Table 3.10.

Table 3.10: Final parameters used for numerical sensitivity analysis

Parameter (Symbol)	Value
Density (ρ)	2650 kg/m^3
Young's Modulus (E)	70 MPa
Normal restitution coefficient (e_n)	0.50
Tangential restitution coefficient (e_t)	0.60
Particle-particle friction coefficient (μ_p)	0.45
Particle-wall friction coefficient (μ_w)	0.70
Coefficient of rolling friction (μ_r)	0.001
Rotation rate (ω)	0.0027 rad/s

A total of six simulations, with the six different particle shapes, were performed for the sensitivity analysis. Table 3.11 shows the number of particles used for each of the six shapes used for the sensitivity analysis.

In each of the six simulations performed in Blaze-DEM, the various particles were rained in from the top of the medium abutment model. The particles were then allowed to settle to a state of zero velocity under only gravitational loads. Once the particles were settled, the model abutment was cyclically rotated in the active (unloading) and passive (loading) directions of the granular backfill 25 times.

Table 3.11: Varied parameters used for numerical sensitivity analysis

Test number	Particle shape	Number of particles
1	Spheres	140 000
2	Cubes	90 000
3	Triangular Prisms	100 000
4	Dodecahedrons	110 000
5	Tetrahedrons	100 000
6	Truncated Tetrahedrons	100 000

To investigate the results from the numerical sensitivity analysis, a number of parameters were observed for each of the cycles when the abutment was at its fully loaded and unloaded positions in the passive and active directions respectively. These parameters could be compared to theoretical values for the various particle shapes investigated. The effect of the particles' sphericities and angles of repose on these parameters were investigated.

The bulk density variations of the granular backfill were studied as the number of cycles increased. This was performed to investigate the degree of densification for the various particle shapes. The change in spatial density distributions in the granular backfill was also investigated for the different particle shapes. This was executed by splitting the backfill into zones of equal widths and analysing the densities in each zone.

As with the experiments performed by Xu *et al.* (2007) and Barker and Carder (2001), the mobilised lateral earth pressure coefficients (K) for the various shapes of granular backfill against the abutment were investigated. These values could be compared to the theoretical passive coefficient values (K_p). The theoretical value could be calculated using the estimated angle of repose (Φ') obtained from the drop tests and Equation 3.2 as follows:

$$K_p = \frac{1 + \sin \Phi'}{1 - \sin \Phi'} \tag{3.2}$$

Where:

K_p	Passive lateral earth pressure coefficient
Φ'	Angle of repose [°]

The horizontal stress distributions with depth along the abutment for the various particle shapes were also compared to theoretical values in a similar manner as the work done by Breña *et al.* (2007) and Khodair (2006). The force chain magnitudes in the granular backfill were analysed for the various particle shapes as performed by Azéma *et al.* (2009). Finally, the mean interparticle contact forces in the granular backfill, as well as the settlement of the backfill, could be analysed, which was similar to work done by England *et al.* (2000) and Ng *et al.* (1998).

The initial and final values as well as the difference in these values for the bulk densities, the lateral earth pressure coefficients, as well as the backfill settlements, were investigated. This was performed by calculating the correlation coefficients of the parameters when compared to the various particle shape sphericities and angles of repose. Exponential and linear trendlines were fitted to the data sets. In each comparison, the trendline with the higher coefficient of determination (R^2) was considered.

3.10 SUMMARY

DEM modelling was used to perform a numerical sensitivity analysis investigating the effect of granular particle shape on the response of backfill retained by integral bridge abutments. A total of six particle shapes were used for the sensitivity analysis. The sensitivity analysis was performed for a theoretical integral bridge abutment model.

The particles used in the DEM simulations required calibration of the particle-particle friction coefficient to a desired angle of repose. The Young's Modulus value for the particles was reduced to increase the computational efficiency. A verification of the reduction of this value was performed. Verification tests were performed on the particle size, the rotation rate and the number of particles used for the sensitivity analysis.

A comparison between the results from Blaze-DEM and STAR-CCM+ was performed to justify the numerical sensitivity analysis being performed in Blaze-DEM. This was done since Blaze-DEM could yield a much faster level of performance as opposed to STAR-CCM+.

A number of parameters of the granular backfill were investigated and compared to theoretical values to perform the sensitivity analysis. These parameters included the lateral earth pressure coefficients, the horizontal stress distributions, the change in bulk density of the backfill, the backfill settlement and the forces in the backfill. The parameters for the various shapes were compared to the shapes' sphericities and angles of repose to investigate the effect of the granular particle shape on the response of backfill retained by integral bridge abutments.

4 PRESENTATION AND ANALYSIS OF RESULTS

4.1 INTRODUCTION

A numerical sensitivity analysis was performed, to investigate the effect of granular particle shape on the response of backfill retained by integral bridge abutments. The numerical sensitivity analysis was performed by using the Discrete Element Method (DEM). Numerous DEM codes are available, however, STAR-CCM+ and Blaze-DEM were used in this study.

The parameters used in the DEM simulations required calibration to ensure that the results of the numerical sensitivity analysis were accurate. This chapter presents the results obtained from the calibration tests performed on the particle-particle friction coefficient used in the DEM simulations.

It is known that DEM simulations are computationally expensive. Two methods were used to reduce the computational times of the simulations. The first was to reduce the Young’s Modulus of the DEM particles. The results from the verification tests of these reduced Young’s Modulus values are included. A comparison of the computational times for the chosen Young’s Modulus values is shown to express the benefits of reducing this value.

The second method used to reduce the computational times was to explore different software packages. Blaze-DEM offers an elevated level of performance since it makes use of the processing capabilities of the Graphics Processing Unit (GPU) rather than the Central Processing Unit (CPU). Blaze-DEM is a research code under development. Therefore, comparison tests were performed between STAR-CCM+ and Blaze-DEM to justify the use of Blaze-DEM for the numerical sensitivity analysis. The computational benefits of using Blaze-DEM as opposed to STAR-CCM+ are presented.

The results from the independence studies performed on the particle size, rotation rate and number of particles used for the sensitivity analysis are shown.

Lastly, the results of the numerical sensitivity analysis are presented with a discussion on the parameters investigated. The bulk backfill densities, lateral earth pressure coefficients, backfill settlements, horizontal stress distributions, mean interparticle contact forces and force chains for the various particle shapes were investigated.

4.2 CALIBRATION OF PARTICLE-PARTICLE FRICTION COEFFICIENT

As stated by Coetzee (2017), the input parameters used in DEM simulations play a key role in the accuracy of the results obtained. Nakashima *et al.* (2011) and Coetzee (2016) reported that the angle of repose of a granular material is directly related to its particle-particle friction coefficient (coefficient of sliding friction). Drop tests were therefore performed in STAR-CCM+ to calibrate the DEM particles to a desired angle of repose.

A further six drop tests were performed in Blaze-DEM with the six particle shapes used for the numerical sensitivity analysis. This was performed to obtain an estimation of the angles of repose for the six particle shapes (spheres, dodecahedrons, cubes, truncated tetrahedrons, triangular prisms and tetrahedrons).

4.2.1 STAR-CCM+ drop tests

A total of six drop tests were performed in STAR-CCM+, with different combinations of the number of clumps used and the particle-particle friction coefficient. The particle-particle friction coefficient ranged from 0.3 to 0.6 and two-sphere as well as three-sphere clumped models were used.

It was found that a particle-particle friction coefficient of 0.45 should be used to obtain an angle of repose of 33° to 34°. These results were similar to those obtained by Coetzee (2016). Figure 4.1 illustrates the angle of repose of 33° obtained from the two-sphere clumps with a coefficient of 0.45. The coefficient of 0.45 was used for the remainder of the verification simulations as well as in the sensitivity analysis.

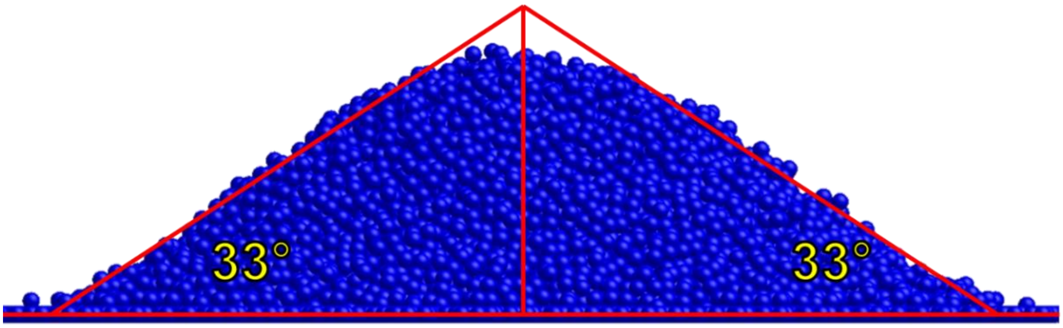

Figure 4.1: Angle of repose of two-sphere clumps from STAR-CCM+

Table 4.1 presents the results of the angles of repose for the six drop tests executed in STAR-CCM+. The table shows that using higher particle-particle friction coefficients resulted in higher angles of repose. The table also shows that the two-sphere clump models yielded slightly lower angles of repose than the three-sphere clump models.

Table 4.1: Results of angles of repose from drop tests in STAR-CCM+

Test number	Number of clumps	Particle-particle friction coefficient	Angle of repose
1	two-spheres	0.30	28°
2	three-spheres	0.30	29°
3	two-spheres	0.45	33°
4	three-spheres	0.45	34°
5	two-spheres	0.60	37°
6	three-spheres	0.60	38°

4.2.2 Blaze-DEM drop tests

The six drop tests carried out in Blaze-DEM were performed using only single particles. Single particles were utilised since Blaze-DEM did not allow for clumped particles to be modelled. The six shapes considered were spheres, dodecahedrons, cubes, truncated tetrahedrons, triangular prisms and tetrahedrons. A particle-particle friction coefficient of 0.45 obtained from the STAR-CCM+ drop tests was used for these simulations.

Constant angle of repose values were obtained for the spheres and dodecahedrons. However, for the cubes, truncated tetrahedrons, triangular prisms and tetrahedrons, two sets of angles of repose were obtained for each shape. This was suggested to be a result of too few particles used for the drop tests, resulting in inconsistent heap sizes. Upper and lower bound angles of repose were therefore measured for these shapes. A summary of the angles of repose obtained from the six drop tests performed in Blaze-DEM is presented in Table 4.2. The table also displays the sphericities of the six particle shapes investigated.

Table 4.2: Results of angles of repose from drop tests in Blaze-DEM

Particle shape	**Sphericity**	**Angle of repose**		
		Lower Bound	**Upper Bound**	**Average**
Spheres	1.00	13.0°	13.0°	13.0°
Dodecahedrons	0.911	16.0°	16.0°	16.0°
Cubes	0.806	42.0°	48.0°	45.0°
Truncated tetrahedrons	0.775	19.0°	22.0°	20.5°
Triangular prisms	0.716	24.0°	31.0°	27.5°
Tetrahedrons	0.671	27.0°	42.0°	34.5°

Blaze-DEM only offered a perspective view of the particles during simulations. Therefore, the images obtained from Blaze-DEM were not used to measure the angles of repose from the drop tests, since the dimensions were distorted. Instead, the particles' coordinates were used to plot circular points in 2D for the particles' positions. The angles of repose for the six particles were measured from the circular points.

Figures 4.2 to 4.5 depict the angles of repose obtained from the spheres, dodecahedrons, tetrahedrons and cubes respectively. The figures display the constant angles of repose for the spheres and dodecahedrons. The upper and lower bound angles of repose obtained from the different heaps for the tetrahedrons and cubes are also illustrated.

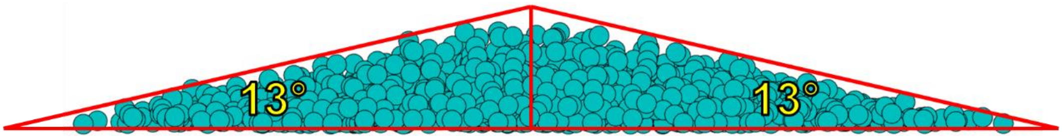

Figure 4.2: Angle of repose of spheres from Blaze-DEM

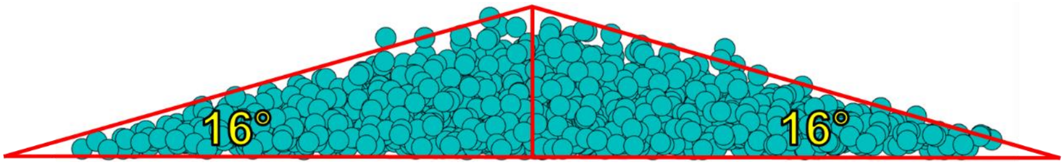

Figure 4.3: Angle of repose of dodecahedrons from Blaze-DEM

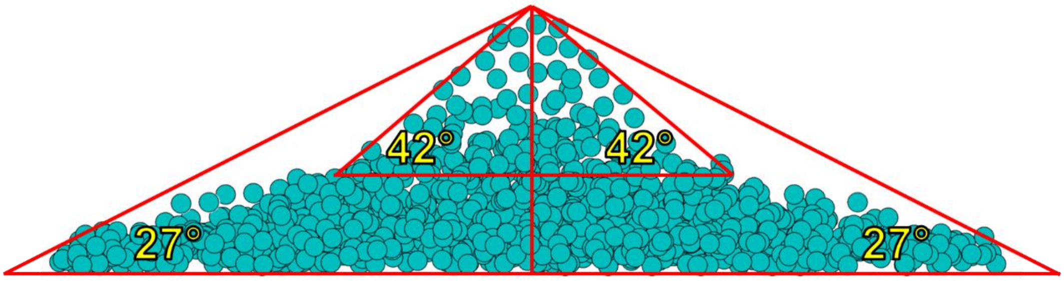

Figure 4.4: Angle of repose of tetrahedrons from Blaze-DEM

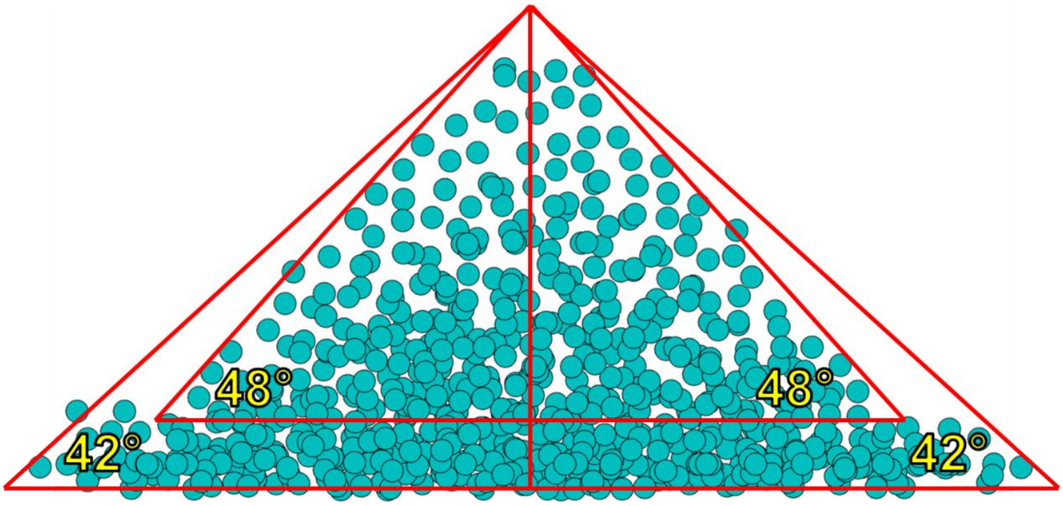

Figure 4.5: Angle of repose of cubes from Blaze-DEM

The effect of sphericity of a particle on the average angle of repose obtained from the drop tests is depicted in Figure 4.6. The figure shows that for all shapes, except the cubes, the sphericities decreased as the angle of repose increased. The cubes, with the third highest sphericity, did not follow this trend as it had the largest angle of repose (48°).

Two exponential trendlines were fitted to the data, one with all the shapes considered and one with the cubes excluded. The trendline with all the shapes resulted in a coefficient of determination (R^2) of 0.56, whereas a coefficient of determination of 0.95 was obtained when the cubes were excluded. The results therefore indicate that, apart from the cubes, the angle of repose of a particle increases exponentially as its sphericity decreases.

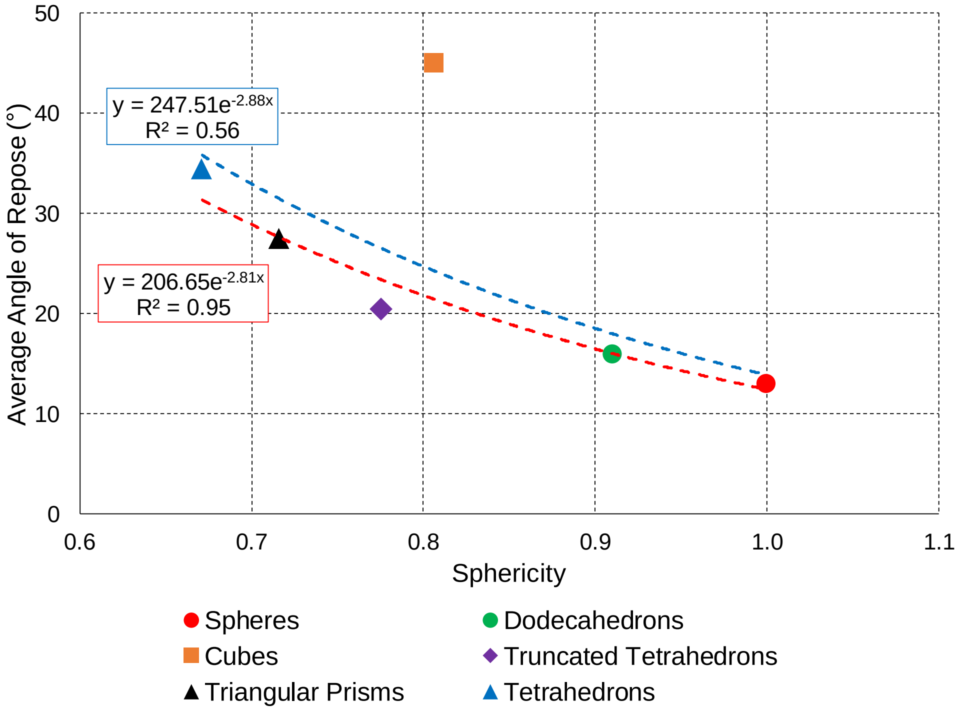

Figure 4.6: Effect of sphericity on average angle of repose

The angles of repose obtained from the drop tests in Blaze-DEM were not suggested to be an accurate representation of the true value of the particles' angles of repose. It has, however, been suggested that these drop tests may give an indication of the variation of the angles of repose between the various particle shapes modelled. For these reasons, the angles of repose were not used when calculating the lateral earth pressure coefficients. It is suggested that the true angles of repose of the convex polyhedra shapes lie within the ranges obtained from the lower and upper bounds for that particle.

4.3 REDUCTION OF YOUNG'S MODULUS VALUE

As proposed by Coetzee (2016), the theoretical Young's Modulus value for silica quartz was reduced to speed up the computational times in STAR-CCM+. Reduction factors of 10 000, 1 000 and 100 were applied to the theoretical value of 70 GPa to obtain 7 MPa, 70 MPa and 700 MPa respectively. The small abutment model was used to assess the effects of using various reduced values of Young's Modulus. A total of 60 000 spherical particles with diameters of

5 mm were filled into the model space. A single, full rotational cycle of the model abutment was applied to the particles for the different Young’s Modulus values.

4.3.1 Computational times of reduced Young’s Modulus values

A small fraction of the single rotational cycle (0.01 cycles) was simulated for the 70 GPa particles and the expected time to simulate the entire cycle was calculated. This was performed to compare how much faster the reduced Young’s Modulus values simulated.

Figure 4.7 illustrates the computational times of the different Young’s Modulus values. A summary of the computational times obtained for the single, full rotational cycle of the abutment for each of the Young’s Modulus values is presented in Table 4.3. The table shows that using the 70 GPa particles for the simulation would have resulted in excessively long simulations times.

The simulation with the 700 MPa particles completed a full cycle almost eight times faster than the expected computational times of the 70 GPa particles. The computational times obtained from the 70 MPa and 7 MPa particles provided much faster times than the 70 GPa particles, with the 70 MPa particles running 32.9 times faster and the 7 MPa particles over 100 times faster. The time factor of 32.9 obtained from the 70 MPa particles was almost identical to the time factor of 31.6 obtained by Xu *et al.* (2002), when applying the same reduction factor to 70 GPa particles.

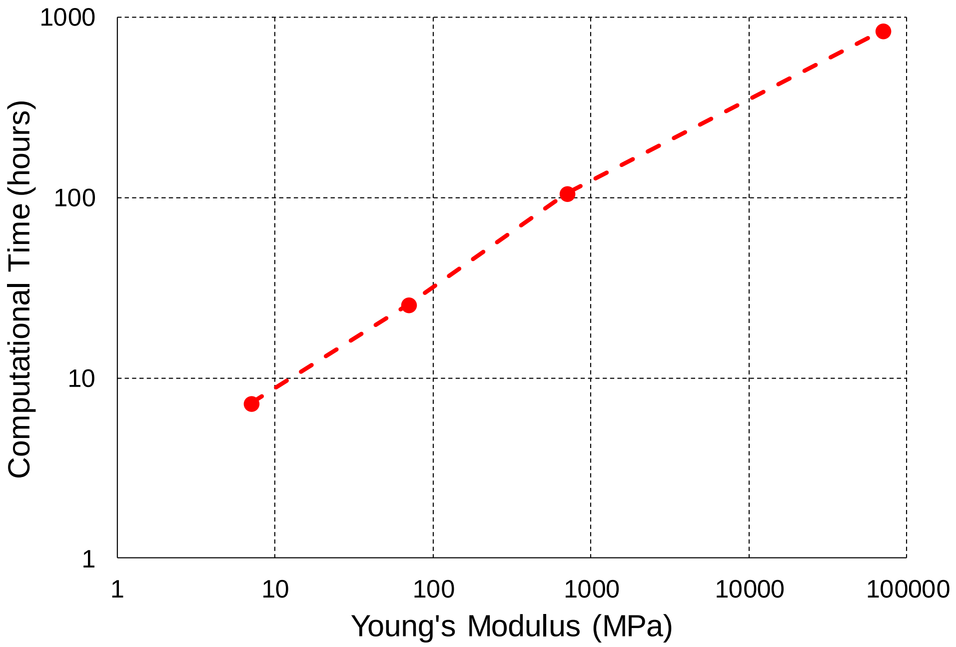

Figure 4.7: Computational time versus Young’s Modulus

Table 4.3: Summary of computational times for different Young's Modulus values

Young's Modulus	Reduction factor	Time taken for a single, full rotational cycle	Times faster than 70 GPa particles
7 MPa	10 000	7.31 hours (0.30 days)	115.10 ×
70 MPa	1 000	25.56 hours (1.07 days)	32.92 ×
700 MPa	100	106.10 hours (4.42 days)	7.93 ×
70 GPa	1	841.75 hours (35.08 days)	-

4.3.2 Density and average normal particle overlap with depth

The density and average normal overlap between the particles with depth in the model were studied for the different Young's Modulus values. Figure 4.8 illustrates the comparison of the densities for the 7, 70 and 700 MPa particles. The figure shows that the results from the 70 MPa and 700 MPa particles yielded densities which increased uniformly as the depth increased. Figure 4.9 presents the average normal particle overlap for the different Young's Modulus values. A similar behaviour was observed for the particle overlaps as with the densities for the 70 MPa and 700 MPa particles.

The increase in densities with depth was not uniform near the bottom of the model for the 7 MPa particles. This non-uniform increase in density signified that the 7 MPa particles resulted in unrealistic deformations of the particles, since the load due to self-weight was the largest near the bottom of the model. This non-uniform behaviour was also observed with the average overlap between the 7 MPa particles near the bottom of the model. For these reasons, it is therefore suggested that a Young's Modulus of 7 MPa is too soft to model granular backfill behaviour realistically.

Since the 70 MPa and 700 MPa particles produced comparable results, it was determined that a Young's Modulus of 70 MPa would be the most practical for the verification test for density and particle overlap with depth. This value would be expected to offer the lowest computational times without significantly compromising the accuracy of the results.

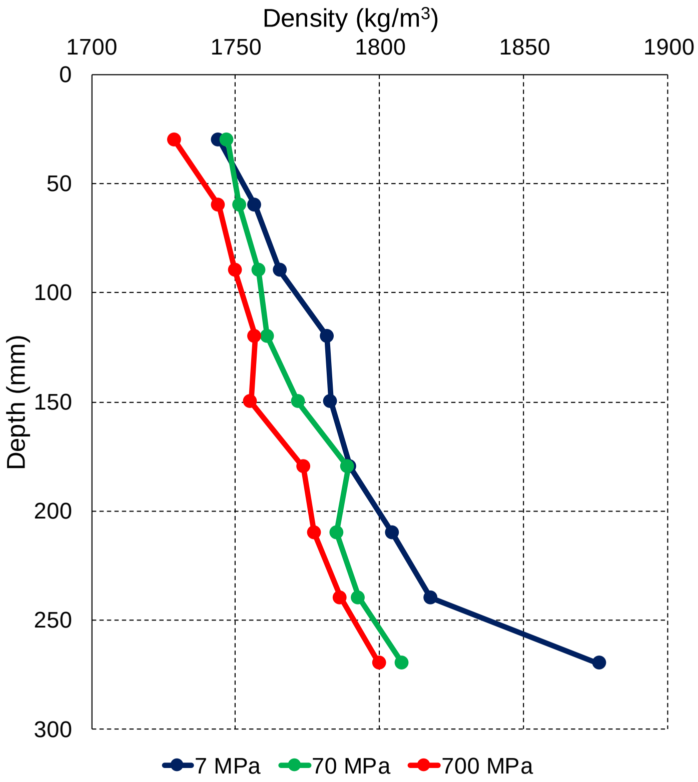

Figure 4.8: Densities with depth comparison for various Young’s Modulus values

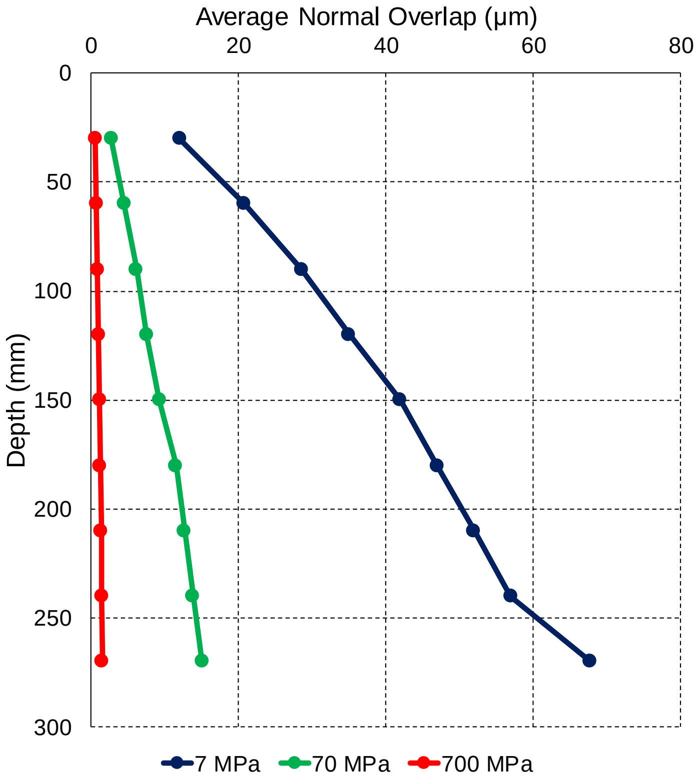

Figure 4.9: Particle overlap with depth comparison for various Young’s Modulus values

4.3.3 Coefficient of active state lateral earth pressure

The next verification test investigated the lateral earth pressure coefficients for the reduced Young's Modulus values. Since only one load cycle was imposed on the granular backfill, and because the imposed movement of the rotating wall was small, the passive state was not reached. It was also expected that passive state would not be reached even with a large number of cycles, since only spherical particles were used and no interlocking between the particles was possible. Therefore, only the active state earth pressure coefficients were compared.

Two theoretical active lateral earth pressure coefficient values were calculated since two angles of repose were obtained for the spheres. An angle of repose of 33° was obtained from the two-sphere clumped models used in STAR-CCM+, while an angle of repose of 13° was obtained from the single spheres used in Blaze-DEM. A theoretical value of 0.295 was calculated for the angle of repose of 33° and a value of 0.633 was calculated for the 13° angle of repose. The coefficients obtained from the DEM simulations for the reduced Young's Modulus values were compared to both theoretical values.

The comparison of the lateral earth pressure coefficients for the active state is shown in Figure 4.10. The figure presents the earth pressure coefficients obtained for the three reduced Young's Modulus values as well as the theoretical values calculated. The figure shows that the earth pressure coefficients were approaching the value of 0.295 obtained from the multi-sphere drop tests as the Young's Modulus approached the theoretical value of 70 GPa. However, the values were relatively far from the value calculated from the single sphere drop test.

The results of the active earth pressure coefficient comparison were in line with the suggestion made by Coetzee (2017). When using drop tests, Coetzee (2017) proposed that clumped models should be used to estimate the angle of repose of spherical particles. It was therefore assumed that for the spherical particles, the angle of repose of 33° was a better representation of its internal friction angle, than the angle of repose of 13° obtained from the single sphere drop tests. This implied that the theoretical value of 0.295 for the active earth pressure coefficient should be used for the reduction in Young's Modulus verification.

The lateral earth pressure coefficients obtained from the 70 MPa and 700 MPa particles returned values relatively close to the theoretical value. The Young's Modulus of 7 MPa, which was deemed too soft for the density with depth verification test, resulted in a coefficient significantly higher than the theoretical value of 0.295. This was suggested to be due to larger deformations occurring in these particles when the wall moved to the active side and therefore unrealistically high forces were present on the abutment.

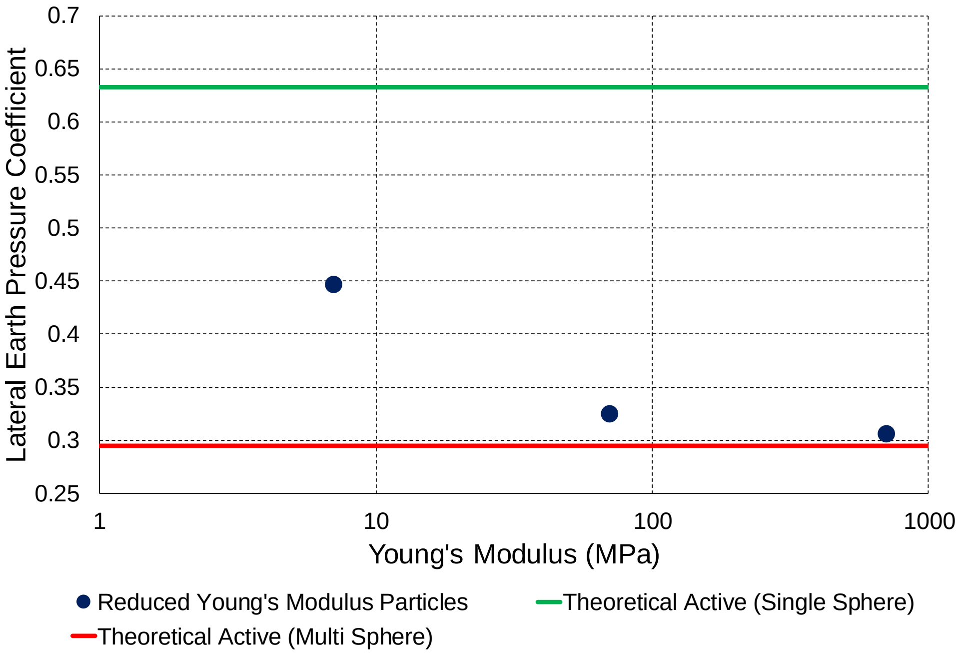

Figure 4.10: Active earth pressure coefficient comparison for various Young's Modulus values

As seen the density with depth verification test, the 70 MPa and 700 MPa particles resulted in similar behaviours to what was expected from the 70 GPa particles. This indicated that a Young's Modulus of 70 MPa would suitably represent the verification test for the lateral earth pressure coefficients, as it would result in the lowest computational times without a loss of significant accuracy.

4.3.4 Average normal overlap between the particles

The final verification test performed on the reduced Young's Modulus values aimed to evaluate the average normal overlap between the particles. Limits for the overlap between the particles were obtained from literature. These limits suggested that the overlap should not exceed a certain percentage of the radius of the particle. Limits of 1% (Coetzee, 2017), 0.5% (Cleary, 2010) and 0.3% (Lommen, 2014) of the particle radius were used for this assessment.

The average normal particle overlaps for the reduced Young's Modulus values are shown in Figure 4.11. The figure also presents the limits obtained from literature as dashed lines. The results show that the average overlap from the 700 MPa particles was well below all the limits obtained from literature. The particles with a Young's Modulus of 7 MPa exceeded each of these limits. The average normal overlap resulting from the 70 MPa particles adhered to the 1% and 0.5% limits, however, was relatively close to the 0.3% limit.

The results from the overlap verification test show that a reduction factor of 100 (700 MPa) to the Young's Modulus would be expected to produce accurate results, while a reduction factor of 10 000 (7 MPa) would compromise the accuracy. The 70 MPa particles (reduction of 1 000) would also be expected to yield relatively accurate results. However, this would not be the most conservative approach, since the overlap for these particles were close to the lowest limit.

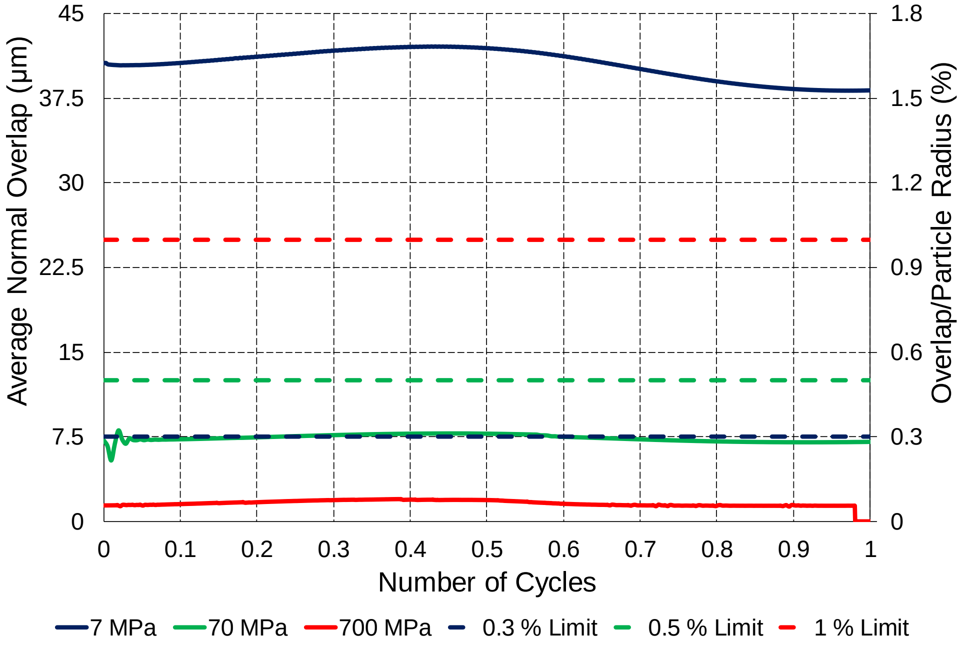

Figure 4.11: Average normal overlap comparison for various Young's Modulus values

Based on the three verification tests performed, it was decided that a Young's Modulus of 70 MPa would be used for the particles, i.e. a reduction factor of 1 000 applied to the theoretical Young's Modulus value of 70 GPa for silica quartz. An identical reduction factor was successfully used by Härtl and Ooi (2008). The work done by Xu *et al.* (2002) also involved reducing a Young's Modulus from 70 GPa to 70 MPa with comparable results. This value was expected to yield the quickest simulation times, without significantly compromising the accuracy of the results.

4.4 SOFTWARE COMPARISON

The next step used to reduce the computational times was to use Blaze-DEM to perform the simulations, rather than STAR-CCM+. Blaze-DEM offers an elevated level of performance as opposed to STAR-CCM+ since it makes use of the processing capabilities of the Graphics Processing Unit rather than the Central Processing Unit as done by STAR-CCM+ (Govender, 2015).

A concern with Blaze-DEM, is that it is a research code under development and not commercial software such as STAR-CCM+. This meant that the results for the specific application simulated needed to be verified. Two sets of simulations were performed in each of the software packages. The first set of simulations was performed with the small abutment model and 60 000 spheres. The second set involved 90 000 cubes with the medium abutment model.

The lateral earth pressure coefficients and densities were analysed for the two sets of simulations in STAR-CCM+ and Blaze-DEM. In both software packages, the model abutment was rotated 25 times in the active and passive directions. The size of the model, the rotation rate and magnitude, as well as the parameters used for the particles, were identical in each software package for the relevant comparison simulations.

The only difference between the simulations in the two software packages was the method with which the particles were placed in the relevant models. In STAR-CCM+, the particles were placed in a grid (with random orientations for the cubes) and allowed to settle under gravitational loads until a state of zero velocity was reached. This procedure was followed since it greatly reduced the computational costs, as all the particles could be generated in the first iteration. However, the computational times were not a drawback in Blaze-DEM and the particles were therefore dropped into the respective models from a height of 350 mm.

A minor variation of the initial bulk densities was present for the different injection methods in the two software packages. The initial bulk densities were slightly lower in STAR-CCM+ as opposed to Blaze-DEM. However, after the 25 cycles in each test, the differences between the densities were negligible i.e. less than 1% difference. It was therefore suggested that the different injection methods would not greatly affect the results from the software verification. The DEM models used in STAR-CCM+ and Blaze-DEM are shown in Figures 4.12 and 4.13 respectively. The figures show the models with spheres after 25 cycles of the abutment.

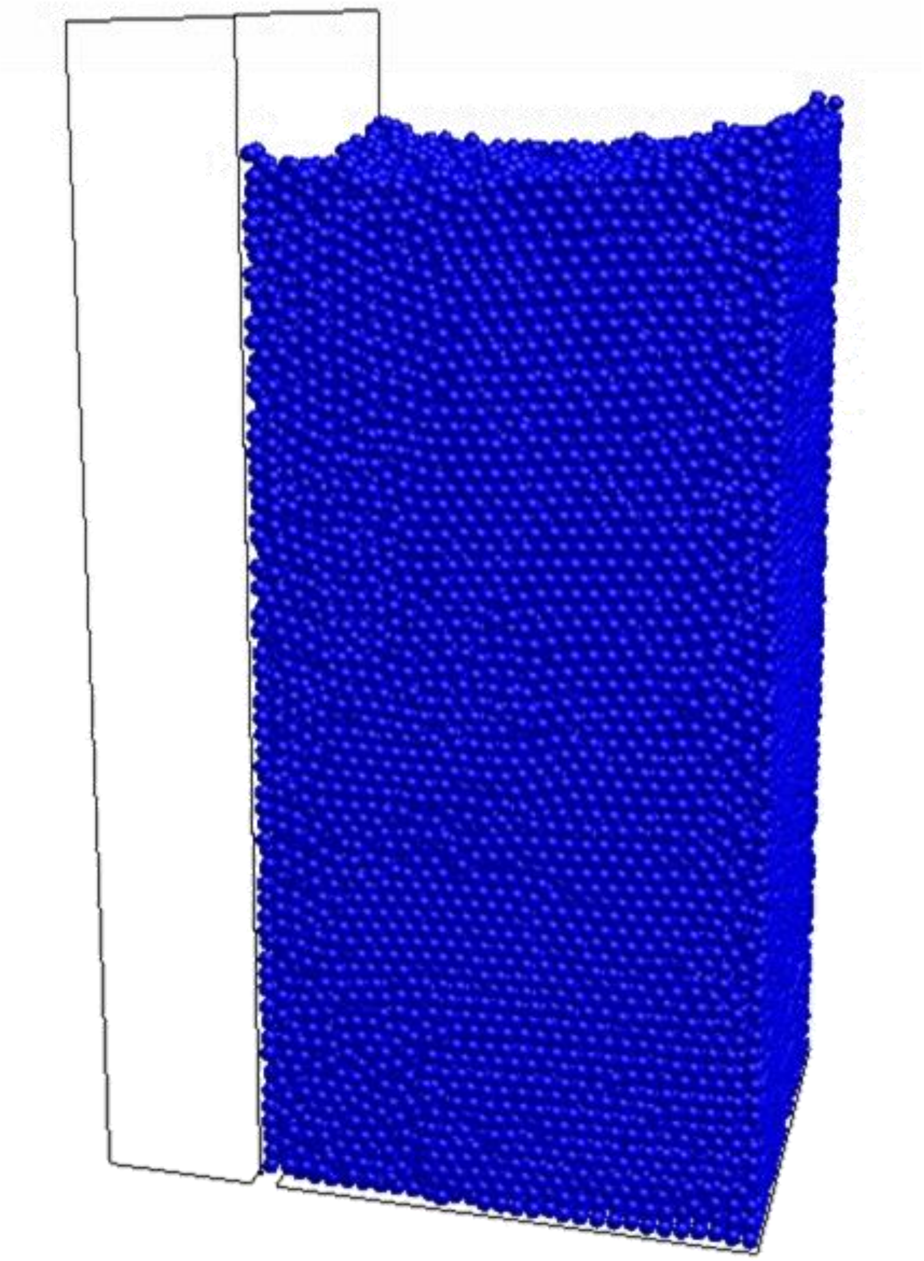

Figure 4.12: DEM model with spheres after 25 cycles in STAR-CCM+

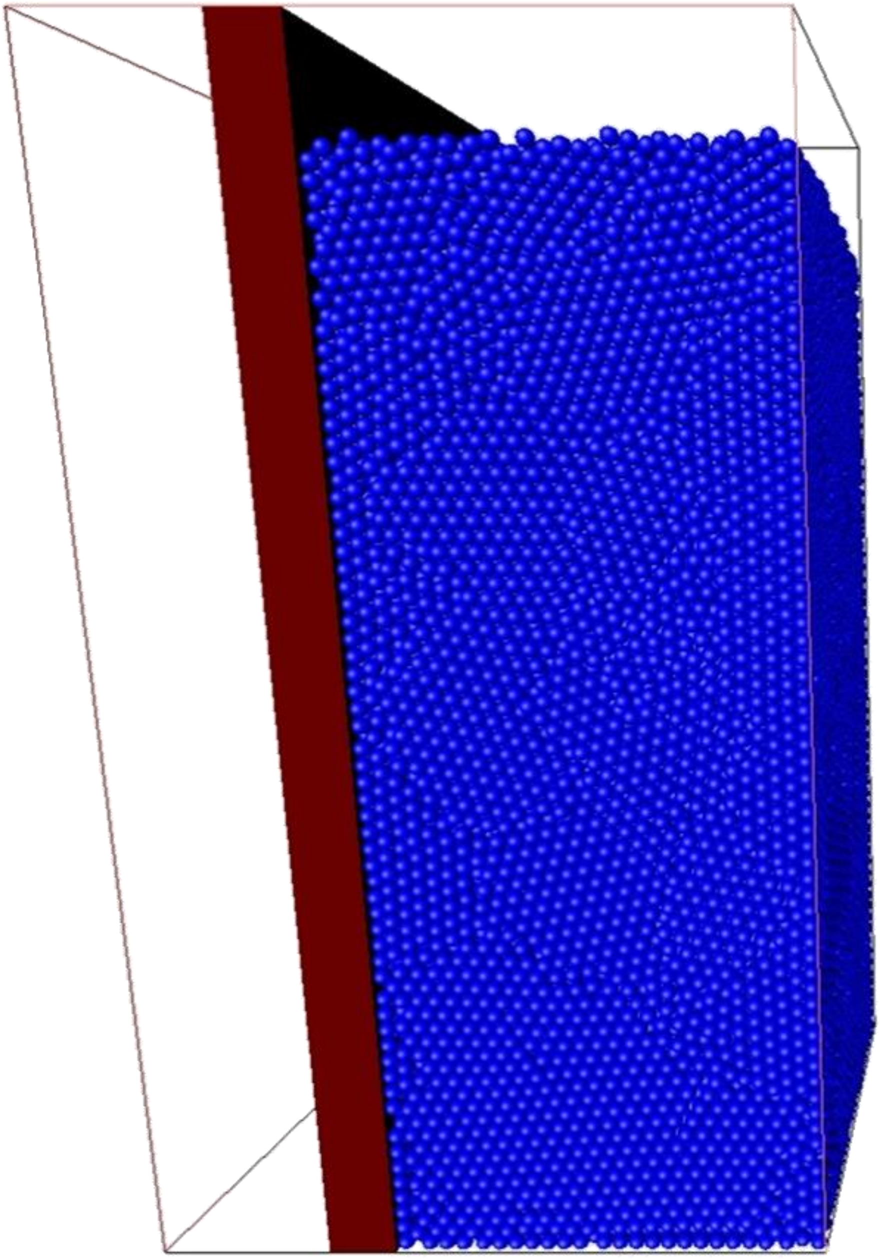

Figure 4.13: DEM model with spheres after 25 cycles in Blaze-DEM

4.4.1 Computational times of software packages

A total of 639 hours (26.63 days) were required to complete the 25 cycles with the small abutment model and spheres in STAR-CCM+. Blaze-DEM allows the option of performing simulations without a live graphics output, i.e. without displaying the DEM particles while the simulation was performed. Blaze-DEM required 23.58 hours for the same simulation with a live output and only 3.94 hours were required when performing the simulation without a live output.

The comparison using the 90 000 cubes required 1 004 hours (41.82 days) of computational time in STAR-CCM+. The Blaze-DEM simulation performed without a live graphics output required only 6.48 hours of computational time. This meant that when modelling spheres or cubes, Blaze-DEM could yield results over 150 times faster than STAR-CCM+ and almost 30 times faster when using a live graphics output. A summary of the computational times from the software verification tests is presented in Table 4.6, while Figure 4.14 presents a graph of these computational times.

Table 4.4: Summary of computational times from software verification tests

Software Package	**Spheres**	**Cubes**
STAR-CCM+	639 hours	1004 hours
Blaze-DEM Live Graphics	23.58 hours	34.62 hours
Times faster than STAR-CCM+	27 ×	29 ×
Blaze-DEM No Graphics	3.94 hours	6.48 hours
Times faster than STAR-CCM+	162 ×	155 ×

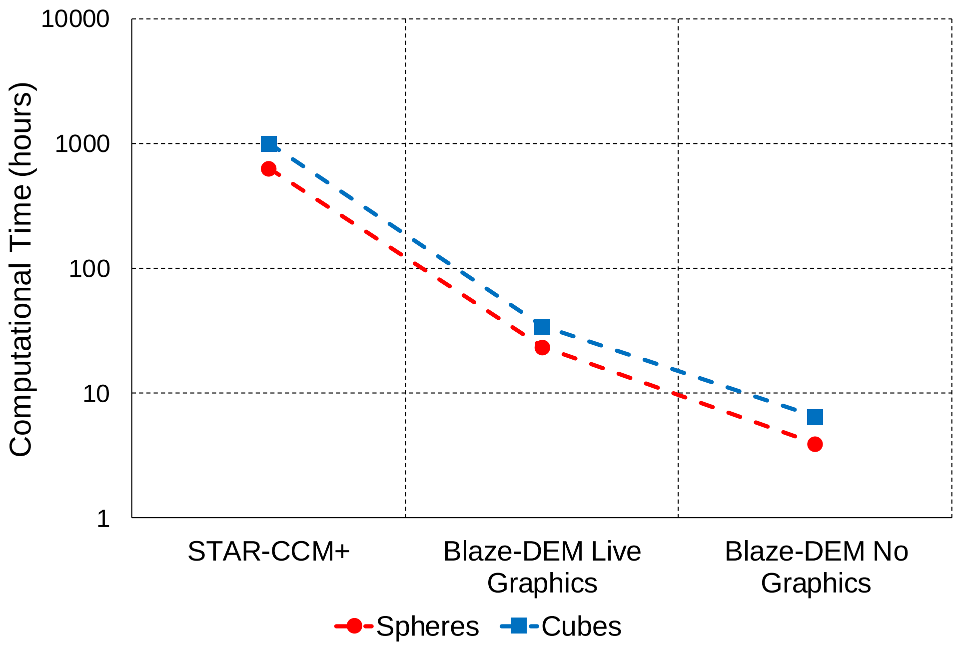

Figure 4.14: Graph of computational times from software verification tests

4.4.2 Software comparison – Spheres

The coefficient of earth pressure results from the two simulations using spheres are illustrated in Figure 4.15. The coefficients were plotted when the model abutment was at the fully loaded position in the passive direction. The figure shows that the coefficient started low in STAR-CCM+ and increased each cycle until it reached a value of approximately 0.673 and began to plateau. In Blaze-DEM however, the coefficient of earth pressure started higher and fluctuated around a value of 0.68.

The reason the coefficient of earth pressure value started lower in STAR-CCM+ was due to the different methods in which the particles were injected in each of the software packages. The movement of the abutment wall in STAR-CCM+ densified the particles with each cycle, until the coefficient of lateral earth pressure stabilised considerably close to that of the Blaze-DEM analysis.

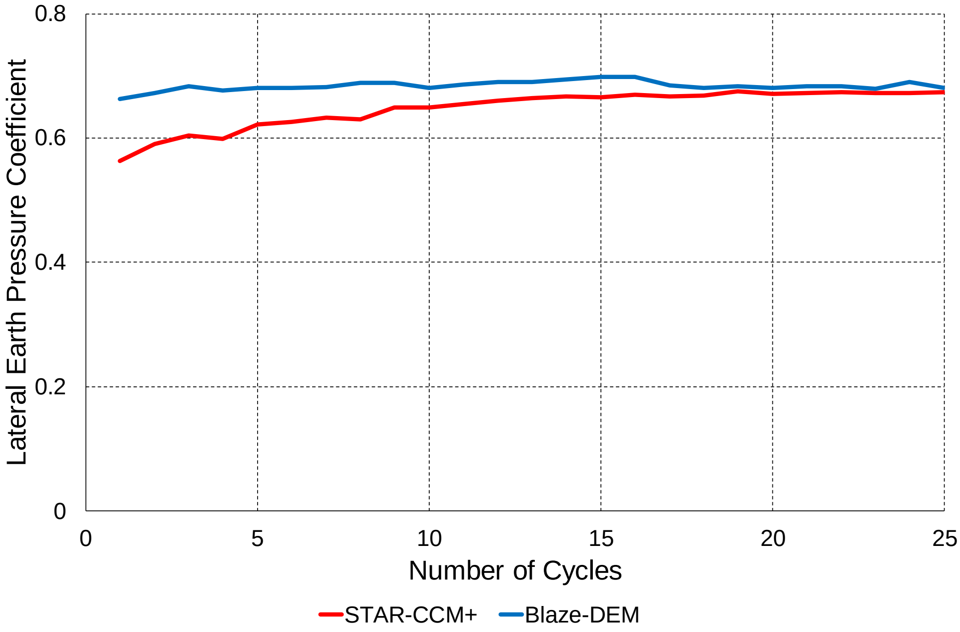

Figure 4.15: Spheres' earth pressure comparison between STAR-CCM+ and Blaze-DEM

A behaviour similar to the lateral earth pressure coefficients was observed for the bulk densities of the particles, as illustrated in Figure 4.16. The figure shows that the bulk densities obtained from the two software packages were considerably far from the maximum possible packing which could be attained with spherical particles of 1962 kg/m^3 (25.95% porosity).

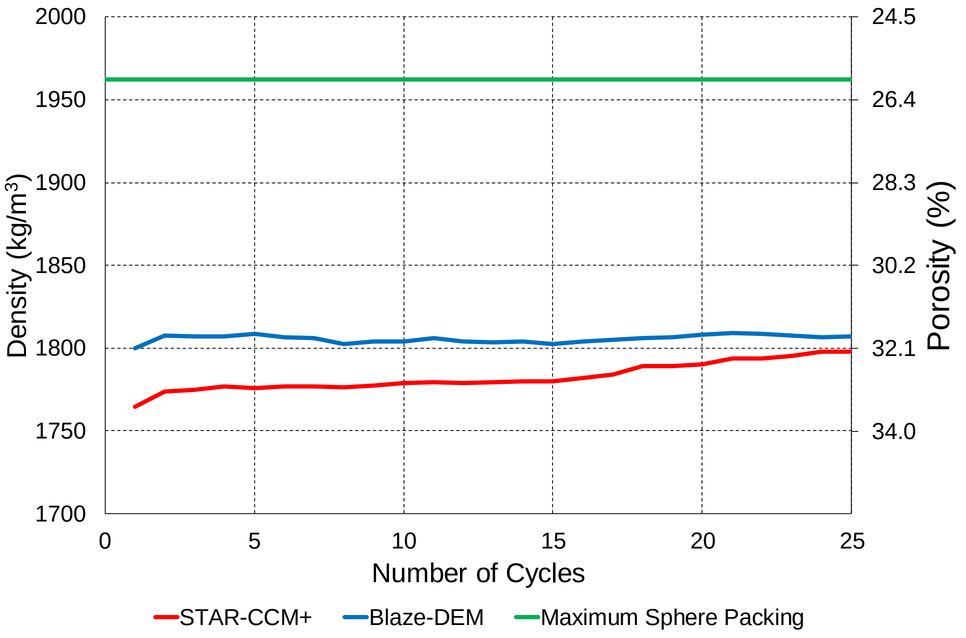

Figure 4.16: Spheres' bulk density comparison between STAR-CCM+ and Blaze-DEM

A summary of the parameters after the first and last cycles is presented in Table 4.4. The table highlights that the differences between the earth pressure coefficients and bulk densities after 25 cycles were similar for each of the software packages. A difference of 0.008 (1.17%) was obtained for the earth pressure coefficients, while the densities differed by 9 kg/m^3 (0.50%) between Blaze-DEM and STAR-CCM+. This difference was considered negligible for the software verification between Blaze-DEM and STAR-CCM+.

Table 4.5: Summary of parameters for sphere comparison test

Parameter	STAR-CCM+	Blaze-DEM	Difference
K after 1 cycle	0.564	0.663	0.099 (14.9%)
K after 25 cycles	0.673	0.681	0.008 (1.17%)
Increase in K	0.109 (19.3%)	0.018 (2.64%)	
Density after 1 cycle	1765 kg/m^3	1800 kg/m^3	35 kg/m^3 (1.94%)
Density after 25 cycles	1798 kg/m^3	1807 kg/m^3	9 kg/m^3 (0.50%)
Increase in density	33 kg/m^3 (1.87%)	7 kg/m^3 (0.39%)	

4.4.3 Software comparison – Cubes

The second comparison between Blaze-DEM and STAR-CCM+ was performed using cubes and the medium abutment model. As with the comparison using the spheres, the cubic particles were injected in Blaze-DEM. However, the particles were placed in a grid with random orientations in STAR-CCM+. The lateral earth pressure coefficients and bulk densities obtained from the two software packages were analysed.

The lateral earth pressure coefficient values and bulk densities for the 25 cycles, when the model abutment was at the fully loaded position in the passive direction, are shown in Figures 4.17 and 4.18 respectively. Figure 4.17 illustrates that the coefficient started lower and increased rapidly as the number of cycles increased in STAR-CCM+. The coefficient started at a value of 1.13 after one cycle and finished at a value of 1.81 after 25 cycles. In Blaze-DEM however, the coefficient started at 1.70 and reached a value of 1.92 after 25 cycles. The difference is again suggested to be a result of the different methods as to which the particles were injected in the two software packages.

The bulk densities, presented in Figure 4.18, were slightly higher for each cycle in Blaze-DEM as opposed to STAR-CCM+. However, both sets of densities were considerably far from the maximum possible packing of cubes (0% porosity). In both software packages, the densities increased relatively linearly as the number of cycles increased. The parameters are summarised in Table 4.5. The table shows that the earth pressure coefficients differed by a value of 0.11 (5.73%) between the two software suites, while the bulk densities differed by a value of 13 kg/m^3 (0.65%). These differences were considered to be negligible for the comparison test between Blaze-DEM and STAR-CCM+ when using cubes.

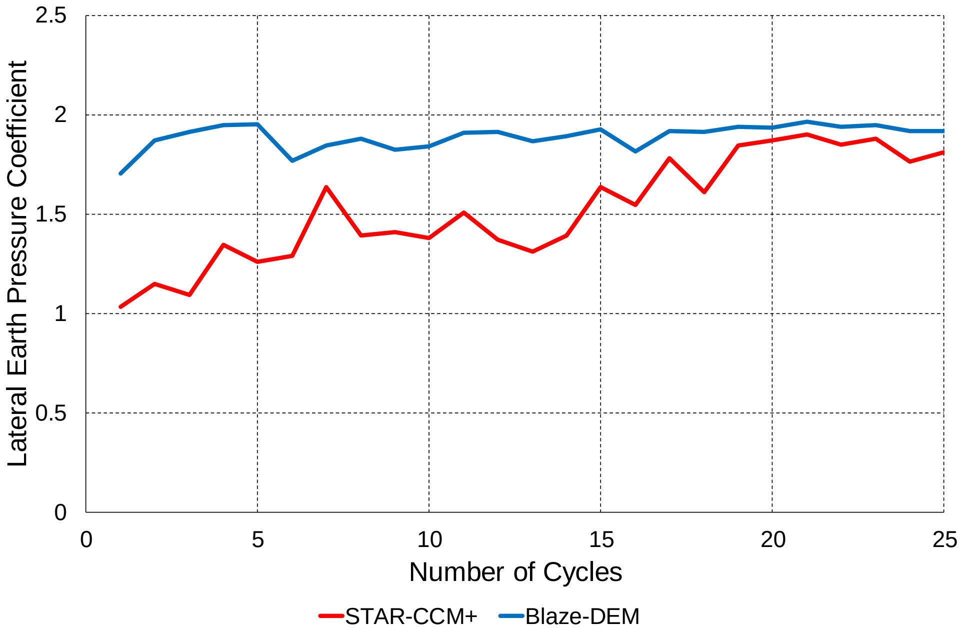

Figure 4.17: Cubes' earth pressure comparison between STAR-CCM+ and Blaze-DEM

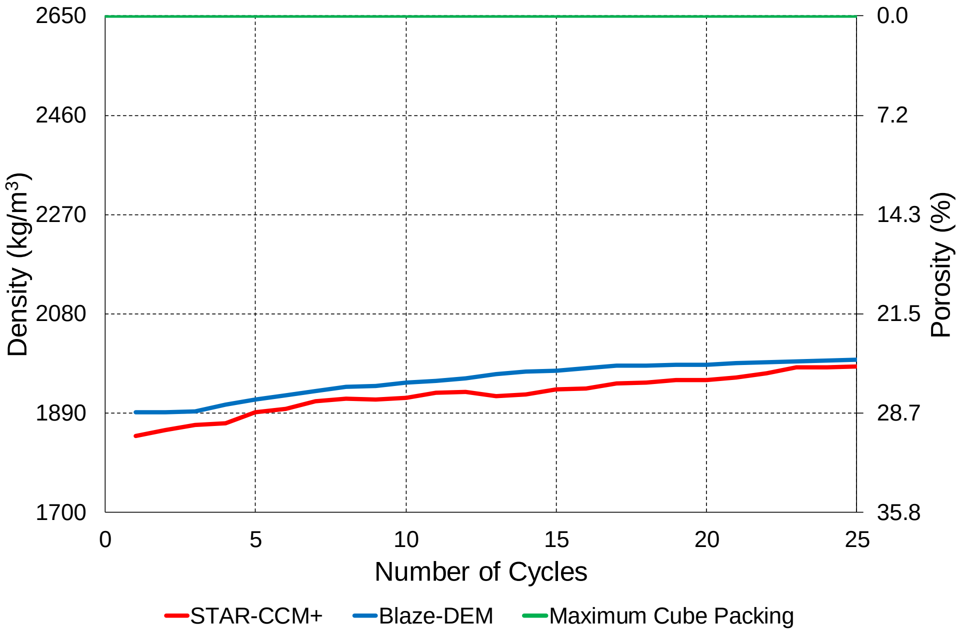

Figure 4.18: Cubes' bulk density comparison between STAR-CCM+ and Blaze-DEM

Table 4.6: Summary of parameters for cube comparison test

Parameter	STAR-CCM+	Blaze-DEM	Difference
K after 1 cycle	1.03	1.70	0.67 (39.4%)
K after 25 cycles	1.81	1.92	0.11 (5.73%)
Increase in K	0.78 (75.7%)	0.22 (12.9%)	
Density after 1 cycle	1845 kg/m^3	1891 kg/m^3	46 kg/m^3 (2.43%)
Density after 25 cycles	1979 kg/m^3	1992 kg/m^3	13 kg/m^3 (0.65%)
Increase in density	134 kg/m^3 (7.26%)	101 kg/m^3 (5.34%)	

Since the results from the small and medium abutment models were similar in STAR-CCM+ and Blaze-DEM after 25 cycles of the model abutments, it was decided that the remaining simulations would be performed in Blaze-DEM. Performing the simulations in Blaze-DEM was expected to give results which were accurate as well as offer much faster computations times than STAR-CCM+.

The results from the software comparisons indicated that the spheres (higher sphericity) experienced small accumulations of pressures and densities, whereas the cubes (higher angularity) underwent much larger accumulations as the number of cycles increased. These results emphasise the need for investigating the effect of granular particle shape on the response of backfill retained by integral bridge abutments. However, before the sensitivity analysis could be performed, the numerical model required verification.

4.5 NUMERICAL MODEL VERIFICATION TESTS

The following section contains the results from simulations performed to investigate the choice of the particle sizes, the rotation rate and the number of particles to be used in the numerical sensitivity analysis. The simulations were performed in Blaze-DEM using the small abutment model for the particle size and rotation rate verifications. The medium and large abutment models were used to verify the number of particles to be utilised for the sensitivity analysis.

4.5.1 Particle size independence study

Verification tests were performed to ensure that the results from the numerical sensitivity analysis would be independent of the particle size chosen. This procedure was followed since it is known that the computational costs of DEM simulations are directly proportional to the particle size. The particle sizes of the granular backfill had to be significantly increased to obtain practical computational times.

Spheres with diameters of 2.5, 4, 5 and 10 mm were simulated using the small abutment model. The lateral earth pressure coefficients (Figure 4.19) and bulk densities (Figure 4.20) for the various spherical particle sizes were investigated for the verification tests.

The coefficients of earth pressure showed that the 2.5, 4 and 5 mm diameter particles produced relatively constant results, while the 10 mm particles yielded slightly unstable results. This was suggested to be due to the number of 10 mm particles being used in the DEM model (8 000 particles) and therefore too few particles being in contact with the abutment (approximately 150 particles). This resulted in unstable behaviour of the particles due to larger variances of forces acting on the abutment. Using smaller particles resulted in more points being in consistent contact with the abutment. Table 4.7 presents the number of particles in contact with the abutment for the various sphere sizes.

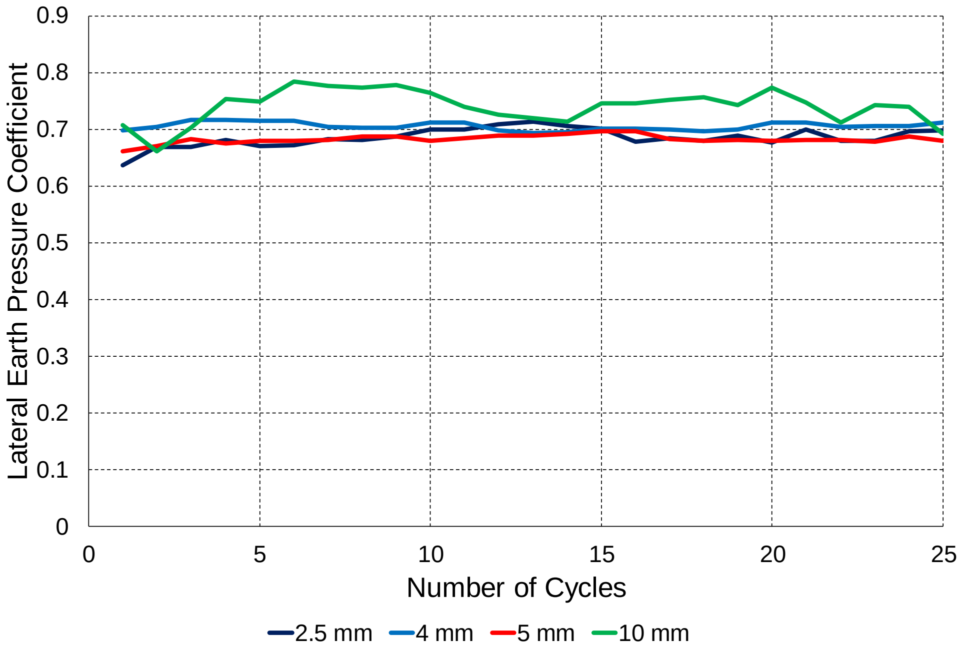

Figure 4.19: Lateral earth pressure coefficient comparison for various particle sizes

Table 4.7: Summary of particle size verification test

Test number	Particle diameter	Number of particles	Average number of particles in contact with the abutment
1	2.5 mm	500 000	10 000
2	4 mm	150 000	3 000
3	5 mm	60 000	1 200
4	10 mm	8 000	150

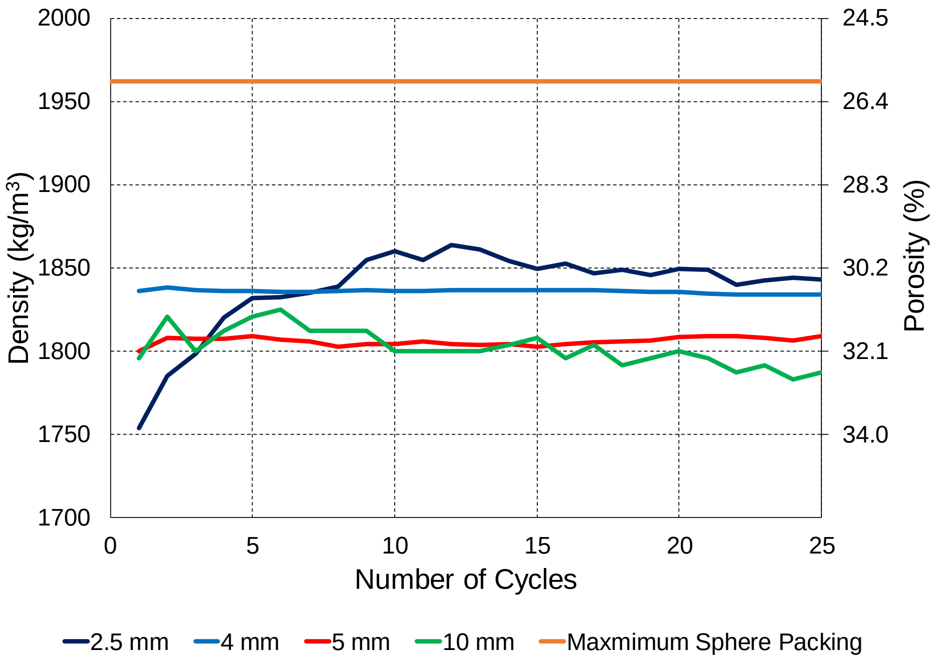

Figure 4.20: Bulk density comparison of various particle sizes

The bulk backfill densities for the different particle sizes are presented in Figure 4.20. The figure shows that the 4 mm and 5 mm particles produced constant densities with an increase in cycles. As expected, the 4 mm particles resulted in slightly higher densities compared to the 5 mm particles, since a higher packing could be obtained due to the movements of the abutment being large relative to the size of the particles. The 2.5 mm particles started with a lower density and compacted quite significantly with an increase in cycles.

The 10 mm particle delivered erratic results again, where the density began to decrease as the number of cycles increased. This is suggested to be attributed to too few particles being utilised in the model. The bulk densities obtained from the various particle sizes were considerably far from the maximum possible packing for spherical particles of 1962 kg/m^3 (25.95% porosity).

It was decided that a particle size of 5 mm would be used for the remaining simulations based on the above analysis. This particle size was expected to yield stable results while providing the quickest simulation times.

4.5.2 Rotation rate independence study

The next verification test performed investigated the effect of the rotation rate of the model abutment. Since the rotation rate experienced by full-scale integral bridges is extremely slow, the rate had to be increased significantly. The original rate used was at 0.0027 rad/s (0.5 Hz). Rotation rates three times faster (0.0081 rad/s) and three times slower (0.0009 rad/s) were also tested.

The results of the coefficients of earth pressure when the model abutment was at the fully loaded position in the passive direction from the three rotation rates are shown in Figure 4.21. The figure shows that the three rotation rates yielded similar coefficients of earth pressure of around 0.68. The fastest rate produced slightly unstable lateral earth pressure coefficient values while the slowest rate yielded the most stable values. The results indicate that the original rate of rotation of 0.0027 rad/s would be slow enough for the remaining simulations since the results were considered to be sufficiently stable.

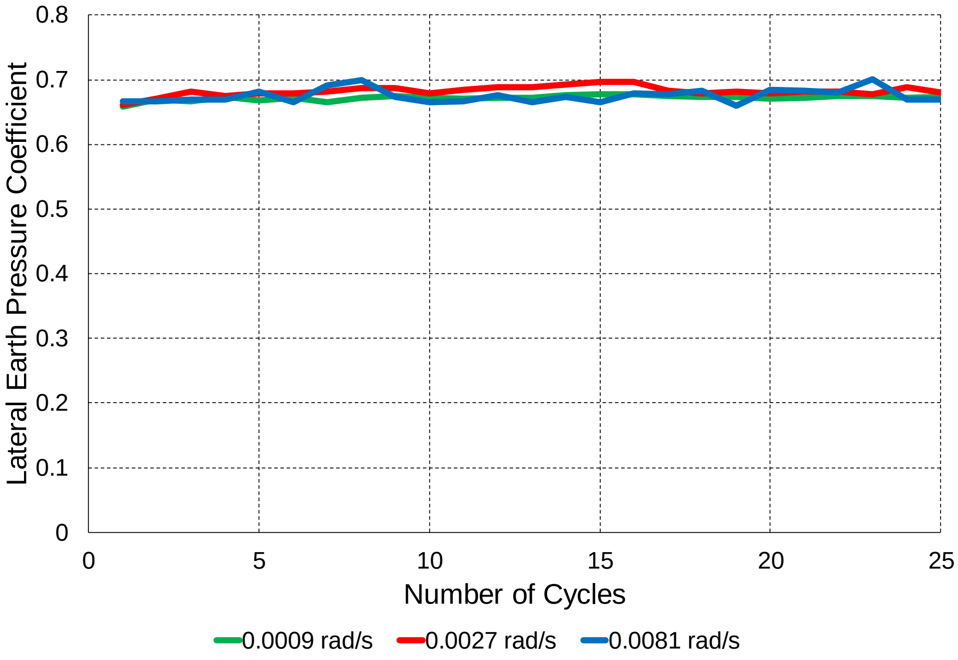

Figure 4.21: Lateral earth pressure coefficient comparison for different cycling rates

4.5.3 Model size independence study

The final verification test performed was on the number of particles to be used for the sensitivity analysis. The medium and large abutment models were used for this verification. A total of 140 000 spherical particles, with diameters of 5 mm, were placed in the medium abutment model space, whereas 1 500 000 spherical particles were used with the large abutment model. The abutment from the medium abutment model was cyclically rotated 25 times in the fully loaded and unloaded positions, while the abutment from the large abutment model was rotated 100 times.

The lateral earth pressure coefficients obtained from the two model sizes are presented in Figure 4.22. The coefficients are plotted for when the model abutment was at the fully loaded position in the passive direction. The figure shows that the coefficient values were almost identical for the different number of particles used.

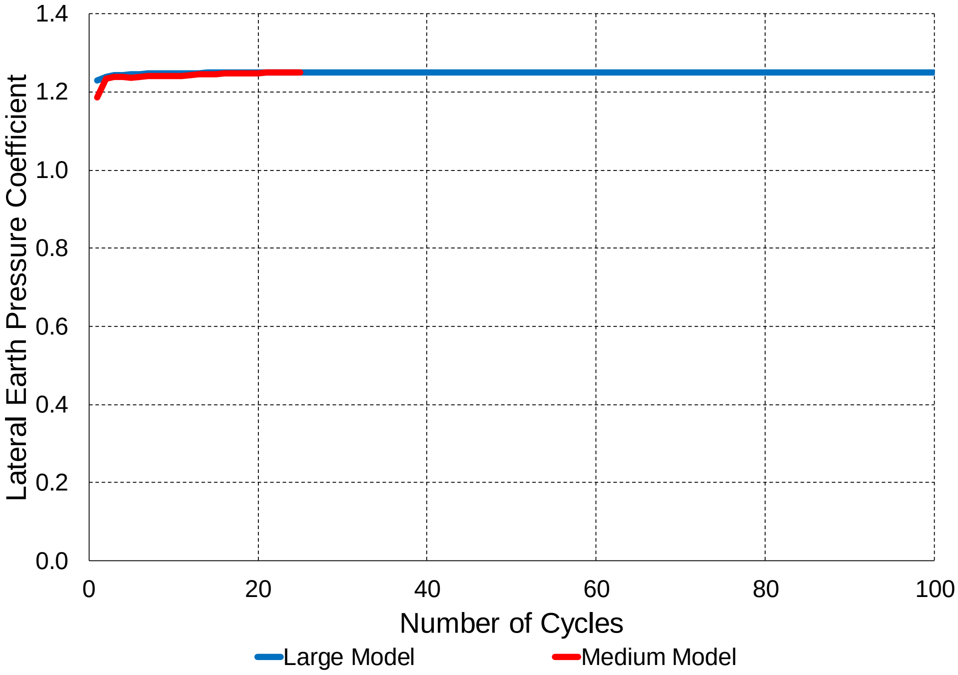

Figure 4.22: Lateral earth pressure coefficient comparison for different model sizes

The bulk backfill densities of the two model sizes are illustrated in Figure 4.23. The figure shows that the densities from the medium abutment model started 1% lower (19 kg/m^3) than those from the larger model, however, after a few cycles, the densities reached similar values (0.1% difference).

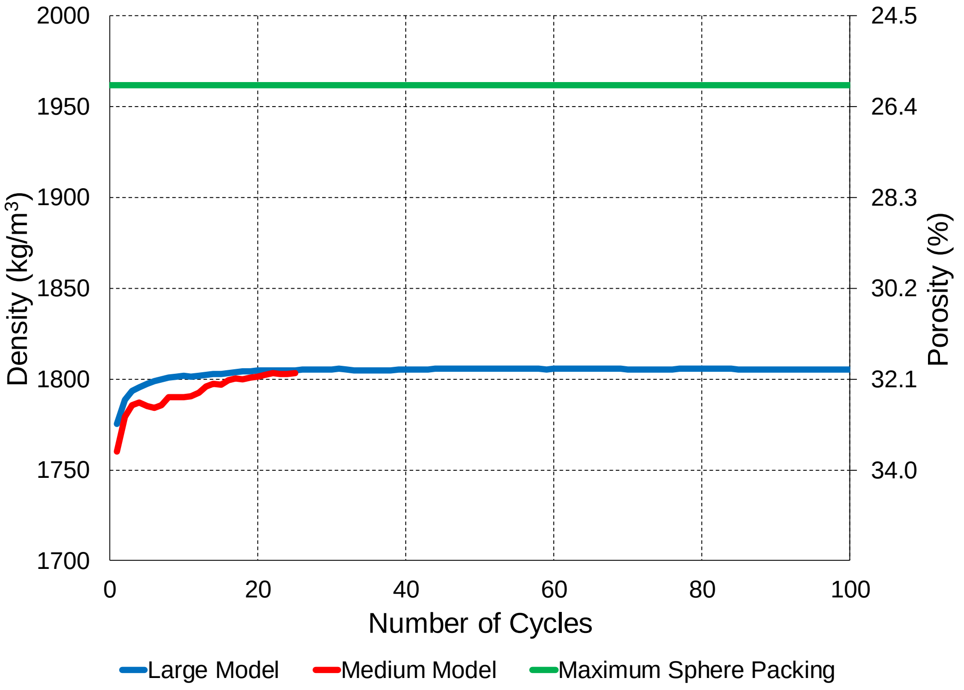

Figure 4.23: Bulk density comparison for different model sizes

In each of the models, the bulk densities were noticeably far from the maximum sphere packing of 1962 kg/m^3 (25.95% porosity). The results from the verification test on the model size indicate that 140 000 spherical particles with 25 cycles of the model abutment would be sufficient for the numerical sensitivity analysis.

4.6 PARTICLE SHAPE NUMERICAL SENSITIVITY ANALYSIS

Using the six different particle shapes, a total of six simulations were performed, to study the effect of granular particle shape on the response of backfill retained by integral bridge abutments. The simulations were performed in Blaze-DEM with the medium abutment model. For each of the simulations, the particles were injected from the top of the model and allowed to settle under only gravitational loads until a state of zero velocity was reached. The model abutment was then cyclically rotated 25 times at full loading and unloading in the passive and active directions respectively.

The parameters used for the simulations were based on the calibration and verification tests. The particle-particle friction coefficient of 0.45, the reduced Young's Modulus of 70 MPa, the average particle size of 5 mm and the rotation rate of 0.0027 rad/s were used for the simulations.

The effect of particle shape on various parameters was investigated as the model abutment was cyclically rotated. These parameters were the bulk backfill densities, lateral earth pressure coefficients, particle settlements, horizontal stress distributions, mean interparticle forces and force chains of the granular backfill. Correlation coefficients were calculated to study the effect of sphericity and angle of repose on the initial and final parameter values as well as the change in these values. Exponential and linear trendlines were fitted to the data sets. In each of the comparisons, the trendline with the higher coefficient of determination (R^2) is presented.

The angles of repose obtained from the drop tests performed in Blaze-DEM were used for the investigations in the numerical sensitivity analysis. These angles of repose were obtained using single particles. Upper and lower bound angles of repose were obtained for the convex polyhedra shapes and the average angle of repose was calculated from these bounds. Therefore, for ease of reading in this section, these angles of repose are referred to as average angles of repose (average AoRs). It should be noted that these values are not necessarily the exact angles of repose of the particles considered. Instead, they are expected to provide an estimation of the variation between the angles of repose for the six particle shapes modelled. It is suggested that the true angle of repose of the convex polyhedra shapes lie close to the average AoR used in this study.

Figures 4.24, 4.25 and 4.26 depict the medium abutment model with spheres, dodecahedrons and triangular prisms respectively. The figures show the particles after they were injected and allowed to settle under gravitational loads, i.e. before the model abutment was rotated.

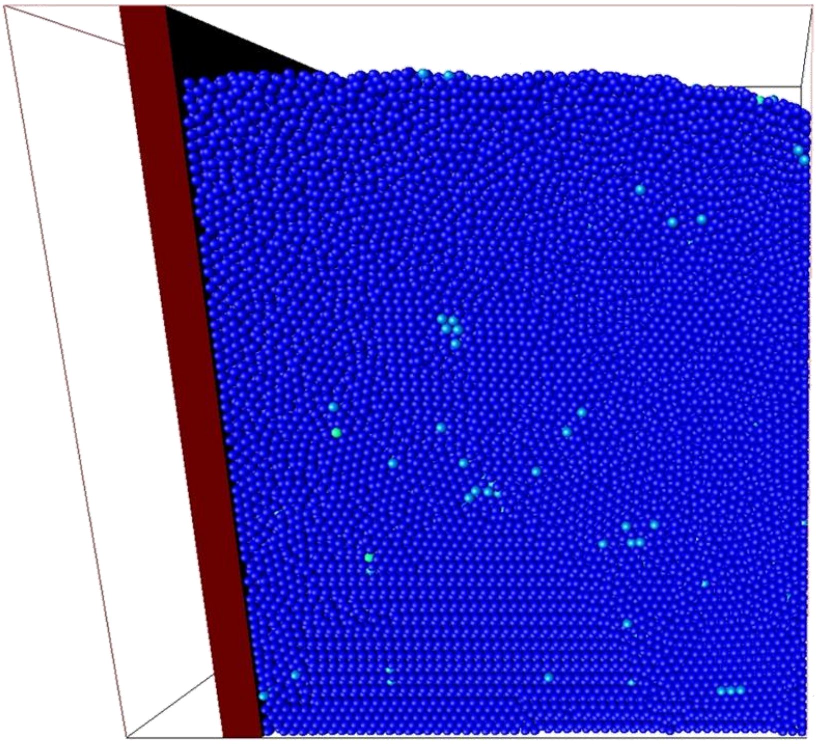

Figure 4.24: 140 000 spheres after injection in Blaze-DEM

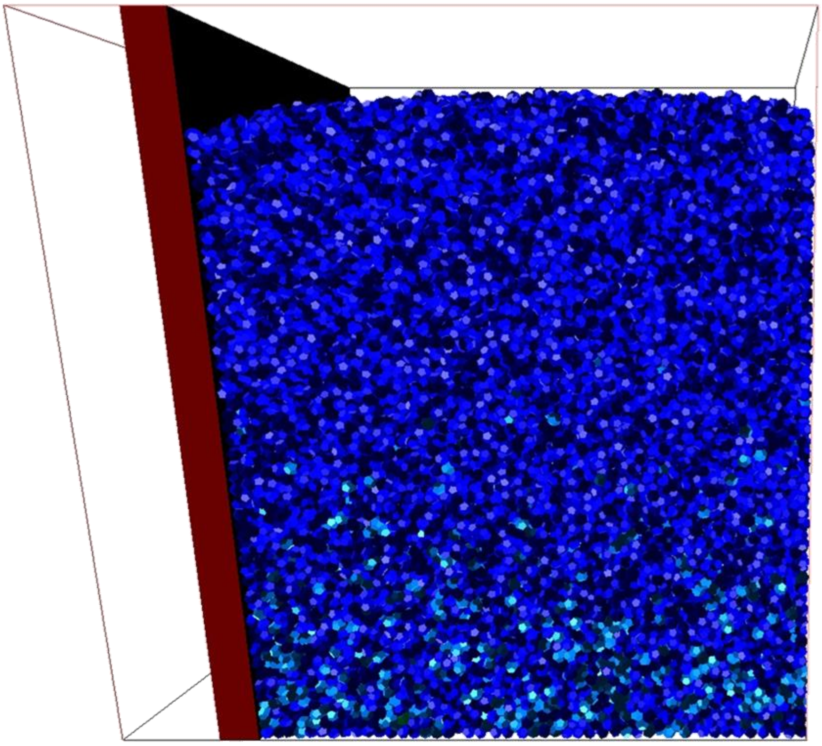

Figure 4.25: 110 000 dodecahedrons after injection in Blaze-DEM

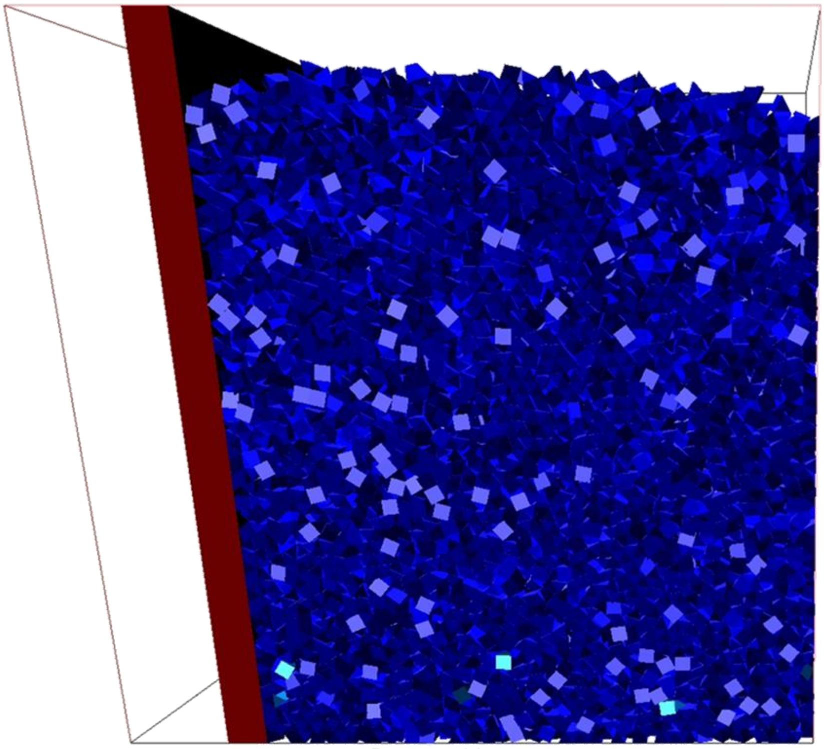

Figure 4.26: 100 000 triangular prisms after injection in Blaze-DEM

4.6.1 Bulk backfill density

The bulk densities and porosities of the granular backfill retained by the abutment for the six particle shapes were investigated. The initial densities and porosities for the different shapes are presented in Figure 4.27. The figure shows that after injection, the particles' initial densities varied. The figure also illustrates that the porosity increased as the sphericity increased for most of the particles. A linear trendline, with an R^2 value of 0.79, was fitted to the data as shown in the figure. This suggested that a 79% linear relationship exists between the initial bulk density for granular particles behind integral bridge abutments and the particle's sphericity.

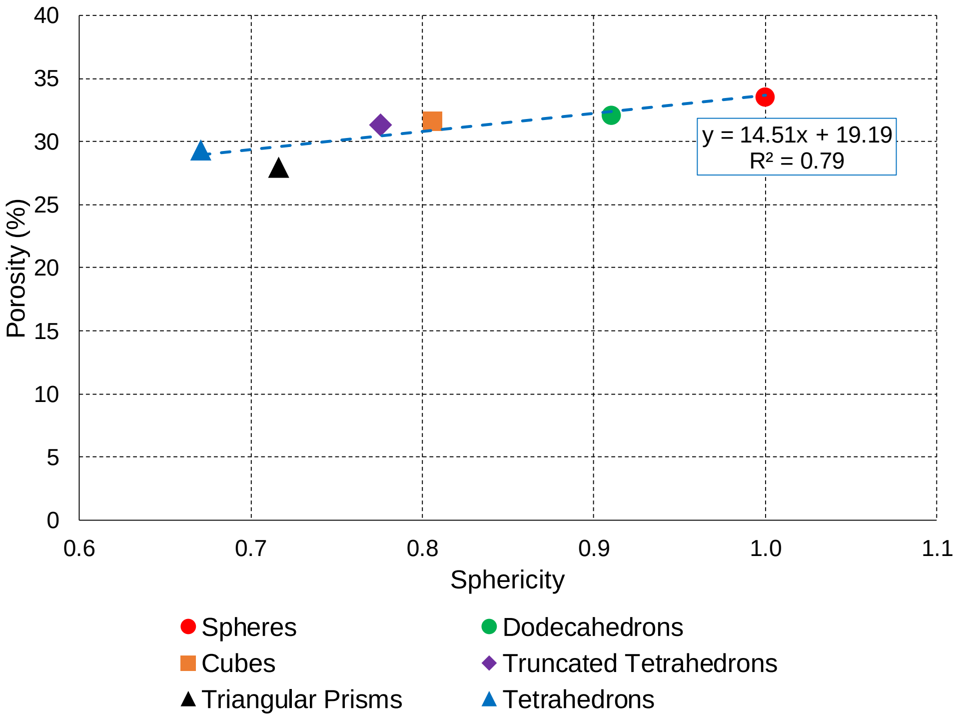

Figure 4.27: Effect of sphericity on initial porosities

The bulk densities for the six particle shapes and the 25 cycles are presented in Figure 4.28. The figure also shows the maximum possible packing which could be obtained with the spheres i.e. 1962 kg/m^3 (25.95% porosity). The maximum possible packing which could be achieved with the triangular prisms or the cubes (0% porosity) is also shown. The results show that the spheres were moderately far from their maximum possible particle packing, however, the cubes and triangular prisms were considerably far from their maximum possible packing.

The bulk density plot for the 25 imposed cycles shows that the magnitude of the densities followed a trend based on the average AoR of the particle shapes. The degree of densification, after 25 cycles, increased as the average AoR of the particle increased.

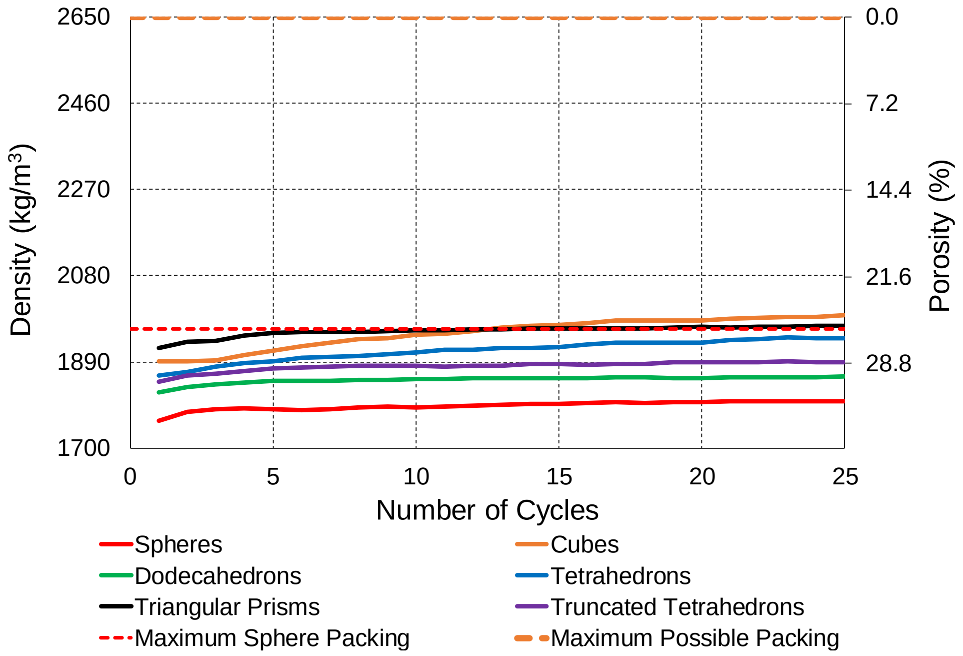

Figure 4.28: Bulk density comparison for various particle shapes

The percentages of the change in bulk densities against the average AoRs for the different particle shapes are illustrated in Figure 4.29. The figure illustrates that the amount the density increased by was related to the average AoR of the particle. An exponential trend was observed between the particles' average AoRs and the degrees of densification. It was found that higher percentages of density increases were observed for particle shapes with higher average AoRs.

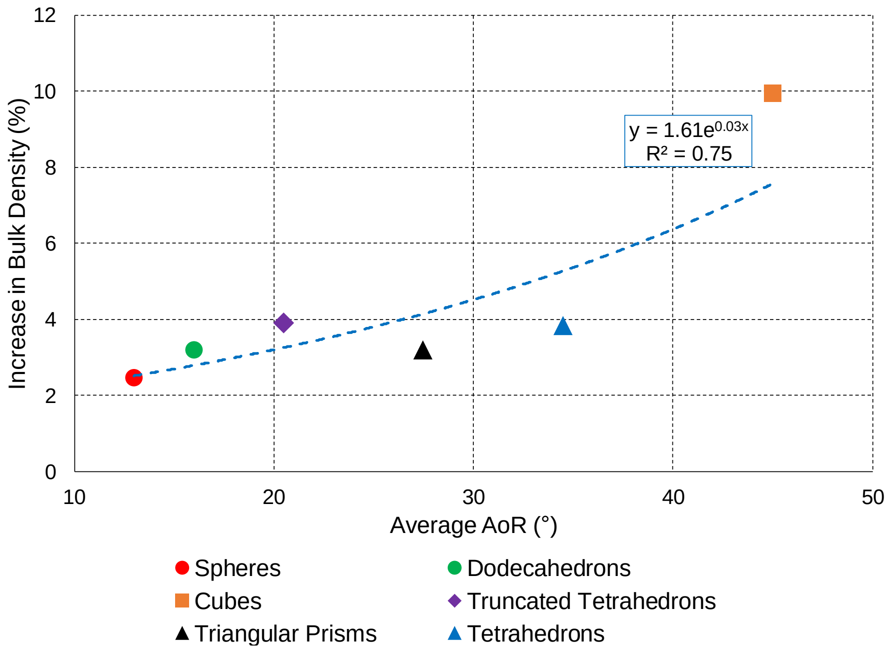

Figure 4.29: Effect of average AoR on increase in bulk density

The spatial density distributions in the granular backfill were investigated for the different particle shapes. This process involved splitting the backfill into 8 zones of equal width. The 8 zones used for the spatial density distribution investigation are presented in Figure 4.30. Zone 1 represents the strip of backfill closest to the model abutment, while Zone 8 refers to the strip furthest from the abutment.

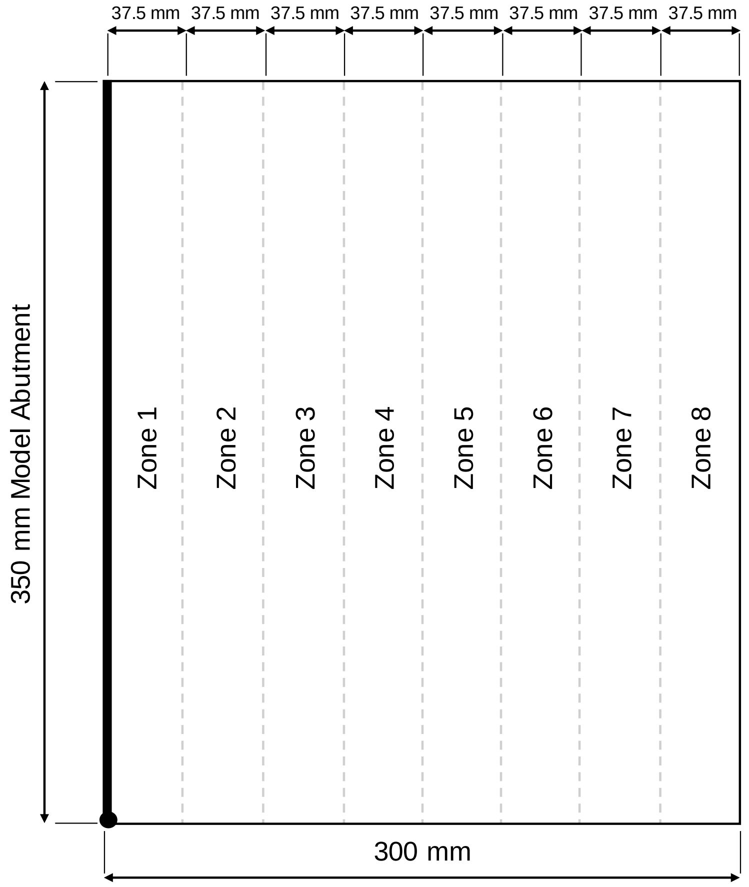

Figure 4.30: Zones used for spatial density distribution investigation

Figures 4.31 to 4.33 illustrate the spatial density distributions of the spheres, cubes and tetrahedrons respectively. The differences between the densities in Zone 1 and the average of the other 7 zones were investigated and compared to the sphericities of the various particles. This comparison is presented in Figure 4.34. The figure shows that the difference in densities increased with a 96% linear relationship as the sphericity decreased.

The results from the spatial density distribution investigation indicate that the particles with higher sphericities experienced movements and densifications over larger domains. However, the particles with higher angularities experienced movements that were mainly restricted close to the abutment i.e. particle movements and densifications were more localised.

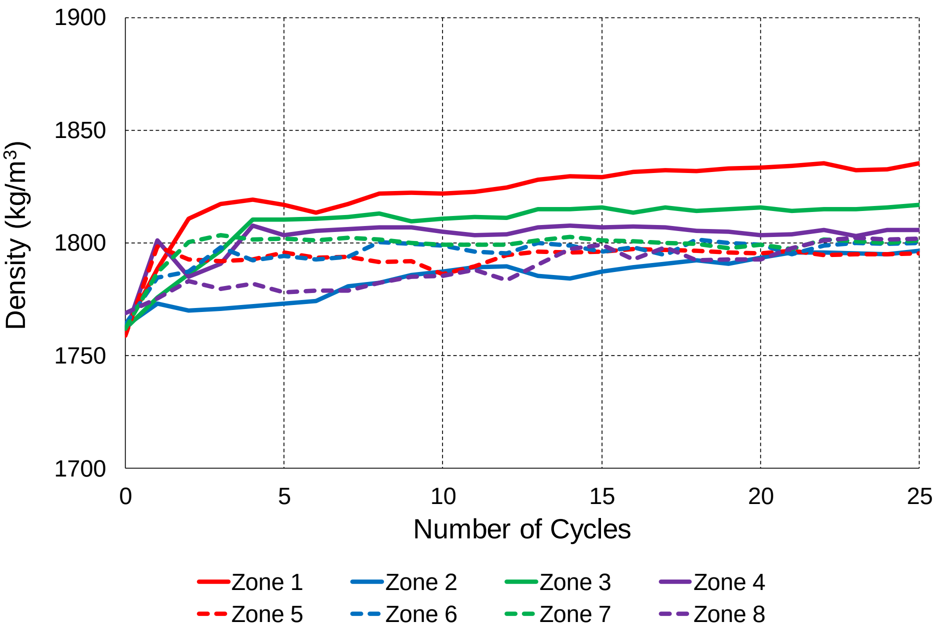

Figure 4.31: Spatial density distributions for spheres

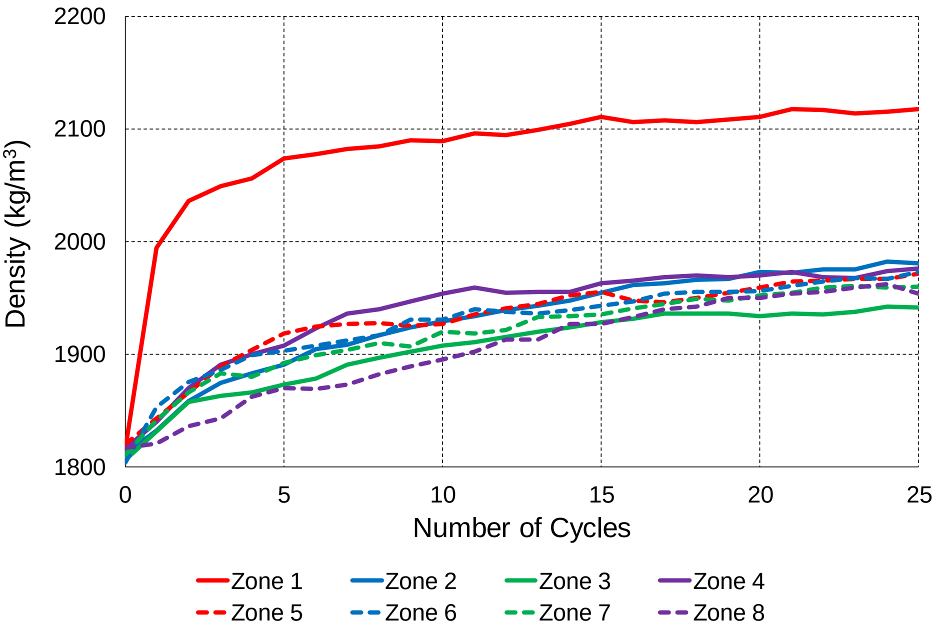

Figure 4.32: Spatial density distributions for cubes

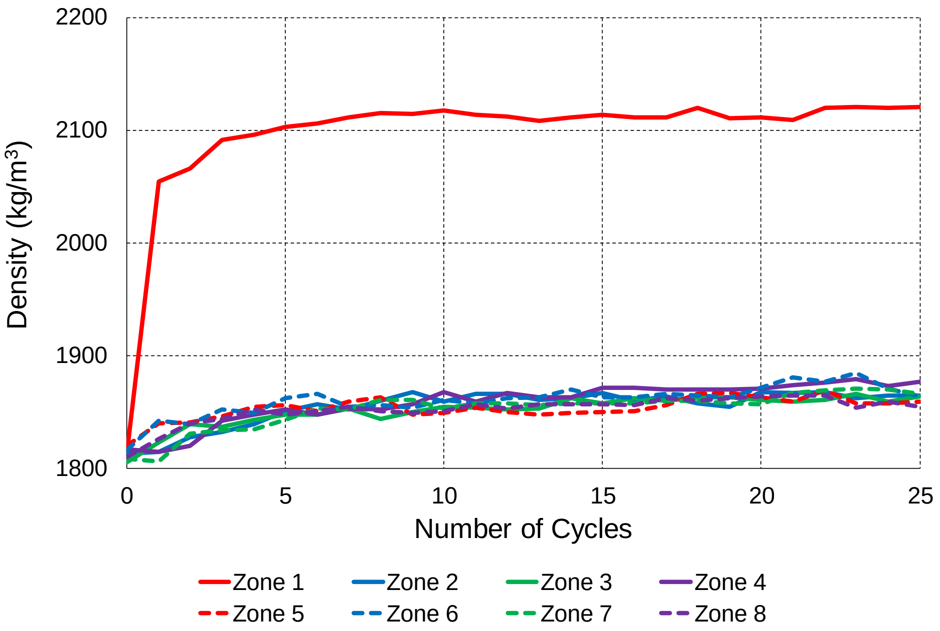

Figure 4.33: Spatial density distributions for tetrahedrons

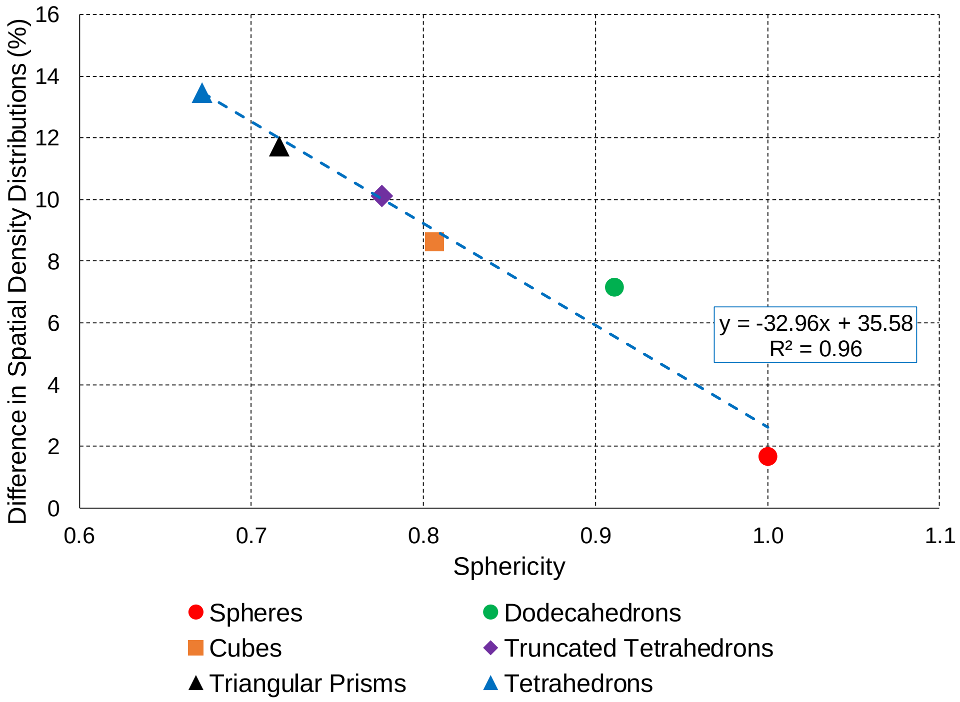

Figure 4.34: Effect of sphericity on spatial density distribution difference

Table 4.8 summarises the correlation coefficients $\left(\rho_{X,Y}\right)$ obtained from the various bulk density parameters investigated. The results presented in the table indicate that the initial bulk density of granular backfill retained by integral bridge abutments is correlated to the sphericity of the particles. The results also indicate that the type of movements experienced by the backfill retained by the abutment is 96% linearly related to the sphericity of a particle. Particle shapes with higher angularities underwent larger movements closer to the abutment which was rotated, i.e. localised movements. However, particle shapes with higher sphericities experienced movements and densifications over larger domains.

The correlation coefficient results also indicate that a particle's final bulk density, as well as the degree of densification it undergoes, is correlated to its average AoR. The particle shapes with higher average AoRs experienced larger degrees of densification, whereas the shapes with lower average AoRs underwent smaller degrees of densification. The graphs showing the effects of average AoR and sphericity on the bulk density values not shown in this section are presented in Appendix A.

Table 4.8: Correlation coefficients obtained from bulk densities

Parameter (X)	**Sphericity (Y)**		**Average AoR (Y)**	
	$\rho_{X,Y}$	**Location**	$\rho_{X,Y}$	**Location**
Initial bulk density	**-0.891**	Figure 4.27	0.432	Figure A.1
Final bulk density	-0.803	Figure A.2	**0.906**	Figure A.3
Percentage increase in bulk density	-0.179	Figure A.4	**0.830**	Figure 4.29
Percentage difference in density distributions	**-0.979**	Figure 4.34	0.568	Figure A.5

4.6.2 Lateral earth pressure coefficient

The lateral earth pressure coefficients, obtained for the six particle shapes when the model abutment was at the fully loaded position in the passive direction, are presented in Figure 4.35. The figure shows that the initial earth pressure coefficients for the different particle shapes were relatively far apart. This was due to the different initial bulk densities observed for the various particle shapes.

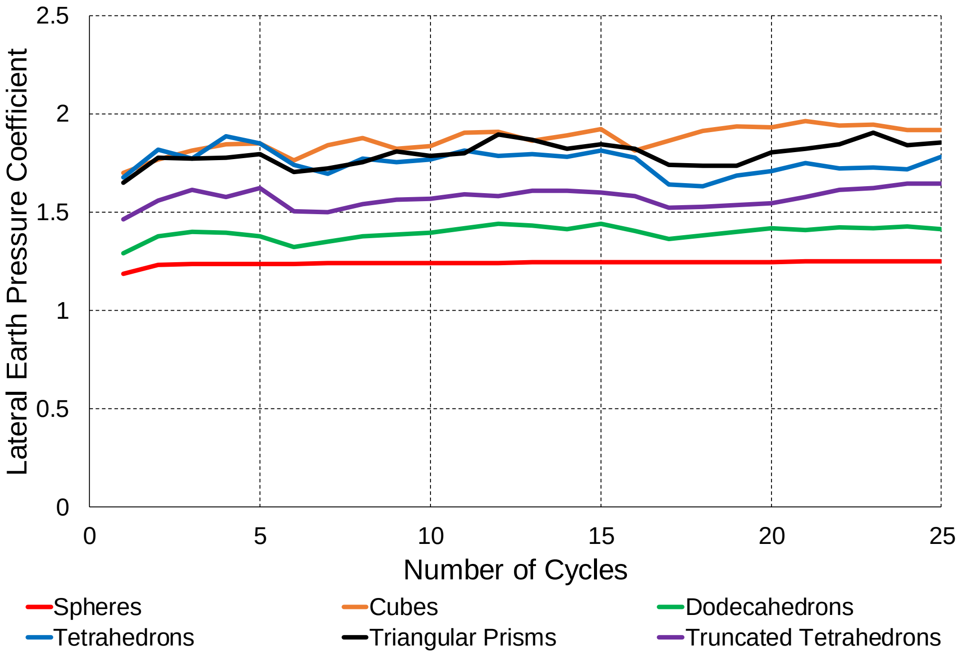

Figure 4.35: Lateral earth pressure coefficient comparison for six particle shapes

The lateral earth pressure coefficients were normalised by dividing each particles' coefficient, after 25 cycles, with its respective initial bulk density. The resulting values were then multiplied by the initial bulk density obtained from the spheres. This meant that the differences in initial bulk densities did not affect the investigation of the effect particle shape on the lateral earth pressures.

It is known that the lateral earth pressure is related to the vertical earth pressure and that the vertical earth pressure is a function of the density of the system. The normalised lateral earth pressure coefficients were therefore normalised again by dividing the coefficients of the six particles, for the 25 cycles, with the bulk density at the respective cycle. The subsequent values were then multiplied by the new initial bulk density of the respective particle shape. This meant that the lateral earth pressures could be studied without the effect of the bulk density. The effect of particle shape on the earth pressures was therefore isolated.

The final normalised lateral earth pressure coefficients are shown in Figure 4.36. The figure shows that the shape of the particles influenced the lateral earth pressures acting on the model abutment. This effect was studied by investigating the initial and final lateral earth pressure values as well as the change in these values.

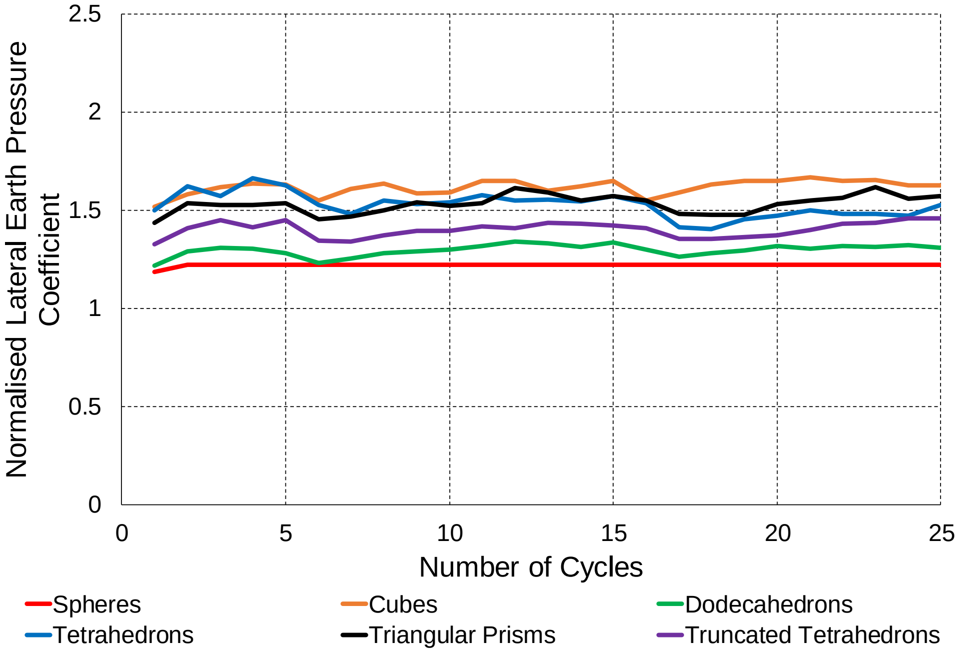

Figure 4.36: Normalised earth pressure coefficient comparison for six particle shapes

To further study the effect of particle shape on the lateral earth pressures, the normalised earth pressure coefficients were plotted against the average AoRs and sphericities for the different particle shapes. Figure 4.37 presents the effect of the average AoR on the normalised initial lateral earth pressure coefficients. The figure shows that the lateral earth pressures increased as the average AoR of the particle increased. This linear trend was also observed in the final values of the lateral earth pressure coefficients.

Figure 4.38 illustrates the effect of sphericity on the percentage increase in the normalised lateral earth pressure coefficients. The figure shows that for particle shapes with higher sphericities, the build-up of lateral earth pressure behind the model abutment was lower, while particle shapes with lower sphericities (higher angularities) had a greater build-up of lateral pressures. A linear trendline with an R^2 value of 0.92 was obtained for the data set. These results were in line to that which was suggested by Höhner *et al.* (2012). Appendix B contains the graphs not shown in this section, illustrating the effects of average AoR and sphericity on the lateral earth pressure coefficient values.

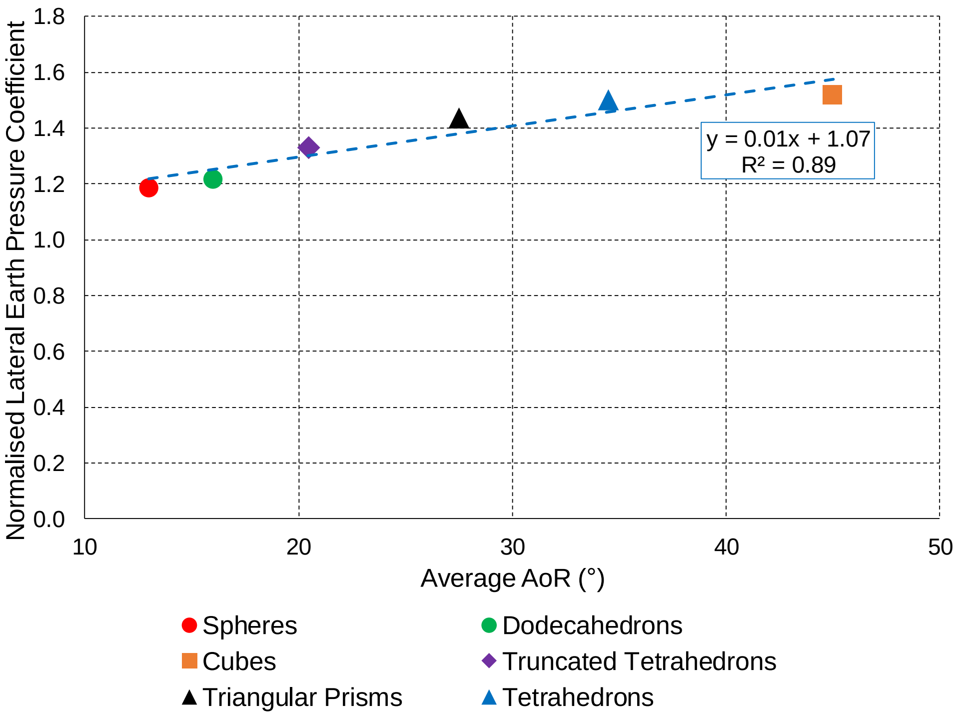

Figure 4.37: Effect of average AoR on normalised initial earth pressure coefficient

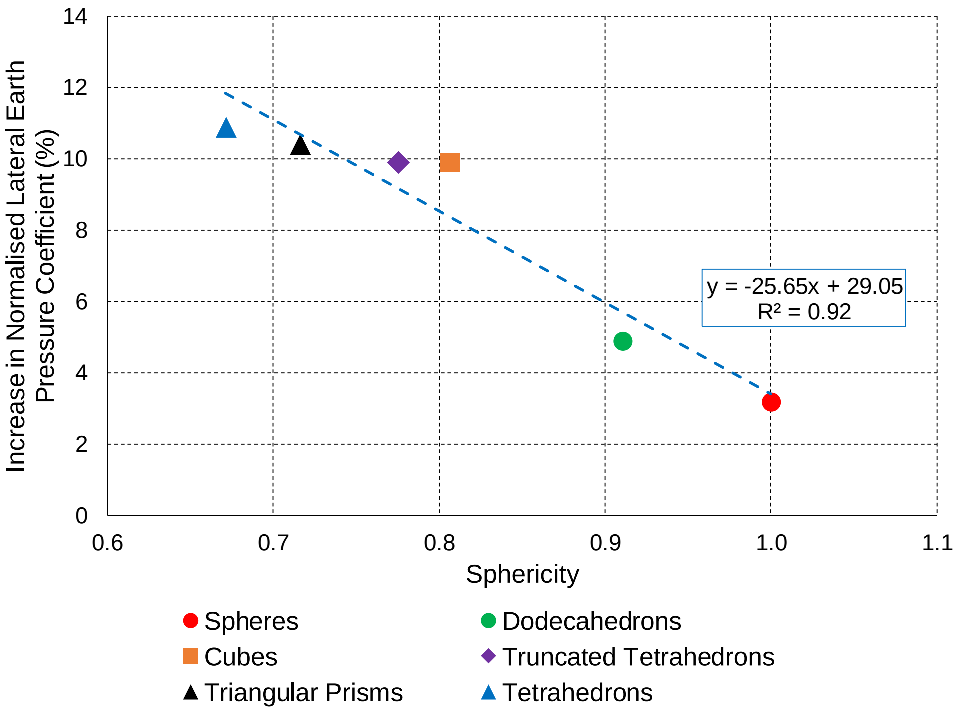

Figure 4.38: Effect of sphericity on increase in normalised lateral earth pressure coefficient

A summary of the correlation coefficients $\left(\rho_{X,Y}\right)$ obtained from the various normalised lateral earth pressure coefficients with the average AoRs and sphericities is presented in Table 4.9. The results shown in the table indicate that the magnitudes of the initial and final normalised earth pressure coefficients behind integral bridge abutments are over 90% corelated to the average AoR of the material used as backfill. The amount of build-up of earth pressures behind integral bridge abutments is almost 96% correlated to the sphericity of the particles used as backfill.

Table 4.9: Correlation coefficients obtained from normalised lateral earth pressures

Parameter (X)	**Sphericity (Y)**		**Average AoR (Y)**	
	$\boldsymbol{\rho_{X,Y}}$	**Location**	$\boldsymbol{\rho_{X,Y}}$	**Location**
Normalised initial lateral earth pressure coefficient	-0.838	Figure B.1	**0.945**	Figure 4.37
Normalised final lateral earth pressure coefficient	-0.878	Figure B.2	**0.918**	Figure B.3
Percentage increase in normalised lateral earth pressure coefficient	**-0.958**	Figure 4.38	0.739	Figure B.4

4.6.3 Backfill settlement

The backfill settlements of the six particle shapes, for the 25 cycles, are presented in Figure 4.39. As with the lateral earth pressure coefficients, the effect of density on the backfill settlement was removed by normalising the settlements with the bulk density at each cycle. This allowed for the effect of only the particle shape on backfill settlement to be studied. The normalised backfill settlements are shown in Figure 4.40.

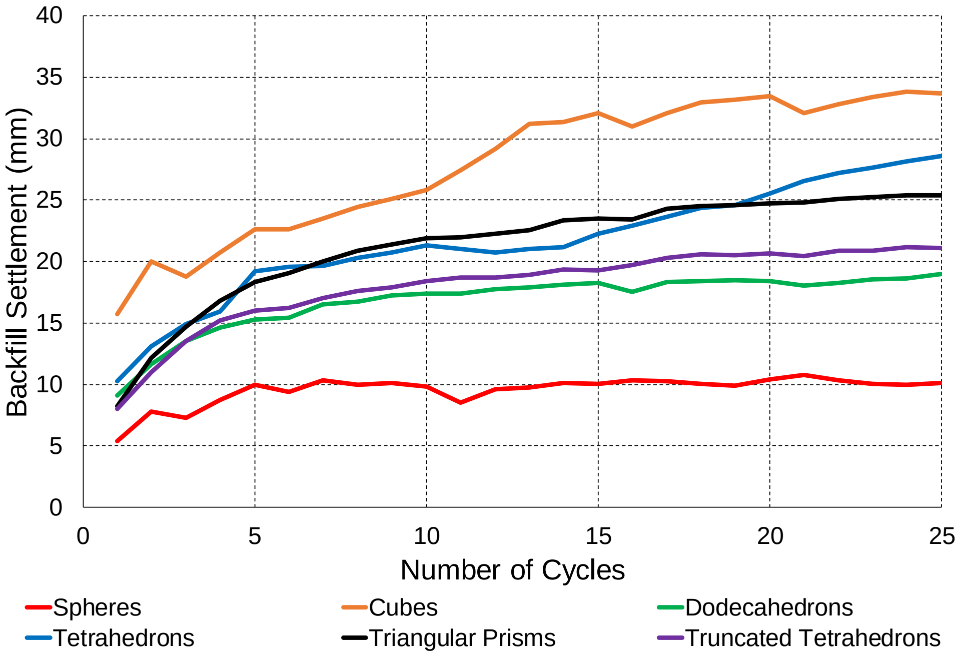

Figure 4.39: Backfill settlement comparison for six particle shapes

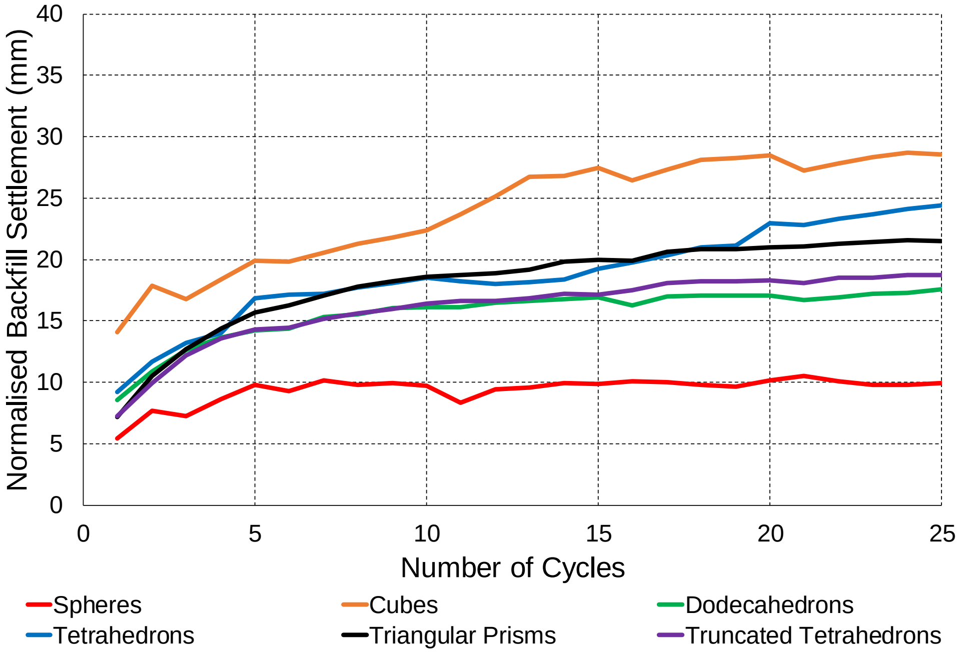

Figure 4.40: Normalised backfill settlement comparison for six particle shapes

The effect of the average AoR of the particle on the normalised final backfill settlement values is shown in Figure 4.41. The results shown in the figure indicate that the amount of settlement of particles behind integral bridge abutments and the particles’ average AoRs are 90% linearly related. The amount of backfill settlement increased as the average AoR of the particle increased. This behaviour was also observed for the initial backfill settlements with the average AoRs of the particles.

The effect of a particle's sphericity on the increase in normalised backfill settlement is illustrated in Figure 4.42. The percentage increase was calculated as the amount the settlement increased by from the first cycle to the last cycle for the respective particle shapes. An exponential trendline with a coefficient of determination of 0.73 was fitted to the data in the figure. The results indicate that the percentage change in backfill settlement increases as the particle's sphericity decreases.

A summary of the correlation coefficients $\left(\rho_{X,Y}\right)$ obtained from the various normalised backfill settlements and the average AoRs as well as the sphericities is presented in Table 4.10. As with the lateral earth pressure coefficients, the results presented in the table indicate that the magnitudes of the initial and final normalised backfill settlements behind integral bridge abutments are related to the average AoR of the material. However, the amount of change of settlement behind integral bridge abutments is more closely related to the sphericity of the particles than its average AoR. The graphs showing the effects of sphericity and average AoR on the backfill settlement values not shown in this section are presented in Appendix C.

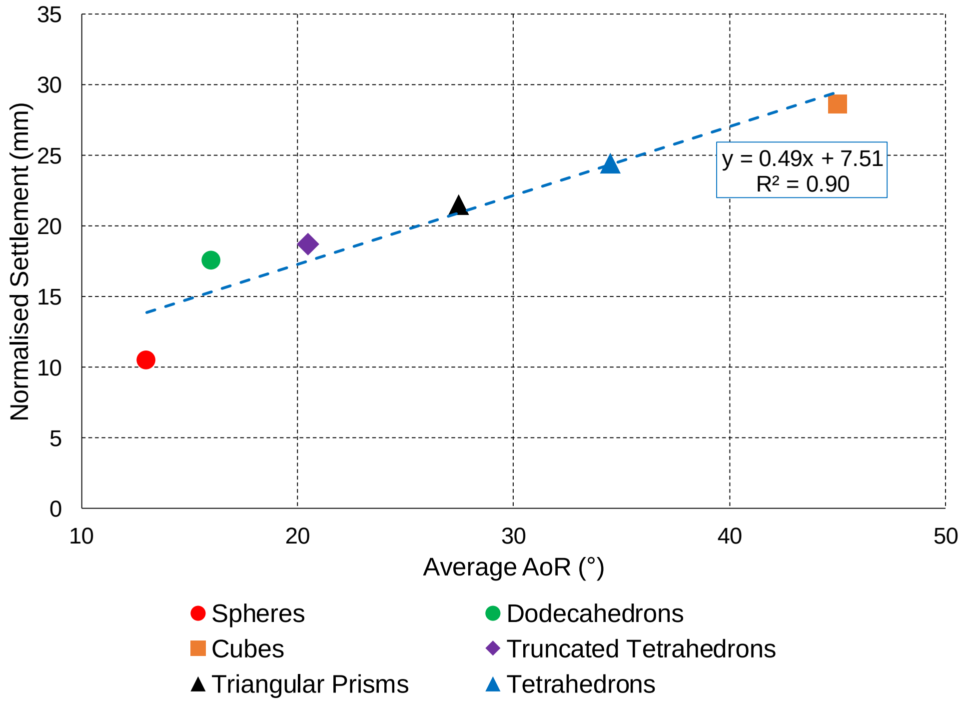

Figure 4.41: Effect of average AoR on normalised final backfill settlement values

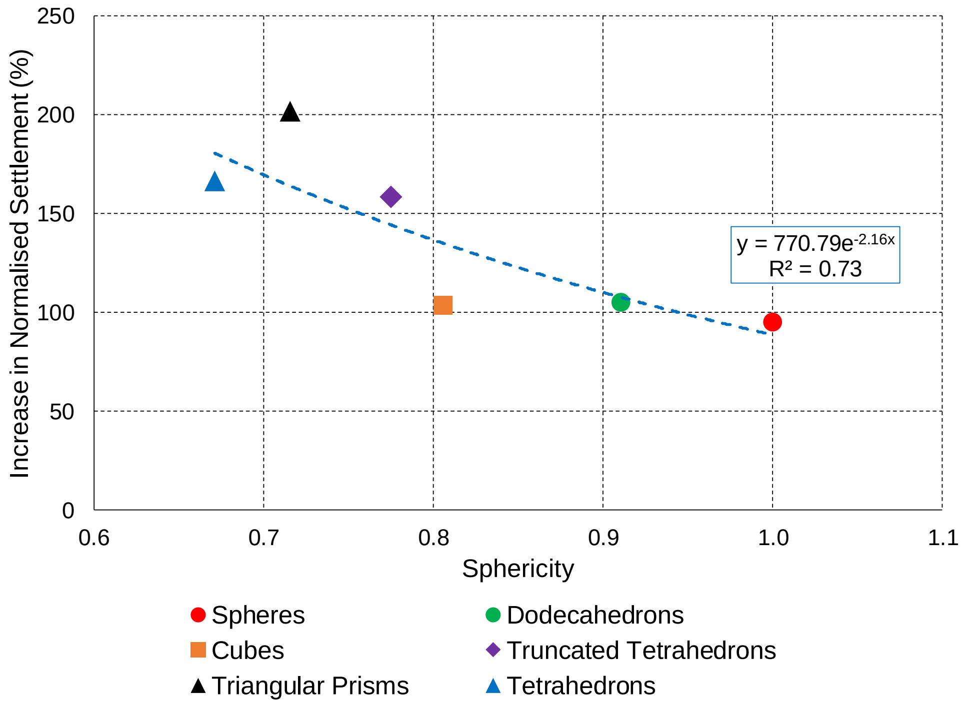

Figure 4.42: Effect of sphericity on increase in normalised backfill settlement values

Table 4.10: Correlation coefficients obtained from backfill settlement values

Parameter (X)	**Sphericity (Y)**		**Average AoR (Y)**	
	$\rho_{X,Y}$	**Location**	$\rho_{X,Y}$	**Location**
Normalised initial backfill settlement	-0.288	Figure C.1	**0.863**	Figure 4.41
Normalised final backfill settlement	-0.732	Figure C.2	**0.951**	Figure C.3
Percentage increase in normalised backfill settlement	**-0.827**	Figure 4.42	0.178	Figure C.4

4.6.4 Horizontal stress distribution

The horizontal stress distributions acting on the model abutment were analysed for the six particle shapes investigated. Figures 4.43, 4.44 and 4.45 portray the stress distributions after the first, tenth and last cycles respectively. The figure illustrates the stress distributions when the model abutment was fully loaded and unloaded in the passive and active directions respectively. The figure further illustrates the theoretical active and passive distributions calculated for the spheres. Only the theoretical values for the spherical particles with an angle of repose of 33° were calculated. This was done since the drop tests performed with clumps were suggested to provide an accurate representation of the internal friction angle of the particle.

The figures show that, after the first cycle, each of the particle shapes yielded distributions almost identical to the active case calculated for the spheres. After the tenth and last cycles, these unloading distributions all increased, excluding those from the spheres, which were still relatively close to the theoretical active state values. The unloading distributions obtained from the spheres remained similar to the theoretical values for each of the 25 cycles. For each of the cycles, the loaded stress distributions followed trends similar to those observed with the lateral earth pressure coefficients. The shapes with lower sphericities resulted in higher stress distributions.

Figure 4.46 shows the percentage difference in horizontal stress distributions between the first and last cycles when the model abutment was at the loaded positions i.e. in the passive direction. The figure illustrates that the spheres experienced a relatively constant increase in stress with depth. However, the remaining five shapes underwent much larger and more erratic horizontal stress distribution increases.

The spheres showed similar load distributions for each of the cycles, which were relatively far from the theoretical passive values calculated. This is proposed to be a result of the lack of any angular edges for the spheres. These perfectly rounded shapes meant that there was no possibility for particle interlocking and a little chance of particle reorientation. The spherical particles, therefore, maintained a similar packing with each cycle. This follows the suggestions by Xu *et al.* (2007), Clayton *et al.* (2006) and Wesseloo (2004) that the particle shape, particularly the sphericity, plays a significant role on the behaviour of granular materials, especially upon cyclic loading.

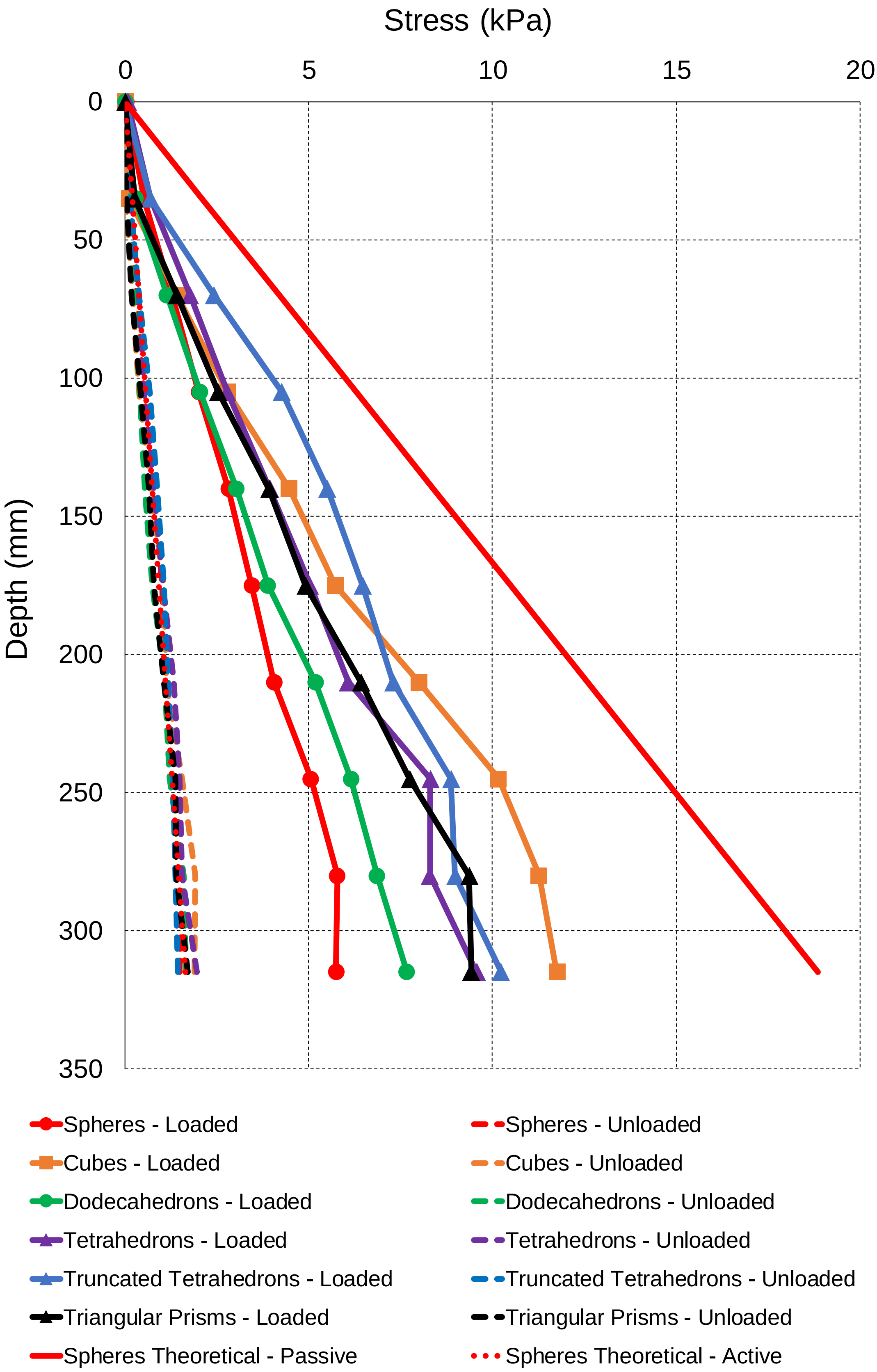

Figure 4.43: Horizontal stress distributions acting on the model abutment after 1 cycle

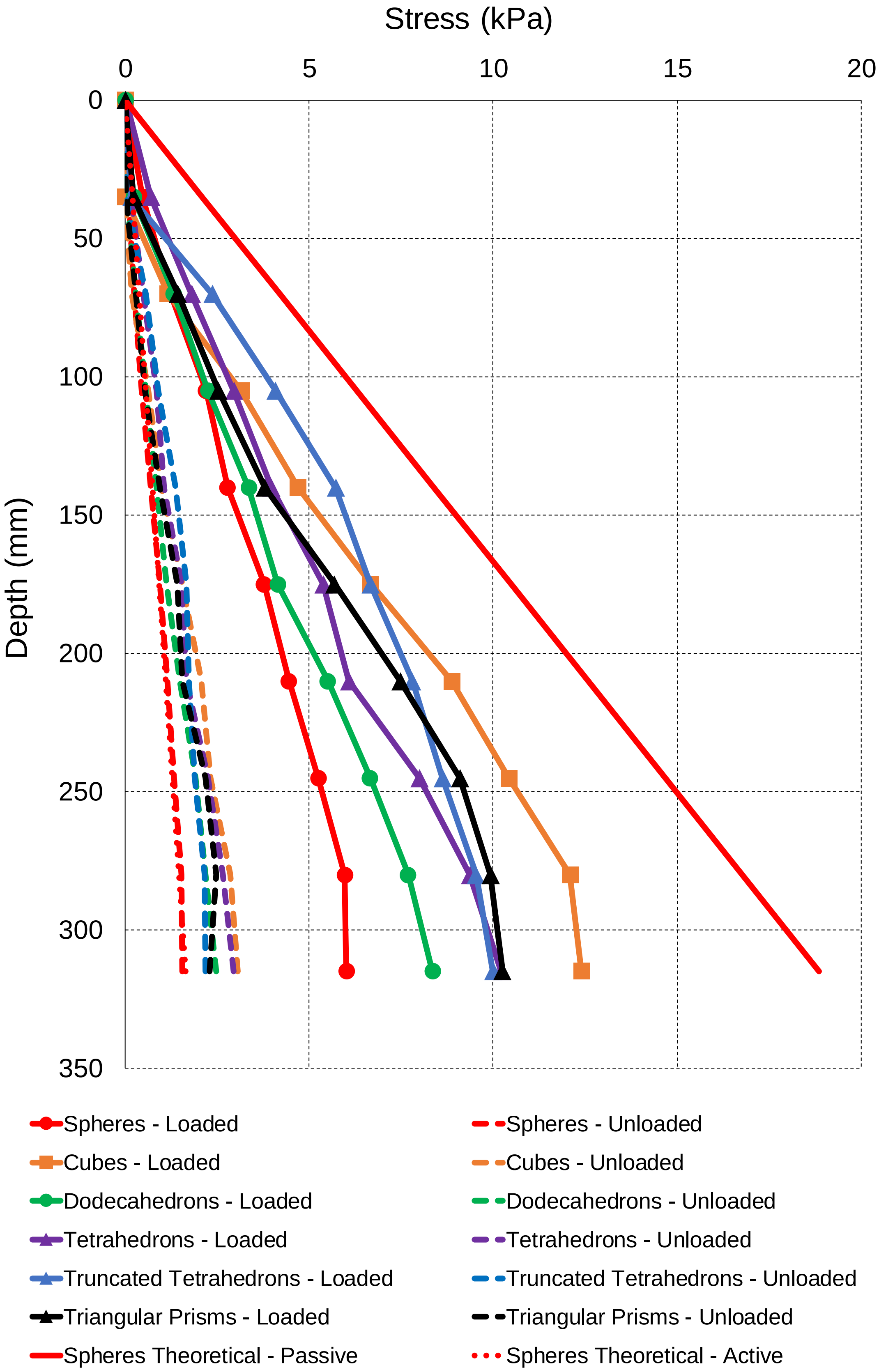

Figure 4.44: Horizontal stress distributions acting on the model abutment after 10 cycles

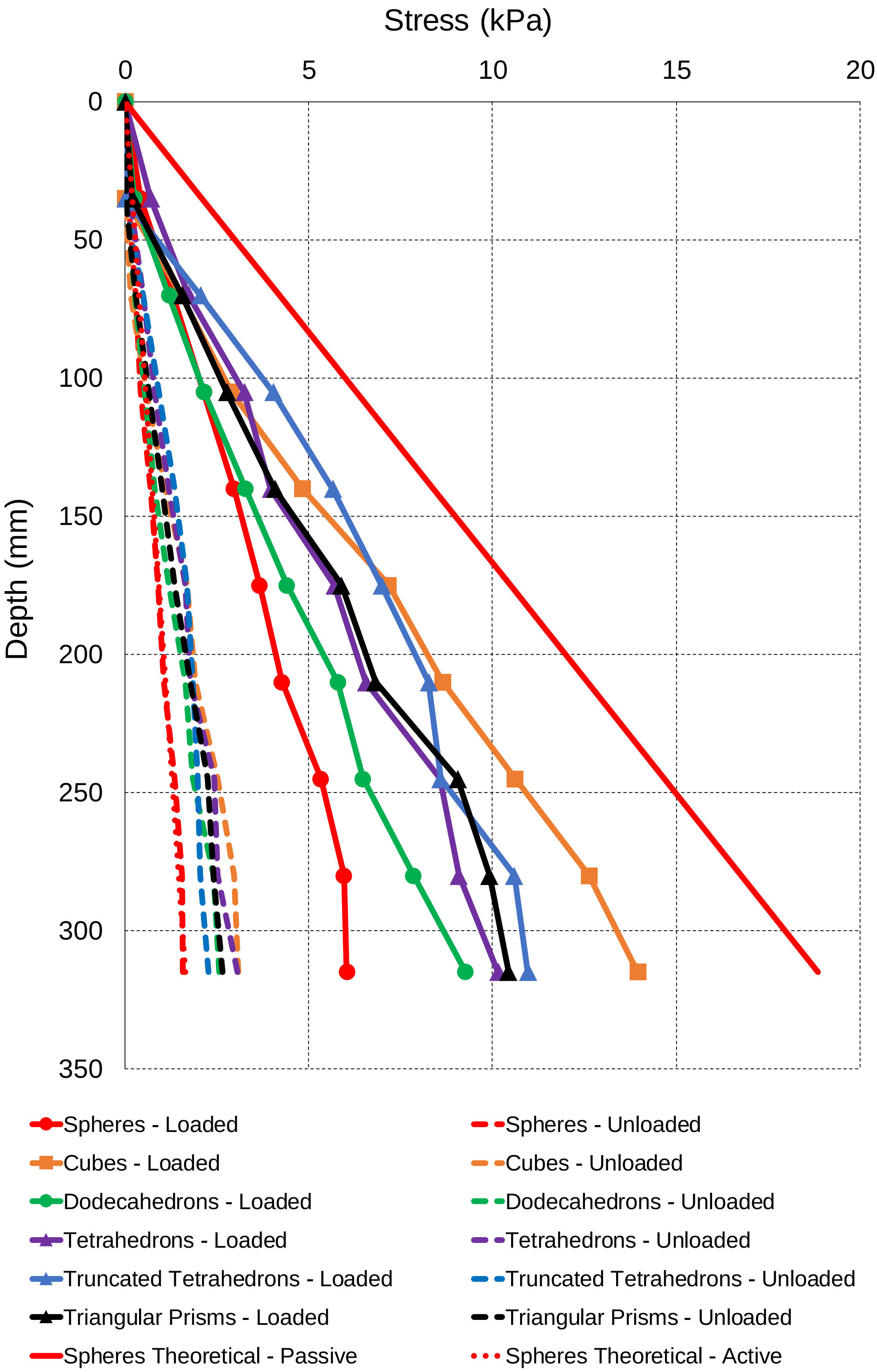

Figure 4.45: Horizontal stress distributions acting on the model abutment after 25 cycles

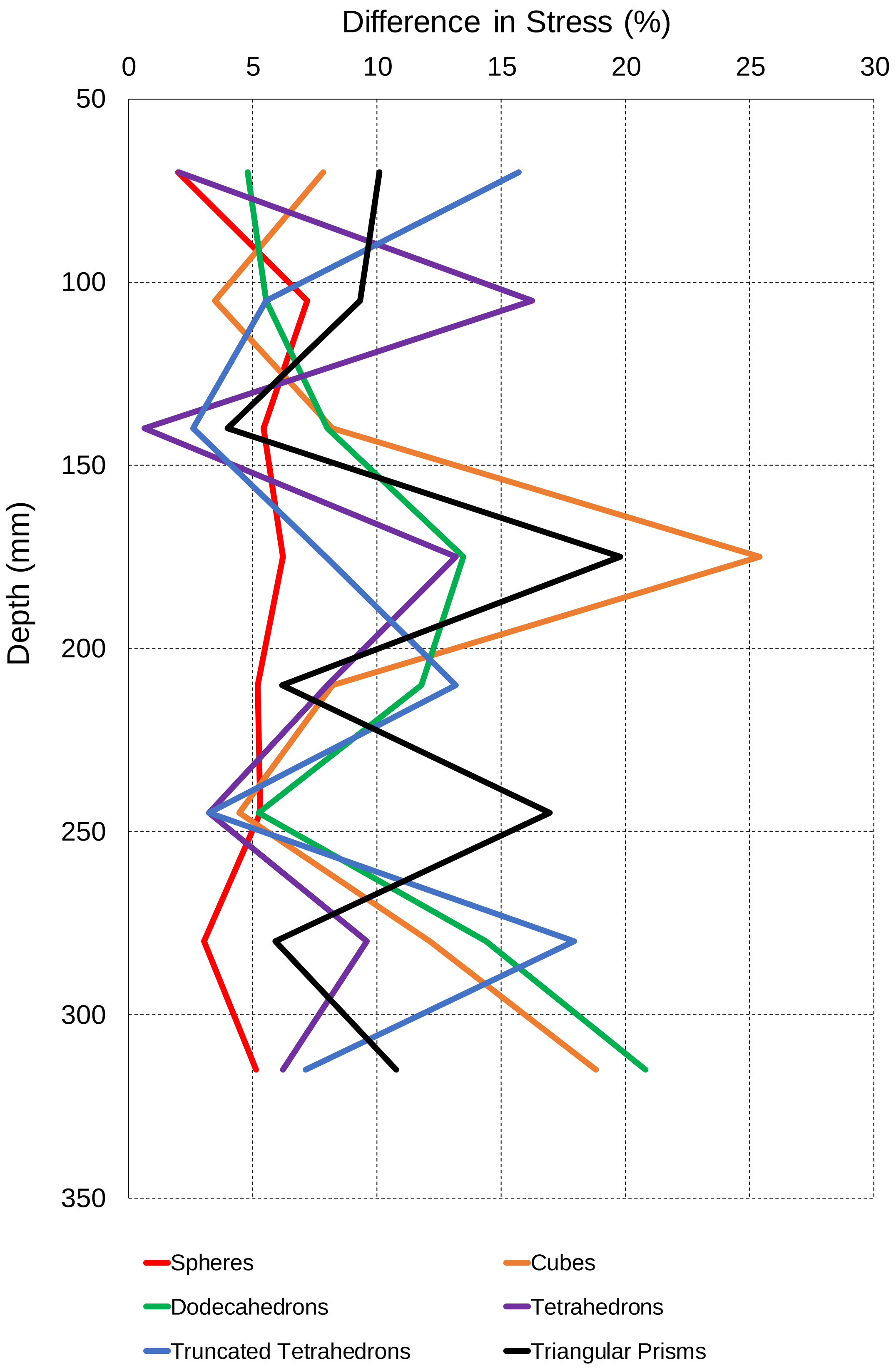

Figure 4.46: Difference in horizontal stress distributions between first and last cycles

4.6.5 Mean interparticle contact forces

The mean interparticle contact forces in the granular backfill for the spheres and cubes were investigated as they experienced the lowest and the highest lateral earth pressure coefficients, bulk densities and backfill settlements respectively. The contact forces plotted in this section were obtained for the first and last cycles of the abutment when the abutment was at the fully loaded position in the passive direction.

Figures 4.47 and 4.48 depict the contact force gradients in the spheres after the first and last cycles respectively. The figures illustrate similar contact forces for the respective number of cycles in the spheres. These plots also illustrate relatively horizontal contact force gradients similar to what was expected from self-weight distributions. The maximum contact force in the plots for the spheres was 0.15 N.

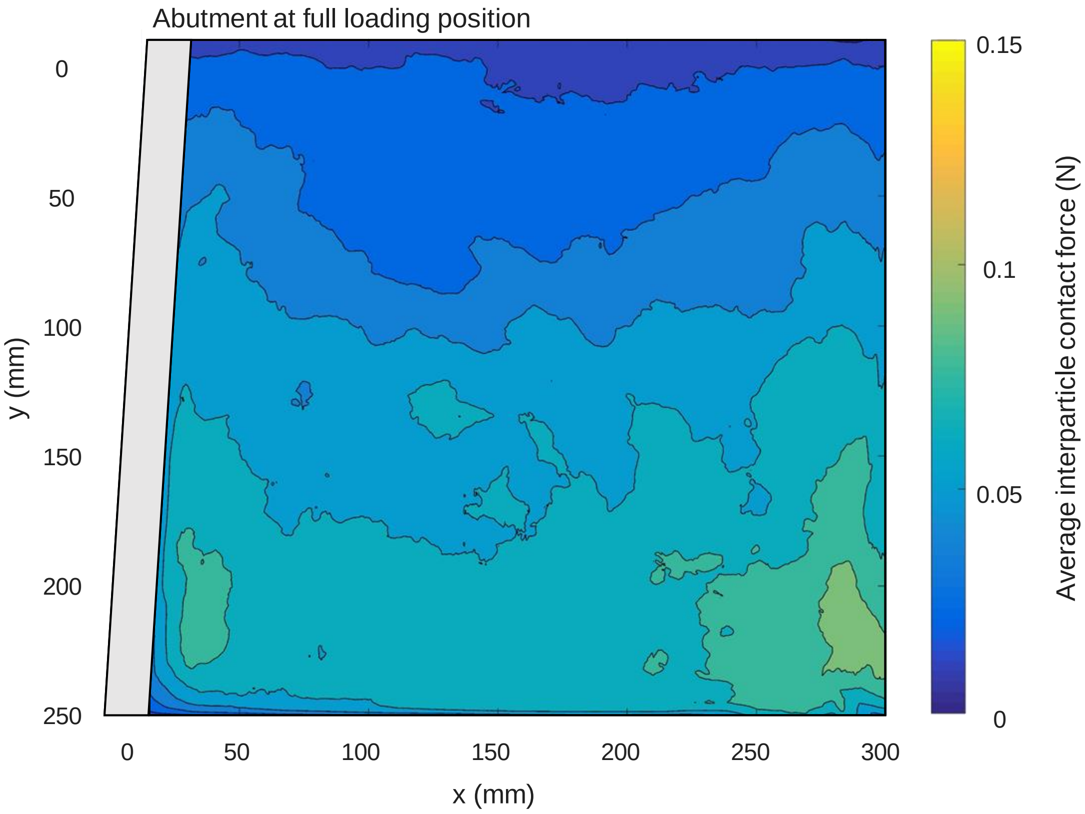

Figure 4.47: Contact force distribution in spheres after first cycle

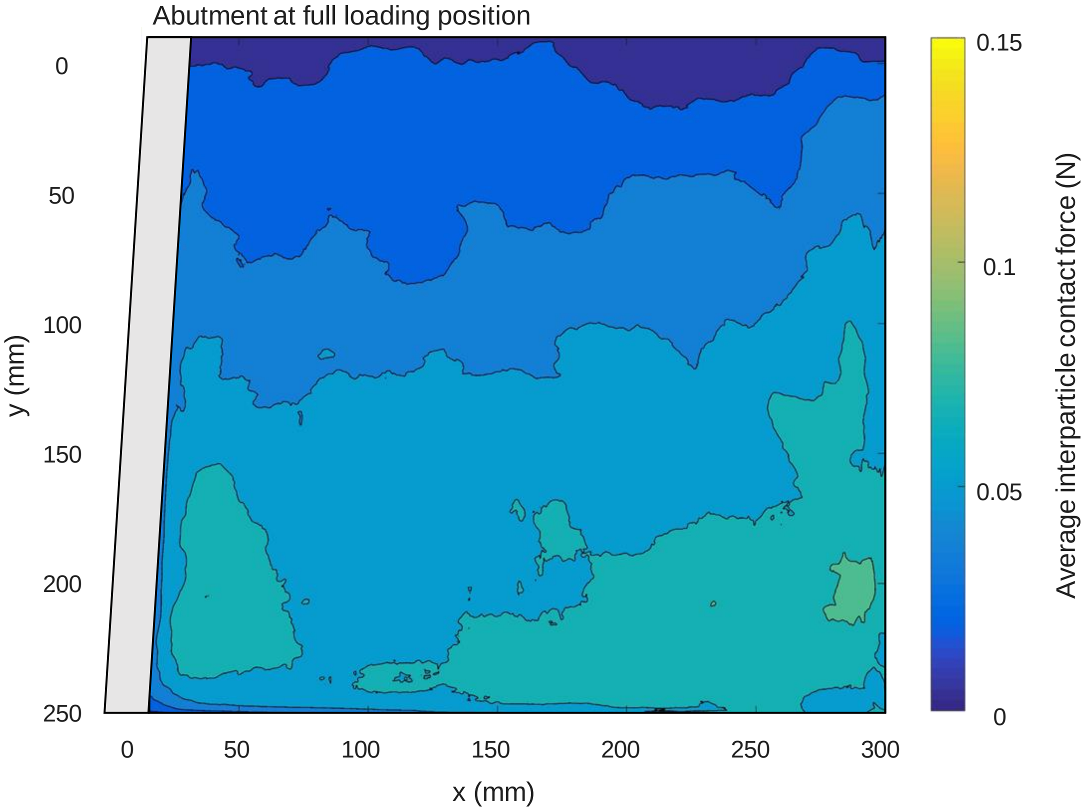

Figure 4.48: Contact force distribution in spheres after last cycle

The average interparticle contact forces obtained from the cubes for the first and last cycles are depicted in Figures 4.49 and 4.50 respectively. The figure showing the contact forces after the first cycle illustrate large mean contact forces acting far from the abutment. The force gradients are shown to be at higher angles as opposed to the horizontal gradients observed with the spheres. After 25 cycles, the angled gradients observed with the cubes settled to horizontal gradients similar to those obtained from the spheres. The maximum contact force in the plots for the cubes was 0.2 N, which was higher than the 0.15 N observed with the spheres.

The difference in the plots for the cubes is suggested to be a result of reorientation of the particles. After the first cycle, the cubes were loosely packed and arranged with random orientations. These random orientations were suggested to result in larger contact forces in the granular backfill. As seen in Figure 4.49, the forces were large in the granular backfill, however, the forces acting on the abutment were relatively low.

By the last cycle, the cubes had settled into a denser packing and the forces reached a horizontal distribution state, with larger forces acting on the abutment as depicted in Figure 4.50. This was suggested to be one of the reasons for the larger increases in stress accumulation for the cubes when compared to the spheres.

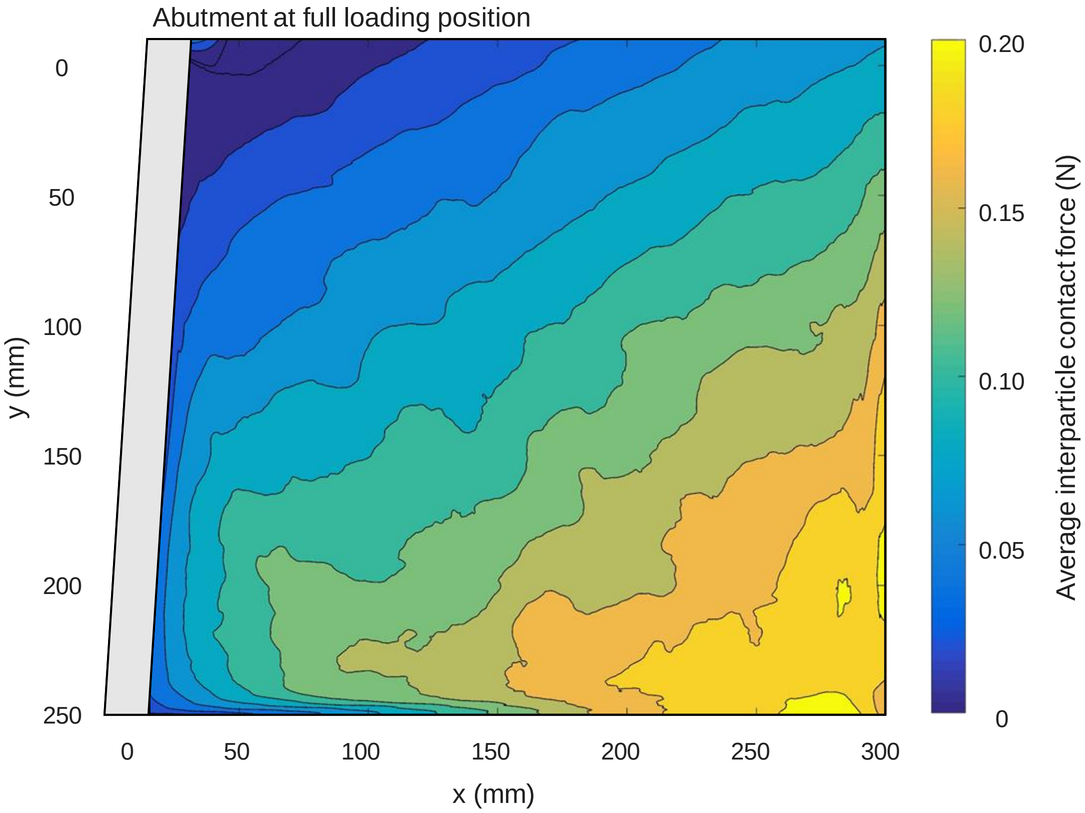

Figure 4.49: Contact force distribution in cubes after first cycle

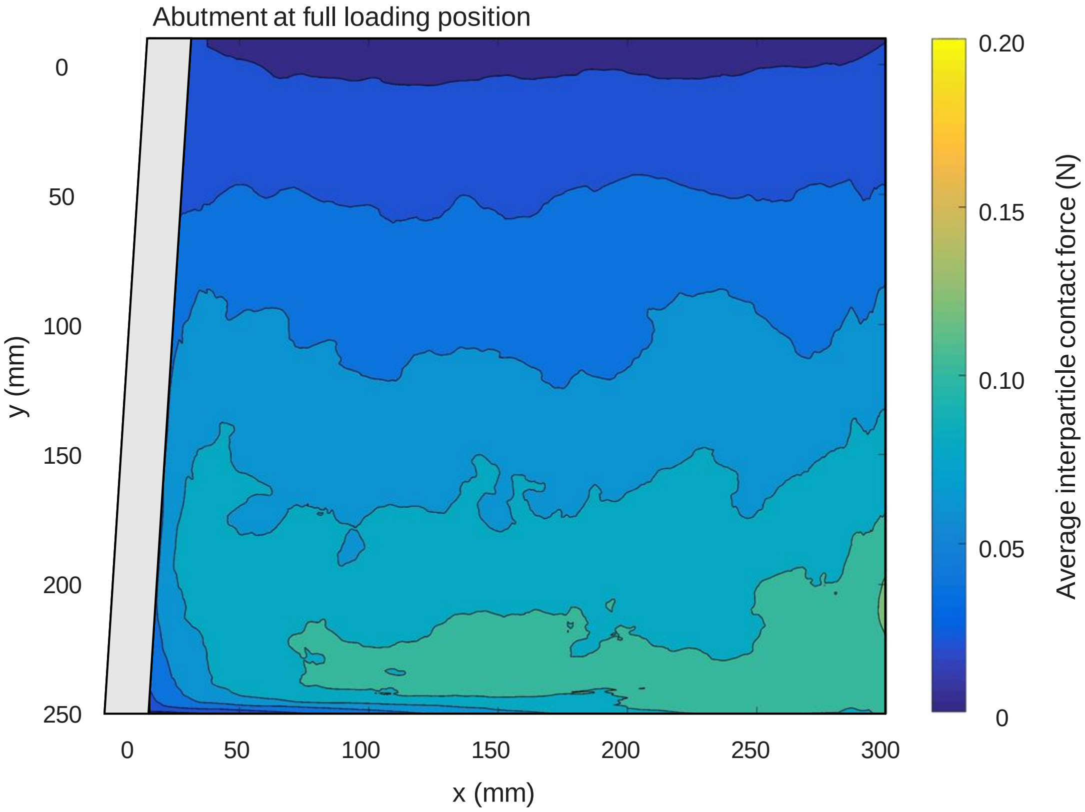

Figure 4.50: Contact force distribution in cubes after last cycle

Illustrations of the cubes from the first and last cycles are shown in Figure 4.51 and 4.52 respectively. The figures depict the packing of the cubes with a few key zones highlighted. The first figure shows the particles with random orientations, which resulted in large forces in the granular backfill, but lower forces on the abutment. Figure 4.52 presents a few of the zones where cubes which started with random orientations eventually re-orientated to come together after a number of cycles to form intact groups of cubes acting as a unit. This resulted in a stiffer matrix in the backfill and is suggested to be one of the causes of the larger forces acting on the abutment with increasing cycles.

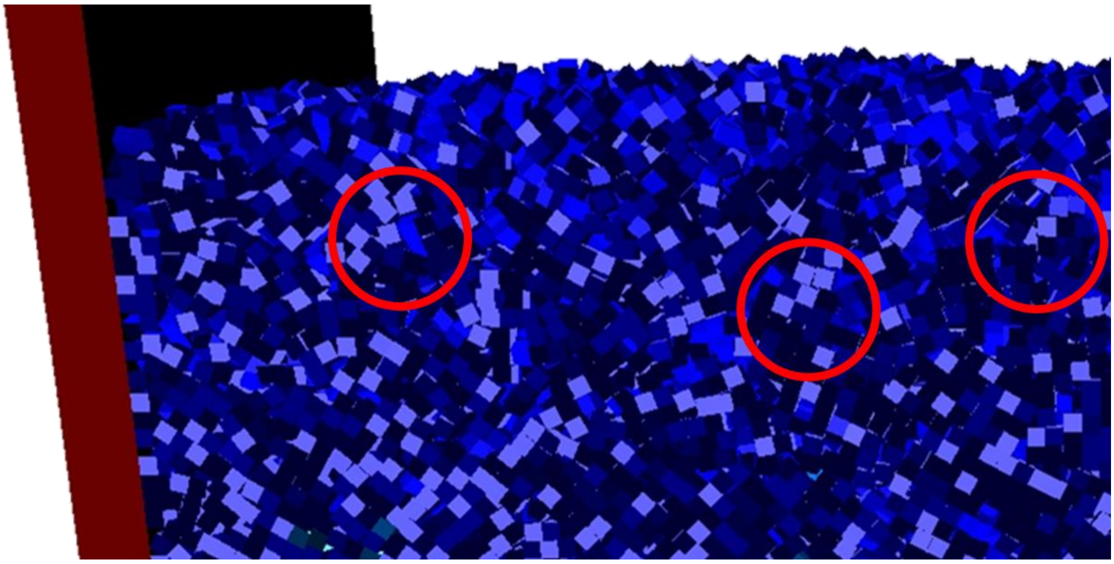

Figure 4.51: Cubes from medium abutment model after first cycle in Blaze-DEM

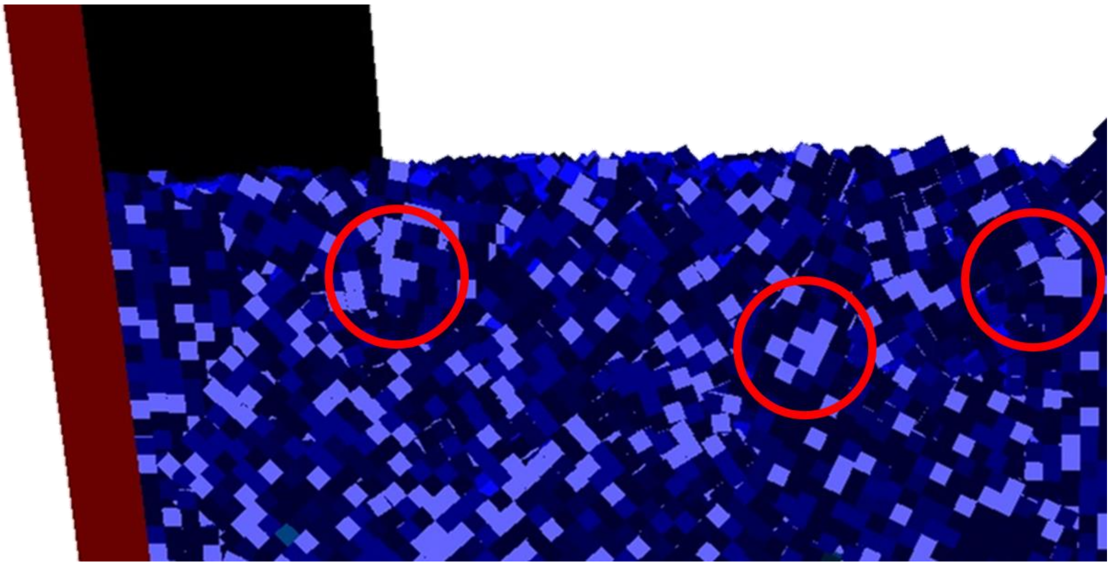

Figure 4.52: Cubes from medium abutment model after last cycle in Blaze-DEM

4.6.6 Force chain magnitudes

The force chain magnitudes were investigated for the six particle shapes modelled in the numerical sensitivity analysis. The force chains were obtained for the entire granular backfill domain for each of the shapes. The domain was split into quartiles to study the behaviour of the force chains for the different particle shapes.

The force chain magnitudes for the spheres, cubes, triangular prisms and tetrahedrons are considered in this section. These four shapes were selected since they were assumed to adequately cover the range of particle sphericities investigated. Figure 4.53 illustrates the force chain magnitudes for the four particle shapes. The figure shows a top view of the medium abutment model. This is shown when the abutment was at its fully loaded position in the passive direction after the last cycle. The figure also indicates the directions of the forces in the backfill.

Figure 4.53 indicates that the spheres' force chain magnitudes were small compared to the convex polyhedra shapes. The force chain magnitudes in the spheres were relatively constant throughout the entire backfill. These results indicate that when the spheres were loaded, the forces were relatively evenly distributed to the majority of the backfill domain.

An analysis of the force chain results with respect to sphericity indicates that as a particle's sphericity decreases, the magnitudes of the force chains acting near the imposed loading increases for all particle shapes except for cubes. The cubes experienced larger force chain magnitudes than the less spherical triangular prisms in the first quartile. The tetrahedrons, which are the least spherical, experienced the largest force chains in the first quartile. The cubes resulted in the largest forces which acted directly on the model abutment, which was also observed in the lateral earth pressure coefficient investigations.

The results from the force chain analysis were in line with the investigation performed on the spatial density distributions. These results indicated that the particles with higher sphericities underwent movements over larger domains i.e. movements were more globalised. This meant that relatively constant forces were present within the entire backfill region. The particles with lower sphericities experienced movements that were mainly restricted close to the abutment i.e. movements were more localised. This indicated that much larger forces acted on the abutment than in the backfill region further away from it.

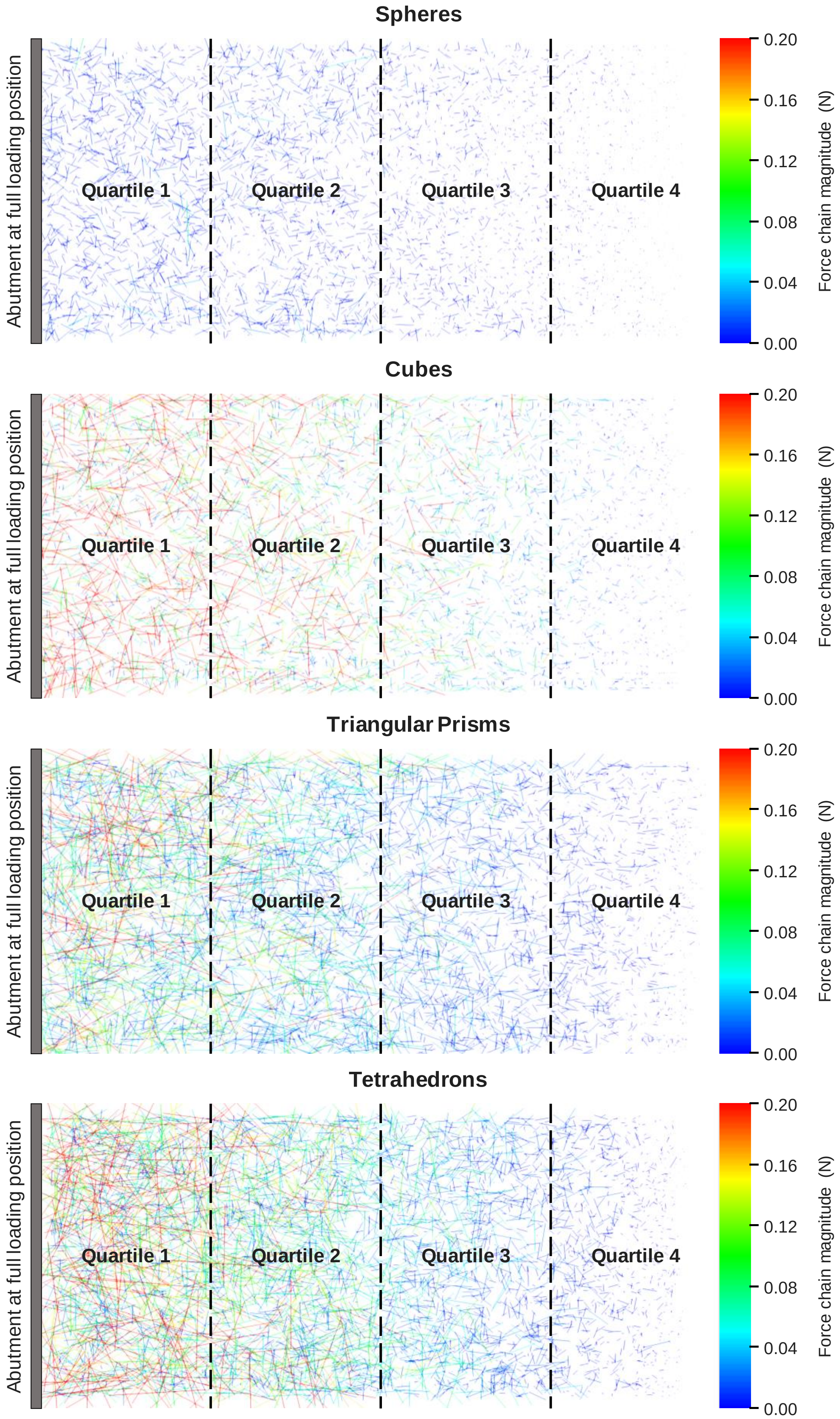

Figure 4.53: Force chain magnitudes observed in selected particle shapes

4.7 SUMMARY

The Discrete Element Method was used to perform a numerical sensitivity analysis investigating the effect of granular particle shape on the response of backfill retained by integral bridge abutments. A total of six particle shapes were modelled, namely spheres and the following convex polyhedra shapes: dodecahedrons, truncated tetrahedrons, tetrahedrons, triangular prisms and cubes. The shapes of the particles were classified by their sphericities. The spheres had the highest sphericity (lowest angularity) of 1.0, while the tetrahedrons had the lowest sphericity (highest angularity) of 0.671. The granular backfill was subjected to cyclic loading to study the effect of these shapes on the bulk densities, the lateral earth pressure coefficients, the particle settlements, the horizontal stress distributions, the mean interparticle contact forces and the force chains in the backfill.

The DEM particles required calibration of the particle-particle friction coefficient to perform the simulations. Drop tests with only gravitational loads were performed, as proposed by Coetzee (2017), on the spherical particles until a desired angle of repose of 33° was obtained. A coefficient value of 0.45 was found to yield this angle of repose. These drop tests were performed in STAR-CCM+ using multi-sphere models.

Drop tests were performed with the six particle shapes in Blaze-DEM using single particles. The resulting angles of repose were not suggested to be an accurate representation of the true value of the particles' angles of repose. Instead, they were used to investigate the variation between the angles of repose for the six particle shapes modelled.

The particle's Young's Modulus value was reduced to speed up the computational times of the DEM simulations, as suggested by Coetzee (2016). Verification tests were performed to determine the extent to which the value could be reduced. The Young's Modulus was reduced from a theoretical value of 70 GPa to a value of 70 MPa (reduction factor of 1 000), to obtain computational times 32.9 times faster than the theoretical value, while still yielding relatively accurate results. These results were almost identical to the results obtained by Xu *et al.* (2002), where the same theoretical value of 70 GPa was also successfully reduced by a factor of 1 000 to obtain simulation times 31.6 times faster.

Two software packages were used for the study, namely STAR-CCM+ and Blaze-DEM. A comparison between the two software packages revealed that Blaze-DEM could offer computational times over 150 times faster than STAR-CCM+. This was due to the different computational methods used for the two packages. Blaze-DEM uses the computational capabilities of a Graphics Processing Unit, whereas STAR-CCM+ makes use of the Central Processing Unit (Govender, 2015). Hence, the numerical sensitivity analysis was performed using Blaze-DEM.

The bulk densities, lateral earth pressure coefficients, particle settlements, horizontal stress distributions, mean interparticle contact forces and force chains in the granular backfill were investigated for the six selected particle shapes.

The results from the investigations indicated that the magnitudes of the initial bulk densities were related to the sphericities of the particles used as backfill. The degree of densification, however, was more closely related to the average AoR of the backfill material than its sphericity. Particles with higher average AoRs experienced larger degrees of densification.

The results from the spatial density distribution and force chain analyses indicated that the particle shapes with higher sphericities experienced movements and densifications over a larger domain. The particle shapes with lower sphericities underwent larger movements and densifications near the abutment which was cyclically loaded into the backfill, i.e. movements that were more localised.

It was found that the magnitudes of the lateral earth pressure coefficients and backfill settlements were linearly related to the average AoR of the material. The particles with higher average AoRs resulted in larger earth pressure coefficients and settlements. It was also found that the build-up in earth pressure coefficients and settlements was highly linearly related to the sphericity of the particle used as backfill. The particle shapes with lower sphericities resulted in larger increases in earth pressure coefficients and settlements.

The results from the horizontal stress distribution and mean interparticle contact force analyses indicated that particle reorientation, especially for the particles with lower sphericities, played a significant role in the build-up of stresses acting on the abutment. It was found that for the particle shapes with higher sphericities, less particle interlocking and reorientation was possible and the backfill consequently maintained similar packings. This is in line with suggestions made by Höhner *et al.* (2012), Govender *et al.* (2014) and Azéma *et al.* (2009), that the shape of a particle plays a significant role in the behaviour of granular materials.

The results from the numerical sensitivity analysis indicated that the sphericity of the particle plays a key role in the accumulation of stresses in granular backfill retained by integral bridge abutments subjected to cyclic thermal loading. It was found that for particle shapes with higher sphericities, the magnitudes of stresses and the resulting build-up of stresses were less than that for the particles with lower sphericities.

The numerical sensitivity analysis results also indicated that the slight accumulation of stress observed in the particles with higher sphericities was primarily due to the densification of the particles. However, the larger stress accumulations observed in the shapes with lower sphericities is suggested to be a result of not only densification, but also a result of particle reorientation and interlocking.

5 CONCLUSIONS AND RECOMMENDATIONS

This chapter contains the conclusions derived from the various Discrete Element Method (DEM) simulations performed in this study. The recommendations made for further research are also provided. The conclusions presented are derived from the following:

- The drop tests performed in STAR-CCM+ used to calibrate the particle-particle friction coefficient of the DEM particles.
- The drop tests performed in Blaze-DEM to investigate the effect of a particle's sphericity on its angle of repose.
- The tests performed to verify the reduction of the Young's Modulus value to speed up the computational times of the DEM simulations.
- The tests performed to compare the results obtained from STAR-CCM+ and Blaze-DEM.
- The tests used to verify the particle size and number of particles used in the DEM simulations.
- The numerical sensitivity analysis performed to investigate the effect of granular particle shape on the response of backfill retained by integral bridge abutments.

5.1 CONCLUSIONS FROM CALIBRATION TESTS

The DEM particles were calibrated by performing drop tests in STAR-CCM+ with only gravitational loads. As suggested by Nakashima *et al.* (2011) and Coetzee (2016), the particle-particle friction coefficient, as well as the number of sphere-clumps, were changed until a desired angle of repose was obtained. When using spheres, it was found that a friction coefficient of 0.45 would result in an angle of repose of 33°. It was also found that higher coefficients or more sphere-clumps increased the resulting angle of repose. These results were comparable to those obtained by Coetzee (2016).

The results of the drop tests performed in Blaze-DEM, with the six particle shapes, indicated that the angle of repose of a particle increases as its sphericity decreases. Based on the drop tests performed in Blaze-DEM, it is suggested that performing these tests using single particles does not provide an accurate representation of the particles' true angles of repose or internal friction angles. The single particles did not form a heap of particles as required for the drop tests. However, it does provide a range of values within which the true angle of repose is expected to be.

The Young’s Modulus of the DEM particles was reduced to speed up the computational times as proposed by Coetzee (2016). A theoretical value of 70 GPa was reduced by factors of 100, 1 000 and 10 000 i.e. to values of 7 MPa, 70 MPa and 700 MPa. Verification tests were performed to determine which of the values would still yield realistic results. It was found that 70 MPa (reduction factor of 1 000) was the lowest Young’s Modulus value which would still deliver sufficiently accurate results. The results analysed included the lateral earth pressures, the densities and overlap with depth and the normal overlaps between the particles of the granular backfill.

The Young’s Modulus value of 70 MPa yielded simulation times 32.9 times faster than the particles with a theoretical value of 70 GPa. These results were comparable to the time reduction factor of 31.6 obtained by Xu *et al.* (2002) when applying the same reduction factor to 70 GPa particles.

5.2 CONCLUSIONS FROM VERIFICATION TESTS

Two DEM software packages were compared for this study, namely STAR-CCM+, a commercial code, and Blaze-DEM, a research code under development at the University of Pretoria, created by Govender (2015). The primary difference between the software suites is the computing methods. STAR-CCM+ makes use of the traditional method of using a Central Processing Unit (CPU), while Blaze-DEM uses the Graphics Processing Unit (GPU). Using the GPU to perform DEM simulations results in an elevated level of performance and it was found that Blaze-DEM could offer computational times over 150 times faster for the equivalent simulation in STAR-CCM+. This increase in computational ability now enables the possibility of parameter studies to be performed using DEM simulations.

A test was performed in Blaze-DEM to determine the size of the spherical particles required to accurately model granular behaviour behind integral bridge abutments. Coetzee (2016) stated that the computational time required for a DEM simulation is inversely proportional to the diameter of the spheres used in the simulation. The diameters were therefore required to be as large as possible to reduce the computational times. It was found that spheres with diameters of up to 5 mm could be used to accurately model the behaviour of granular backfill retained by integral bridge abutments, for the geometric and imposed loading conditions used in this study.

Blaze-DEM was also used to determine how many particles would be required to accurately model the behaviour of granular backfill retained by integral bridge abutments. The timestep used for a DEM simulation is directly proportional to the number of particles used in the simulation (Coetzee, 2016). Therefore, the number of particles were required to be as low as possible to have practical computational times. It was found, for the geometry and imposed loads used in this study, that at least 140 000 spherical particles, with diameters of 5 mm, would be sufficient to accurately model granular material behaviour behind integral bridge abutments.

5.3 CONCLUSIONS FROM NUMERICAL SENSITIVITY ANALYSIS

A numerical sensitivity analysis was performed, using DEM simulations, to investigate the effect of granular particle shape on the response of backfill retained by integral bridge abutments. The backfill was subjected to cyclic thermal displacements of a model integral bridge abutment. The shapes modelled included spheres and the following convex polyhedra shapes: dodecahedrons, truncated tetrahedrons, tetrahedrons, triangular prisms and cubes.

The bulk densities, the lateral earth pressure coefficients, the particle settlements, the horizontal stress distributions, the mean interparticle contact forces and the force chains in the granular backfill were investigated for the six selected particle shapes. The values of the parameters were compared to the respective particles' sphericities and average angles of repose. The sphericities were calculated as proposed by Wadell (1935) and the average angles of repose were calculated from the upper and lower bounds obtained from the drop tests performed in Blaze-DEM.

The results from the investigations showed that the particle shapes with lower sphericities (higher angularities) underwent larger movements and densifications that were localised near the abutment which was cyclically displaced into the backfill. However, the particle shapes with higher sphericities (lower angularities) experienced movements and densifications over larger domains within the granular backfill.

It was found that the magnitudes of the initial bulk densities were related to the sphericities of the particles used as backfill. The particle shapes with higher sphericities resulted in lower bulk density magnitudes. The degree of densification of the particles due to imposed loading was more closely related to the average angle of repose of the backfill material than its sphericity. The particle shapes with higher average angles of repose experienced larger degrees of densification.

The magnitudes of the lateral earth pressure coefficients and backfill settlements were found to be correlated to the average angle of repose of the material. The particle shapes with lower average angles of repose resulted in lower values of earth pressure coefficients and settlements. The results indicated that the magnitudes of the build-up in earth pressure coefficients and settlements were more closely related to the sphericity of the particle used as backfill than its average angle of repose. The particle shapes with lower sphericities (higher angularities) underwent larger accumulations of earth pressures and settlements. These results were in line with the suggestion made by Xu *et al.* (2007), that the shape of a particle, specifically its sphericity, of the granular backfill plays a significant role in the lateral earth pressure build-up behind integral bridge abutments.

The analyses of results of the mean interparticle contact forces and horizontal stress distributions indicate that the larger build-up of horizontal stresses observed with the particles with lower sphericities was due to densification as well as particle reorientation. However, the smaller accumulations of horizontal stresses observed in the particles with higher sphericities were primarily due to densification.

When subjected to cyclic imposed loading, particle shapes with higher angularities (lower sphericities) could experience physical mechanisms which resulted in redistribution of the forces within the system of particles. This resulted in large stress accumulations acting on the integral bridge abutment as the number of loading cycles increased. These mechanisms were interlocking between the particles or particle reorientation.

It was less likely that the particle shapes with higher sphericities could interlock with one another or re-orientate themselves. This was suggested to be a result of these shapes having more spherical (smoother) edges as opposed to the less spherical (more angular) shapes which had edges with sharper angles. Smaller accumulations of stresses were therefore present on the abutment for the shapes with higher sphericities.

It was therefore found that the sphericity of the particle shapes used as backfill has a significant impact on the accumulation of stresses acting on integral bridge abutments subjected to cyclic thermal loading. A slight accumulation of stress was observed in the particles with higher sphericities, which was a result of primarily densification of the particles. However, the larger stress accumulations observed in the shapes with higher angularities is suggested to be a result of not only densification, but also a result of particle interlocking and reorientation.

5.4 RECOMMENDATIONS

The following recommendations are made for further work:

- More cycles should be imposed on the backfill to better represent the daily and seasonal temperature variations over a longer period.
- Larger models of the granular backfill should be used to model a greater portion of the backfill.
- Granular particles with varying material properties should be tested to obtain a broader range of results for the sensitivity analysis.

- Young’s Modulus values with smaller reduction factors could be used for the particles to obtain results with greater accuracies.
- Physical experiments should be performed under similar conditions to the DEM simulations to validate the results of the numerical modelling.
- Data from existing integral bridges of the variation of pressures acting on the abutments should be obtained, specifically, the Van Zylspruit Bridge in South Africa monitored by Skorpen *et al.* (2016), to compare with the results of the numerical modelling.
- Optimisation studies should be performed to better understand the effect of the number of particles and particle sizes used to model the behaviour of granular backfill retained by integral bridge abutments when using DEM simulations.
- A greater variety of particle shapes could be used to obtain a larger range of results for the sensitivity analysis.
- Direct shear tests should be performed on the various single particle shapes to obtain a better representation of their internal friction angles. These friction angles could then be used to calculate theoretical lateral earth pressure coefficients for the convex polyhedra shapes.
- The equivalent sphere-clumped shapes of the convex polyhedra particles tested should be used to better understand the effect of angularity and sphericity in DEM simulations.
- Non-convex polyhedra could also be used as granular backfill retained by the abutment models. A non-convex polyhedron has the property that when a line is constructed between any two points in the shape, the full length of the line segment joining them might not be contained within the polyhedron. These shapes could result in greater interlocking mechanisms between the particles and may result in further stress accumulations as opposed to the convex polyhedra shapes.

6 REFERENCES

Azéma, E. Radjai, F. Peyroux, R. and Saussine, G. 2009. Influence of particle shape on shear stress in granular media. *Traffic and Granular Flows, Paris, France*. p497-505.

Barker, K. J. and D. R. Carder. 2001. *Performance of an integral bridge over the M1- A1 Link Road at Bramham Crossroads*. Highway Agency, Transport Research Laboratory, Crowthorne, Berks. TRL Report TRL521.

Biddle, A. R., Iles, D. C. and Yandzio, E. D. 1997. Integral steel bridges: *Design guidance, Publication* No. P163. Ascot: Steel Construction Institute.

Bloodworth, A., Xu, M., Banks, J. and Clayton, C. 2012. Predicting the Earth Pressure on Integral Bridge Abutments. *J. Bridge Eng*., 17(2), pp.371-381.

Boac, J., Ambrose, R., Casada, M., Maghirang, R. and Maier, D. 2014. Applications of Discrete Element Method in Modeling of Grain Postharvest Operations. *Food Engineering Reviews*, 6(4), pp.128-149.

Breña, S., Bonczar, C., Civjan, S., DeJong, J. and Crovo, D. 2007. Evaluation of Seasonal and Yearly Behavior of an Integral Abutment Bridge. *Journal of Bridge Engineering*, 12(3), pp.296-305.

Brookes, C. 2010. Application of the finite/Discrete Element Method to arches. *Proceedings of the Institution of Civil Engineers, Engineering and Computational Mechanics* 163(3): 203–211.

Clayton, C., Xu, M. and Bloodworth, A. 2006. A laboratory study of the development of earth pressure behind integral bridge abutments. *Géotechnique*, 56(8), pp.561-571.

Cleary, P. 2010. DEM prediction of industrial and geophysical particle flows. *Particuology*, 8(2), pp.106-118.

Cleary, P. and Sawley, M. 2002. DEM modelling of industrial granular flows: 3D case studies and the effect of particle shape on hopper discharge. *Applied Mathematical Modelling*, 26(2), pp.89-111.

Coetzee, C. 2016. Calibration of the Discrete Element Method and the effect of particle shape. *Powder Technology*, 297, pp.50-70.

Coetzee, C. 2017. Review: Calibration of the Discrete Element Method. *Powder Technology*, 310, pp.104-142.

Cosgrove, E.F., and Lehane, B.H. 2003. Cyclic loading of loose backfill placed adjacent to integral bridge abutments. *International Journal of Physical Modelling in Geotechnics*, 3(3): 9–16.

Cundall, P. 1988. Formulation of a three-dimensional distinct element model—Part I. A scheme to detect and represent contacts in a system composed of many polyhedral blocks. *International Journal of Rock Mechanics and Mining Sciences and Geomechanics Abstracts*, 25(3), pp.107-116.

Cundall, P. A. and Strack, O. D. L. 1979. A discrete numerical model for granular assemblies, *Geotechnique*, 29, pp. 47-65.

Derakhshani, S., Schott, D. and Lodewijks, G. 2015. Micro–macro properties of quartz sand: Experimental investigation and DEM simulation. Powder Technology, 269, pp.127-138.

EDEM, DEM Solutions Ltd., 2017. *User's Guide*, Version 2.7, Edinburgh, UK.

Emerson, M. 1976. *Bridge temperatures estimated from the shade temperature*. 1st ed. Crowthorne, Berks: Bridge Construction Division, Structures Department, Transport and Road Research Laboratory.

England, G.L., Tsang, C.M., and Bush, D. 2000. Integral bridges— A fundamental approach to the time temperature loading problem. *Thomas Telford*, London.

Feng, Y. and Loughran, J. 2009. On upscaling of discrete element models: similarity principles. *Engineering Computations*, 26(6), pp.599-609.

Goh, D. 2001. *The behavior of shallow abutments of integral bridges.* PhD thesis. University of Birmingham, Edgbaston, Birmingham, UK.

Govender, N. 2015. *Blaze-DEM: A GPU based large scale 3D discrete element particle transport framework.* PhD thesis. University of Pretoria.

Govender, N., Rajamani, R., Kok, S. and Wilke, D. 2015. Discrete element simulation of mill charge in 3D using the BLAZE-DEM GPU framework. *Minerals Engineering*, 79, pp.152-168.

Govender, N., Wilke, D. and Kok, S. 2015. Collision detection of convex polyhedra on the NVIDIA GPU architecture for the discrete element method. *Applied Mathematics and Computation*, 267, pp.810-829.

Govender, N., Wilke, D. and Kok, S. 2016. Blaze-DEMGPU: Modular high performance DEM framework for the GPU architecture. *SoftwareX*, 5, pp.62-66.

Govender, N., Wilke, D., Kok, S. and Els, R. 2014. Development of a convex polyhedral discrete element simulation framework for NVIDIA Kepler based GPUs. *Journal of Computational and Applied Mathematics*, 270, pp.386-400.

Harada T. 2008. GPU Gems 3: *Real-time rigid body simulation on GPUs*, Vol. 3.

Härtl, J. and Ooi, J. 2008. Experiments and simulations of direct shear tests: porosity, contact friction and bulk friction. *Granular Matter*, 10(4), pp.263-271.

Highway Agency, 2003. The Design of integral bridges. *Design Manual for Roads and Bridges (DMRB)/ BA42*, HMSO, London. 1, Section 3, part 12.

Hlungwani, O., Rikhotso, J., Dong, H. and Moys, M. 2003. Further validation of DEM modeling of milling: effects of liner profile and mill speed. *Minerals Engineering*, 16(10), pp.993-998.

Höhner, D., Wirtz, S. and Scherer, V. 2012. A numerical study on the influence of particle shape on hopper discharge within the polyhedral and multi-sphere discrete element method. *Powder Technology*, 226, pp.16-28.

Höhner, D., Wirtz, S. and Scherer, V. 2014. A study on the influence of particle shape and shape approximation on particle mechanics in a rotating drum using the discrete element method. *Powder Technology*, 253, pp.256-265.

Jae Lee S. 2014. *Developments in large scale discrete element with polyhedral particles simulations.* PhD thesis. University of Illinois.

Khodair, Y. 2009. Lateral earth pressure behind an integral abutment. *Structure and Infrastructure Engineering*, 5(2), pp.123-136.

Kloss, C., Goniva, C., Hager, A., Amberger, S. and Pirker, S. 2012. Models, algorithms and validation for opensource DEM and CFD-DEM. *Progress in Computational Fluid Dynamics, An International Journal*, 12(2/3), p.140.

Lehane, B. 2011. Lateral soil stiffness adjacent to deep integral bridge abutments. *Géotechnique*, 61(7), pp.593-603.

Lim, W. and McDowell, G. 2005. Discrete element modelling of railway ballast. *Granular Matter*, 7(1), pp.19-29.

Lommen, S., Schott, D. and Lodewijks, G. 2014. DEM speedup: Stiffness effects on behavior of bulk material. *Particuology*, 12, pp.107-112.

Longmore, J., Marais, P. and Kuttel, M. 2013. Towards realistic and interactive sand simulation: A GPU-based framework. *Powder Technology*, 235, pp.983-1000.

Lu Y, Frost D. 2010. Three-dimensional DEM modelling of triaxial compression of sands. *Soil behavior and geo-micromechanics* (GSP 200), ASCE; p. 220–6.

Lu, N. and Likos, W. 2004. *Unsaturated soil mechanics*. Hoboken, N.J.: Wiley.

M. Hu, C. O’Sullivan, R.R. Jardine, and M. Jiang. 2010. Study on the deformation of loose sand under cyclic loading by DEM simulation. In R. Meier, A. Abbo, and L. Wang, editors, *Soil Behavior and Geo-Micromechanics*, pages 212–219. American Society of Civil Engineers.

Mourad, S. and Tabsh, S. 1999. Deck Slab Stresses in Integral Abutment Bridges. *Journal of Bridge Engineering*, 4(2), pp.125-130.

Movahedifar, M. and Bolouri-Bazaz, J. 2014. An investigation on the effect of cyclic displacement on the integral bridge abutment. *Journal of Civil Engineering and Management*, 20(2), pp.256-269.

Nakashima, H., Shioji, Y., Kobayashi, T., Aoki, S., Shimizu, H., Miyasaka, J. and Ohdoi, K. 2011. Determining the angle of repose of sand under low-gravity conditions using Discrete Element Method. *Journal of Terramechanics*, 48(1), pp.17-26.

Neubauer G, Radek CA. 2014. GPU based particle simulation framework with fluid coupling ability, *NVIDIA GTC 2014*, San Jose, USA,

Ng, C.W.W., Springman, S.M., and Norrish, A.R.M. 1998. Centrifuge modelling of spread-base integral bridge abutments. *Journal of Geotechnical and Geoenvironmental Engineering, ASCE*, 124(5): 376–388.

Obermayr, M., Vrettos, C., Eberhard, P. and Däuwel, T. 2014. A discrete element model and its experimental validation for the prediction of draft forces in cohesive soil. *Journal of Terramechanics*, 53, pp.93-104.

Roeder, C. 2003. Proposed Design Method for Thermal Bridge Movements. *Journal of Bridge Engineering*, 8(1), pp.12-19.

Skorpen, S., Kearsley, E., Clayton, C. and Kruger, E. 2016. The Initial Environmental Effects on the Design of a 90m Long Integral Bridge in South Africa. In: *FIB symposium 2016 Performance-Based Approaches for Concrete Structures*.

Springman, S.M., Norrish, A., and Ng, C.W.W. 1996. Cyclic loading of sand behind integral bridge abutments. *Transport Research Laboratory*, Crowthorne, Berkshire, UK. TRL Report 146.

STAR-CCM+, Siemens Product Lifecycle Management Software Inc, 2017. *User's Guide*, Version 12.04, Melville, NY.

Tapper, L., and Lehane, B.M. 2004. Lateral stress development on integral bridge abutments. In *Proceedings of the 18th Australasian Conference on the Mechanics of Structures and Materials*, Perth, Australia, 1–3 December 2004. Taylor and Francis, London. Vol. 2, pp. 1069–1075.

Venugopal, R. and Rajamani, R. 2001. 3D simulation of charge motion in tumbling mills by the discrete element method. *Powder Technology*, 115(2), pp.157-166.

Wadell, H. 1935. Volume, Shape, and Roundness of Quartz Particles. *The Journal of Geology*, 43(3), pp.250-280.

Wesseloo, J. 2004. *The strength and stiffness of geocell support packs*. PhD thesis. University of Pretoria, South Africa.

Widulinski, L., Kozicki, J. and Tejchman, J. 2010. Comparative Modeling of Shear Localization in Granular Bodies with FEM and DEM. *GeoShanghai 2010 International Conference, Soil Behavior and Geo-Micromechanics*, pp. 198-203.

Wood, D.M. 2004. *Geotechnical Modelling*. Spon Press, Taylor and Francis Group, London and New York.

Xu, M. 2005. *The Behaviour of Soil behind Full-height Integral Abutments.* PhD thesis. University of Southampton.

Xu, M., Clayton, C. and Bloodworth, A. 2007. The earth pressure behind full-height frame integral abutments supporting granular backfill. *Canadian Geotechnical Journal*, 44(3), pp.284-298.

Xu, Y., Kafui, K., Thornton, C. and Lian, G. 2002. Effects of Material Properties on Granular Flow in a Silo Using DEM Simulation. *Particulate Science and Technology*, 20(2), pp.109-124.

Yan, Z., Wilkinson, S., Stitt, E. and Marigo, M. 2015. Discrete element modelling (DEM) input parameters: understanding their impact on model predictions using statistical analysis. *Computational Particle Mechanics*, 2(3), pp.283-299.

Yap, FL. 2001. *The Application of the Discrete Element Method to Integral Bridge Backfill*. PhD thesis. University of Southampton.

APPENDIX A

ADDITIONAL BULK DENSITY GRAPHS

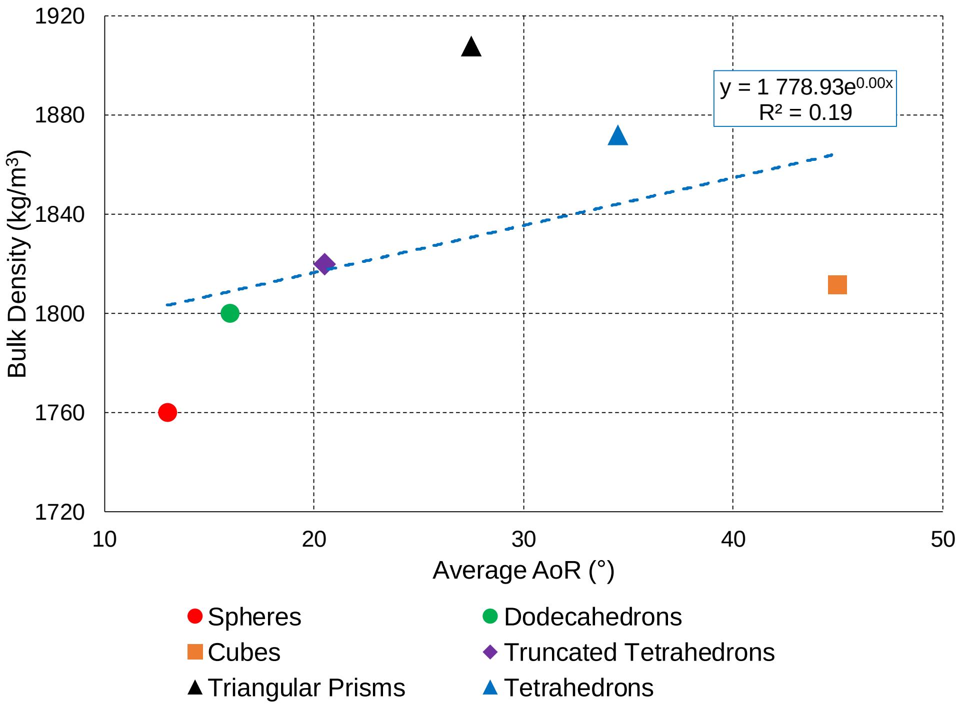

Figure A.1: Effect of average AoR on initial bulk density

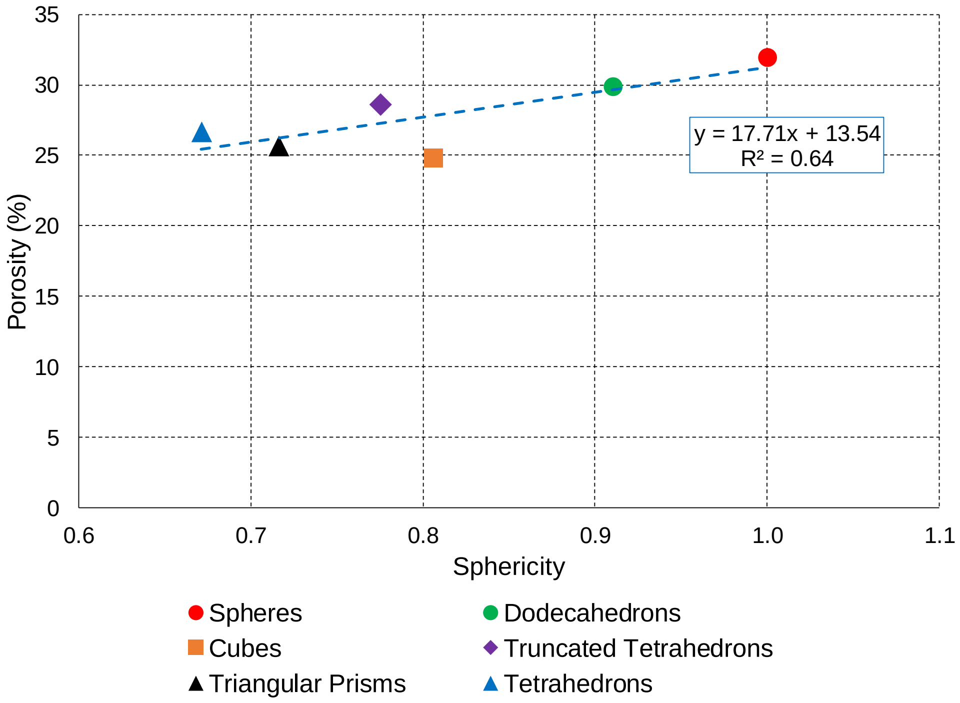

Figure A.2: Effect sphericity on final porosity

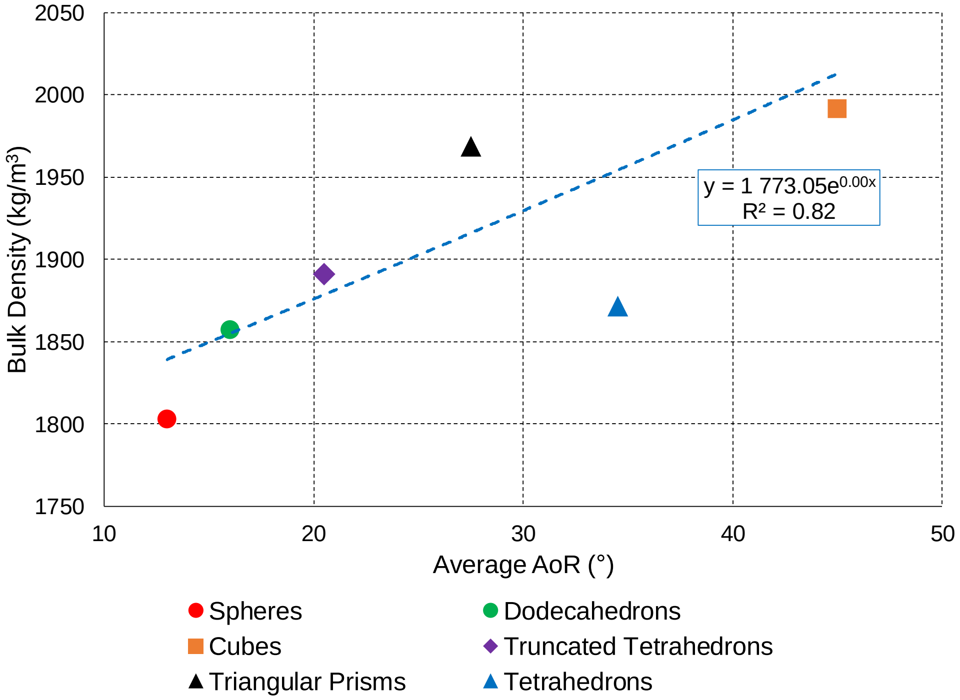

Figure A.3: Effect of average AoR on final bulk density

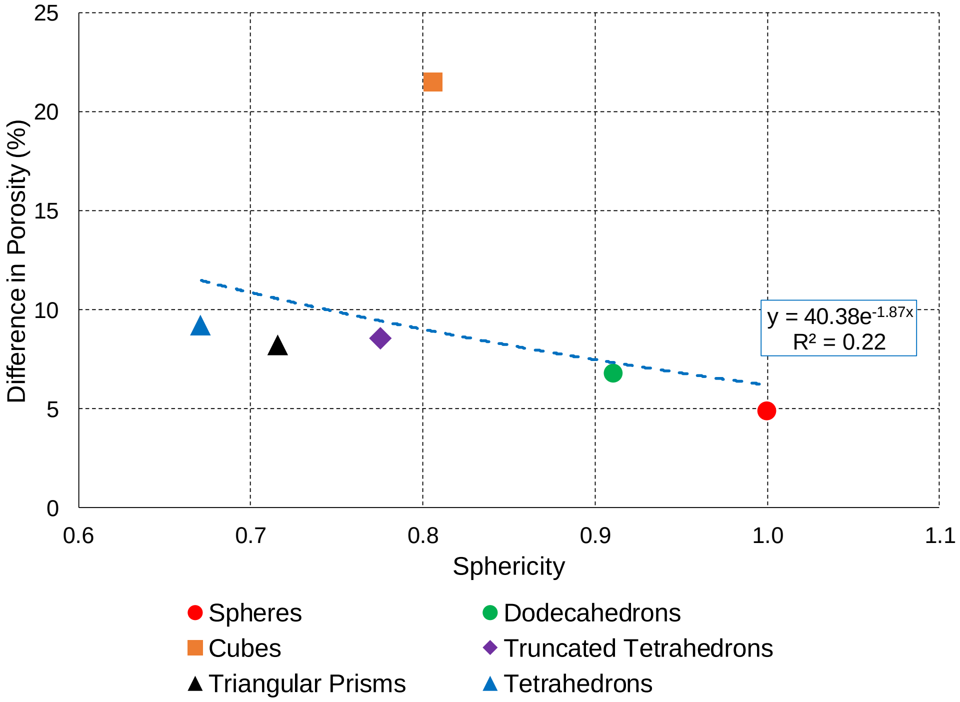

Figure A.4: Effect of sphericity on difference in porosity

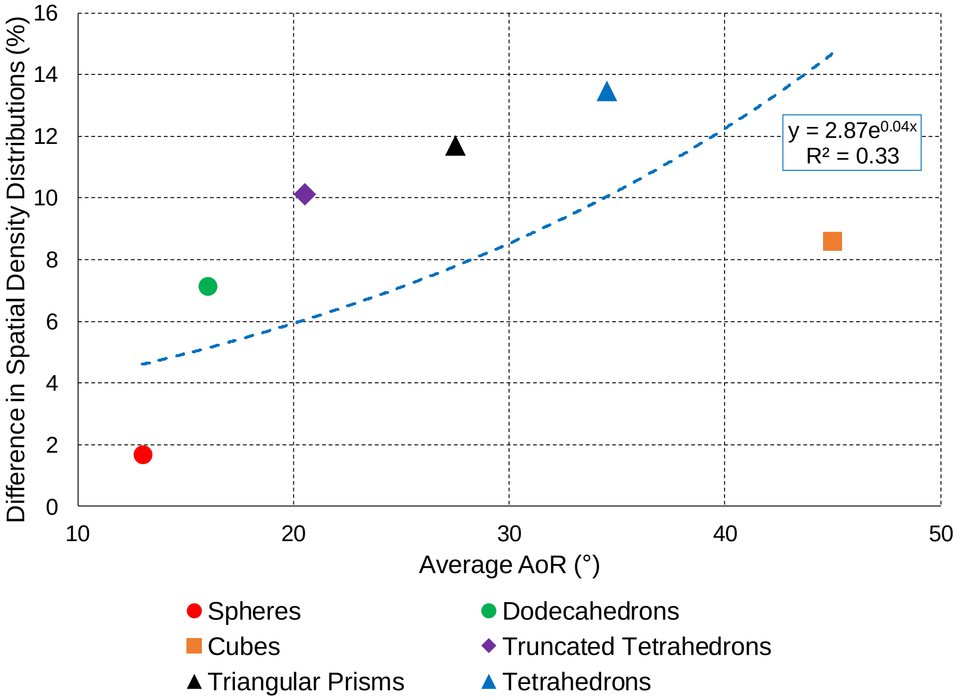

Figure A.5: Effect of average AoR on difference in spatial density distributions

APPENDIX B

ADDITIONAL EARTH PRESSURE GRAPHS

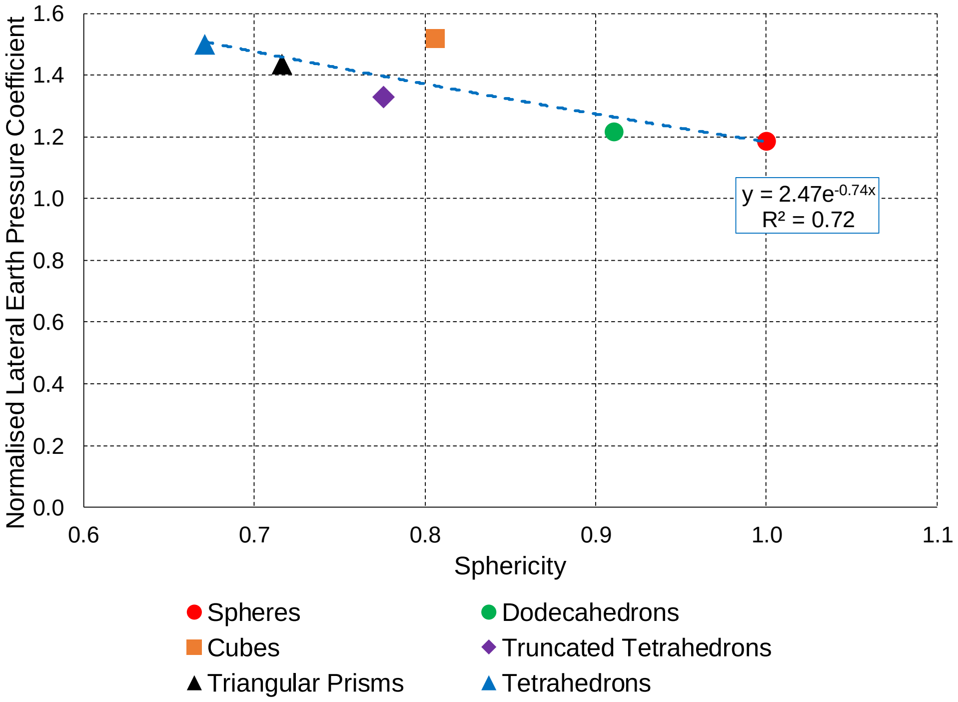

Figure B.1: Effect of sphericity on initial lateral earth pressure coefficients

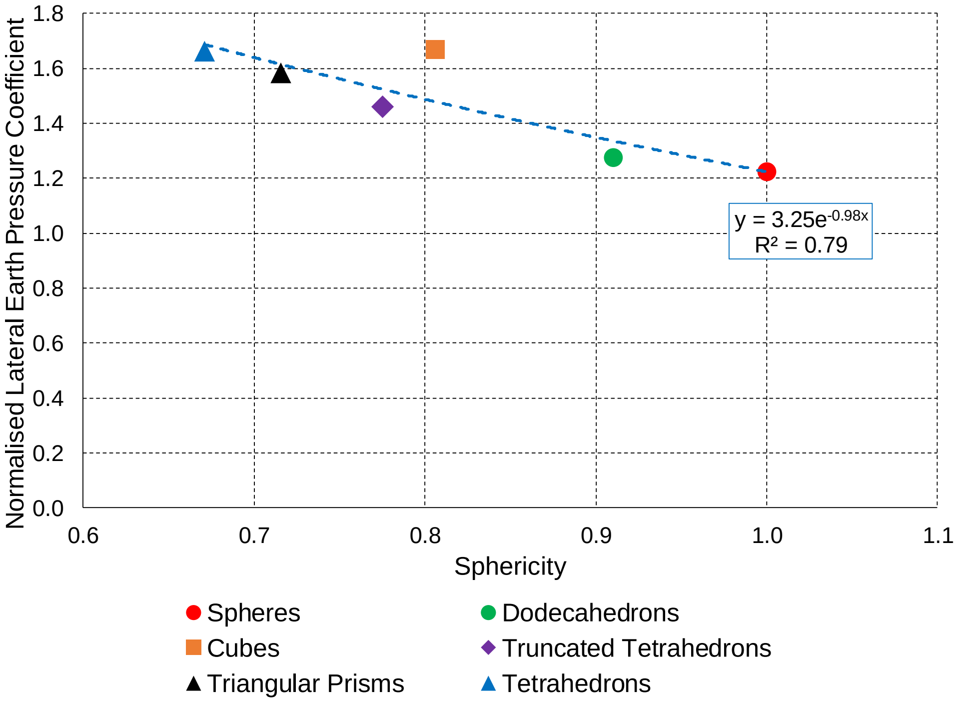

Figure B.2: Effect of sphericity on final lateral earth pressure coefficients

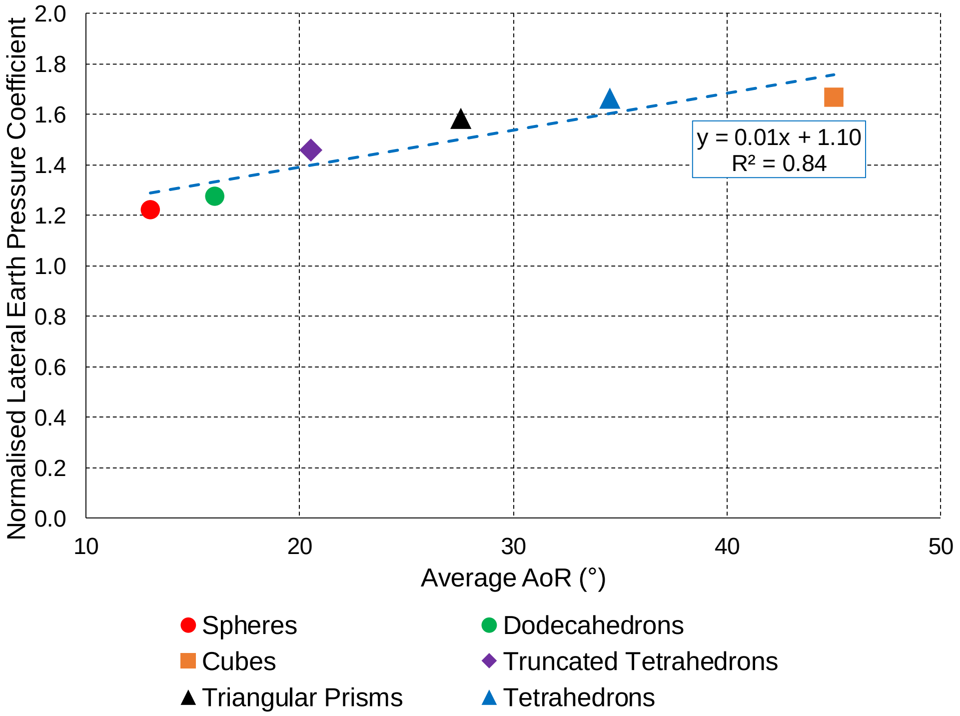

Figure B.3: Effect of average AoR on final lateral earth pressure coefficients

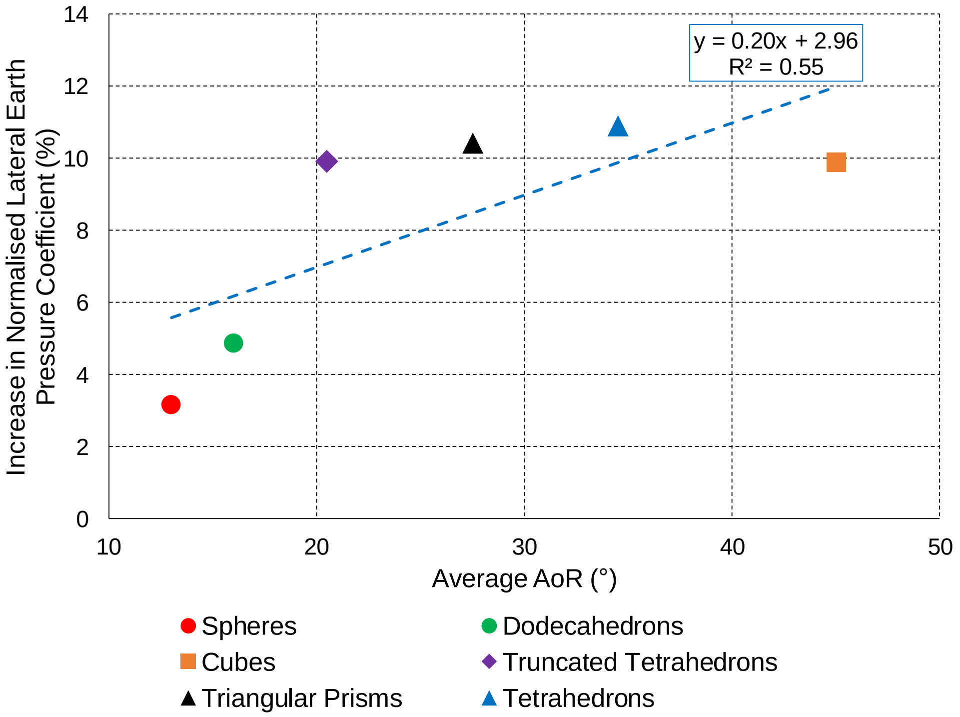

Figure B.4: Effect of average AoR on increase in lateral earth pressure coefficients

APPENDIX C

ADDITIONAL SETTLEMENT GRAPHS

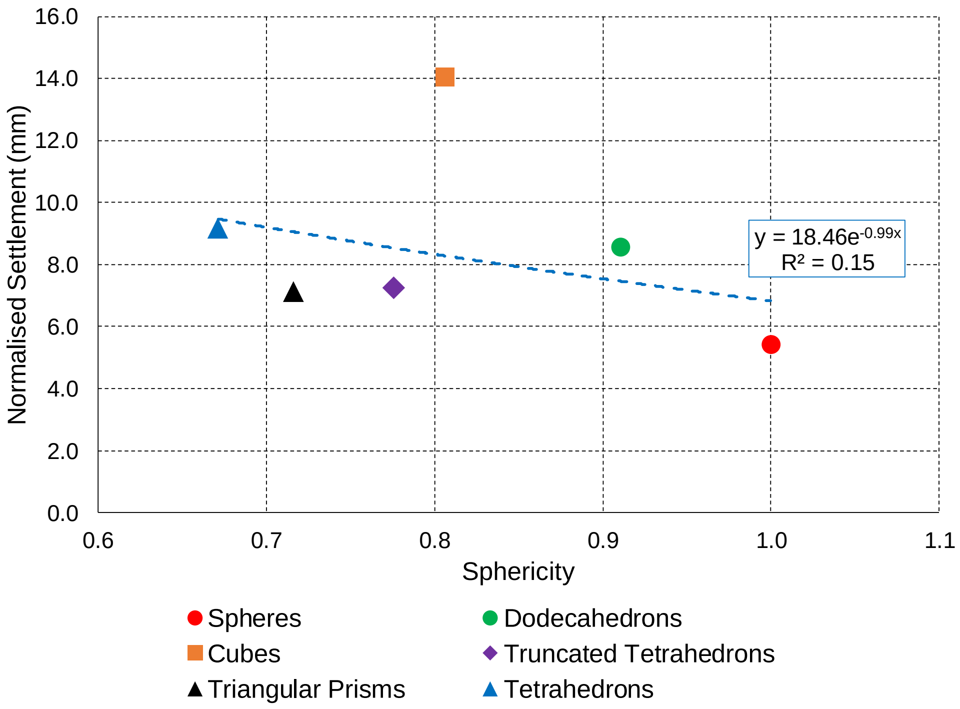

Figure C.1: Effect of sphericity on initial backfill settlements

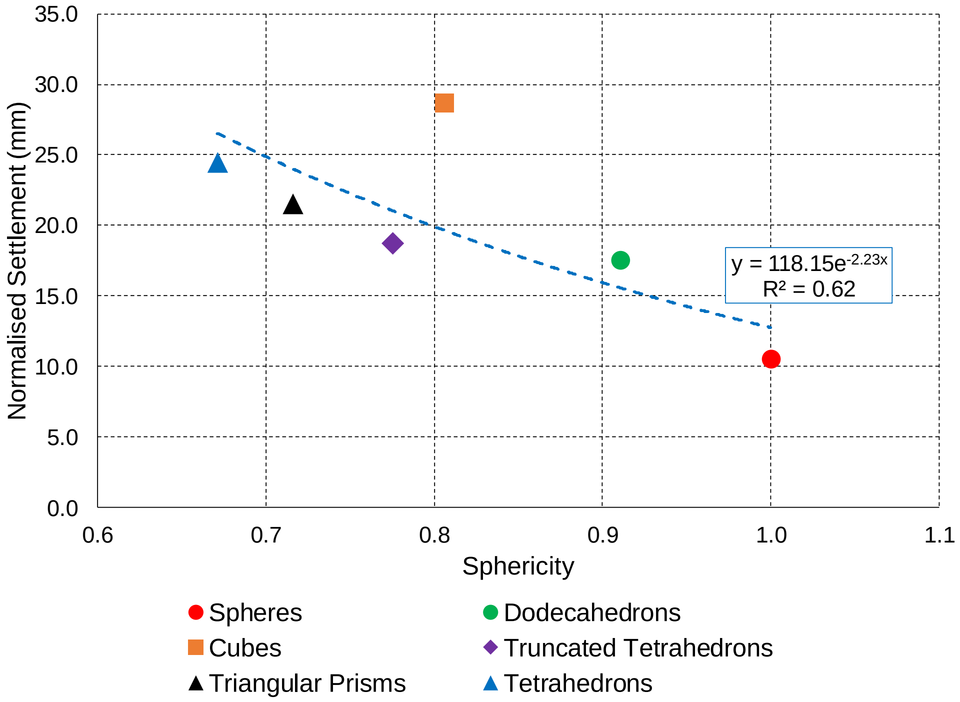

Figure C.2: Effect of sphericity on final backfill settlements

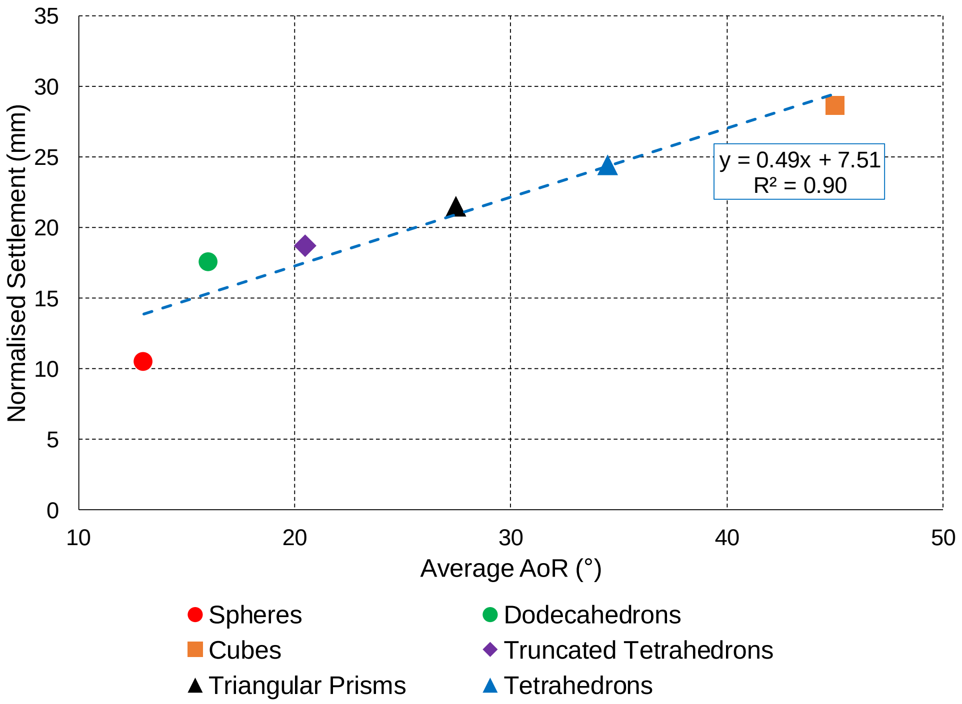

Figure C.3: Effect of average AoR on final backfill settlements

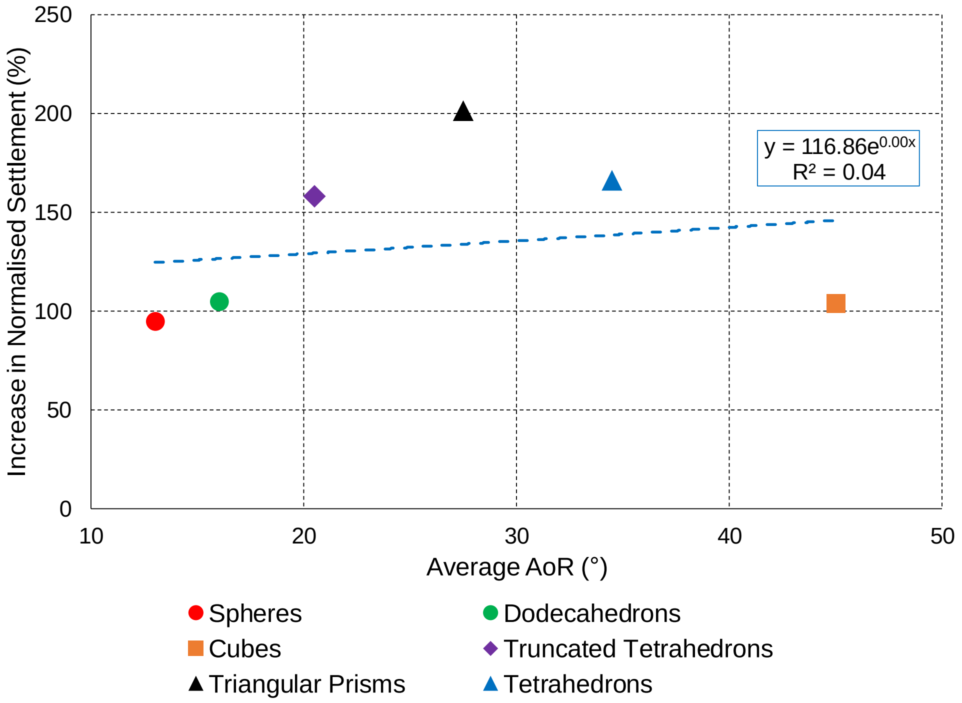

Figure C.4: Effect of average AoR on increase in backfill settlements